AALBORG UNIVERSITY
STUDENT REPORT

Master's Thesis

Performance Oriented Control of Digital Displacement Wind Turbine Transmission

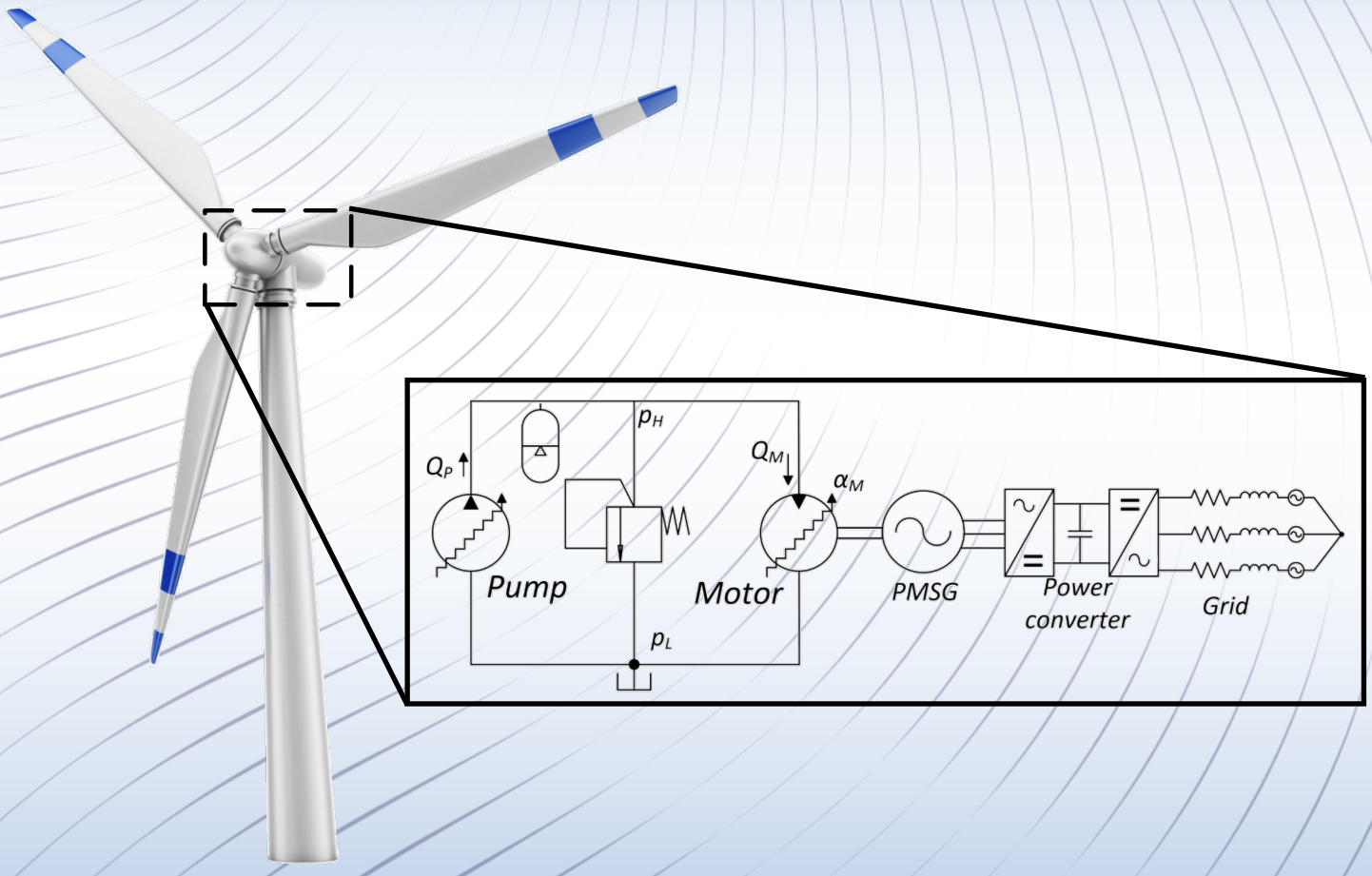

DEPARTMENT OF ENERGY TECHNOLOGY

10th MSc Mechatronic Control Engineering

MCE4-1024

June 1st 2017

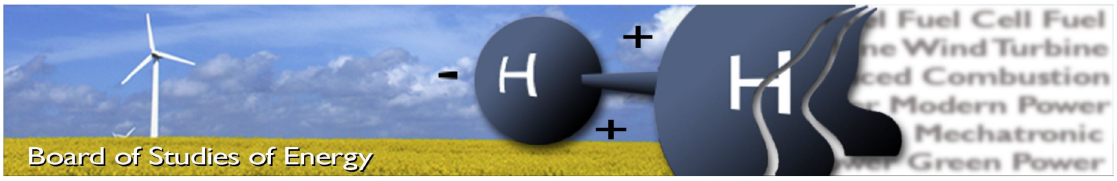

Title:	Performance Oriented Control of Digital Displacement Wind Turbine Transmission
Semester:	Mechatronic Control Engineering: 10^{th} Semester
Semester theme:	Master's Thesis in Mechatronic Control Engineering
Project period:	02.02.17 to 01.06.17
ECTS:	30
Supervisor:	Niels Henrik Pedersen & Torben O. Andersen
Project group:	MCE4-1024

Nicolai Krøgh Daugbjerg

Rasmus Kinch

Henrik Felthaus Hauge

Copies:	3
Pages, total:	209
Appendices:	7, A-G
Supplements:	2, A-B

SYNOPSIS:
The use of a Digital Fluid Power Transmission (DFPT), in a 5 MW offshore wind turbine is investigated in this thesis. The focus is to design a controller for the DFPT system to maximise the energy extraction. Mechanical and electrical requirements to the wind turbine are investigated to set up requirements for the system operation. The system consists of a DFPT, a generator and back-to-back converter, thus non-linear models of these systems are developed. To maximise the amount of energy extracted from the wind turbine, control systems for the DFPT, the generator and the grid side of the back-to-back converter are developed. The system performance is evaluated given a wind profile with a mean wind speed of 8 m/s and compared to a conventional wind turbine model (NREL). It was found that the DFPT system was able to perform comparable to the NREL in tip-speed-ratio tracking with an RMS error of 0.06. The stresses on the rotor axis of the DFPT and NREL reference turbines showed the DFPT added approximately 24.000 stress cycles, hence a relative larger accumulated fatigue damage compared to the NREL. A more detailed analysis of the mechanical structure must be conducted to estimate the expected lifetime.

By signing this document, each member of the group confirms that all participated in the project work and thereby all members are collectively liable for the content of the report. Furthermore, all group members confirm that the report does not include plagiarism.

Summary

The use of a hydrostatic transmission in a 5 MW offshore wind turbine is investigated in this thesis. To increase the efficiency a Digital Fluid Power Transmission (DFPT) is utilised. The DFPT is based on a technology called Digital Displacement® (DD) machines developed in the 1980s by a team on Edinburgh University. The basic idea is to utilise on/off valves to control the flow to and from a cylinder. Each machine consists of many cylinders, hence if the flow from one cylinder is not needed it can be set to idle, thus a high efficiency is obtained.

The main objective in this thesis is to develop a controller for the DFPT which is able to track the optimal Tip-Speed-Ratio λ^* as good as the NREL reference wind turbine, without violating the electrical and mechanical requirements. The mechanical requirement takes basis in a comparison between the NREL reference wind turbine and the wind turbine with the DFPT, where it is required to be as good or better than the NREL. The electrical requirements takes basis in simplified Danish grid codes from Energinet.

A non-linear model of the DFPT and electrical system is developed. The DFPT consists of both a DD pump, DD motor and an accumulator. The electrical part of the wind turbine consists of a Permanent Magnet Synchronous Generator (PMSG) and a back-to-back converter.

To control the system, different controllers are designed for the DFPT, the generator and for the grid side of the back-to-back converter. The DFPT is controlled by a discrete Linear Quadratic Regulator (LQR) controller which controls the pressure in the high pressure manifold of the DFPT. The generator is controlled by a Field Oriented Controller (FOC) with the objective to maintain a constant angular velocity of the generator. The grid controller is a Voltage Oriented Controller (VOC). A Phase Locked Loop (PLL) is used to control the frequency of the three phase voltage signals to allow for grid synchronisation. The active power P is controlled in order to obtain a somewhat constant DC-link voltage. The reactive power Q is controlled to be able to comply with the grid code requirements related to the power factor.

To be able to evaluate the system it was divided into two systems and two simulations due the comprehensive computational time, a simulation of the DFPT-PMSG and a simulation of the electrical grid respectively. The system performance is evaluated over a period of 700 seconds with a wind profile with a mean of 8/s as input. It was found that the DFPT system was able to follow the performance of the NREL, with the control objective of maximizing the energy extraction by maintaining an optimal tip-speed-ratio with an RMS error of 0.06 which is considered a small deviation. The mechanical evaluation and comparison with the NREL showed that due to the discrete nature of the DD machines the rotor shaft was exposed for approximately 24.000 extra stress cycles compared to the NREL, hence a relatively larger accumulated fatigue damage was seen. The evaluation of the electrical grid showed that it was possible to maintain a somewhat constant DC-link voltage i.e. the amount of power delivered by the generator was equal to the power injected to the grid. Furthermore, it was found that the simplified requirements was obeyed.

Preface

This report is written by MCE4-1024 at the Department of Energy Technology at Aalborg University in the spring of 2017. This report is the results of a 10^{th} semester project. The theme of the 10^{th} semester project is *Master's Thesis in Mechatronic Control Engineering*.

Acknowledgements
A special thanks goes to Tamas Kerekes and Kaiyuan Lu who have been helpful with answering questions regarding the electrical system. Thanks to Sergey Sorokin who have been helpful whenever questions regarding the mechanical analysis occurred.

The following software has been used in the process of writing this report:

- **MathWorks MATLAB** - for data analysis, visualisation and simulation of the dynamic model in correlation with Simulink.
- **MathWorks Simulink** - for dynamic modelling of the system.
- **Microsoft Visio** - for hydraulic drawings and block diagrams.

Reader's Guide: All used literature is listed in the bibliography at the end of the report, before the appendices, and will be in the following format:

{ Author(s) (Year), *Title*, Publisher, Edition, ISBN, URL }

ISBN and URL will be presented where applicable and available. The bibliography is sorted alphabetically after the surname of the first author. A specific reference in the text to an entry will appear as following:

[Author's surname (et al.), Year]

After the bibliography, relevant appendices describing derivations validation of methods etc. Supplements are included after the appendices containing the simulation constants and relevant material used during the project.

Nomenclature

General

Matrices are in upper-case boldface characters ($\mathbf{X}$).
Vectors are in lower-case boldface characters ($\mathbf{x}$).
Scalars are in light-face characters (x).

The system considered in this thesis consists of a hydraulic system and an electrical system. The hydraulic and electrical systems share many Greek and Latin symbols and subscripts. For ease of understanding, the Greek and Latin symbols and subscripts are divided up for the hydraulic system (including the general wind turbine theory) and the electrical system. The dimensionless symbols, operators and abbreviations are for both the hydraulic and electrical system.

Hydraulic System

Greek Symbols

Symbol	Unit	Description
α	$-$	Displacement fraction
β	bar	Bulk modulus
η	%	Efficiency
θ	rad	Angle
λ	-	Tip-speed ratio
ρ	$\frac{kg}{m^3}$	Density
σ	Pa	Stress
τ	Pa	Shear Stress
ϕ	rad	Closing angle of the valves
ψ	rad	Rotor blade pitch angle
ω	$\frac{rad}{s}$	Angular velocity
$\dot{\omega}$	$\frac{rad}{s^2}$	Angular acceleration

Latin Symbols

Symbol	Unit	Description
A	m^2	Area
B_v	$\frac{Ns}{m}$	Viscous friction
C_p	$-$	Power Coefficient
C_q	$-$	Torque Coefficient
D	m	Diameter
F	N	Force
FD	$-$	Fatigue damage
J	$kg\,m^2$	Inertia
k_f	$\frac{m^3/s}{\sqrt{Pa}}$	Valve Coefficient
L	m	Length
p	Pa	Pressure
P	$\frac{J}{s}$	Power
Q	$\frac{m^3}{s}$	Flow
r	m	Radius
T	Nm	Torque
T_s	s	Sampling time
t	s	Time
V	m^3	Volume
v	m/s	Wind velocity
x	m	Position
$\dot{x}$	$\frac{m}{s}$	Velocity
$\ddot{x}$	$\frac{m}{s^2}$	Acceleration

Subscripts

Symbol	Description
0	Linearisation parameter
abs	Absolute
air	Air
acc	Accumulator
atm	Atmospheric
c	Chamber
cl	Closing angle
cyl	Cylinder
e	Eccentric shaft
ef	Effective
err	Error
f	Fluid
g	Gas
H	High pressure manifold
HPV	High Pressure Valve
l	Lobes
leak	Leakage

Symbol	Description
L	Low pressure manifold
LPV	Low Pressure Valve
M	Motor
m	Module
max	Maximum value
min	Minimum value
mean	Mean value
nom	Nominal
oil	Oil
P	Pump
p	Piston
pr	Precharge
r	Rotor
v	Valve
w	wind
pipe	Pipe volume
tot	Total
%-air	Percent air content in oil

Electrical System

Greek Symbols

Symbol	Unit	Description
ϵ	rad	Sector Angle
η	%	Efficiency
θ	rad	Angle
λ	Vs	Flux Linkage
φ	rad	Power Factor Angle
ω	$\frac{rad}{s}$	Angular velocity

Latin Symbols

Symbol	Unit	Description
B_v	$\frac{Ns}{m}$	Viscous friction
C	F	Capacitance
D	[–]	Duty Cycle
d	[–]	Dwell Times
f	Hz	Frequency
i	A	Current
J	$kg\,m^2$	Inertia
$\mathbf{K_s}$	[–]	Transformation Matrix
L	H	Inductance

Symbol	Unit	Description
P	$\frac{J}{s}$	Active Power
PF	[−]	Power Factor
Q	VAR	Reactive Power
R	Ω	Resistance
S	VA	Apparent Power
T	Nm	Torque
t	s	Time
u	V	Voltage
Z	Ω	Impedance

Subscripts

Symbol	Description
α	α-axis
$\alpha\beta$	$\alpha\beta$-reference frame
β	β-axis
λ	Flux
abc	*abc*-reference frame
b	base value
d	Direct-axis
dc	Direct Current
el	Electrical
g	Generator
gd	Grid
l	Load
ll	line-to-line
M	Motor
max	Maximum value
mech	Mechanical
mpm	Maximum Flux Linkage
n	Nominal
pk	Peak value
pp	Pole Pairs
r	Rotor
s	Stator
sw	Switching
t	Transformer
q	Quadrature-axis
qd	*qd*-reference frame
tot	Total

Dimensionless Symbols

Symbol	Name	Description
i	Counter	Counter for number of similar components
k	Samples	Sample counter in the discrete model
N	Number	Describes a number

Operators

Symbol	Description
$\dot{x}$	First order time derivative
$\ddot{x}$	Second order time derivative
$\overline{x}$	Non-dimensional quantity
$\hat{x}$	Estimated value
x^*	Reference value
x^T	Transposed
s	Laplace operator
z	Discrete operator

Abbreviation

Symbol	Description
AC	Aternating Current
BDC	Bottom Dead Center
DC	Direct Current
DD	Digital Displacement®
DFIG	Doubly Fed Induction Generator
DFPT	Digital Fluid Power Transmission
DLTI	Discrete Linear Time Invariant
DSM	Delta Sigma Modulator
FAST	Fatigue, Aerodynamic, Structure and Turbulence
HP	High Pressure
HPM	High Pressure Manifold
HPV	High Pressure Valve
kW	Kilo Watt
LCOE	Levelised Cost of Electricity
LP	Low Pressure
LPM	Low Pressure Manifold
LPV	High Pressure Valve
MHI	Mitsubishi Heavy Industries

Symbol	Description
MIMO	Multiple Input Multiple Output
MPPT	Maximum Power Point Tracking
NREL	National Renewable Energy Laboratory
MW	Mega Watt
MWh	Mega Watt Hours
NC	Normally Closed
NO	Normally Open
O	Origo
O&M	Operation and Maintenance
PF	Power Factor
PLL	Phase Locked Loop
PMSG	Permanent Magnet Synchronous Generator
PMSM	Permanent Magnet Synchronous Motor
POC	Point of Connection
PWM	Pulse Width Modulation
RMS	Root Mean Square
RPM	Revolutions per minute
SISO	Single Input Single Output
SVM	Space Vector Modulation
SVPWM	Space Vector Pulse Width Modulation
TDC	Top Dead Center
TSO	Transmission System Operator
TSR	Tip Speed Ratio
VOC	Voltage Oriented Control

Contents

CHAPTER 1

Introduction

This Master's thesis serve to investigate the potential use of a hydrostatic transmission as drive train in a 5 MW horizontal axis wind turbine, where a controller must be designed for the hydrostatic transmission in order to maximise the energy extraction.
The project is a theoretical project, hence no experimental setup is used to evaluate the performance. Therefore, a non-linear model of the hydrostatic drive train is made and used to evaluate the performance. The first chapter will serve as an introduction to the field of hydrostatic based drive trains, starting from clarifying the potential of hydrostatic based drive trains and ending with a requirement specification for the system and the problem statement as seen in Figure 1.1.

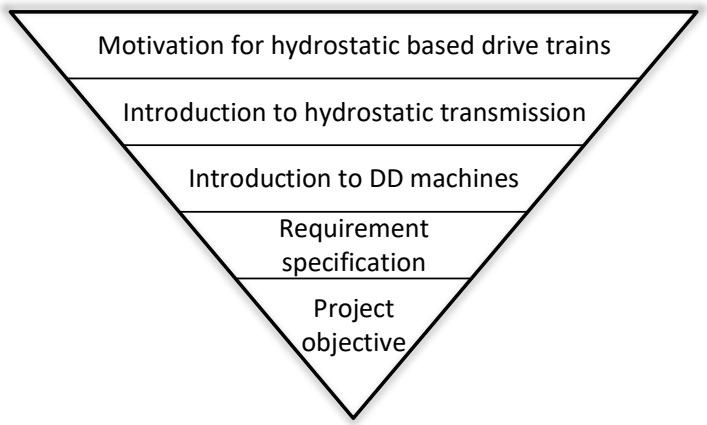

Figure 1.1: Illustrates the steps followed in the first part of the project until the project objective. As the triangle indicates the steps will be more specific along the process.

The steps illustrated in Figure 1.1 are described below:

Motivation for hydrostatic bassed drive train: To investigate the potential of hydrostatic based drive trains the general trends within wind power are investigated including global installed capacity and prices. The prices for a MWh produced by an offshore wind turbine are compared to other technologies and found to be twice as expensive as an onshore wind turbine Siemens [2014]. To be able to reduce the price per MWh a study of the reliability of commercial wind turbines is presented.

Introduction to hydrostatic transmission: In order to give the reader an understanding of the hydrostatic transmission based drive train, a description of the working principles of the hydrostatic transmission is outlined.
The basic idea behind the ***control*** of the hydrostatic transmission is described for maximum energy extraction.
In the end of this section the ***advantages and disadvantages*** of utilising a hydrostatic transmission are outlined. The main disadvantage is the efficiency of the machines utilised, hence a ***comparison of the efficiency*** of the conventional hydraulic machines and Digital Displacement® (DD) machines is carried out in order

to search for alternatives to the conventional hydrostatic drive train.

Introduction to DD machines: To allow for this report to be read without prior knowledge to DD machines, a detailed description of the working principle of the Digital Fluid Power Transmission (DFPT) is given. This includes a description of the DD pump and DD motor.
With the operation description the ***advantages and challenges*** utilising the DD machines will be scrutinised. Important challenges are control development and mechanical stress pulsations due to the discrete machine nature. In order to evaluate the DFPT a requirement specification for the system must be established.

Requirement specification: A requirement specification is outlined, in order to be able to evaluate the control and system performance. The requirement specification will be related to mechanical requirements and electrical requirements found in the Danish grid codes specifications.

Project objective: With the problems identified for utilising the DD machines in hydrostatic based transmission system and with the requirement specification it is possible to state the project objective.

1.1 Potential of Alternative Drive Trains

In the recent years wind energy has attracted increasing attention as an alternative energy source to fossil fuels. Concurrently with the increased attention, the size of the wind turbines has increased from 2 MW in 2000 (Vestas V80) to 8 MW with the wind turbine V164 from Vestas [MHI Vestas Offshore Wind, 2014]. As seen in Table 1.1 the globally installed wind capacity has also increased by 104% from 2011 to 2016. Due to the increased size of wind turbines and better wind conditions on the sea the wind turbines are moved out on the sea in large offshore wind farms. The total global offshore wind capacity has increased with 249% in the same period.

Year	Total Installed capacity[MW]	Offshore Capacity [MW]
2011	238,110	4,117
2016	486,746	14,384
Growth in %	104%	249%

Table 1.1: Shows total globally installed wind capacity and the offshore wind capacity in 2011 and 2016 and the growth in percentage [Fried, 2017].

However, the price of a MWh produced by an offshore wind turbine is higher compared to a MWh produced by an onshore wind turbine. A popular way to compare the cost of different technologies is by comparing the Levelised Cost of Electricity (LCOE) which is the ratio between the total cost over the lifetime of the wind turbine(including capital investment, operation and maintenance (O&M) costs, fuel price and financing costs) and the total energy production as given by the following relation [Siemens, 2014].

$$\text{LCOE} = \frac{\text{Total cost over lifetime}}{\text{Electricity produced over lifetime}}$$

A comparison of different technologies, based on the LCOE of the given technology, is seen in Table 1.2.

	Nuclear	Coal	Gas	Photovoltaics	Onshore Wind	Offshore Wind
LCOE $\left[\frac{€}{MWh}\right]$	79	63	60	145	81	140

Table 1.2: Comparison of the LCOE of different energy sources [Siemens, 2014].

As seen in Table 1.2 offshore wind is the second most expensive energy source after photovoltaics and is roughly twice as expensive as onshore wind turbines. Compared to fossil fuels the offshore wind turbines are roughly 2.5 times more expensive. Therefore, it is of great interest to decrease the LCOE of offshore wind energy. There are two ways to decrease the LCOE, either by decreasing the total cost of the wind turbine or by increasing the total amount of produced electricity. Some of the possibilities are listed below:

Total cost over lifetime:

- Decrease the capital investment of a wind turbine by reducing the production price of a wind turbine.
- Decreasing the O&M costs by minimising the number of failures.

Electricity produced over lifetime:

- Decreasing the number of failures in order to increase the operation time.
- Increase the output power of the wind turbines.

As listed, several of the possibilities include minimising the number of failures, i.e. maintaining a high effective operation time compared to the potential operation time (this ratio is also known as *availability*), hence the reliability of the wind turbine should be increased in order to increase the availability. Therefore, an investigation of the failures and the reason to them are conducted in the following section.

Reliability and Availability

In a report by ReliaWind an investigation of the reliability of large wind turbines were carried out, where each component contribution to the total downtime were scrutinised [Bueno Gayo, 2011]. The results are seen in Figure 1.2 and shows that the power module has the highest percentage of downtime contribution with approximately 38% where the frequency converter is the main contributor with approximately 17%. The mechanical drive train contributes with approximately 7% where the gearbox is the main reason for failure.

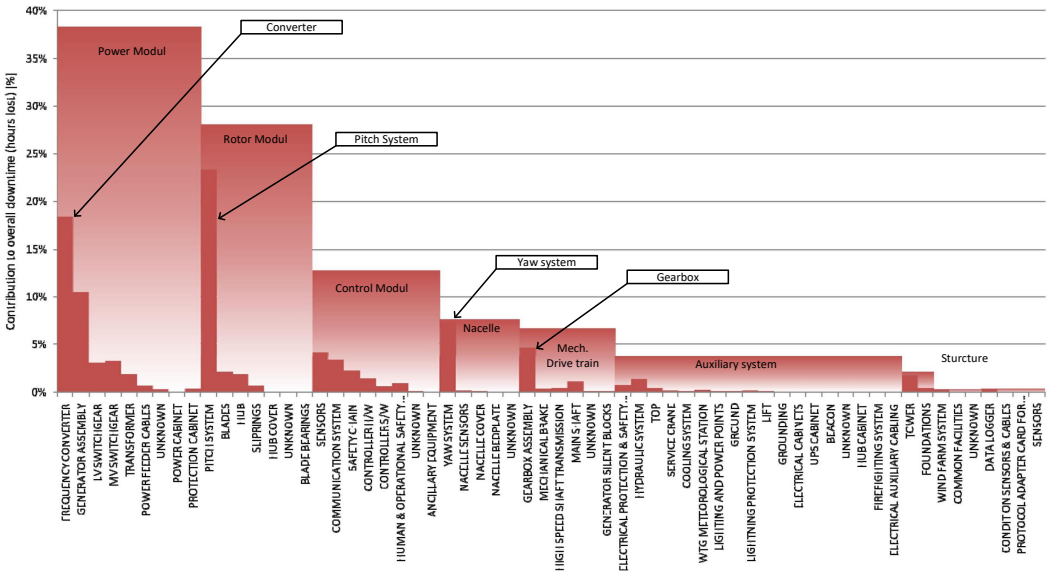

Figure 1.2: Contribution from individually parts to the total downtime. The parts are grouped under their respective subsystem [Bueno Gayo, 2011, p. 11](Modified).

The frequency converter and the mechanical drive train are both part of the drive train which converts the energy captured from the wind into electricity which can be send to the electrical grid. An alternative to the conventional gearbox, is the hydrostatic transmission based drive train. One of the main advantages of the hydrostatic transmission based drive train is the high power to weight ratio compared to the conventional gearbox. It may be possible to reduce the structural requirements of the tower and thus decrease the capital investment. Furthermore, it is theoretically possible to remove the frequency converter, if the generator can be driven at constant speed and hence deliver a constant frequency to the grid. This will be elaborated in the following section together with a detailed description of the hydrostatic based drive train concept.

1.2 Hydrostatic Transmission

Through this section the concept of a hydrostatic transmission based drive train will be explained by the use of the conventional hydraulic transmission seen in Figure 1.3. As seen in the Figure 1.3 the hydraulic system consists of a fixed displacement pump, which is directly connected to the rotor, an accumulator, a pressure relief valve and a variable displacement motor which is connected directly to a generator.
The blades captures energy from the wind with speed v, which drives the rotor with speed ω_r. The rotor drives a fixed displacement pump, hence generating a fluid flow, Q_P. The flow is lead to a variable displacement motor where the fluid flow, Q_M, drives the motor. The generator is directly connected to the motor shaft which rotates with speed ω_M. The accumulator is utilised to reduce the pressure ripples, which may occur due to wind gusts, or to store excessive energy. The pressure relief valve is a safety valve which is utilised in case of failures in the system, where the system pressure increases above the maximum allowed pressure in the system.
Due to the variable displacement motor, the gearing ratio is continuous in a given interval

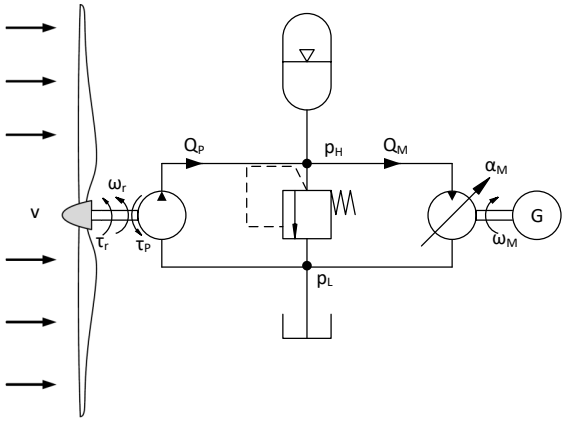

Figure 1.3: Conceptual drawing of a hydrostatic transmission system.

compared to fixed gears which have discrete ratio step. Therefore, it is possible to obtain a constant motor speed and generator. If the generator maintains a constant speed the frequency of the electrical output is constant, thus it is possible to obtain the same frequency as the grid, hence the need for a power converter, and thereby the source to 17% of the downtime, is eliminated. Removing the power converter eliminates the possibility of controlling the power factor. Thus it is difficult to predict the behaviour of the power factor.
The generator is an essential part of the drive train and converts the rotational energy of the motor into electrical energy. Conventional drive trains utilises mainly two generator topologies, Permanent Magnet Synchronous Generator (PMSG) or Doubly Fed Induction Generator (DFIG) as seen in Figure 1.4 and 1.5 respectively.

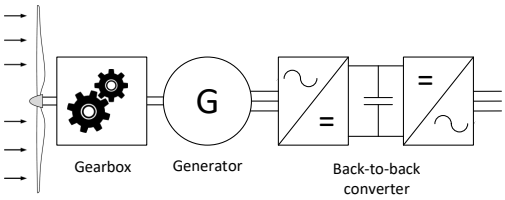

Figure 1.4: The rotor is connected to a gearbox which drives a fast rotating PMSG. Between the grid and the PMSG a full power back-to-back converter is needed. An example of a commercial wind turbine with this topology is the Vestas V164.

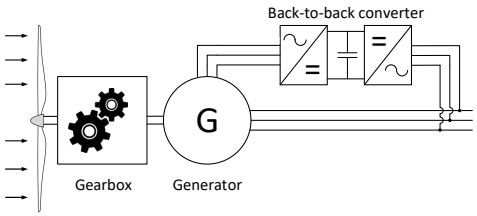

Figure 1.5: The rotor is connected to a gearbox which drives DFIG. Utilising the DFIG makes it possible to utilise a partial scale power converter which is used to excite the rotor windings. An example of a commercial wind turbine with this topology is the Sinovel SL6000.

They both utilise a power converter e.g. a back-to-back converter, in order to ensure the right frequency is delivered to the grid and to be able to control the active and reactive power which is related to the power factor (see Appendix E for explanation of reactive

and active power). The power converter utilised together with the DFIG is furthermore utilised to excite the rotor field windings, in order to generate a magnetic field. Hence the DFIG cannot be utilised without a power converter. The PMSG, however, has already a magnetic field due to the permanent magnets on the rotor. The power converter is utilised to control the frequency, reactive and active power thereby also the power factor. Since the PMSG has the theoretically capability of operating without the power converter, the PMSG is chosen for further investigation in this project.

To understand what the hydrostatic transmission system controls and how the generator can be used, the control of the system will be briefly explained in the section below.

Control of Hydrostatic Transmission

The main purpose of a wind turbine is to extract as much energy as possible from the wind. The power production is controlled by two control systems (transmission and pitch) operating below and above the rated wind speed v_r respectively. As seen in Figure 1.3 the pump is a fixed displacement pump, thus it is not possible to give a control input to the pump. The variable displacement motor however, can be controlled by controlling the displacement reference (α_M) to the motor.
One of the advantages of the hydrostatic transmission system is the theoretical possibility of removing the frequency converter. However, the motor is directly connected to the generator, hence the speed of the motor must be constant in order to maintain a constant frequency of the electrical output from the generator. However, since the motor is controlling the power production it cannot control the speed of the motor. The generator, however, can control the speed of the shaft, by controlling the torque of the generator, hence maintaining a constant frequency of the output. This solution does however require a power converter in order to control the speed of the generator.

Advantages Utilising Hydrostatic Transmission

Utilising the hydrostatic transmission has advantages, some of them have already been discussed however, they are summarised below for convenience [Roemer, 2014, p. 6]:

Robust under rugged conditions: Utilising a hydrostatic transmission mechanically decouples the generator from the rotor, since the power is transferred through the fluid. Thus the hydrostatic transmission will act as a filter, hereby making the transmission robust under rugged conditions.

High power to weight ratio: The hydrostatic transmission has a high power to weight ratio which may minimise the mechanical structure requirements e.g. tower strength, thus minimise the total cost of the turbine.

Energy storage: An accumulator is easily installed on the high pressure line for energy storage.

Even though the advantages of the hydrostatic transmission are appealing, there is a lack of commercial interest. This may be explained by the poor efficiency of conventional hydraulic machines compared to the relatively high efficiency of conventional drive trains. At 40% of rated power conventional drive trains have efficiencies above 90% [Roemer, 2014, p. 4], compared to approximately 85% and 75% for Bent-axis machines and Swash-

plate machines respectively as seen in Figure 1.6. An alternative to the conventional hydraulic machines are Digital Displacement® (DD) machines, a technology developed in the 1980s by a team at Edinburgh University. Mitsubishi Heavy Industries (MHI) utilised DD machines in their 7 MW wind turbine prototype, called SeaAngel, to improve the efficiency of the hydrostatic based drive train. A comparison of the conventional hydraulic machines and DD machines is therefore carried out in the following section to clarify the potential of DD machines as a replacement of the conventional hydraulic machines.

Efficiency Comparison

In Taylor et al. [2011] the efficiency and losses as a function of the relative displacement at 1500 RPM were examined for a DD pump, a bent-axis pump and a swash-plate pump. The results can be seen in Figure 1.6.

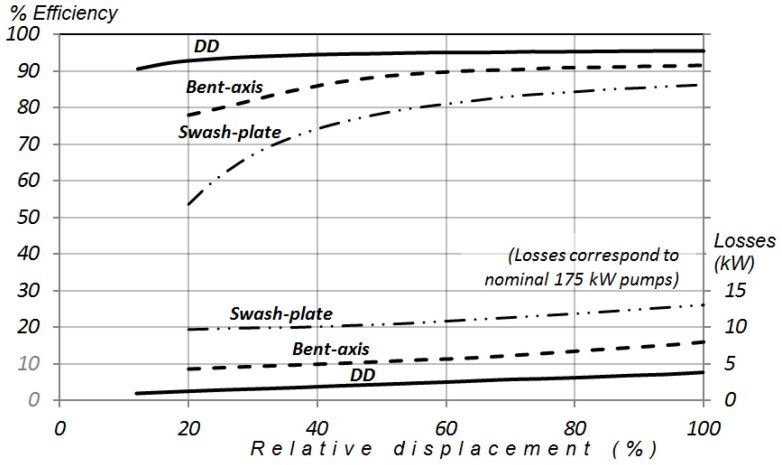

Figure 1.6: The efficiency and losses as a function of the relative displacement at 1500 RPM. The rated power for the pumps are 175kW [Taylor et al., 2011].

From Figure 1.6 it is clear to see the apparent advantage of utilising the DD pump. The efficiency for the DD pump does not get below 90%, even though the relative displacement is below 20%. Comparing this with the conventional hydraulic pumps i.e. Swash-plate and Bent-axis machines they get below 60% and 80% respectively when the relative displacement is 20%. Even at 100% the conventional pumps does not reach the efficiency of the DD pump. There is created a basis for utilising the DD pumps instead of the conventional pumps. Thus a more detailed investigation of the working principles of the DD machines is needed. This investigation will be carried out in the following section.

1.3 Working Principle of DD Machines

The hydrostatic transmission based on the DD machines will be referred to as Digital Fluid Power Transmission (DFPT) throughout the rest of the report. The DFPT considered in this project can be seen in Figure 1.7.
The DFPT consist of a fixed DD pump, a DD motor, an accumulator and a pressure relief valve as seen in Figure 1.7. The workings of the DFPT are similar to the conventional

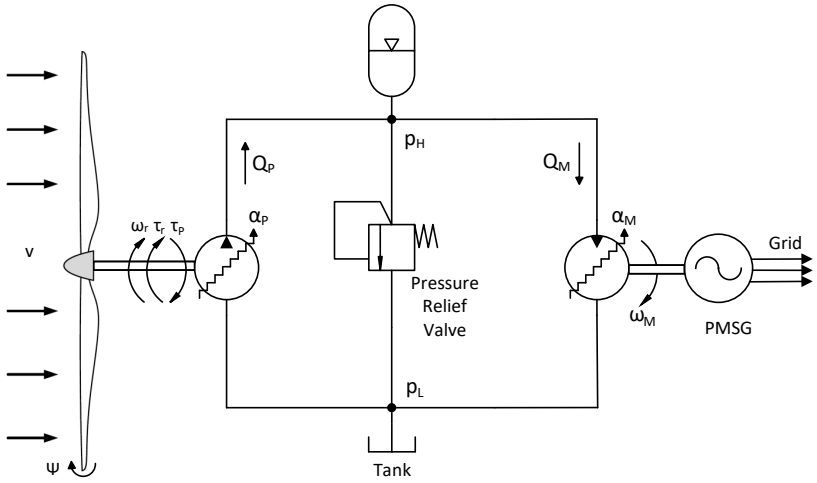

Figure 1.7: Sketch of the DFPT together with the generator and the rotor. The DFPT consists of a fixed displacement DD pump and a variable displacement DD motor.

hydrostatic transmission described in Section 1.2. Therefore, the accumulator and the pressure relief valve will not be explained in detail. Instead, this section will focus on a detailed description of the DD pump and DD motor, which are the main difference between the conventional hydrostatic transmission and the DFPT, starting with the DD pump in the next section, then followed by the DD motor. The description will be based on the 7 MW wind turbine prototype design for the SeaAngel from MHI.

Digital Displacement Pump

The DD pump is based on circular modules, where each module consist of a large number of cylinders radially mounted and evenly distributed in the module. The flow to and from the cylinders are controlled by two fast switching seat valves (on/off valves), one controlling the flow from the low pressure manifold (LPM) and one controlling the flow to the HPM. A DD pump, with four modules and 32 valves in each module, is illustrated in Figure 1.8.

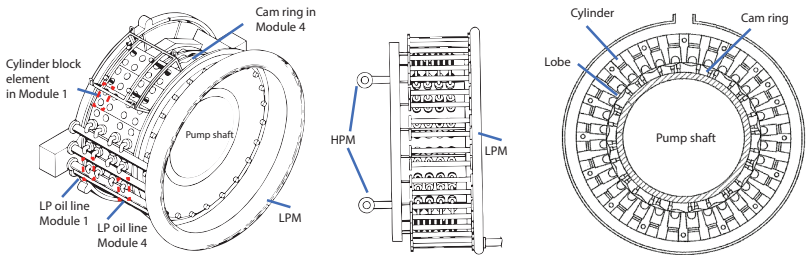

Figure 1.8: Prototype of the DD pump. Left: Overview of pump where all four modules are shown. Middle: Side view of pump where the HP lines are shown. Right: Cross sectional view of pump where the cam ring, 32 cylinders and 24 lobes are illustrated [Kameda et al., 2014] (modified).

On the surface of the shaft a cam ring is attached as illustrated in Figure 1.9. The cam ring consist of 24 lobes which have sine wave like shape as indicated in the figure. The cam ring based design of the DD pump is chosen due to the high torque input from the rotor and relatively low rotor speed.

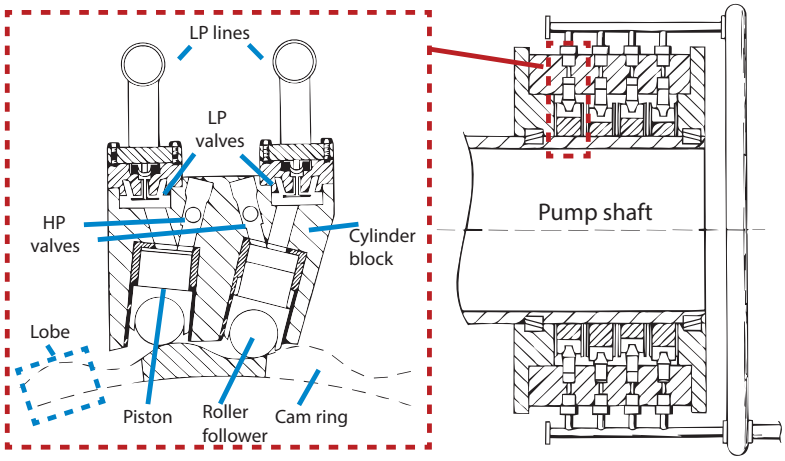

Figure 1.9: Side cross sectional view with zoom of one cylinder block with a cam ring, two cylinder chamber volumes and the connected valves [Kameda et al., 2014] (modified).

The low rotor speed would result in a relatively small pump flow unless the number of cylinders is increased, making the pump big and heavy. However, with the cam ring design the speed of the cylinders point of view, is proportional to the number of lobes, N_l, in a cam ring as seen in the following relation:

$$\omega_c = \omega_r \cdot N_l$$

Thus each cylinder goes through the number of lobe cycles for each revolution of the pump shaft which increases the pump flow without increasing the size of the pump. Hereby a large displacement volume is obtained and hence high torque, while the pump shaft speed is low.
As seen in Figure 1.9 the cylinders are connected to the cam ring via a roller bearing. A detailed description of the workings of the cylinder will be carried out in Section 1.3.1 in the end of this section.

Digital Displacement Motor

The difference between the DD motor and DD pump is that the DD motor is a fast rotating machine, hence the lobes are replaced by an eccentric shaft. The DD motor consist, as the DD pump, of modules where each module has a large number of cylinders radially mounted and evenly distributed in the module. The eccentric shaft is directly connected to the generator shaft hence the speed of the motor is equal to the speed of the generator. A sketch of the DD motor is seen in Figure 1.10 where a front view of the DD motor is illustrated to the left and a cross sectional sketch is displayed to the right.
As seen in Figure 1.10 (to the right) the cylinders are connected to the eccentric shaft

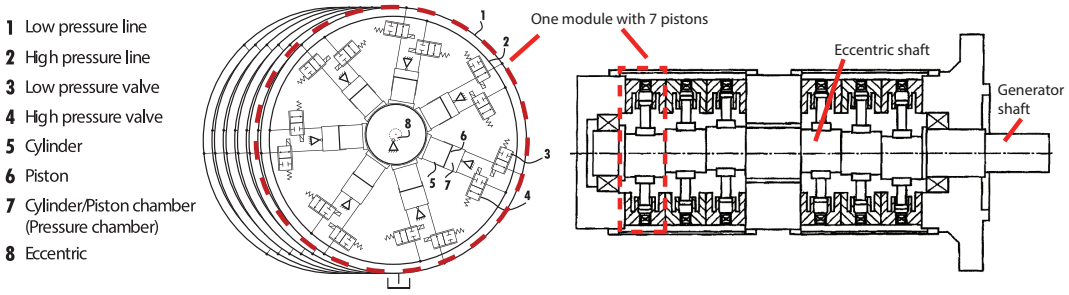

Figure 1.10: Left side: Front view sketch of a DD motor Sniegucki et al. [2013],[Pedersen, 2016*b*] (modified). Right side: Cross sectional sketch of a DD motor [Kazuhisa, Tsutsumi; Atsushi, Maekawa; Masayuki, Shimizu; Stephen, Salter; Uwe, Stein; William, Rampen; Robert, Fox; Hauke, 2010] (modified)

and the flow to and from the cylinder chamber is controlled by two seat valves (on/off switching valves). The workings of a single chamber is explained in detail in Section 1.3.1.

1.3.1 Operation Principles of DD Machines

This section serves to give a detailed description of the working principle of the DD machines which is needed to yield an understanding of the working of the DFPT. Being able to describe the operation principles, a definition of the valve actuation is needed, hence this section will contain the following:

- Definition of control strategy for valve actuation.
- Description of the operation principles of the DD machines.

Control Strategy of Valves

Three operation modes are based on a full stroke strategy, meaning that the decision to either idle (in-active cylinder) or initiate a pumping/motoring stroke (active cylinder) for each cylinder is made only once per revolution of the pump/motor shaft respectively. Utilising the full stroke strategy the control signal to the valves is synchronously updated, since the valves are equally distributed in the module. This strategy is chosen to allow for the use of classical discrete control theory.

Furthermore, considering the energy efficiency of the operation of the DD machines, it is possible to utilise passive actuations of the valves by using the kinetic energy in the cylinder pistons during operation of the DD machines. The idea is to avoid opening against high pressures which may be achieved by proper operation of the DD machines. Hereby it can be avoided to use double acting valve coil actuators and instead use a single acting which is used to actively close the valves (the timing of the actuation signal is of great importance, thus these will be denoted by *italic text* in the following subsections). The opening of the valves will thus be achieved by passive actuation such as pressure forces and e.g. a passive spring. The active closing and passive openings are further elaborated in the following explaining the operation principles of the DD machines.

The operation principles will be explained in the following manner:

- Pumping stroke
- Motoring stroke
- Idling stroke

where the idle operation principle will be explained in general since both the DD pump and DD motor are able to idle.

Pumping Stroke

The operation principle of the DD pump is based on the generalised single cylinder chamber in Figure 1.11 and the signals for one pumping stroke illustrated in Figure 1.12. The generalised sketch of the DD pump consists of a cam ring, a piston, the connected valves to the cylinder chamber pressure and arrows indicating the movements.

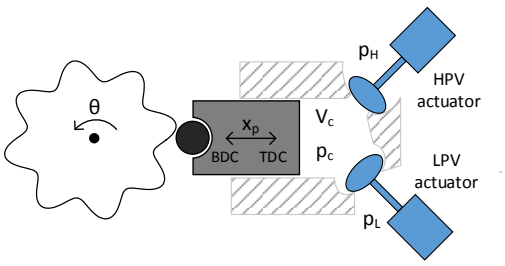

Figure 1.11: Conceptual drawing of a single chamber in the pump.

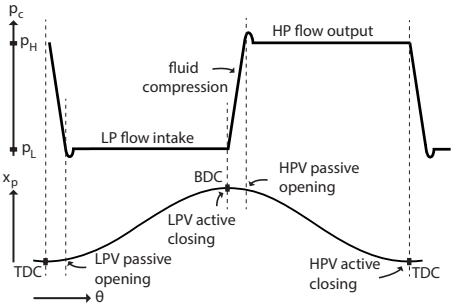

Figure 1.12: Illustrates the behaviour of the chamber pressure as the position of the piston changes.

The end positions of the piston stroke are defined as:

- Top Dead Center (TDC): Defined where the chamber volume V_c is at minimum.
- Bottom Dead Center (BDC): Defined where the chamber volume V_c is at maximum.

The operation principle will be elaborated in the following, starting the position of the piston in TDC.

As the cam ring rotates the piston moves towards BDC causing an increase in the chamber volume. This results in a suction effect inside the chamber, since no flow is fed into the chamber (the HPV is held closed by pressure force from the high pressure manifold p_H), leading to a passive opening of the LPV since $p_c < p_L$. In order to initialise the pumping stroke, the *LPV is actively closed* such that it is fully closed at BDC. Since both valves are closed and the piston compresses the fluid inside the chamber, the pressure p_c increases causing a passive opening of the HPV since $p_c > p_H$. The LPV is held closed since $p_c > p_L$. The HPV is open, hence high pressurised fluid is led to the HPM defining the pumping stroke. The pumping stroke is ended at TDC, where the *HPV is actively closed* in order to avoid a counter acting force from the piston. Hereby, the operation cycle is repeated where the low pressure flow intake is initialised.

Motoring Stroke

The operation principle of the DD motor is based on the generalised sketch in Figure 1.13 and the signals for one motoring stroke is illustrated in Figure 1.14. The generalised sketch consists of an eccentric shaft, a piston, the connected valves to the cylinder chamber volume and arrows indicating the movements.

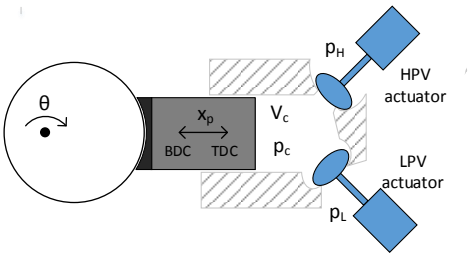

Figure 1.13: Conceptual drawing of a single chamber in the motor.

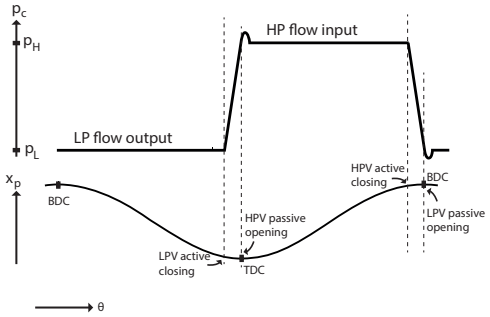

Figure 1.14: Illustrates the behaviour of the chamber pressure as the position of the piston changes.

The operation principle will be elaborated in the following, starting the position of the piston in BDC. It is assumed that the eccentric shaft contains sufficient kinetic energy, such that it is able to drive the piston. The piston movement is needed in order to obtain a proper functioning of the DD motor.

As the eccentric shaft rotates the piston moves towards TDC hereby outputting the de-pressurised fluid flow to the low pressure manifold since the LPV is open and HPV is held closed by pressure force from the HPM ($p_c < p_H$). In order to obtain a proper initialisation of the motoring stroke, the HPV must be fully open exactly at TDC. This is achieved by *actively closing the LPV* near TDC creating a rapid fluid compression inside the chamber such that $p_c > p_H$ hereby passive opening the HPV. The LPV is held closed by the pressure force ($p_c > p_L$). The eccentric shaft is hereby driven towards BDC by the high pressure force from the chamber fluid defining the motoring stroke. The LPV must be fully open at BDC in order to avoid a counter acting force from the piston, which requires that the *HPV must be actively closed* before reaching BDC. Since no flow is fed to the chamber and the chamber volume expands, a suction effect is created inside the chamber causing the LPV to passively opens ($p_c < p_L$). When the LPV is fully open the operation cycle is repeated where the low pressure flow is led to the LPM. The chamber pressure is kept at low pressure level at $p_c \approx p_L$ since the LPV is open throughout the entire cycle as indicated in Figure 1.15.

Idling Stroke

The idling mode is the key advantage of the DD machines. Since both the DD pump and DD motor are able to idle, the idle operation principle will be explained in general thus both Figure 1.11 and Figure 1.13 can be used as reference. An idling stroke is illustrated in Figure 1.15 showing the pressure levels, the piston movement and the state of the LPV

and HPV respectively. A state of 0 indicates fully closed whereas a state of 1 indicates fully open.

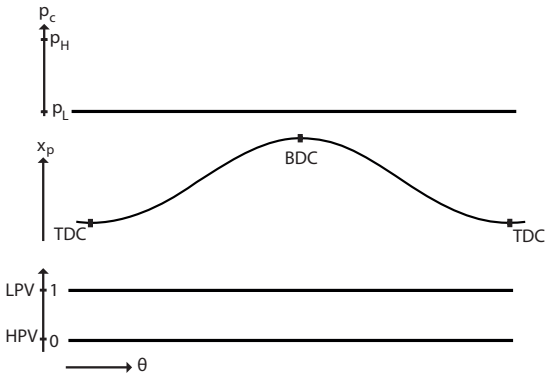

Figure 1.15: Illustrates the behaviour of the chamber pressure as the position of the piston changes during an idling stroke.

As the piston inside the cylinder goes from TDC to BDC the chamber volume increases. The increasing volume creates a suction effect which keeps the LPV passively open ($p_c < p_L$), hence no need for a actuation force to keep the LPV open. This allows for the oil to be displaced to and from the LPM, where the effective displacement of the chamber fluid is zero, without any significant pressure losses hereby obtaining a larger efficiency of the DD machines.

Timing of the Valve Actuation

One of the most important things in operation of the DD machines is the timing of the closing signals to the valves. If the timing of the valves are off, the efficiency of the DD machines will be lowered or the machine will not operated as intended. In the worst case the DD machines will not work at all. This is one of the challenging parts of DD machines, since in order to obtain the highest efficiency the valves should be closed near BDC or TDC (ideally at BDC or TDC), however, this is not possible due to the dynamics of the valves. As a result of this, the closing signals must be given before reaching BDC/TDC. The timing of the valves thus becomes a trade-off decision between efficiency and functional operation, where the functional operation is the most important constraint. This means that the valves must be closed rather to early than late on the cost of efficiency. The following section will briefly focus on the advantages and challenges using DD machines.

1.4 Advantages and Challenges using DFPT

Utilising DFPT gives the same advantages as the conventional hydrostatic transmission and adds additional advantages to the list. These are briefly described below.

High efficiency: The DD machines have high efficiency, since inactive cylinders can be set to idle, hence keeping the pressure loss across the cylinder at a minimum.

Fast response: The DD machines have relatively high bandwidth, thus being able to go from minimum to maximum displacement during a half revolution.

Cooling requirements: Due to the high efficiency the cooling requirements of the oil are reduced [Artemis, 2017].

Scaleability: DD machines are easily scaled due to the module based structure.

Maintainance: Most of the components in a DD machine can be swapped out utilising an internal crane within the nacelle [Artemis, 2017].

Despite the advantages mentioned there are some challenges utilising the DD technology which are described below.

Pressure/torque pulsations: Due to the discrete nature of DD machines pressure ripples and torque ripples are present in the system which may lead to additional mechanical stress to the system.

Control of the system: The control of the valves must be accurate in order to reach a high efficiency. Furthermore, a proper control sequence with the right timing must be found due to the high number of cylinders.

In order to be able to evaluate the control performance a requirement specification must be outlined in order to do so. This is done in the following section.

1.5 Requirement Specification

To be able to evaluate the performance of the DFPT a requirement specification is outlined. This requirement specification will be based on electrical requirements and mechanical requirements. The mechanical stress requirements are related to influence of torque pulsations, in the DFPT, on the wind turbine structure while the grid requirements are related to the power factor and frequency delivered on the electrical grid. These requirements will be further described in the following.

1.5.1 Mechanical Stress

In order to evaluate the influence of the torque ripples, in relation to the mechanical structure of the wind turbine, an analysis of the mechanical stresses is carried out. It is chosen to limit the analysis to focus on the rotor shaft to give an indication of, whether the torque ripples are problematic. This delimitation is based on assuming the blades and hub to be a rigid body, thus the interaction from the blades and hub does not alter the analysis at the rotor and generator shaft. This assumption is considered valid for the purpose of this study, however, in general this assumption does not hold true since there will be damping of the torque interaction between these components.

Furthermore, it is chosen to use the NREL reference 5 MW wind turbine with mechanical gearbox as benchmark for the torque ripples. This comparison method is chosen, since the NREL reference model is readily available to the authors through the open-source software tool FAST ((Fatigue, Aerodynamic, Structure, and Turbulence), developed by [Jonkman et al., 2009] and provided by the group's supervisor [Pedersen, 2016*a*]. Hereby, the comparison criteria can be created utilising the same simulation data available for both the NREL with mechanical gearbox and NREL with DFPT.

The mechanical stresses on the rotor shaft are related to the torques illustrated in Figure 1.16 showing the NREL with mechanical gearbox, and Figure 1.17 showing the NREL with DFPT. The generator torque, T_G', in Figure 1.16 is transformed to the rotor side through the gearing ratio of 97.

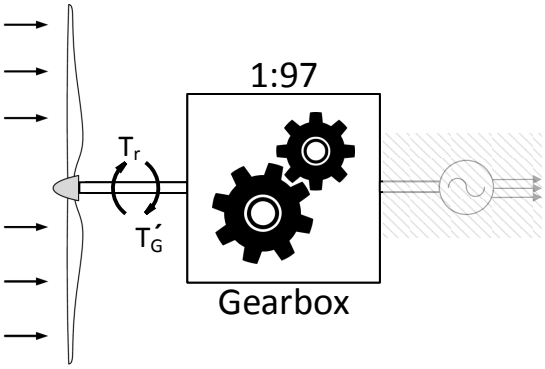

Figure 1.16: Torque on rotor shaft for 5 MW NREL wind turbine with mechanical gearbox.

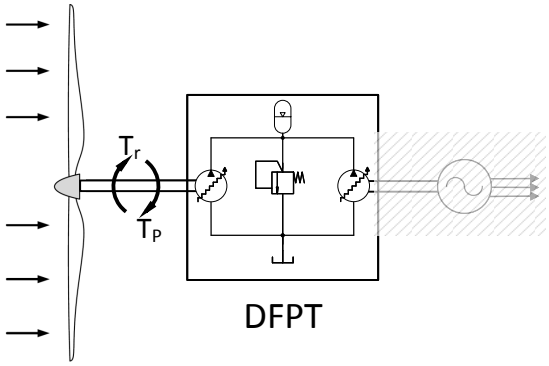

Figure 1.17: Torque on rotor shaft for 5 MW NREL wind turbine with DFPT.

The loading history on the rotor shaft is achieved from simulation data from FAST for the 5 MW NREL reference wind turbine. The output data, used for this comparison, is the torques, forces and bending moments acting on the shafts, which are needed in the evaluation of the torque ripples.

The result of the stress analysis is a fatigue damage calculation, which is a measure of, how much the shaft is damaged when exerted to a number of load cycles. The calculation of the fatigue damage requires five comprehensive steps and thus only the final result of this analysis is presented in this section. A detailed description of the analysis is presented in Appendix B.

In order to create the benchmark of the fatigue damage calculation, the NREL wind turbine model is simulated for 700 seconds given a wind profile with mean wind speed of 8 m/s. By measuring the torques, forces and bending moments at the main rotor shaft and conducting step 1-5 of the stress analysis, the fatigue damage value, FD, is found and is given in Table 1.3. The fatigue damage value for the NREL with mechanical gearbox acts as a maximum acceptable threshold for the NREL DFPT as indicated in Figure 1.18.

Requirement	Value
Fatigue damage FD	$8.2 \cdot 10^{-11}$ [-]

Table 1.3: NREL benchmark fatigue damage.

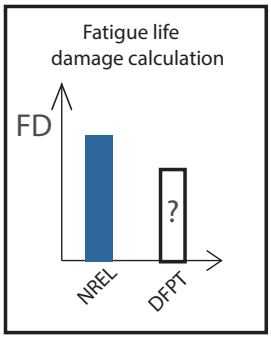

Figure 1.18: Final step of stress analysis.

A fatigue damage value of zero may be seen as unloaded and never used component, whereas a value of one indicates a failed component. The low fatigue value in Table 1.3 thus indicates a low fatigue damage. This is also expected and is considered feasible since the material is chosen to be high strength steel combined with the relatively low number of cycles observed in the 700 seconds of simulation.

Having obtained the benchmark for the mechanical requirement, the electrical requirements will be investigated in the following section.

1.5.2 Electrical Grid

The purpose of this section is to investigate the electrical requirements for connection of a 5 MW wind turbine to the electrical grid.

For evaluation of the electrical performance of the hydrostatic transmission based drive train it is chosen to evaluate the requirements based on the grid codes from the Danish national transmission system operator Energinet.dk [2016].

Requirement Delimitation

The 5 MW power rating, for the NREL wind turbine, is defined as a category C wind turbine in the grid codes by [Energinet.dk, 2016, p. 21]. A category C wind turbine has a power rating in the range of 1.5 MW to 25 MW, thus the following requirements will be described for the wind turbine in category C.

The electrical grid requirements for a 5 MW wind turbine are considered comprehensive by review of the grid codes. The majority of the requirements are related to protective measures in case of grid instabilities for both the wind turbine and electrical grid. The grid codes can be separated into the following two categories:

- Performance oriented requirements.
- Wind turbine and electrical grid safety requirements.

In this project the objective is to evaluate the performance of the DFPT, hence the grid is assumed to be faultless, thus the large amount of comprehensive security measures are

disregarded. The security measures should of course be considered before installation but is for this project considered out of the scope.

From Energinet.dk [2016] the following performance oriented requirements will be investigated:

- Voltage range, U
- Frequency range, f
- Power factor, PF

The voltage range, frequency range and power factor requirements will be investigated individually in the following sections and in the end of this chapter the requirements will be outlined in a table. Some of the requirements are overlapping and the requirements utilised will be marked with **blue** and the requirements disregarded are marked with **red** in the following figures.

Voltage and frequency range

The wind turbine is connected to the electrical grid as shown in Figure 1.19 where the focus, in this project, is on the *normal operating voltage* range of the wind turbine electrical system at the Point of Connection (POC), U_{POC}, shown to the left of the grid connected transformer. The transformer and the electrical grid connection point, U_{grid}, within the red dotted hatched rectangle indicates that the requirements from these components are not in scope of this project. In Section 5.3 the voltage of the electrical system will be specified at the POC, U_{POC}, for the wind turbine.

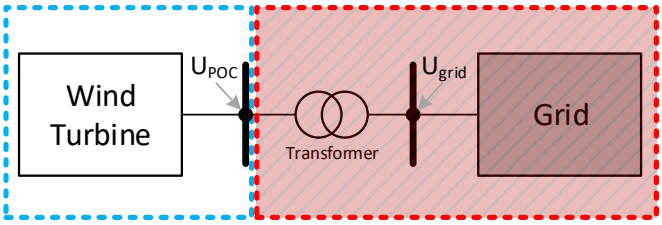

Figure 1.19: Normal operating voltage at wind turbine electrical system for the POC to grid transformer. The black bars at U_{POC} and U_{grid} indicate that these points are the Points of Common Coupling (PCC), meaning that additional components can connect at these points.

The voltage range and frequency range of the electrical system are specified in Figure 1.20. The figure show the frequency on the horizontal axis and the voltage on the vertical axis. The normal production area for the voltage and frequency is in the range 49 to 51 Hz [Energinet.dk, 2016, p. 30] and an allowable voltage deviation of $\pm 10\% \cdot U_{POC}$ to the transformer at the POC. These voltage and frequency ranges are chosen as the allowable operating range for the DFPT performance evaluation.

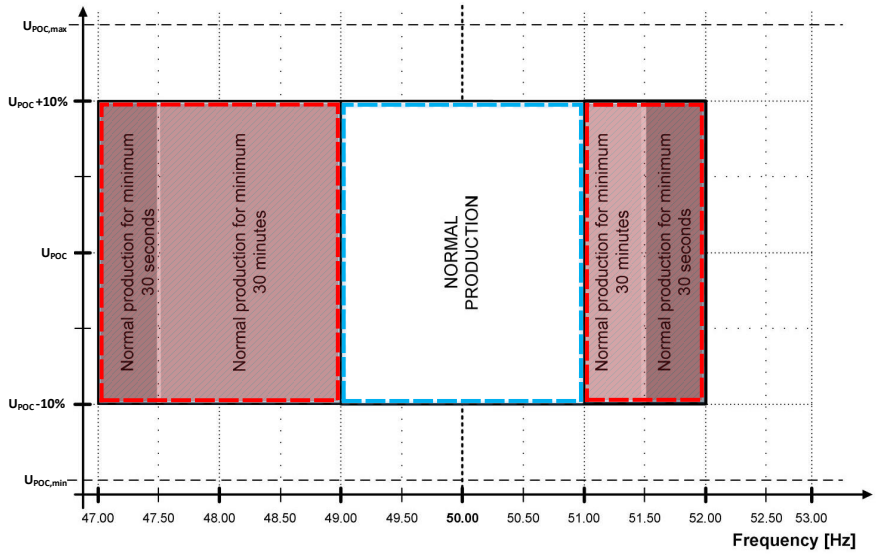

Figure 1.20: Normal operating voltage range and frequency operation range [Energinet.dk, 2016, p. 30] (Figure modified).

In Figure 1.21 the electrical system of the wind turbine is shown where the frequency f from the electrical grid at POC is input to the grid side part of the back-to-back converter. The grid side of the back-to-back converter must be able to deliver the same frequency as the grid frequency defined in the range of 49 to 51 Hz during normal production.

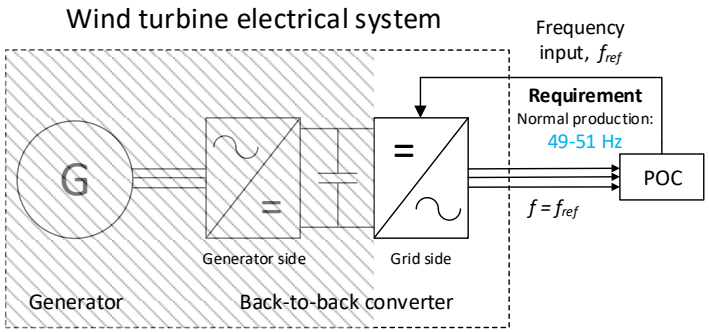

Figure 1.21: Frequency input to the electrical system of the wind turbine. The hatched area indicate that this part of the wind turbine electrical system does not have significant influence on the frequency control at POC to the grid since the DC-link in the back-to-back converter decouples generator side with grid side.

Power factor

The electrical system of the wind turbine must have the ability to control the power factor and the operating range for the export of active power and the export and import of reactive power. These requirements are specified in Figure 1.22 and Figure 1.23 where the hatched areas marked within the blue dotted lines indicate the allowable operating ranges.

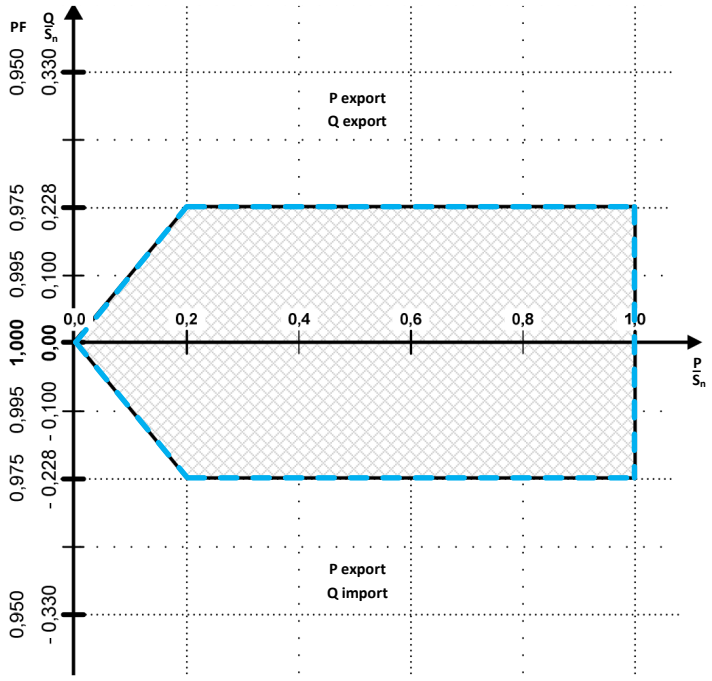

Figure 1.22: Requirements for reactive power delivery in relation to active power [Energinet.dk, 2016, p. 62] (Figure modified).

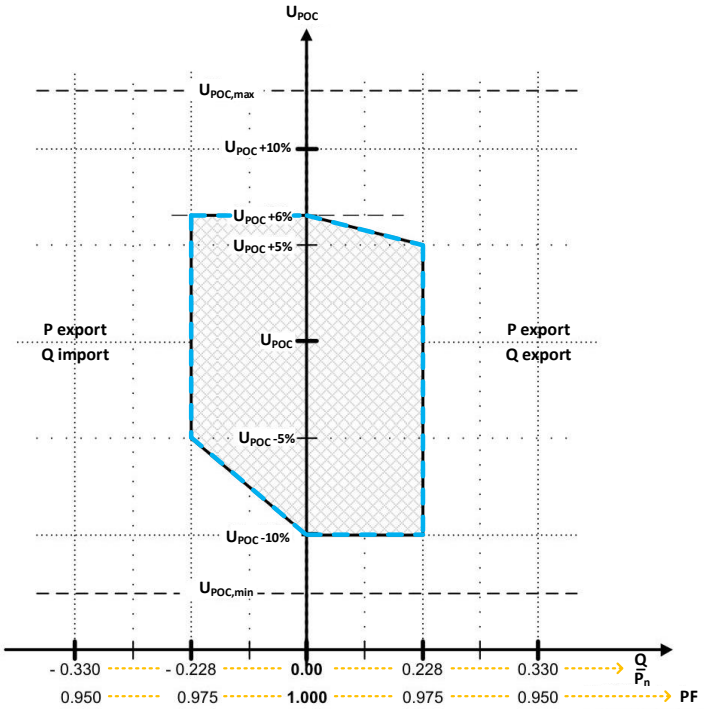

Figure 1.23: Requirements for reactive power delivery in relation to U_{POC} [Energinet.dk, 2016, p. 63] (Figure modified).

For better understanding of the figures, the variables on the axes of the figures are explained below, and the electrical theory describing the correlation between power factor

and the active and reactive power is given in Appendix E.

- $\frac{P}{S_n}$: The numerator is the active power P exported from the wind turbine electrical system. The denominator is the nominal apparent power S_n of the wind turbine electrical system, which is a constant value. The variable $\frac{P}{S_n}$ is therefore a normalised ratio between active power in relation to the constant apparent power of the wind turbine electrical system.
- $\frac{Q}{S_n}$: The numerator is the reactive power Q exported or imported from the wind turbine electrical system. The denominator is the nominal apparent power S_n of the wind turbine electrical system, which is a constant value. The variable $\frac{Q}{S_n}$ is therefore a normalised ratio between reactive power in relation to the constant nominal apparent power of the wind turbine electrical system.
- PF: PF is the power factor, where the power factor angle is $\varphi = arctan(\frac{Q}{P})$ from Appendix E, given as the ratio of the reactive power in the numerator to the active power in the denominator, and the power factor then is $PF = cos(\varphi)$.
- $\frac{Q}{P_n}$: The numerator is the reactive power Q exported or imported from the wind turbine electrical system. The denominator is the rated active power P_n of the wind turbine electrical system, which is a constant value. The variable $\frac{Q}{P_n}$ is therefore a normalised ratio between reactive power in relation to the constant rated active power of the wind turbine electrical system.
- U_{POC}: U_{POC} is the voltage of the wind turbine electrical system at the POC.

Having obtained an understanding of the variables used on the axes in Figure 1.22 and Figure 1.23 the meaning of the figures will be described below:

Figure 1.22 shows that when the normalised power decreases then the requirement to the power factor increases, thus the amount of allowable exported or imported reactive power must be reduced.

Figure 1.23 shows the allowable voltage range from the POC voltage depending on the power factor. In the case where reactive power is exported and the power factor decreases, the maximum allowable voltage range decreases for the positive range from $U_{POC} + 6\%$ to $U_{POC} + 5\%$ of the voltage range, while the negative range remains at $U_{POC} - 10\%$. For the case where reactive power is imported and the power factor decreases, the maximum allowable voltage range remains at $U_{POC} + 6\%$ while the negative range decreases from $U_{POC} - 10\%$ to $U_{POC} - 5\%$ of the voltage range.

Summary of grid requirements

The chosen grid requirements, based on the previous section, for performance evaluation of the DFPT during normal operation are summarised in Table 1.4. This project will investigate the compliance with the electrical requirement specification stated in Table 1.4 for the generator with a back-to-back converter. This is illustrated in Figure 1.24.
In Figure 1.24 the generator and back-to-back converter are connected to a grid transmission model, which is the model of the transmission cables. After the grid model, the grid requirements are compared at POC.

Requirement	Symbol	Range
Voltage	U	$[-10\%... + 6\%]\ U_{POC}$
Frequency	f	[49...51] Hz
Power factor	PF	[0.975...1.00]

Table 1.4: Summary of requirement specifications for performance evaluation during normal operation of the DFPT transmission.

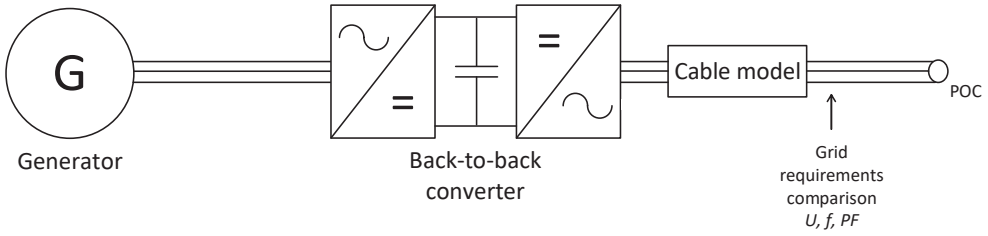

Figure 1.24: Illustration of the investigation of power quality before and after a back-to-back converter based on the stated grid requirements.

1.6 Project Objective

The purpose of this Master's Thesis is to evaluate the performance of the 5 MW NREL wind turbine with a DFPT instead of conventional gears. The performance evaluation will take basis in the requirement specification outlined in Section 1.5 and how the DFPT performance MPPT throughout region II. This leads to the following problem statement.

How can a controller be designed for a DFPT system, utilised in a wind turbine, in order to maximise the energy extraction, when operating below rated wind speed, without violating the electrical and mechanical requirement specifications?

To be able to answer this several steps must be made including making a model of the DFPT and electrical model used to evaluate the performance. The steps will be explained in the methodology presented in the following chapter.

CHAPTER 2

Methodology

The purpose of the project methodology is to outline the project approach for the reader. The following text, separated in six sections, will describe the project methodology flow chart illustrated in Figure 2.1.

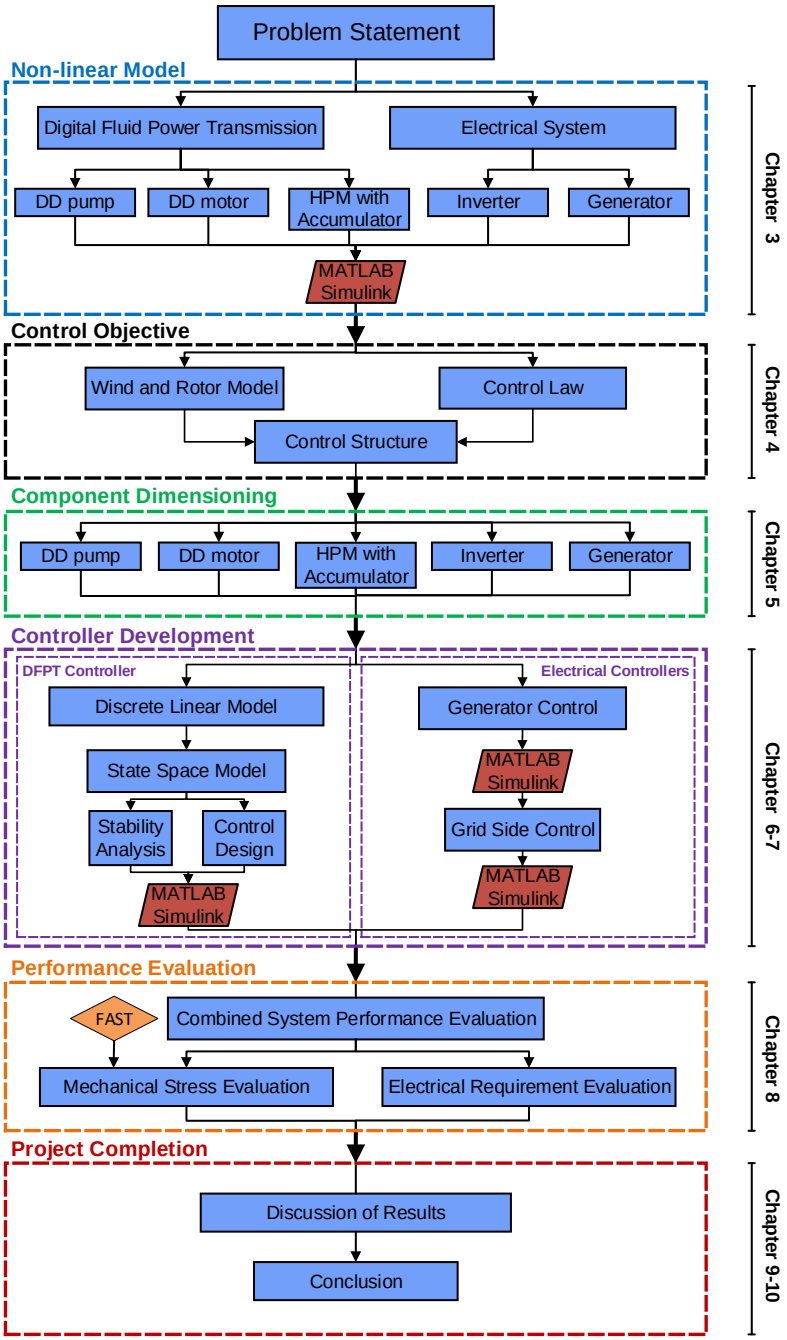

Figure 2.1: The flow chart shows the utilised project methodology. **Blue shapes** show chapters and sections. **Red shapes** show software used for modelling and design. An **orange shape** indicates an externally utilised tool in the project.

Ch. 3: Non-linear Model

The non-linear model is designed to be able to simulate the dynamic behaviour of the complete system. Since the system is complex and no experimental setup exists and identification methods therefore cannot be used, it is necessary to develop a model to characterise the system.

The non-linear model will be setup utilising the governing equations for the system components in the DFPT and the electrical system. These system components will be combined into a non-linear model and is implemented in the MATLAB/Simulink environment for dynamic system simulation.

Ch. 4: Control Objective

This chapter will outline the delimitation for the control objective for the developed controller with the focus to maximise the power production of the wind turbine below rated conditions. Therefore, a simple wind and rotor model is used together with a chosen control law to design a control structure for the system.

Ch. 5: Component Dimensioning

The dimensioning of the system will be conducted to properly dimension the system components, from the non-linear model, to each other and to match the power rating of the 5 MW NREL reference wind turbine.

The components are dimensioning in a first iteration from best available experience. This means that the system should be able to fulfil the control objective specified in Chapter 4.

Ch. 6-7: Controller Development

To control the combined system, controllers for the hydraulic DFPT and the electrical subsystems will be designed. The DFPT controller is designed from a discrete linear model of the DFPT behaviour. This discrete linear model is set on state space form to allow for model based state feedback control. To investigate the performance of the control design, a stability analysis of the control design is conducted. The control design and stability analysis in developed utilising MATLAB/Simulink.

For the electrical subsystem both a controller for the generator speed and afterwards a controller for the electrical grid frequency, voltage and current will be designed utilising MATLAB/Simulink.

Ch. 8: Performance Evaluation

The performance evaluation consists of an evaluation of the mechanical stress on the rotor axis and an evaluation in regards to the performance of the electrical system.

To benchmark the performance of these two systems, the evaluation of the mechanical and electrical requirements will be compared to a conventional turbine to investigate if the utilised system is able to perform to comply with the requirements specification. The externally utilised FAST tool will provide the torque input for the mechanical stress evaluation.

Ch. 9-10: Project Completion

In the project completion section the obtained results will be evaluated in relation to the utilised evaluation methods. Also the project will be summarised in a conclusion and ideas for future improvements will be stated.

CHAPTER 3

Non-linear Model

Chapter Contents

This chapter starts out by presenting the two subsystems that the system has been divided into, the hydraulic subsystem and the electrical subsystem. The assumptions used to simplify the non-linear model are presented and briefly discussed. The assumptions are followed by the governing equations of the models which forms the hydraulic and electrical subsystem. The governing equations of the models are combined in a MATLAB/Simulink environment which enables simulations of the system.

The are no experimental setup of the system, hence no experimental validation can be made of the model. To validate the model it is compared to identical models of the system presented in different articles.

3.1 DFPT and Electrical System

The system is divided into two subsystems. One subsystem containing the hydraulic components and one subsystem containing the electrical components. This is illustrated in Figure 3.1 where the hydraulic subsystem are represented by the blue dashed box and the red dashed box representing the electrical subsystem.

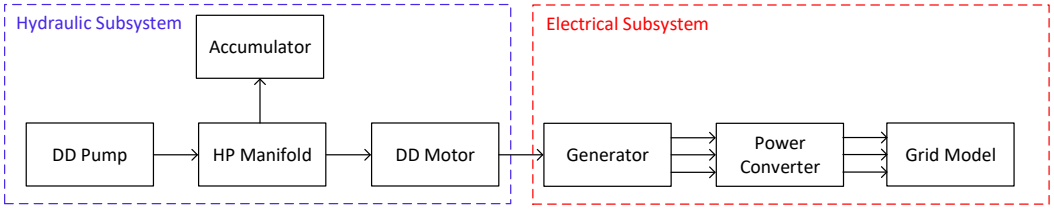

Figure 3.1: Block diagram illustrating the different elements of the two subsystems.

The composition of the chapter is similar to the flow seen in Figure 3.1 starting with the governing equations for the hydraulic subsystem, followed by the governing equations for the electrical subsystem. The constants utilised for the model can be found in Appendix

3.2 Modelling Assumptions

To simplify the model some assumptions have been made during the modelling of the two subsystems. These assumptions are made in order to be able to create a model suitable for evaluation of the DFPT with PMSG. If a more advanced and detailed approach is utilised, more accurate results with respect to experimentally testing may be obtained, however, this lead to heavy computational time of the simulations. Therefore, the simplifications may result in better control performance compared to the experimentally performance in real life, but are considered adequately to give an indication of the control performance for the wind turbine transmission.

Hydraulic Assumptions

- The flow across the orifices is **assumed turbulent**.
- To utilise the continuity equation it is assumed that the **density within the control volume is constant**.
- The **hoses are assumed stiff**, hence the volume is fixed and does not influence the flow.
- The **acceleration of the valves** are assumed constant, hence the modelling of the valves are independent of a specific valve geometry or mass. Furthermore, it allows for comparison with previous studies.
- It is assumed that **no viscous friction or stiction exist** between the piston and cylinder wall. However, this is accounted for by including this frictional loss as a hydro-mechanical efficiency which is included in the overall torque calculation.
- An ideal pressure boost circuit is assumed to be able to hold a **constant pressure in the LPM** of $p_L = 10$ bar during all operating conditions.

Electrical Assumptions

- The stator windings (a, b and c) are assumed **identical displaced** 120°, with N_s **equivalent turns and resistance** R_s.
- The **resistance** R_s **is assumed constant** and the **capacitance is neglected** hence the power losses are constant.
- **Damper windings are neglected**, since the electrical conductivity of permanent magnets are relatively low and neglected.
- **Magnetic hysteresis and saturation** are neglected.
- The system is **assumed to be a balanced and symmetrical** system, thus the zero component $f_0 = 0$
- The power converter is **assumed ideal**, hence the switches are infinitely fast. Thus the modelling of the power converter is reduced to Space Vector Modulation (SVM).

3.3 Hydraulic Subsystem

This section will present the governing equations utilised to model the hydraulic subsystem. Firstly, the governing equations for the DD pump is presented. Since the DD pump consist of multiple identical chambers, the derivation will be based on a single cylinder chamber. Secondly, the model of the DD motor is presented in similar manner as the pump. After the derivation of the single chambers, the model of the DD pump and DD motor are extended to include all the cylinders. Then, the high pressure manifold with accumulator is modelled. Lastly, the governing equations of the effective bulk modulus is presented in the end of this section.

3.3.1 Digital Displacement Pump

Firstly, the relation between the speed of the pump shaft and the position of the cylinder piston is derived. Secondly, the derivation of the reactive pump torque is covered followed by the hydraulics describing the flow and pressure in the pump, where a dynamic simulation of a single chamber is presented.

Kinematics

The derivation of the pump kinematics relating the pump shaft speed ω_r to a cylinder piston position x_p is based on Figure 3.2. Figure 3.2 shows the origo O of the pump shaft with the cam ring on the circumference and a zoom plot of a single cylinder, three lobes and the hydraulic circuit connected to the chamber.

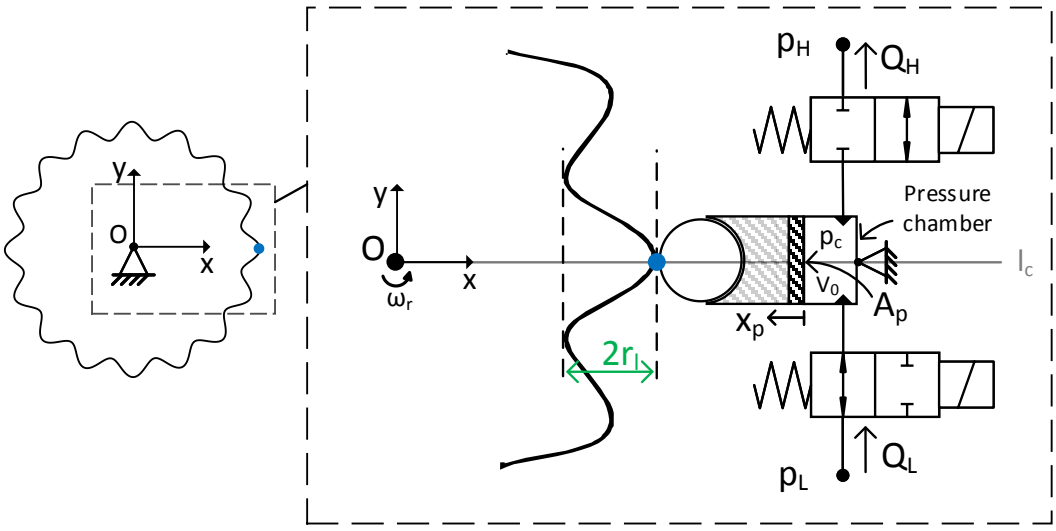

Figure 3.2: Conceptual sketch of one pressure chamber in a DD pump. It shows a zoom view of the cam ring with three lobes. r_l is the half lobe height and A_p is the piston area.

Since the cam ring utilises a roller-follower, the piston will move along the line l_c in a reciprocating motion when the pump is rotating with speed ω_r [Norton, 2004, p. 382].

The angular position of the pump shaft $\theta_r(t)$ is given by Equation (3.1).

$$\theta_r = \int_0^t \omega_r dt \qquad 0 \leq \theta_r \leq 2\pi \tag{3.1}$$

When the piston is at the top position of the lobe, the piston position will be x_p=0 and x_p=2 r_l when the piston is at the bottom of the lobe hence the piston is fully extracted. Thus the piston position can be described by Equation (3.2) [Norton, 2004, p. 389].

$$x_p = r_l\Big(1 - \cos\big(\theta_c + \theta_r\big)\Big) \qquad 0 \leq x_p \leq 2r_l \tag{3.2}$$

Where θ_c is the stationary angular location of the cylinder placed along the line l_c with respect to the x-axis.

The cylinders in the pump are evenly distributed in the modules and each module is shifted by $\frac{2\pi}{N_{c,tot}}$ in order to yield a smooth flow and torque contribution from each cylinder. The stationary angular location of the i-th cylinder can thus be given as in Equation (3.3).

$$\theta_{c,i} = \frac{2\pi}{N_{c,tot}} \cdot (0 : N_{c,i} - 1) \;\text{ for } i \in \{1, 2, \ldots, N_{c,tot}\} \tag{3.3}$$

For each revolution of the pump shaft, the number of piston strokes equals the number of lobes, N_l, hence the angle encountered by the cylinder becomes θ_l=$N_l\theta_r$. Furthermore, inserting $\theta_{c,i}$ into Equation (3.2) the piston position for all the cylinders $x_{p,i}$ is achieved in Equation (3.4).

$$x_{p,i} = r_l\left(1 - \cos\overbrace{(\theta_{c,i} + N_l\theta_r)}^{\theta_{l,i}}\right) \tag{3.4}$$

Where $\theta_{l,i}$ is the uniquely defined lobe cylinder angle for the i-th cylinder.

Reactive Pump Torque

The torque contribution, τ_c, from each cylinder in the pump is derived based on Figure 3.3, where the point of application between the roller-follower and the cam ring is illustrated by the blue dot.

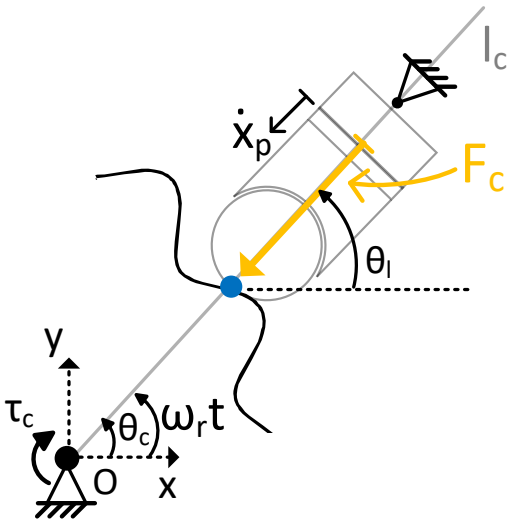

Figure 3.3: Conceptual sketch used for derivation of the reactive pump torque. The illustration shows the origo O of the pump shaft and the direction of the acting forces and torques.

The torque contribution is found by considering energy conversion in the rotational energy in the pump to the translational energy in the piston. Recalling the assumption of no energy loss during energy transformation, hence P_{rot}=P_{trl}, the torque can be described as in Equation (3.5).

$$\tau_c \omega_r = -F_c \dot{x}_p \qquad \Rightarrow \qquad \tau_c = -\frac{F_c \dot{x}_p}{\omega_r} \tag{3.5}$$

Where $\dot{x}_p$ is the speed of the piston and F_c is the pressure force exerted by the hydraulic pressure as F_c=$p_c A_p$ and acts as reactive force to the applied pump torque, which explains the negative sign.

Taking the derivative of Equation (3.2) with respect to time, $\dot{x}_p$ can be found as in Equation (3.6).

$$\dot{x}_p = r_l \omega_r \sin \underbrace{(\theta_c + \theta_r)}_{\theta_l} \tag{3.6}$$

Inserting Equation (3.6) into Equation (3.5), an expression for torque the contribution for a single cylinder is given by Equation (3.7).

$$\tau_c = -\frac{F_c r_l \omega_r \sin(\theta_l)}{\omega_r} = -p_c A_p r_l \sin(\theta_l) \tag{3.7}$$

The reader should recall, that it is assumed that no viscous friction and stiction exist between the piston and cylinder walls. It is chosen to include this frictional loss as a hydro-mechanical efficiency which is included in the overall reactive pump torque.

Referring to Figure 3.3, when the piston is either in the top position (θ_l=0) or bottom position (θ_l=π) of a lobe there is no effective torque contribution since the piston impacts the lobe at a turning point. At (θ_l=π) a pump stroke is initialised and ends at (θ_l=2π),

hence contributing to the pump flow and hereby having the largest reactive torque contribution. From $0 \leq \theta_l \leq \pi$ the intake flow leads to minimal chamber pressure, p_c, hence $\tau_c \approx 0$.

Hydraulics

The hydraulic circuit illustrated in Figure 3.2 is used to describe the flow and pressure related to a single cylinder chamber. The LPV and HPV are connected to the cylinder chamber and are used to control the low pressure flow Q_L and high pressure flow Q_H to and from the cylinder chamber. The pressure dynamics within the chamber is given by the continuity equation in Equation (3.8).

$$\dot{p}_c = \frac{\beta_{ef}}{V_c}\left(Q_L - Q_H - \dot{V}_c\right) \tag{3.8}$$

Where β_{ef} is the effective bulk modulus of the oil which is described in Section 3.3.4, $\dot{V}_c$ is the flow caused by the expansion of the chamber volume and $V_c = A_p\, x_p$ is the chamber volume given by Equation (3.9).

$$V_c(\theta_l) = \frac{V_p}{2}\Big(1 - \cos(\theta_l)\Big) + V_0 \tag{3.9}$$

Where $V_p = 2 r_l A_p$ is the maximum displacement volume and V_0 is the dead volume.

The flow $\dot{V}_c$ is found by the derivative of Equation (3.9) and is given in Equation (3.10).

$$\dot{V}_c(\theta_l, \omega_r) = \frac{V_p}{2} N_l \omega_r \sin(\theta_l) \tag{3.10}$$

The flow through the HPV and LPV are described by the orifice equations given in Equation (3.11) assuming turbulent flows.

$$\begin{aligned} Q_L &= \frac{\overline{x}_L}{k_f}\sqrt{|p_L - p_c|}\; sign(p_L - p_c) \\ Q_H &= \frac{\overline{x}_H}{k_f}\sqrt{|p_c - p_H|}\; sign(p_c - p_H) \end{aligned} \tag{3.11}$$

Where $\overline{x}$ is the normalised plunger position in the valves, k_f is the flow coefficient for the valve and is assumed equal for both valves.

Valve Dynamics and Valve Actuation

The valve dynamics have been simplified assuming no switching delay and constant plunger acceleration $\ddot{x}_v$ which only depends on the switching time t_s. This simplification is made in order to make the dynamics independent of the specific valve geometries and masses which is done to generalise the model. By doing this, the dynamics from flow forces, pressure forces and damping effects in the valve plunger are not modelled, which is done to reduce the simulation time. In reality, these dynamic should be modelled to obtain more accurate results with respect to the actual performance of the DD pump, but is regarded acceptable for the purpose in this study, since the simulation time is found to be a major issue as discussed later in this section.

The plunger acceleration during passive opening is given by Equation (3.12).

$$\ddot{x}_{v+} = \begin{cases} \frac{4}{t_s^2} & 0 \leq t \leq \frac{t_s}{2} \\ -\frac{4}{t_s^2} & \frac{t_s}{2} \leq t \leq t_s \end{cases} \tag{3.12}$$

The generalised model does not include the pressure forces acting on the plunger. However, passive opening of the LPV is defined utilising the pressure condition $p_c < p_L$. Similar conditions exist for the HPV where $p_c > p_H$.

The acceleration during the closing of the valves is given by $\ddot{x}_{v-} = -\ddot{x}_{v+}$. The active closing of the LPV and HPV is achieved by defining the closing angles $\theta_{L,cl}$ and $\theta_{H,cl}$ respectively which initialises the closing of the valves i.e. the valves are actively closed when $\theta_l \geq \theta_{cl}$. The values for these angles can be found in Supplement A.

The valve switching time influences the efficiency of the DD pump significantly and is thus further described in the following section.

Valve Efficiency

The efficiency of the individual DD valves is essential for the efficiency of the whole DD machine. In Roemer [2014, p. 46] this valve efficiency was investigated for different valve switching time compared to the revolution time of the DD machine. In this study, the valve efficiency was based on a DD motor rotating at 1500 RPM. It was found that the valve switching time should be chosen below a switching time of 14 % of the motor revolution time. The valve switching time should preferable be chosen as low as possible, and a normalized switching time of 2-3 % is the preferable range, considered an ideal trade-off to the motor revolution time is should be obtained as a lower switching time.

The utilised normalised switching time is chosen to Equation (3.13).

$$\%\bar{t}_s = \frac{t_s}{T_{rev}} = \frac{1\ ms}{40\ ms} \cdot 100\% = 2.5\% \tag{3.13}$$

Where 2.5% is in the middle of the ideal range of the valve normalised switching time. For simplicity, it is chosen utilise the same switching time for valves utilised in the DD pump.

The valve actuation strategy is utilised in a dynamic simulation of a single cylinder chamber which is presented in the following.

Single Chamber Simulation

The dynamic model of a cylinder chamber is simulated for one pumping stroke and one idling stroke. The variable model parameters such as the pressures HPM, LPM and the pump shaft speed are held fixed. Furthermore, the simulation time step t_{step} is fixed and chosen to be able to capture the flow dynamics and to avoid numerical problems.

The input parameters used for the simulation are given in Table 3.1 where the additional constants used for the simulation can be found in Supplement A.

The simulation results are presented in Figure 3.4.

ω_r	t_{cycle}	t_s	t_{step}	p_H	p_L
12.1 RPM	$\frac{2\pi}{\omega_r N_l}$=0.31 s	1 ms	0.1 μs	360 bar	10 bar

Table 3.1: Input parameters used for simulation.

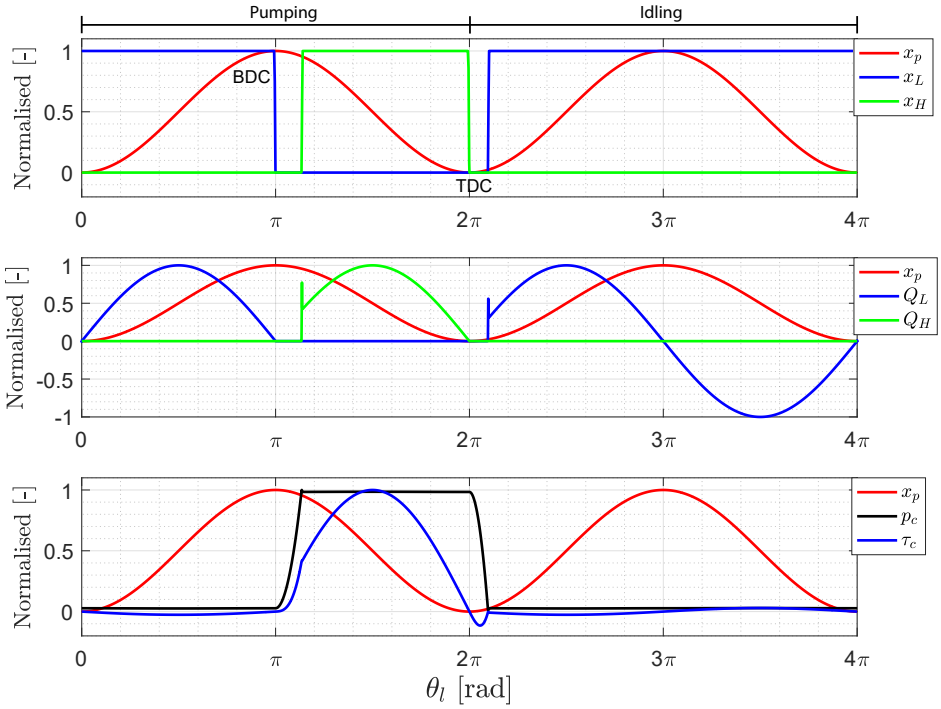

Figure 3.4: Simulation results for one full pumping stroke ($0 \leq \theta_l \leq 2\pi$) and one idling stroke ($2\pi \leq \theta_l \leq 4\pi$) for fixed pump speed $\omega_r = 12.1RPM$. The signals are normalised with $Q_{max} = 290^{L}/_{min}$, $p_{max} = 366bar$, $\tau_{max} = 8.5kNm$ and $x_{p,max} = 2r_l$.

The flow intake is seen for $0 \leq \theta_l \leq \pi$ where the LPV is open hence $p_c \approx p_L$. The LPV is actively closed near BDC, due to valve dynamics such that it is fully closed at $\theta_l = \pi$. The piston x_p is driven towards TDC, hereby compressing the fluid in the chamber leading to an increase in p_c. When p_c exceeds the high pressure p_H the HPV is passively opened by the pressure force and pressurised fluid Q_H is led to the high pressure manifold.

When the piston reaches TDC the HPV is actively closed in order to be fully closed at $\theta_l = 2\pi$ hereby ending the pumping stroke. By active closing the HPV no back flow ($Q_H < 0$) is seen hereby avoiding flow from the high pressure manifold into the pressure chamber, thus avoiding counteracting torque. However, the reactive torque is seen to yield a negative undershoot since the cylinder momentarily pushes the lobes in the operation direction of the pump shaft since $p_c > p_L$. When p_c has decreased below p_L, the LPV is passively opened and low pressure/torque levels are observed. The LPV is held open throughout the entire stroke ($2\pi \leq \theta_l \leq 4\pi$) hereby indicating an idle operation mode where the low pressure flow Q_L is displaced from and to the low pressure manifold.

3.3.2 Digital Displacement Motor

Since the DD motor has many similarities to the pump, the DD motor will be described in a similar approach. Firstly, the kinematics of the motor relating the motor shaft speed to a cylinder piston position is derived. Then, the torque produced by each cylinder is described followed by the hydraulic circuit of the cylinder chamber. Lastly, a dynamic simulation of a single chamber pressure is presented.

Kinematics

The modelling of a single chamber is based on the hydraulic sketch of a single chamber in Figure 3.5.

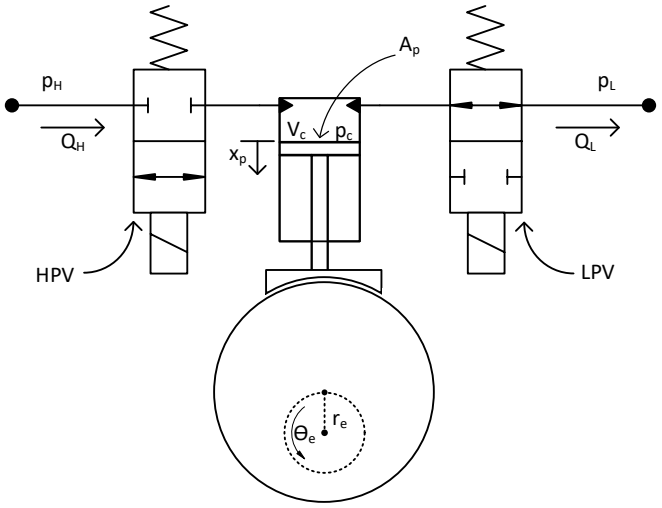

Figure 3.5: Conceptual hydraulic sketch of one cylinder chamber in a DD motor.

As illustrated in Figure 3.5 a single cylinder is connected to an eccentric shaft. A HPV and a LPV are used to control the flow from the high pressure manifold and the low pressure manifold respectively.

The piston position x_p can be described by Equation (3.14).

$$x_p = r_e \left(1 - cos(\theta_e)\right), \qquad 0 \leq x_p \leq 2r_e \tag{3.14}$$

Where r_e is the radius of the eccentric shaft and θ_e is the angular position of the eccentric shaft.

The angle of the eccentric shaft is uniquely defined for each cylinder as the cylinders are evenly distributed in a module and each module is shifted with $\frac{2\pi}{N_{c,tot}}$, hence the eccentric shaft angle for each cylinder is given by Equation (3.15).

$$\theta_{e,i} = \int_0^t \omega_M dt + \left(\frac{2\pi}{N_{c,tot}} \cdot (0 : N_{c,i} - 1)\right) \quad i \in \{1, 2, \ldots, N_{c,tot}\}, \qquad 0 \leq \theta_{e,i} \leq 2\pi \tag{3.15}$$

With ω_M being the angular velocity of the motor, $N_{c,tot}$ is the total number of cylinder chambers in the motor, $N_{c,i}$ is the number of the cylinder considered and t is the time.

Motor Torque

The torque T_c produced by each cylinder in the motor is derived based on Figure 3.6. ω_M is the rotational speed of the eccentric shaft and θ_e is the angular position of the eccentric shaft with respect to neutral axis of the cylinder (dashed line).

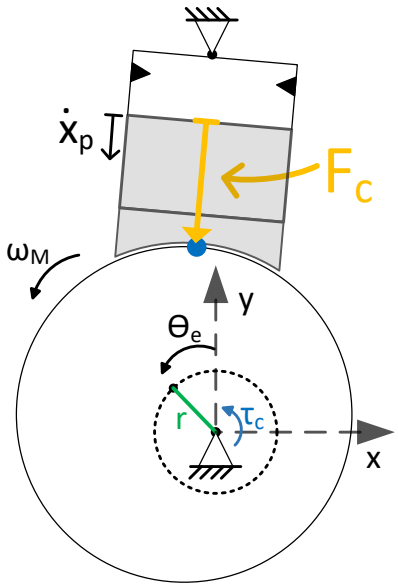

Figure 3.6: Conceptual sketch used for derivation of the motor torque.

The torque contribution from a single cylinder is found in the same manner as in the pump, with $P_{trl} = P_{rot}$, and is given in Equation (3.16).

$$T_c = p_c A_p r_e \sin(\theta_e) \tag{3.16}$$

Where positive sign convention is used since the pressure force drives the eccentric shaft.

The reader should recall, that it is assumed that no viscous friction and stiction exist between the piston and cylinder walls. It is chosen to include this frictional loss as a hydro-mechanical efficiency which is included in the overall motor torque.

Referring to Figure 3.6, when the piston is either in the top position (θ_e=0) or bottom position (θ_e=π), there is no effective torque contribution, since the axis of interaction between the piston and eccentric shaft is parallel to each other. At (θ_e=0) a motor stroke is initialised and ends at (θ_e=π), hence the high pressure flow drives the eccentric shaft and hereby having the largest torque contribution. From $\pi \leq \theta_e \leq 2\pi$ the low pressure fluid is led out to the LPM at minimal chamber pressure, p_c, hence $\tau_c \approx 0$.

Hydraulics

The pressure dynamics within the cylinder chamber is given by the continuity equation in Equation (3.17).

$$\dot{p}_c = \frac{\beta_{ef}}{V_c}\left(Q_H - Q_L - \dot{V}_c\right) \tag{3.17}$$

Where β_{ef} is the effective bulk modulus and is given by Equation (3.24). V_c is the chamber volume given by Equation (3.18) as a function of the angle of the eccentric shaft θ_e.

$$V_c\left(\theta_e\right) = \frac{V_{max}}{2}\left(1 - cos\left(\theta_e\right)\right) + V_0 \tag{3.18}$$

V_0 is the dead volume of the cylinder chamber and V_m is the maximum expansion of the cylinder chamber and is given by Equation (3.19).

$$V_{max} = 2r_e A_p \tag{3.19}$$

volume expansion of the chamber and given by Equation (3.20).

$$\dot{V}_c\left(\theta_e, \dot{\theta}_e\right) = \frac{V_{max}}{2}\underbrace{\dot{\theta}_e}_{\omega_M} sin\left(\theta_e\right) \tag{3.20}$$

The flows Q_L and Q_H are the flows through the LPV and HPV respectively and are found utilising the orifice equations in Equation (3.21) under the assumption that the flow across the orifices are turbulent.

$$\begin{aligned} Q_L &= \frac{\overline{x}_L}{k_f}\sqrt{|p_c - p_L|}sign\left(p_c - p_L\right) \\ Q_H &= \frac{\overline{x}_H}{k_f}\sqrt{|p_H - p_c|}sign\left(p_H - p_c\right) \end{aligned} \tag{3.21}$$

Where $\overline{x}_L$ and $\overline{x}_H$ are the normalised valve positions and k_f is the flow coefficient.

Due to the similarities between the DD pump and DD motor, the valve dynamic and valve actuation are defined in similar manner as the pump.

Figure 3.7 displays the simulation results of a motoring stroke and an idling stroke, given the input parameters listed in Table 3.2.

ω_M	t_{cycle}	t_s	t_{step}	p_H	p_L
1500 RPM	$\frac{2\pi}{\omega_M}$=0.04 s	1 ms	0.1 μs	360 bar	10 bar

Table 3.2: Input parameters used for simulation.

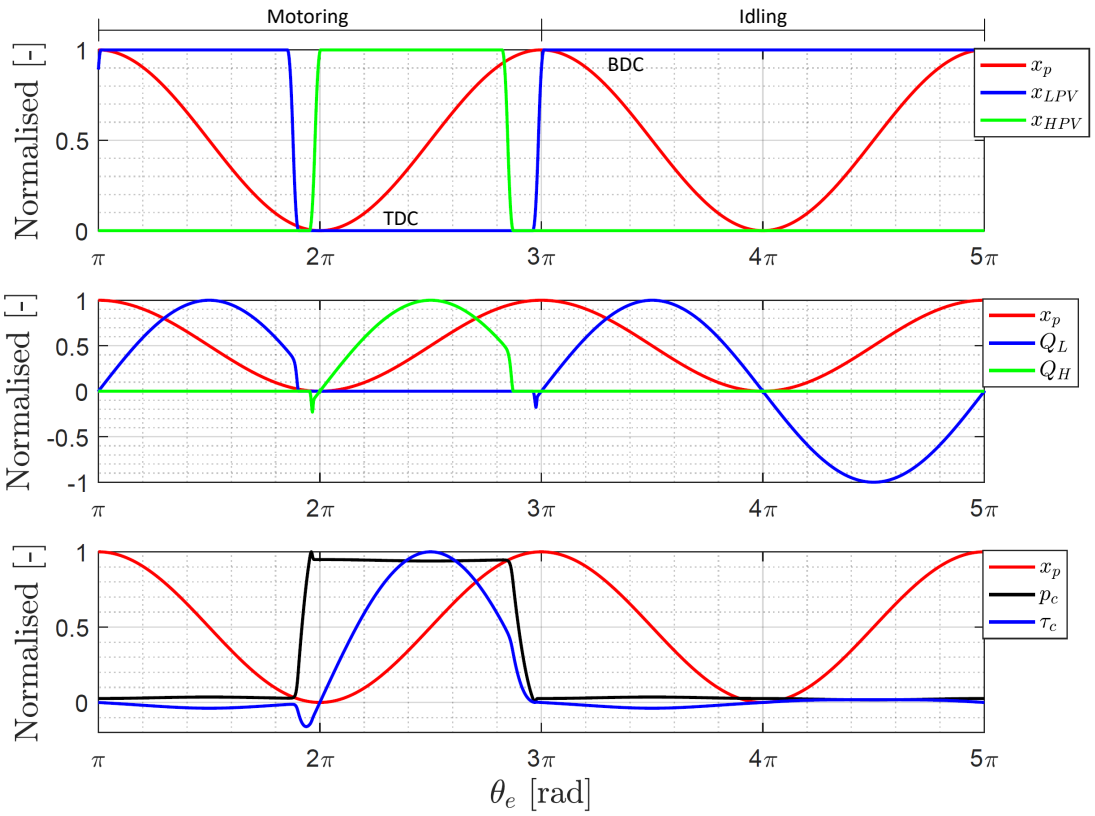

Figure 3.7: A single chamber simulated at rated condition and constant speed (1500RPM). The simulation is started in motoring mode at bottom position BDC ($\theta_e = \pi$) and after one stroke (2π) the idling mode of the motor is seen. Q_{max} is found to be $722\frac{L}{min}$ and the maximum peak pressure chamber is found to be 379bar.

During the motoring stroke it can be seen that the LPV is open from π and is actively closed just before 2π. Due to the sudden closing of the LPV the pressure p_c increases due to the compression of the fluid until p_c exceeds the p_H resulting in a passive opening of the HPV is observed which equalises the pressures $p_c \approx p_H$. The HPV is fully opened at exactly 2π in order to maximise the efficiency. The passively opening of the valve results in a backflow which results in a negative torque contribution which works against the rotation direction. The HPV is kept open until it is actively closed just before 3π which leads to a decreasing p_c due to a decompression of the fluid. When $p_c < p_L$ a passive opening of the valve is observed due to suction and $p_c \approx p_L$. During the idling stroke it is seen that the LPV actively kept opened for a whole revolution. This ensures a minimal pressure inside the camber thus the pressure lose is kept at a minimum to ensure highest efficiency.

3.3.3 Total Flow and Torque

In the preceding sections, the single cylinder flow and torque have been modelled for both the DD pump and DD motor, thus the aim of this section is to establish the total flow and torque contributions. Again, since similarities exist between the pump and motor, the total flow and torque will be found in similar manner.

The total flow Q_{tot} and torque T_{tot} are found by summing the instantaneous contributions Q_H and T_c from each individual cylinder chamber. However, since the simulation of the full scale dynamic models requires a time step size of $10^{-7}s$ the computational time is comprehensive, hence it is not applicable for evaluation of the control of the transmission for the wind turbine.

To reduce the computational time, of the full scale models, significantly it is chosen to implement Q_H and T_c as 3D lookup table data. This is achieved by simulating a single pressure chamber for one full pumping/motoring stroke and one full idling stroke for various pressure levels of p_H and shaft speeds ω_r/ω_M, and logging the corresponding Q_H and T_c. One drawback of this method is that p_H and ω_r are held fixed during a full stroke where it in reality might be varying, thus the pressure gradient within the cylinder chamber is an approximation. However, this method is considered acceptable since it is a trade-off issue between simulation speed and simulation accuracy.

One of the advantages with the lookup table is the larger simulation time step size. The accuracy of the lookup tables for different time steps is investigated in Appendix A.2, where a worst case operation comparison of the lookup tables to the dynamic models is conducted.

With regard to the pump, it is found that the relative RMS error of Q_H and T_c is found to be 1 % and 0.005 % respectively. For the motor the relative RMS error is found to be 0.25 % for Q_H and 0.05 % for T_C, which is considered acceptable for the performance evaluation. Furthermore, it is found that a time step size of $10^{-5}s$ is sufficient in order to capture the dynamics.

Utilising the lookup tables, the total pump flow and reactive pump torque can thus be found by superposition of each individual chamber described by Equation (3.22).

$$\begin{aligned} Q_P &= \sum_{i=1}^{N_{cP,tot}} Q_H(i) \\ T_P &= -\frac{V_p}{2} N_l \sum_{i=1}^{N_{cP,tot}} p_c(i) \sin\left(\theta_l(i)\right) \end{aligned} \tag{3.22}$$

Where the single cylinder torque is multiplied with the number of lobes to include the total number of strokes per pump revolution.

Similar, the total motor flow and torque are given in Equation (3.23).

$$\begin{aligned} Q_M &= \sum_{i=1}^{N_{cM,tot}} Q_H(i) \\ T_M &= \frac{V_{max}}{2} \sum_{i=1}^{N_{cM,tot}} p_c(i) \sin\left(\theta_e(i)\right) \end{aligned} \tag{3.23}$$

3.3.4 Effective Bulk Modulus

The effective bulk modulus is a measure of the oil stiffness and is utilised in order to take the presence of air, trapped inside the system, into account. Utilising the effective bulk modulus instead of a constant will have the largest effect at low pressures. Assuming addibatic conditions the effective bulk modulus is given by Equation (3.24) [Andersen, 2003].

$$\beta_{ef} = \frac{1}{\frac{1}{\beta_{oil}} + \frac{V_{\%-air}}{\beta_{air}}} \tag{3.24}$$

where

$$V_{\%-air} = V_{\%-air,atm} \cdot \left(\frac{p_{atm}}{p_{abs}}\right)^{\frac{1}{\kappa}}$$

$$\beta_{air} = \kappa \cdot (p_{abs})$$

β_{oil} is the stiffness of the oil without any air entrapped, β_{air} is the stiffness of the air, $V_{\%-air}$ is volumetric ratio of the air entrapped in the oil and κ is the specific heat ratio which is equal to 1.4 for an addibatic process when considering air. p_{atm} is the pressure in the atmosphere and p_{abs} is the absolute pressure in the considered manifold. Effective bulk modulus of the oil for different percentages of entrapped air in the oil is shown in Figure 3.8.

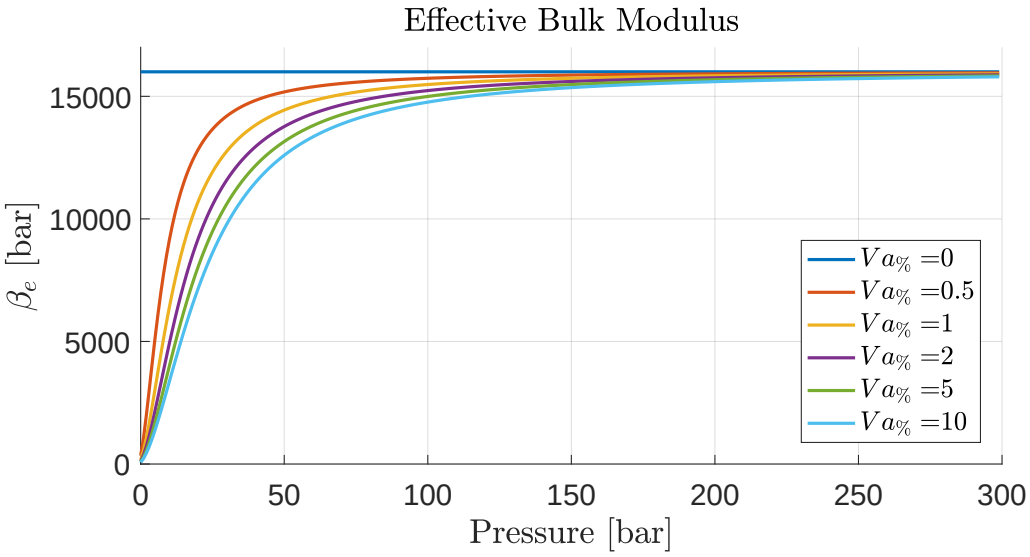

Figure 3.8: Effective bulk modulus of the oil for different percentages of entrapped air in the oil.

3.3.5 High Pressure Manifold With Accumulator

The combined manifold and accumulator model is based on Andersen [2007, Chap. 6.2-6.3] and Rabi [2009, Chap. 6.2]. The focus is to dampen pressure pulsations in relation to control of the DFPT, hence the energy storage ability of the accumulator is not of interest, in respect to store extra hydraulic energy. The approach is to utilise a simple accumulator model and combine it with the manifold utilising equivalent continuity equations.

In Figure 3.9 control volumes and variables for the model of the high pressure manifold with accumulator are shown. The accumulator consists of a gas volume V_g and a fluid

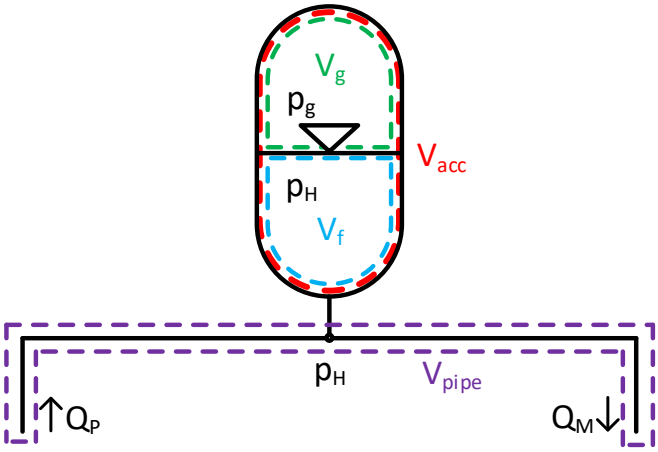

Figure 3.9: Sketch of the control volumes and variables utilised in the modelling of the high pressure manifold with accumulator.

volume V_f.

The total volume of the accumulator is given by Equation (3.25).

$$V_{acc} = V_f + V_g \tag{3.25}$$

The gas and fluid volumes are separated by a bladder in which the gas is contained. Assuming the mass and friction of the bladder to be neglected the pressure of the gas and manifold fluid pressure p_H can be considered equal and is given by Equation (3.26).

$$p_g = p_H \tag{3.26}$$

The volume of the high pressure manifold consists of the volume of the pipes V_{pipe} connecting the DD pump, DD motor and accumulator.

The combined volume of the high pressure manifold with accumulator is given by Equation (3.27).

$$V_H = V_{pipe} + V_{acc} - V_g \tag{3.27}$$

The compression and expansion process, in the accumulator gas chamber, is described by the polytropic relation given by Equation (3.28).

$$p_g V_g^{\kappa} = p_{pr} V_{acc}^{\kappa} = \text{const.} \tag{3.28}$$

Where the time dependent gas volume V_g and gas pressure p_g are equal to a constant relation of the gas precharge pressure p_{pr} and total accumulator gas volume V_{acc}. The rate of change of the accumulator gas pressure will change with the manifold pressure. A fast rate of change will generate more heat loss during gas compression than a slow rate of change. It is assumed that the rate of change will not contribute to any significant heat loss and therefore the specific heat ratio κ is chosen to a value for an adiabatic process where losses, due to heat dissipation to the surroundings, are neglected.

An expressing for V_g is found from Equation (3.28) in the case where the manifold pressure is above the accumulator precharge pressure. The volume of V_g will fill the entire

accumulator volume when the manifold pressure is below the accumulator precharge pressure. The relations for the gas volume depending on the manifold pressure are given by Equation (3.29).

$$V_g = \begin{cases} V_{acc}\left(\frac{p_{pr}}{p_H}\right)^{\frac{1}{\kappa}} & \text{if} \quad p_H > p_{pr} \\ V_{acc} & \text{if} \quad p_H \leq p_{pr} \end{cases} \tag{3.29}$$

Differentiation of Equation (3.25) with respect to time shows that the negative derivative of the gas volume is equal to the derivative of the fluid volume, which is considered equivalent to the flow into the accumulator given by Equations (3.30).

$$\dot{V}_f = -\dot{V}_g \tag{3.30}$$

The orifice into the accumulator is assumed ideal, hence the throttling effect is neglected.

To express the derivative of the gas chamber volume Equation (3.28) is differentiated with respect to time, utilising the chain rule, and is given by Equation (3.31). The full derivation is available in Appendix C.1.

$$\dot{V}_g = \frac{-1}{\kappa}\frac{V_g}{p_g}\dot{p}_g \tag{3.31}$$

The continuity equation describing the manifold with accumulator can be formulated from Figure 3.9 and is given by Equation (3.32).

$$\dot{p}_H = \frac{\beta_e}{V_H}(Q_P - Q_M - \dot{V}_f - k_{leak}\Delta p) \tag{3.32}$$

Where Q_P is the flow from the DD pump, Q_M is the flow to the DD motor and $\dot{V}_f$ is the flow into the accumulator. k_{leak} is a combined leakage coefficient for the DD pump and DD motor which depends on Δp, where $\Delta p = p_H - p_L$ is the pressure difference between the manifold high pressure line and low pressure line.

Inserting Equation (3.30) along with Equation (3.31) into Equation (3.32) and utilising $p_g = p_H$ an equivalent continuity equation for the derivative of the pressure in the high pressure manifold $\dot{p}_H$ can be formulated and is given by Equation (3.33). The full derivation is available in Appendix C.2.

$$\dot{p_H} = \frac{1}{\frac{V_H}{\beta_e} + \frac{1}{\kappa}\frac{V_g}{p_H}}(Q_P - Q_M - k_{leak}\Delta p) \tag{3.33}$$

To alter the behaviour of $\dot{p}_H$ the accumulator precharge pressure p_{pr} and total accumulator volume V_{acc} are to be estimated from parameter sweeps with the following the objective. To reduce the pressure pulsations in the high pressure manifold and at the same time still have a significantly fast pressure response under normal operating conditions of the system.

3.4 Electrical Subsystem

This section will present the governing equations for the electrical subsystem utilised in this project. The electrical subsystem is composed of three different models, a generator model, a back-to-back converter model and a grid model. These three models will be presented in the same order starting with the governing equations for the PMSG.

3.4.1 Permanent Magnet Synchronous Generator

This section is based on [Krause et al., 2013, chap: 3-4] unless otherwise is stated.
A typical two-pole, permanent-magnet AC machine is seen in Figure 3.10. The stator consists of three phases wye-connected stator windings as seen in Figure 3.11 and the rotor consist of surface mounted permanent magnets. In Figure 3.10 the stator windings are illustrated as circles where the crossed circles indicates a current flow into the paper and the circle with the dot indicates the current flows out of the paper.

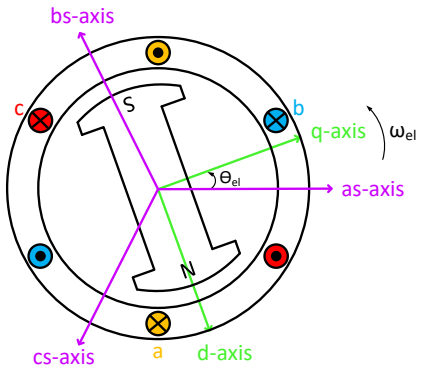

Figure 3.10: Illustration of the rotating qd-reference frame together with the stator windings and the magnetic axis of the stator winding a, b and c.

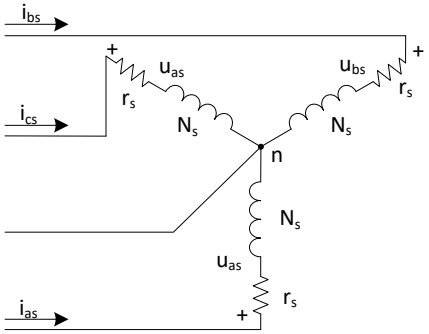

Figure 3.11: Wye-connection of the stator windings in the PMSG.

The as-axis is the magnetic axis of the stator winding a and is perpendicular to the current axis inside the stator windings as seen in Figure 3.10. The following section will present the governing equations for a Permanent Magnet Synchronous Machine in motor mode (PMSM) and in the end of this section converted to generator mode.

Stator Voltage Equations

The governing voltage equations for the PMSM is found utilising the wye-connection circuit displayed in Figure 3.11. The voltage equations for all stator windings are by the matrix seen Equation (3.34).

$$\mathbf{U_{abc}} = \mathbf{R_s i_{abc}} + \frac{d}{dt}\lambda_{\mathbf{abc}} \tag{3.34}$$

where the voltage in each phase can be found as in Equation (3.35).

$$(\mathbf{F_{abcs}})^T = \begin{bmatrix} f_a & f_b & f_c \end{bmatrix} \tag{3.35}$$

where f can be voltage, current etc. $\mathbf{i_{abc}}$ is the current vector containing all three stator currents. The stator resistance matrix $\mathbf{R_s}$ is given by Equation (3.36).

$$\mathbf{R_s} = diag \begin{bmatrix} r_s & r_s & r_s \end{bmatrix} \tag{3.36}$$

The flux linkage vector $\lambda_{\mathbf{abc}}$ is given by Equation (3.37).

$$\boldsymbol{\lambda_{abc}} = \mathbf{L_s i_{abc}} + \boldsymbol{\lambda_{mpm}} \tag{3.37}$$

where $\mathbf{L_s}$ is the inductance matrix and $\lambda_{\mathbf{mpm}}$ is the flux linkage created by the movement of the permanent magnets and given by Equation

$$\lambda_{\mathbf{mpm}} = \lambda_{mpm} \begin{bmatrix} sin\left(\theta_{el}\right) \\ sin\left(\theta_{el} - \frac{2\pi}{3}\right) \\ sin\left(\theta_{el} + \frac{2\pi}{3}\right) \end{bmatrix} \tag{3.38}$$

where λ_{mpm} is the maximum flux linkage of the permanent magnets seen by the stator windings, hence $\frac{d\,\lambda_{mpm}}{dt}$ is the induced open circuit voltage in each stator winding as a results of the rotating permanent magnets.
To eliminate all rotor position-dependent inductances from the voltage equation that occur due to electrical circuits in relative motion and electrical circuits with varying magnetic reluctances, Park's transformation is utilised. Park's transformation will change all variables associated with the stator windings (voltage, flux linkage and currents) to variables related to an arbitrary rotating reference frame, the reference frames utilised in this project is further elaborated in Appendix F. The rotating reference frame used is the *qd reference frame* as seen in Figure 3.10 where the reference frame is marked with **green**.

Rotating Reference Frame

This section will seek to transform the equations presented in Section 3.4.1 from the stationary abc stator reference frame to the rotating qd reference frame. Both frames are illustrated in Figure 3.10 and the geometric relation between the reference frames are given in Equation (3.39).

$$\mathbf{F_{qds}} = \mathbf{K_s F_{abcs}} \tag{3.39}$$

$$\begin{aligned} \left(\mathbf{F_{qds}}\right)^T &= \begin{bmatrix} f_q & f_d & f_0 \end{bmatrix} \\ \left(\mathbf{F_{abcs}}\right)^T &= \begin{bmatrix} f_a & f_b & f_c \end{bmatrix} \end{aligned} \tag{3.40}$$

where $\mathbf{K_s}$ is the transformation matrix used to go from the stationary reference frame to the rotating qd reference frame and is given by (3.41).

$$\mathbf{K_s} = \frac{2}{3} \begin{bmatrix} cos\left(\theta_{el}\right) & cos\left(\theta_{el} - \frac{2\pi}{3}\right) & cos\left(\theta_{el} + \frac{2\pi}{3}\right) \\ sin\left(\theta_{el}\right) & sin\left(\theta_{el} - \frac{2\pi}{3}\right) & sin\left(\theta_{el} + \frac{2\pi}{3}\right) \\ \frac{1}{2} & \frac{1}{2} & \frac{1}{2} \end{bmatrix} \tag{3.41}$$

where the angular position and velocity of the arbitrary reference frame are given by Equation (3.42).

$$\frac{d\,\theta_{el}}{dt} = \omega_{el} \tag{3.42}$$

To transform the voltage equation in abc reference frame to the qd reference frame the circuit it is convenient to split the voltage equations up into resistive and inductive circuit element. The reader should recall that the *capacitance is neglected*, hence these elements are not considered.

Resistive Elements

The resistive circuit elements consist of the resistance in the windings of the stator. The voltage equations for the resistive elements is thus the voltage drop across a resistor and are given by Ohm's law in Equation (3.43).

$$\mathbf{u_{abc}} = \mathbf{R_s i_{abc}} \tag{3.43}$$

From (3.39) Equation (3.44) is obtained.

$$\mathbf{u_{qd0}} = \mathbf{R_s i_{abc} K_s} \Rightarrow \mathbf{U_{qd0}} = \mathbf{R_s i_{qd0}} \tag{3.44}$$

With the voltage drop across the resistive element found, the voltage drop across the inductive element can be examined.

Inductive Elements

The voltage drop across the inductor in the abc reference frame is given by Equation (3.45).

$$\mathbf{U_{abc}} = \frac{d}{dt}\lambda_{\mathbf{abc}} \tag{3.45}$$

Similar to the resistive element Equation (3.39) is utilised to transform the variables from abc to qd.

$$\mathbf{U_{qd0}} = \mathbf{K_s}\frac{d}{dt}\underbrace{\left(\lambda_{\mathbf{qd0}}\mathbf{K_s}^{-\mathbf{1}}\right)}_{\lambda_{\mathbf{abc}}} \tag{3.46}$$

Utilising the product rule Equation (3.46) can be rewritten

$$\mathbf{U_{qd0}} = p\lambda_{\mathbf{qd0}} + \left(\frac{d}{dt}\mathbf{K_s}\mathbf{K_s}^{-1}\right)\lambda_{\mathbf{qd0}} \tag{3.47}$$

where

$$\left(\frac{d}{dt}\mathbf{K_s}\mathbf{K_s}^{-1}\right) = \omega_{el}\begin{bmatrix} 0 & 1 & 0 \\ -1 & 0 & 0 \\ 0 & 0 & 0 \end{bmatrix} \tag{3.48}$$

hence the voltage drop across the inductive element in the qd reference frame is given by Equation (3.49).

$$\mathbf{U_{qd0}} = \frac{d}{dt}\lambda_{\mathbf{qd0}} + \omega_{el}\begin{bmatrix} 0 & 1 & 0 \\ -1 & 0 & 0 \\ 0 & 0 & 0 \end{bmatrix}\lambda_{\mathbf{qd0}} \tag{3.49}$$

The voltage equation, when transformed to the qd reference frame, is given by Equation (3.50) when assuming a symmetrical and balanced system (the zero component $f_0 = 0$).

$$\begin{aligned} u_{qs} &= R_s i_{qs} + \omega_{el}\lambda_{ds} + \frac{d}{dt}\lambda_{qs} \qquad \lambda_{qs} = \underbrace{(L_{Ls} + L_{mq})}_{L_q} i_{qs} \\ u_{ds} &= R_s i_{ds} - \omega_{el}\lambda_{qs} + \frac{d}{dt}\lambda_{ds} \qquad \lambda_{ds} = \underbrace{(L_{Ls} + L_{md})}_{L_d} i_{qs} + \lambda_{mpm} \end{aligned} \tag{3.50}$$

where the electrical angular velocity of the generator is given as

$$\omega_{el} = \omega_g \cdot N_{pp}$$

Where ω_g is the mechanical angular speed of the generator, thus the speed of the DD motor. N_{pp} denotes the number of pole pairs in the PMSG.
The equivalent circuits of the voltage equations are illustrated in Figure 3.12 and 3.13.

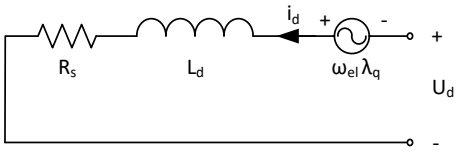

Figure 3.12: An equivalent circuit used to derive the voltage equation of the *d-axis*.

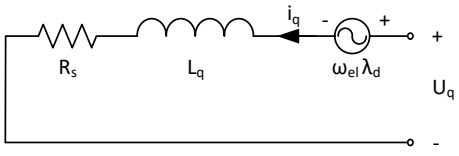

Figure 3.13: An equivalent circuit used to derive the voltage equation of the *q-axis*.

The torque produced by the PMSG is stated in Equation (3.51). As seen the torque equation is simplified due to the fact that the PMSG has surface mounted poles hence the inductance of the d and q-*axis* is equal to each other($L_d = L_q$), hence they cancel out.

$$\begin{aligned} T_e &= \frac{3}{2} N_{pp} \left(\lambda_{mpm} \cdot i_q + \underbrace{(L_d - L_q)}_{=0} \cdot i_d \cdot i_q \right) \\ &\Downarrow \\ T_e &= \frac{3}{2} N_{pp} \left(\lambda_{mpm} i_q \right) \end{aligned} \tag{3.51}$$

Generator Mode

The governing equations presented throughout this section have been for a Permanent magnet Synchrounous machine in motor convention. To go from motor mode to generator made is simply by changing the sign of the stator currents in the equations. Furthermore, newtons second law for the PMSG is given by Equation 3.52.

$$T_l - T_e = \dot{\omega}_g \cdot J \tag{3.52}$$

Where T_l is the load torque, which in this case is the motor torque which drives the generator. Furthermore, power balance for the generator can be made. For a generator the input power should be equal to the output power plus the copper losses as given by Equation (3.53).

$$P_{M,mech} = P_{g,el} + P_{loss} \tag{3.53}$$

where $P_{M,mech}$ is the mechanical power delivered by the DD motor, $P_{g,el}$ is the electrical output power from the PMSG and P_{loss} is the losses located in the stater windings i.e. copper losses. Hence with the power balance the motor to generator conversion is finished and the model of the rest of the electrical subsystem can presented.

3.4.2 Power Converter

The power converter consist of two 3-phase 2-level inverters and a DC-link capacitor in between as seen in Figure 3.14. Thus the first part of this section will describe the model of the 3-phase 2-level inverter and the second part will present the model of the DC-link capacitor.

3-Phase 2-level Inverter

The power converter utilised in this project is a back-to-back converter as seen in Figure 3.14. The AC to DC converter and the DC to AC converter are two identical 3-phase 2-level converters similar to the one illustrated in Figure 3.15. Since they are identical only

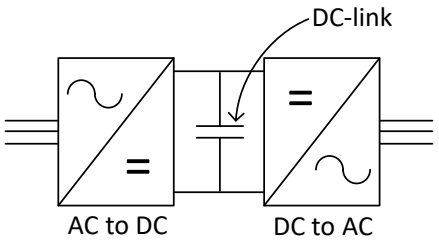

Figure 3.14: A sketch of the back-to-back converter.

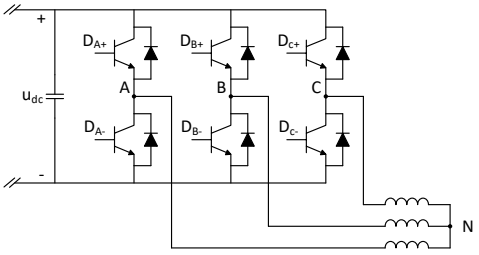

Figure 3.15: Illustration of a utilised in the back-to-back converter 3-phase 2-level inverter.

one of them is considered in this section. As mentioned in Section 3.2 the transistors in the converter is assumed to be ideal, hence the transistors are infinitely fast. Therefore, the model of the power converter is reduced to the modulation technique chosen. It is chosen to utilise Space Vector Pulse Width Modulation (SVPWM) as modulation technique due to the increased voltage output (15% compared to PWM).
Utilising SVPWM make it possible to see the inverter as one system with a binary input sequence. In this case there are six transistors, hence the inverter has six binary inputs where each transistor can be on or off, thus the total number of states is $2^6 = 64$. However, many of the combinations cannot be utilised, since the two transistors in each phase must be in the opposite state of each other, meaning that they are not allowed to be on at the same time, since this would create a low resistance path for the current, which would results in larger current (shoot through currents) resulting in a damaged inverter, furthermore they cannot be turned off at the same since this would not create any signal. This reduces the total number of states to $2^3 = 8$. These eight states are illustrated in Figure 3.16 where the black circle indicates that the transistor is on and the white circle indicates that the transistor is turned off.
From Figure 3.16 it can be seen that the eight states are divided up into two categories, voltage vectors and null vectors, where states defined as voltage vectors are generating a voltage to the phase windings and the null vectors does not generate a voltage to the phase windings. The objective for the SVPWM is to follow the reference voltage $\mathbf{u_{ref}}$ of any angle and magnitude. In Figure 3.17 a reference voltage signal is seen in a SVPWM

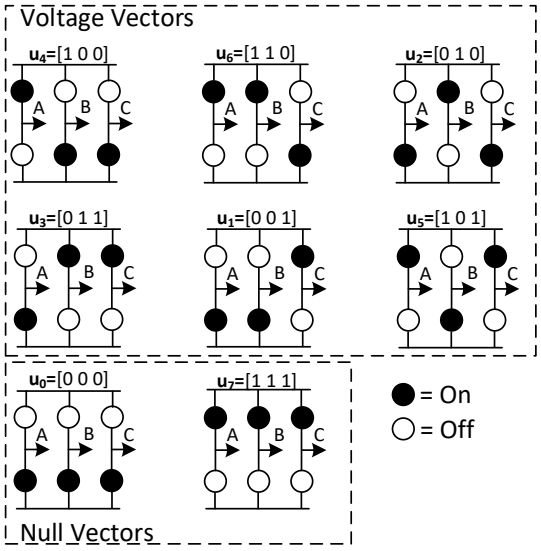

Figure 3.16: Illustration of the eight possible inverter states related voltage vectors.

sector diagram where the inner circle indicates the maximum possible magnitude to create. The number inside a circle indicates the number of the sector. In Figure 3.17 $\mathbf{u_{ref}}$ is placed between two of the voltage vectors, thus in order to follow $\mathbf{u_{ref}}$ the inverter must switch between the two voltage vectors. The null vector is used when $\mathbf{u_{ref}}$ does not require 100% of the voltage range, hence in this case there inverter should switch between the two voltage vectors and a null vector. The rest of this section will focus on how the duty cycles are generated in order to follow $\mathbf{u_{ref}}$.

Duty Cycle Generation

As mentioned the remaining of this section will examine how the duty cycles are generated in order to be able to obtain the right line to line voltages. The line to line voltages are given in Equation (3.54) as a function of the duty cycles.

$$\begin{bmatrix} u_{AB} \\ u_{BC} \\ u_{CA} \end{bmatrix} = u_{dc} \cdot \begin{bmatrix} 1 & -1 & 0 \\ 0 & 1 & -1 \\ -1 & 0 & 1 \end{bmatrix} \begin{bmatrix} D_A \\ D_B \\ D_C \end{bmatrix} \tag{3.54}$$

Where u_{dc} is the DC-link voltage.
$\mathbf{u_{ref}}$ is found by introducing a stationary reference frame $\alpha\beta$ as seen in Figure 3.17, where the stationary reference frame is marked with **purple** and divides the voltages into a real part on the α axis and the imaginary part on the β axis. Hence the voltage references for phase a,b and c can be combined into a real part and an imaginary part as in Equation (7.22).

$$\begin{bmatrix} u_\alpha \\ u_\beta \end{bmatrix} = \frac{2}{3} \cdot \begin{bmatrix} 1 & -\frac{1}{2} & -\frac{1}{2} \\ 0 & \frac{\sqrt{3}}{2} & -\frac{\sqrt{3}}{2} \end{bmatrix} \begin{bmatrix} u_a \\ u_b \\ u_c \end{bmatrix} \tag{3.55}$$

Hence the angle and magnitude of $\mathbf{u_{ref}}$ is found. With the global angle found it is possible to find the local angle ϵ in the sector as seen in Figure 3.17 where ϵ is marked with blue.

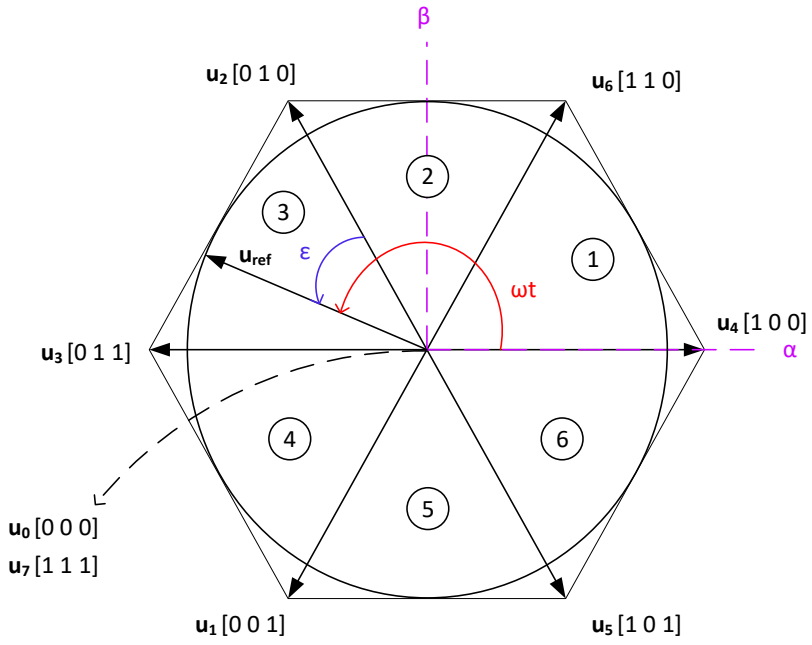

Figure 3.17: A SVPWM diagram illustrting the 6 different sectors and the related voltage vectors and null vectors.

This results in a new expression for $\mathbf{u_{ref}}$ given by (3.56).

$$\begin{aligned} \mathbf{u_{ref}} &= u_0\ cos(\epsilon) + j\ u_0 sin(\epsilon) \\ &= d_x u_A + d_y \left(\frac{1}{2} u_B + j \frac{\sqrt{3}}{2} u_B \right) \end{aligned} \tag{3.56}$$

Where $\mathbf{u_A}$ and $\mathbf{u_B}$ is the lower and upper bound in the sector respectively as seen in Figure 3.18. d_x and d_y defines the magnitude from $\mathbf{u_A}$ and $\mathbf{u_B}$ respectively and u_0 is the magnitude of $\mathbf{u_{ref}}$.
d_x and d_y is found utilising Equation (3.57).

$$\begin{aligned} d_x &= \frac{\sqrt{3} u_0}{U_{dc}} sin\left(60 - \epsilon\right) \\ d_y &= \frac{\sqrt{3} u_0}{U_{dc}} sin\left(\epsilon\right) \end{aligned} \tag{3.57}$$

To show how the duty cycles for each phase is found an example for sector one is carried out. The rest of the sectors can be found in Appendix G.

Sector One

From Figure 3.17 it can be seen that the lower bound of sector one is $\mathbf{u_4}$ and the upper bound is $\mathbf{u_6}$, furthermore both null vectors are available. In Figure 3.19 a duty cycle PWM signal, through one switching period T_{sw}, is illustrated to ease the process. The

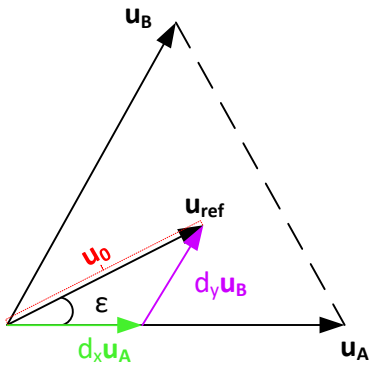

Figure 3.18: Illustration of a single sector, where the lower bound is $\mathbf{u_a}$ and the upper bound is $\mathbf{u_b}$.

different length of D_a, D_b and D_c chosen this way in order to be able to create the four binary combination of the vectors $\mathbf{u_0}$, $\mathbf{u_7}$, $\mathbf{u_4}$ and $\mathbf{u_6}$ with only on switching at a time. Thus a similar figure for another sector would have different length of D_a, D_b and D_c as seen in Appendix G.
It should be noted by the reader that every sector starts with $\mathbf{u_7}$ and ends with $\mathbf{u_0}$ when setting up the PWM signal as in Figure 3.19. Utilising Figure 3.19 as illustration it is

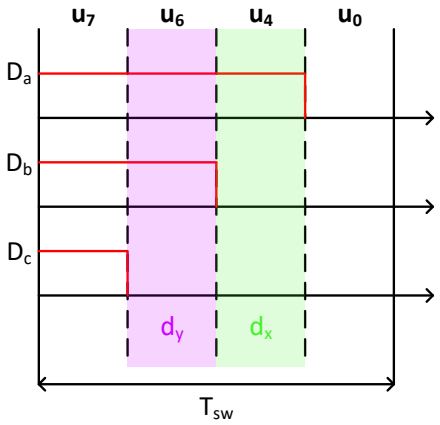

Figure 3.19: Illustration of finding the relation between the duty cycles in the inverter.

possible to set up the relation between the duty cycles of each leg (A,B and C).
d_y is related to $\mathbf{u_6}$ since it is the upper bound of the sector. The binary combination for $\mathbf{u_6}$ is found to be [1 1 0] utilising Figure 3.16. In order to maintain this binary combination D_c must be turned off. Hence the following relation is made:

$$d_y = D_b - D_c$$

d_x is related to $\mathbf{u_4}$ since it is the lower bound of the sector. The binary combination for $\mathbf{u_4}$ is found to be [1 0 0] utilising Figure 3.16. As seen $\mathbf{u_4}$ is in the end of Figure 3.19 and in order to obtain the binary combination [1 0 0] D_a must be one and D_b must go from

one to zero. Hence the following relation can be made

$$d_x = D_a - D_b$$

Since there are three unknown duty cycles D_a, D_b and D_c an extra equation is added, where the combinations of two duty cycles should be equal to 1 trough a whole switching period T_{sw}

$$1 = D_a + D_c$$

Hence it is possible to set up the relation between the duty cycles and d_x d_y. The relation is given by Equation 3.58.

$$\begin{bmatrix} 1 \\ d_x \\ d_y \end{bmatrix} = \begin{bmatrix} 1 & 0 & 1 \\ 1 & -1 & 0 \\ 0 & 1 & -1 \end{bmatrix} \begin{bmatrix} D_a \\ D_b \\ D_c \end{bmatrix} \tag{3.58}$$

By isolating the duty cycle vector as in Equation 3.59 the duty cycles for the sector are found.

$$\begin{bmatrix} D_a \\ D_b \\ D_c \end{bmatrix} = \frac{1}{2} \cdot \begin{bmatrix} 1 & 1 & 1 \\ 1 & -1 & 1 \\ 1 & -1 & -1 \end{bmatrix} \begin{bmatrix} 1 \\ d_x \\ d_y \end{bmatrix} \tag{3.59}$$

DC-Link Model

The non-linear governing equation for the DC-link model is based on the instantaneous input-output power balance for the DC-link based on the dq synchronous rotating reference frame as seen in Figure 3.20 [Teodorescu et al., 2011, sec. 9.3.2].

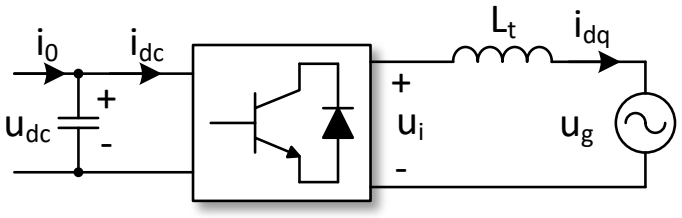

Figure 3.20: Illustration used to model the DC-link.

where u_g is the grid voltage, which is assumed to be ideal. L_t is the total grid inductance, u_i is the voltage delivered by the inverter and i_{dc} is the current delivered to the inverter by the DC-link. i_0 is the current delivered through the generator side inverter and is given by Equation 3.60.

$$i_0 = i_a D_a + i_b D_b + i_c D_c \tag{3.60}$$

Where i_a, i_b and i_c are the stator current in the generator and D_a, D_b and D_c are the duty cycles for the legs of the generator side inverter. Hence the instantaneous input-output power balance for the DC-link in the dq reference frame is given by Equation (3.61).

$$\frac{3}{2}\{u_{gd} i_d + u_{gq} i_q\} = -u_{dc} C \frac{d\, u_{dc}}{dt} + u_{dc} i_0 \tag{3.61}$$

Where ugd and u_{gq} is the grid voltage in the dq reference frame. The left side of Equation (3.61) is the power delivered to the grid and the right side is the power delivered by the generator to the DC-link. Hence in order for the DC-link to be constant the power-balance must be satisfied.

3.4.3 Grid Model

The model of the grid is chosen to be a simple L filter, due to the simplicity of the L-filter. Compared to a more advanced LCL-filter the L-filter requires larger components which is one of the downsides utilising the L-filter. A L filter is seen in Figure 3.21.

Figure 3.21: Illustration of the eight possible inverter states related voltage vectors.

The general voltage equation obtained from Figure 3.21 is given by Equation (3.62).

$$\mathbf{U_i} = R_t\mathbf{I} + \mathbf{U_g} + L_t\frac{d\,\mathbf{I}}{dt} \tag{3.62}$$

Where $\mathbf{U_i}$ is the voltage output from the inverter, $\mathbf{U_g}$ is the voltage obtained from the grid. L_t is the total inductance of the grid and R_t is the total resistance.
The L-filter can be modelled in the dq synchronous rotating reference frame and the voltage equation for the d and q component are given in Equation (3.63) utilising the Park transform [Teodorescu et al., 2011, p. 209]. The Park transformation is found in Appendix F.

$$\begin{aligned}\mathbf{u_{id}} &= R_t\mathbf{i_d} + \mathbf{u_{gd}} + L_t\frac{d\,\mathbf{i_d}}{dt} - \omega L_t\mathbf{i_q}\\ \mathbf{u_{iq}} &= R_t\mathbf{i_q} + \mathbf{u_{gq}} + L_t\frac{d\,\mathbf{i_q}}{dt} + \omega L_t\mathbf{i_d}\end{aligned} \tag{3.63}$$

where the the term $\omega L_t\mathbf{i}$ is cross couplings between the two axes. The cross couplings must be taken into account, hence when the controller for the grid side is designed a decoupling of the two axes must be made in order to avoid a poor dynamic performance.

3.5 Summary

Through this section the non-linear governing equations for the hydraulic subsystem and electrical subsystem have been presented. To be able to utilise the model as an evaluation tool for the controller etc. the dimensions of the system must be calculated in order to fit a 5MW wind turbine. Therefore, the following section will present the methods used for dimensioning the system.

CHAPTER 4

Control Objective

Chapter Contents

The objective with this chapter is to give the reader an understanding of the control law and structures utilised in this project. To do so the power curve of the NREL reference wind turbine is presented in order to clarify the regions which are under consideration. Following this, the control law used to reach the control objective is derived, and in order to do so, aerodynamic static relations of the NREL is considered. In the end of the first section the control region is delimited. This is followed by the control structures of the PMSG and grid side control. In the end of each section the control structure of the controller is presented.

Overall Objective

The main purpose of a wind turbine is to extract as much energy as possible from the wind. The NREL reference wind turbine utilised to evaluate the system is utilising a conventional variable-speed, variable pitch configuration to control the power production. The variable-speed, variable pitch configuration for controlling the power production is based on two control systems (transmission and pitch) operating below and above the rated wind speed v_r respectively as illustrated in Figure 4.1.

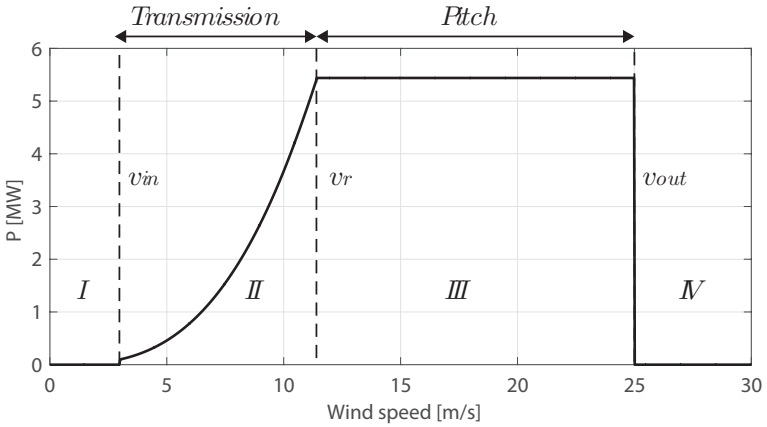

Figure 4.1: Wind regions for working areas of 5 MW NREL wind turbine [Pedersen, 2016*b*, p. 5].

Region I: In region I the velocity of the wind is too low for power production, hence the rotor is blocked and the blades are pitched out in a position where they generates a minimum of lift.

Region II: In region II the blades are pitched in a fixed angle, in order to generate a maximum of lift, hence the power production is controlled by the transmission system.

Region III: In region III the transmission system is at rated conditions, hence it is the control of the pitching system which controls the power production by regulating the pitch angle.

Region IV: In region IV the velocity of the wind is too high and the blades are pitched out in order to generate a minimum of lift and the rotor is mechanically blocked.

As stated in the project objective in the end of Chapter 1 it is desired to design a controller which is used below the rated wind speed, thus region II is of main interest in this project. As seen in Figure 4.1 it is the transmission system which mainly controls the power production. Through region II the power production should follow the curve illustrated in Figure 4.1 i.e. it should perform Maximum Power Point Tracking (MPPT) through region II.

4.1 Controllers

Through this project three main controllers are utilised. One to control the DFPT, one to control the generator and one to control the inverter of the grid side. In order to create a brief overview of the different controllers, why the different controllers are needed and the objective for each controller, a flow diagram is created to visualise the thoughts behind the use of the different controllers. The flow diagram is displayed in Figure 4.2.

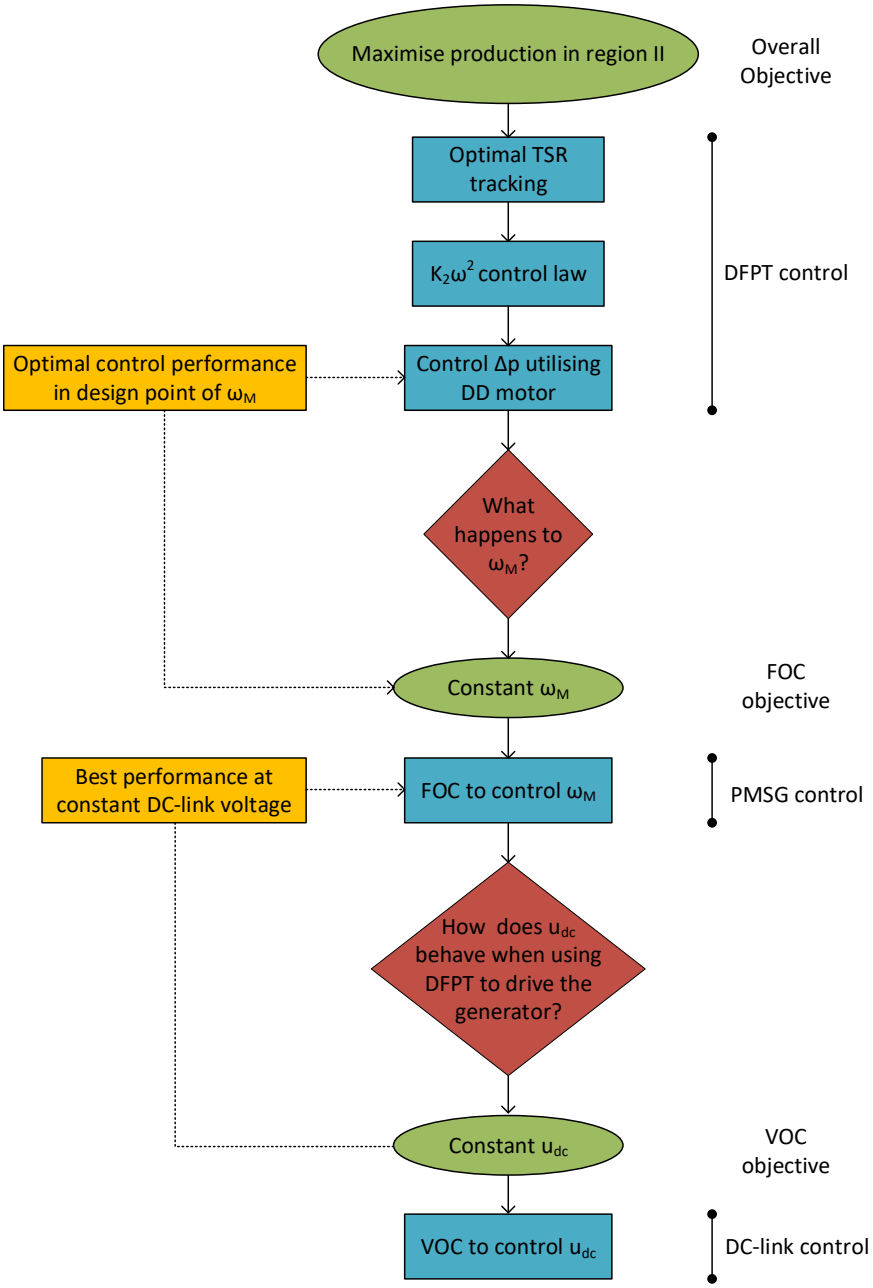

Figure 4.2: Flow diagram of the thought process behind the different controllers.

Figure 4.2 is briefly described below to create an overview. A more detailed description is given in the following sections. Starting from the top: The overall objective is to maximise the energy production throughout region II, to due the optimal Tip-Speed-Ratio should be tracked. A popular choice of control law to due so it the $K_2\omega^2$ control law. From the control law a pressure reference can be derived and used as reference for the controller. In this project the DD pump is fixed, hence the DD motor must be used to control the pressure.
The optimal control performance of the DFPT is in the operation point which the controller have been designed for. However, since the DD motor controls the pressure it

cannot control the shaft velocity. Without any control of the speed it may be difficult to predict how the speed behaves. The generator can be used to control the speed of the DD motor utilising Field Oriented Control (FOC). The objective for the FOC is to maintain a constant motor speed as close as possible to the design point.
Utilising the FOC requires a power converter. The precision of the FOC depends on the DC-link voltage inside the power converter. Ideally the DC-link voltage should be constant in order for the FOC to have a constant voltage input to SWPWM. Here another question may be asked: How does the DC-link voltage behave when the DFPT is used to drive the PMSG, as the discrete effects may influence the torque delivered to the PMSG? Therefore, Voltage Oriented Control (VOC) is utilised to control the DC-link. The objective for the VOC is to keep the DC-link voltage as constant as possible.

Through the rest of the chapter the control objective for the three controllers are described in order to give the reader a good understanding of the objective for the following chapters. Firstly the control objective and structure are defined for the controller used on the DFPT, followed by the FOC and VOC as seen in Figure 4.2.

4.2 DFPT controller

A measure of the power production is the power coefficient (C_p), which is defined as the ratio between the power extracted from the wind and the power in the wind as given by Equation (4.1).

$$C_p(\lambda, \psi) = \frac{P_r}{P_w} \qquad P_r = T_r \omega_r \tag{4.1}$$

As seen C_p is a function of the Tip-Speed-Ratio(TSR or λ) and the pitching angle ψ. Through region II ψ is fixed, hence the TSR is the only parameter which the power coefficient relies on and is defined as the ratio between the velocity of the wind and the tip speed of the blades and is given by Equation (4.2).

$$\lambda = \frac{\omega_r r_r}{v} \tag{4.2}$$

Where ω_r is the angular velocity of the rotor, r_r is the radius of the rotor swept area and v is the velocity of the wind.

In Figure 4.3 the C_p is plotted as a function of the TSR for $\psi = 0$.

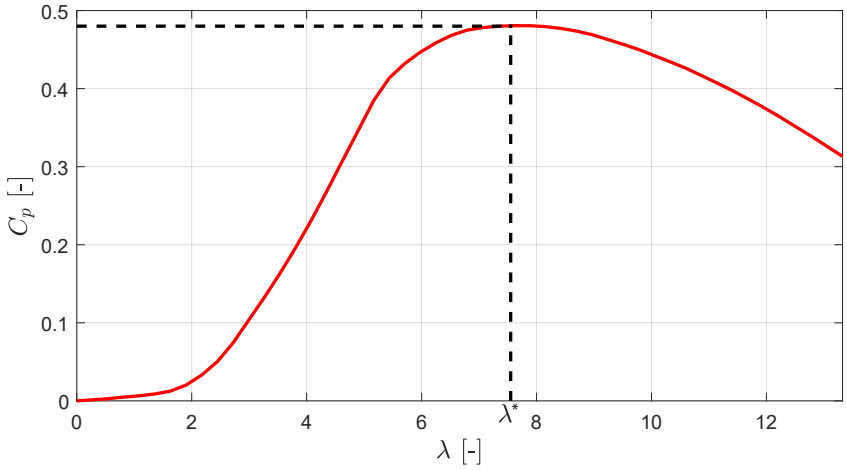

Figure 4.3: Illustration of the C_p coefficient as a function of the TSR, where $\lambda^* = 7.55$.

From Figure 4.3 it can be seen that the C_p has the optimum at a specific TSR i.e. to extract as much energy form the wind as possible C_p must be kept at its optimum which is found at an specific TSR called the optimal TSR (λ^*). Hence MPPT through region II is performed by maintaining λ^*.
To maintain the optimal tip speed ratio a popular choice of control law is the $K_2\omega^2$ [Pedersen, 2016*b*].

4.2.1 $K_2\omega^2$ Control Law

The $K_2\omega^2$ is based on the rotor torque equation given by Equation (4.3).

$$T_r = \frac{1}{2}\,\rho_{air}\,A_r\,r_r\,C_q(\lambda,\psi)v^2 \tag{4.3}$$

where ρ_{air} is the density of air, A_r is the area of the rotor swept area. C_q torque coefficient and is statically related to C_p as seen in Equation (4.4)

$$C_q = \frac{C_p}{\lambda} \tag{4.4}$$

This relation between the two coefficients is used to rewrite the rotor torque equation given by Equation (4.3) so the rotor torque depends on the power coefficient instead of the torque coefficient as seen in (4.5).

$$T_r = \frac{1}{2}\,\rho_{air}\,A_r\,r_r\,\frac{C_p(\lambda,\psi)}{\lambda}v^2 \tag{4.5}$$

Equation (4.5) is a function of λ and the wind speed. However, utilising the wind velocity can cause problems due to stochastic nature of the wind and high frequency fluctuations caused by wind gusts etc. The torque equation can be rewritten utilising the definition of the TSR in Equation (4.2), hence the torque becomes a function of the angular rotor velocity as seen in Equation (4.6).

$$T_r = \frac{1}{2}\,\rho_{air}\,A\,r_r^3\,\frac{C_p(\lambda,\psi)}{\lambda^3}\,\omega_r^2 \tag{4.6}$$

Hence the rotor is used as a low pass filter, filtering the high frequency fluctuation in the wind out. Utilising the knowledge obtained from Figure 4.3, where it was found that the power coefficient was at its optimum when $\lambda = \lambda^*$. The rotor torque can be rewritten as seen in Equation (4.7)

$$T_r^* = \underbrace{\frac{1}{2}\,\rho_{air}\,A\,r_r{}^3\,\frac{C_p^*(\lambda,\psi)}{\lambda^{*3}}}_{K_2}\,\omega_r^2 \tag{4.7}$$

where * denotes the reference. From Equation (4.7) it can be seen, that in order to maintain the optimal TSR i.e the highest possible power production, at a specific angular velocity of the rotor, the torque applied on the rotor by the pump must be equal to T_r^*. This is the so called $K_2\omega^2$ control law. However, the pump is a fixed displacement pump, hence it is not possible to control the pump torque directly. Therefore, the pump torque must be controlled by the DD motor. The two DD machines are coupled via a high pressure manifold i.e. the two machines are coupled via the pressure inside the HPM. Thus in order to control the pump torque a pressure reference for the motor must be derived.

To do so Newtons second law is derived for the rotor based on Figure 4.4.

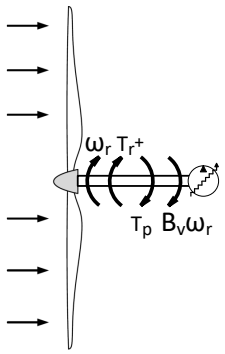

The resulting torque on the rotor axis is given in Equation (4.8).

$$J_r\dot{\omega}_r = T_{res} = T_r - B_v\omega_r - T_p \tag{4.8}$$

The rotor torque reference in Equation (4.7) is rewritten to a difference in the pressure reference by considering Newtons second law of the rotor statically i.e. the acceleration is zero as seen in Equation (4.9).

$$\begin{aligned} \dot{\omega}_r \overset{0}{=} \frac{1}{J_r}\left(T_r^* - B_v\omega_r - \underbrace{\frac{\overline{V}_p\Delta p}{\eta_p}}_{T_p}\right) \\ \Downarrow \\ \Delta p^* = (T_r^* - B_v\omega_r)\,\frac{\eta_p}{\overline{V}_p} \end{aligned} \tag{4.9}$$

where B_v is the simplified viscous friction, $\overline{V}_p$ is the fixed displacement of the pump and η_p is the hydro-mechanical efficiency of the pump. Utilising Equation (4.9) the reference for the pressure difference between the HPM and LPM pressure is found, which can be controlled by the DD motor.

4.2.2 Delimitation

In Jonkman et al. [2009, sec. 7.2] region II is divided up into three regions, region 1.5, region 2 and region 2.5. These extra regions are used as transition regions. Region 1.5 is utilised to set a lower limit of the rotor speed and it reduces the torque ripples in the system since it gives a smooth transition between region I and II instead of a discrete step between the two regions as seen in Figure 4.5 where the black line is the $K_2\omega^2$ control law defining the MPPT curve an the blue line indicates the new transition regions.
A linear transition is utilised between region II and III typically to reduce the noise at tip speed at rated power production. The newly defined transition regions is illustrated together with the other regions in Figure 4.5.

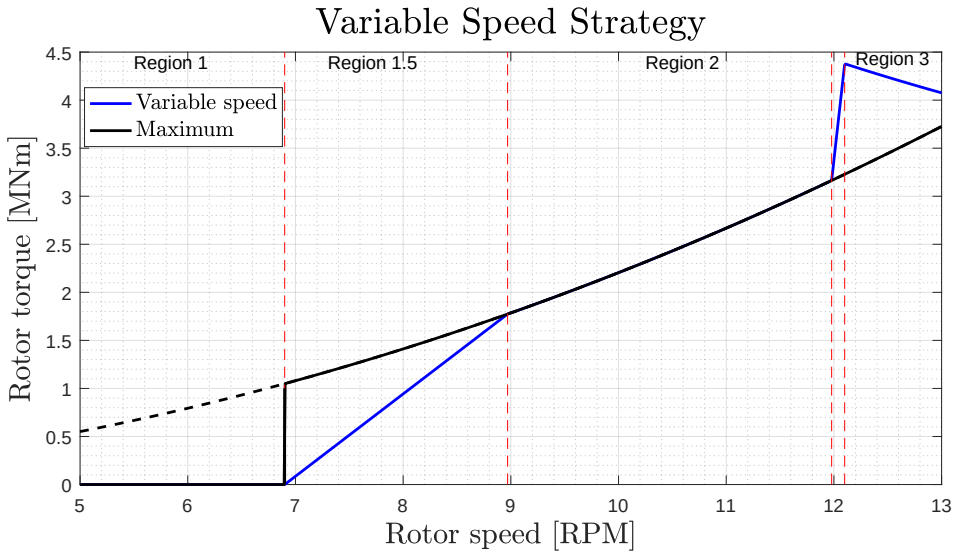

Figure 4.5: Show the rotor torque as a function of the rotor speed. The black line indicates the MPPT line defined by the $K_2\omega^2$ where the blue line takes the transition regions into account.

From Figure 4.5 it should be noted, that it is chosen to utilise the $K_2\omega^2$ control law throughout all regions indicated by the extended black dotted line. However, it is expected to operate in region 1.5 and region II. Throughout the rest of this project the control objective is to control the MPPT in the newly defined region II utilising $K_2\omega^2$ control law. Therefore, the initial conditions will all be based to be within region II, hence start-up of the DFPT and PMSG will not be considered.

4.2.3 Control Structure

The control structure utilised is illustrated in Figure 4.6.

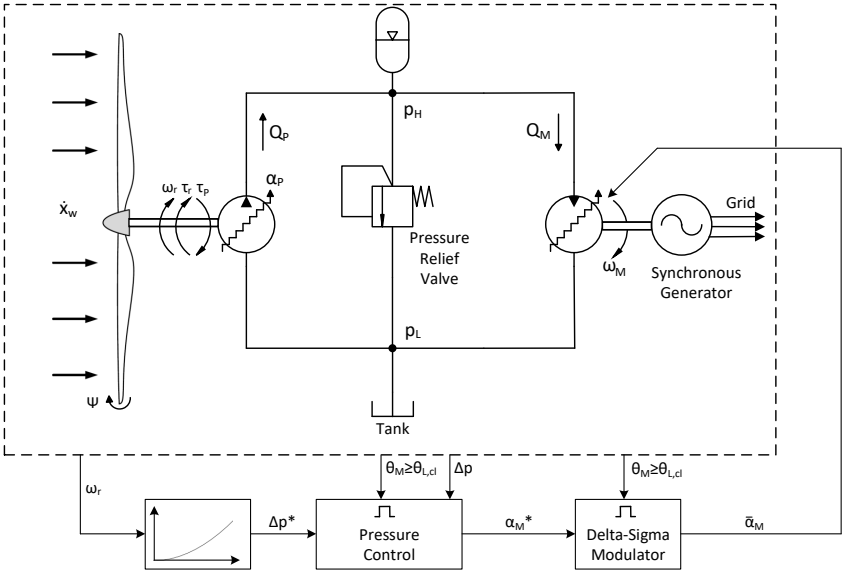

Figure 4.6: Proposed control structure.

The angular velocity of the rotor, ω_r, is measured and is utilised to first calculate the optimal rotor torque τ_r^* and then Δp^* which is the reference. The pressure is compared to the actual pressure in the system and an error signal is generated and is the input to the controller. The output of the controller is a displacement reference to the motor α_M^* which can obtain values in the continuous interval $[0; 1]$. A Delta Sigma Modulator (DSM) is chosen in this study to convert α_M^* into a binary activation sequence, where one is active (motoring mode) and zero is inactive (idling mode). Alternatively to the DSM any 1-bit analogue to digital converter (ADC) could be used for this task.

It is chosen to utilise a full stroke strategy, hence the decision of whether to activate or deactivate the cylinder is made once every revolution. This strategy implies for a discrete controller with the sampling time of given in Equation (4.10).

$$T_s = \frac{2\pi}{\omega_M N_c} \tag{4.10}$$

Where ω_M is the angular velocity of the DD motor and N_c is the number of cylinders in the DD motor.
In this project it is desired to use a discrete deterministic optimal controller for the DFPT. To develop a discrete linear deterministic controller a discrete linear representation of the model must be derived where any stochastic terms are neglected. If these terms were considered a stochastic optimal controller e.g. LQG could be considered instead. Together with the discrete linear model derivation a DSM must be derived and linearised in order to generate the activation sequence.

4.3 Generator Control

Since the DD motor controls the pressure inside the HPM, it cannot control the speed. In order to control the speed of the DD motor the generator must control the speed. The speed of the DD motor must be controlled in order for the pressure controller to work as close as possible to the speed it was designed for, in order to ensure an optimal control performance which in the end leads to an maximal power production for the wind turbine. To control speed of the PMSG a popular choice of controller is the Field Oriented Controller (FOC) which control structure is seen in Figure 4.7.

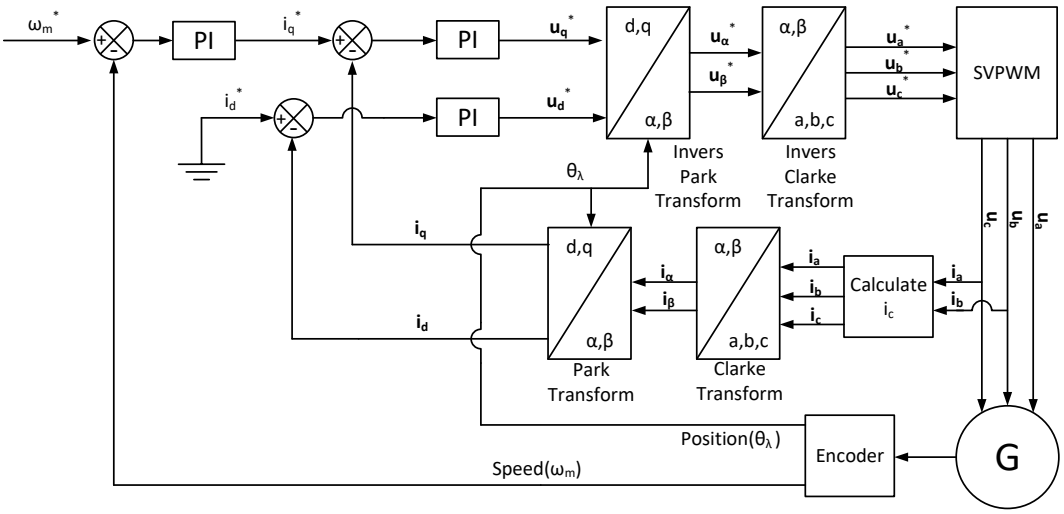

Figure 4.7: Block diagram of the Field Oriented Control utilised to control the speed of the generator.

As seen in Figure 4.7, the outer loop is the motor speed. The two inner loops are the current controllers, where the i_q^* is related to the speed, since i_q controls the torque as described in Chapter 3.

4.4 Grid Side Control

There are two main objectives for the grid side controller: Maintain a constant DC voltage and control the power factor.
The power produced by the generator is directly fed into the back-to-back converter and must be injected to the grid in order to maintain a somewhat constant DC-link. In Figure 4.8 the power flow of the inverter is seen.

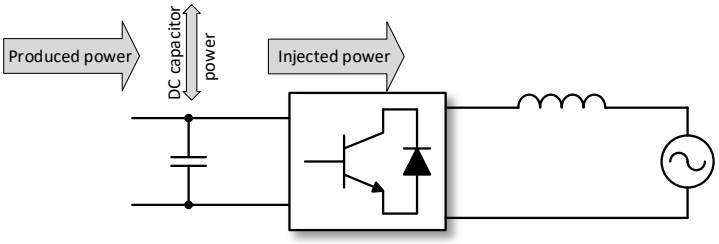

Figure 4.8: Sketch of the power flow in the inverter, which is the base of the DC-link model.

A constant DC-link is desired in order to obtain the best control performance of the FOC. If the power produced exceeds the injected power the DC-link will absorb the extra power, hence the voltage of the DC-link will increase. If the injected power exceeds the delivered power, the DC capacitor injects the extra power, hence the DC voltage will decrease.
The power factor must be controlled in order to meet the requirements propound by the Transmission System Operator (TSO) which may vary during operation. Since there is no TSO in this project and recalling the delimitation stated in Chapter 1, an ideal grid is considered, thus the power factor is one. To control the DC-link and power factor, the active and reactive power must be calculated.
To meet the requirements, Voltage Oriented Control (VOC) is a popular choice. A simplified VOC structure is illustrated in Figure 4.9.

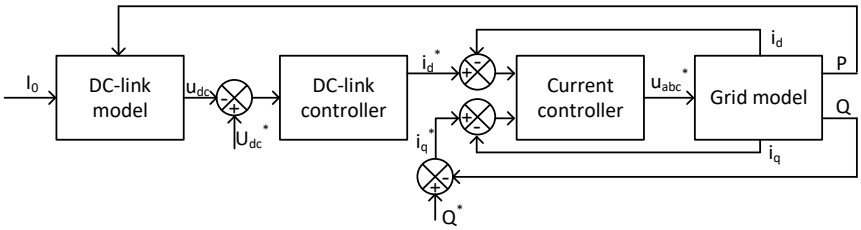

Figure 4.9: Block diagram of Voltage Oriented Control utilised to control the DC-link voltage u_{dc} and power factor of the injected power.

Figure 4.9 shows the outer DC-loop, where the DC voltage is controlled. As seen the DC-link controller controls the i_d^*, hence controls the active power, thus maintaining the right power balance of the DC-link and the reactive power controls the i_q^*. The inner loop consist of two current controllers, which output the corrected values to the grid, hereby obtaining the desired power to the grid.

4.5 Summary

Through this section the objective for the main controllers have been presented together with their respective control structure. The main controller should control the DFPT in order to be able to perform MPPT throughout region II, control the angular velocity of the motor in order to be as close as possible to the desired operation point of the DFPT controller, hence maximise the power produced. Lastly the grid side controller was presented which should control the DC-link voltage in order to get a better control performance of the speed and control the power factor in order to meet the requirement set by the TSO.
The following chapter will find the system parameters and design specifications for the system in order to be able to design the controllers chosen for this project.

CHAPTER 5

Component Dimensioning

Chapter Contents

This chapter will present the dimensioning of the system components. Firstly the DFPT components are dimensioned to fit the 5 MW wind turbine, starting with the DD pump and the DD motor. Secondly the dimensioning of the high pressure manifold with accumulator is conducted. The PMSG is dimensioned and fitted to match the operation range of the DFPT followed by the grid dimensions which are presented and fitted to match the power from the PMSG. In the end of this chapter some of the soft parameters are discussed.

5.1 DFPT Dimensioning

In this section the DD pump and DD motor will be dimensioned to match the operation conditions of the transmission system.

5.1.1 DD Pump Dimensioning

The nominal power of the NREL 5 MW turbine is first to be determined. As the different subsystems have different efficiencies, the nominal power must be larger than 5 MW to be able to deliver 5 MW at rated conditions.

The system operate with three overall efficiencies for the DD pump, the DD motor and the generator. These efficiencies are listed in Table 5.1.

From the efficiencies in Table 5.1 the combined system efficiency is given by Equation (5.1).

$$\eta_{sys} = \eta_P \ \eta_M \ \eta_G = 0.90 \tag{5.1}$$

The nominal power is given by Equation (5.2).

$$P_{nom} = \frac{5 \ MW}{\eta_{sys}} = 5.55 \ MW \tag{5.2}$$

Subsystem	Symbol	Efficiency
DD pump	η_P	0.956
DD motor	η_M	0.956
Generator	η_G	0.986

Table 5.1: Efficiencies for subsystems. The DD pump and DD motor efficiencies are read off from Figure 1.6 at 100% relative displacement. The generator efficiency is specified in Table 5.3.

The nominal torque is given by Equation (5.24).

$$T_{nom} = \frac{P_{nom}}{\omega_{r,nom}} = \frac{5.55\ 10^6\ W}{12.1\ \frac{rev}{min}}\ \frac{1}{2\pi\ \frac{rad}{rev}\ 60\ \frac{s}{min}} = 4.38\ 10^6\ Nm \tag{5.3}$$

The volume of the displaced oil should match the power/torque input during all possible operation conditions within region II.

The maximum operation pressure is chosen to $p_H = 360$ bar, based on Sasaki et al. [2014], and the low pressure line p_L to 10 bar. The nominal displacement volume per one full rotation of the pump shaft is then found by Equation (5.4).

$$V_{P,nom} = \frac{T_{nom}}{p_H - p_L} = \frac{4.38\ 10^6\ Nm}{350\ 10^5\ Pa}\ 1000\frac{L}{m^3}\ 2\pi\ \frac{rad}{rev} \approx 786\ {}^{L}/_{rev} \tag{5.4}$$

The total displacement volume is used for pump dimensioning. The number of modules $N_{P,m}$, the number of lobes $N_{P,lobe}$ and the number of cylinders $N_{P,cyl}$ are chosen as in Pedersen [2016*b*] with the modification that the number of cylinders are 25 instead of 24. Having 24 cylinders in the modules will result in a repeating conditions where two cylinders from different modules will be actuated at the same time, which will disturb the pump operation.

$$N_{P,m} = 4 \qquad N_{P,l} = 16 \qquad N_{P,cyl} = 25 \tag{5.5}$$

Knowing the total displacement per revolution of the pump the individual cylinder displacement volume $V_{P,cyl}$ can be found by Equation (5.6).

$$\begin{aligned} \bar{V}_{P,cyl} &= \frac{V_{P,nom}}{N_{P,m}\ N_{P,cyl}} = \frac{786\ {}^{L}/_{rev}}{4\ modules\ 25\frac{cyl}{modules}} \approx 7.86\ \frac{{}^{L}/_{rev}}{cyl} \\ V_{P,cyl} &= \frac{\bar{V}_{p,cyl}}{N_{P,l}} = \frac{7.86\ \frac{{}^{L}/_{rev}}{cyl}}{\underbrace{16\ {}^{strokes}/_{rev}}_{N_{P,l}}} \approx 0.49\ \frac{{}^{L}/_{stroke}}{cyl} \end{aligned} \tag{5.6}$$

For the cylinder design considerations the diameter of the piston D_P and piston stroke $L_{P,stroke}$ can be determined from the displacement volume with the relation $V_{P,cyl} = \frac{\pi}{4} D_P^2 L_{P,stroke}$. If $D_P >> L_{P,stroke}$ there may be fewer cylinders placed at the circumference however the required height of the pump casing may be reduced. If $D_P << L_{P,stroke}$ a larger number of cylinders may be placed but at the expense of a higher pump casing. Noting that the diameter of the piston is a squared term the case $D_P >> L_{P,stroke}$ is chosen. When doubling D_P the displacement volume is increased by $2^2 = 4$. Based on

this a trade-off relation is chosen to $D_P = 2L_{P,stroke}$ giving uniquely defined cylinder dimensions following in Equation (5.7) when solving for the only unknown $L_{P,stroke}$.

$$\frac{\pi}{4}\left(2L_{P,stroke}\right)^2 L_{P,stroke} = V_{P,cyl} \quad \Rightarrow \quad L_{P,stroke} = 5.4\ cm \text{ and } D_P = 10.8\ cm \tag{5.7}$$

The piston stroke length is evaluated with respect to the lobe height r_l and is given in Equation (5.8).

$$r_l = \frac{L_{P,stroke}}{2} = \frac{5.4\ cm}{2} = 2.7\ cm \tag{5.8}$$

5.1.2 DD Motor Dimensioning

The motor dimensioning is based on a preliminary motor design found in Johansen [2014, p. 12-13]. The motor is operating at 1500 RPM and contains seven cylinders per module and six modules in order to match the desired power rating. This gives a total of 42 cylinders $N_{m,cyl}$ in the DD motor.

When considering the motor design specifications the motor input should match the pump output evaluated under nominal conditions. Assuming a steady state operation Equation (5.9) must be true.

$$\begin{aligned} V_{P,nom}\ \omega_r &= V_{M,nom}\ \omega_M \\ V_{P,nom}\ \omega_r &= \frac{\pi}{4}(D_M)^2 L_{M,stroke} N_{M,cyl}\ \omega_m \end{aligned} \tag{5.9}$$

Where the motor cylinder dimensions, the piston diameter D_M and the piston stroke $L_{M,stroke}$, are the only unknowns.

Since Equation (5.9) has two unknowns a trade-off relation between D_M and $L_{M,stroke}$ can be established similar to the pump dimensions in Equation (5.7). Since high output motor torque not is significantly required compared to the pump the trade-off relation is chosen to $D_M = 1.25L_{M,stroke}$. Solving Equation (5.9) the motor cylinder dimensions can be found.

$$\begin{aligned} \frac{V_{P,nom}\ \omega_r}{N_{M,cyl}\ \omega_M} &= \frac{\pi}{4}\left(1.25L_{M,stroke}\right)^2 L_{M,stroke} \\ \frac{786\ 10^{-3}\ \frac{m^3}{rev}\ 12.1\frac{rev}{min}}{42\ 1500\frac{rev}{min}} \frac{1}{2\pi\frac{rad}{rev}} &= \frac{\pi}{4}\left(1.25L_{M,stroke}\right)^2 L_{M,stroke} \\ \Downarrow \quad L_{M,stroke} &= 4.97\ cm \approx 5.0\ cm \text{ and } D_M = 6.20\ cm \end{aligned} \tag{5.10}$$

Evaluating the piston stroke length with respect to the eccentric shaft the eccentric radius r_e is introduced and is given in Equation (5.11).

$$r_e = \frac{L_{m,stroke}}{2} = \frac{5.0\ cm}{2} = 2.5\ cm \tag{5.11}$$

5.2 High Pressure Manifold With Accumulator

The purpose of this section is to determine the initial parameters for the HPM with accumulator, which are listed as:

- Pipe volume in the HPM V_{pipe}
- Accumulator precharge pressure p_{pr}
- Accumulator volume V_{acc}

These parameters are related as shown in Equation (5.12) which describes the manifold volume, where V_f is the fluid volume in the accumulator. The size of the manifold volume V_H affects the stiffness of the system. V_{pipe} is the constant part of the manifold volume and V_f is the variable part of the manifold volume.

$$V_H = V_{pipe} + \underbrace{V_{acc} - V_{acc}\frac{p_{pr}}{p_H}^{\frac{1}{\kappa}}}_{V_f} \tag{5.12}$$

Since the overall target is to control the DFPT system and be able to damp the pressure pulsations, due to the discrete nature of the DD machines, these parameters must be determined as a trade-off between damping and response time of the system.

HPM Pipe Volume

The manifold pipe volume depends of the manifold inner pipe diameter D_p and pipe length L_p. The rated flow in the system is

$$Q_{rated} = \overline{V}_p \cdot \omega_r = 786\ L/rev \cdot 12.1\ rev/min = 9510.6\ L/min$$

and the flow velocity can be specified from [GS-Hydro, 2017], where the standard is to assume the flow velocity of the fluid to $v_{oil} = 5$ m/s to avoid excessive pressure loss. From Equation (5.13) the inner pipe diameter of the manifold can be calculated specified from [GS-Hydro, 2017, p. 168]. It has been taking into consideration that [GS-Hydro, 2017] do not specify pipe diameters above a nominal diameter of 4"/100 mm for their Stainless Steel pipes rated for 380 bar. Therefore, it is assumed that Equation (5.13) is applicable in this case.

$$D_p = \sqrt{\frac{4 \cdot Q_{rated}}{\pi \cdot v_{oil}}} = 0.200\ m \tag{5.13}$$

To determine an appropriate length of the manifold the Artemis 7 MW wind turbine DD hydrostatic transmission is investigated. Since it has not been possible to obtain a specific value for the volume of this HPM manifold, public available images of the Artemis hydrostatic transmission has been found and by rough estimations from the pictures, a manifold length has been estimated in Supplement B. From the images a V_{pipe} length of $L_p = 4$ m has been estimated.

The manifold constant pipe volume can then be calculated as shown in Equation (5.14).

$$V_{pipe} = \frac{D_p^{\,2}}{4}\pi L_p = 126.8\ L \tag{5.14}$$

Accumulator Precharge Pressure

The precharge pressure p_{pr} of the accumulator affects the behaviour of the fluid volume of the accumulator as seen in Equation (5.15). Therefore, it is investigated how the fluid

volume is affected by the choice of precharge pressure for different HPM pressures p_H. This is illustrated in Figure 5.1 where the fluid volume of the accumulator is normalised to generalise the fluid volume behaviour.

$$V_f = V_{acc} - V_{acc}\left(\frac{p_{pr}}{p_H}\right)^{\frac{1}{\kappa}} \tag{5.15}$$

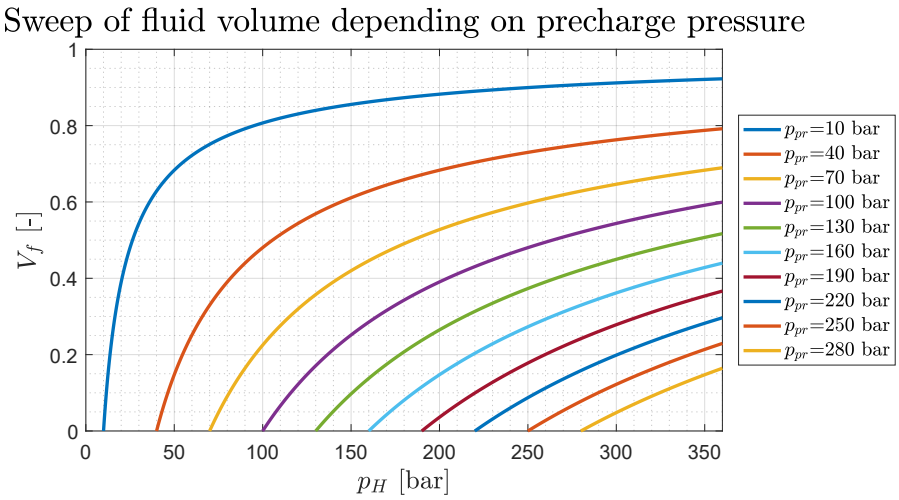

Figure 5.1: Accumulator fluid volume sweep depending on manifold pressure and precharge pressure. The entire pressure operation range operation range of p_H is for generalisation shown. No V_{acc} is chosen.

In Figure 5.1 it is seen that a low precharge pressure gives the largest initial fluid volume gradients relative to the increasing manifold pressure.

The precharge pressure is usually selected in the range given by Equation (5.16) [Rabi, 2009, p.211], hence the accumulator is continuously active during operation.

$$p_{pr} = (0.7, ..., 0.9) \cdot p_{H,min} \tag{5.16}$$

Where $p_{H,min}$ is the minimum pressure in the manifold during normal operation of the system.

However, due to the large pressure operation ratio a choice of low precharge pressure would result in little accumulator dynamic influence around rated pressure conditions at $p_{H,rated} = 360$ bar. Consequently, several accumulators with different precharge pressures could be installed, however, this is considered for future work. As a consequence of only utilising one accumulator and the focus of the control of the DFPT is below rated conditions, it is chosen to dimension the accumulator for region II operation.

5.2.1 Design of Accumulator for Region II

The estimated pressure operating range of the DFPT is found by plotting the region II pressure difference Δp^* as seen in Figure 5.2 where Equation (5.17) is utilised to construct the plot.

$$\Delta p^* = (T_r^* - B_v \omega_r) \frac{\eta_p}{V_p} \qquad T_r^* = \underbrace{\frac{1}{2} \rho_{air} A r_r^3 \frac{C_p^*(\lambda, \psi)}{\lambda^{*3}}}_{K_2} \omega_r^2 \tag{5.17}$$

The minimum and maximum pressures during operation in region II are marked indicated by the horizontal black lines and are at 83 bar and 257 bar at rotor angular velocities of 6.97 RPM and 12.1 RPM respectively. These values are found from Figure 4.5. The average pressure is indicated by the dotted magenta line and is at 170 bar.

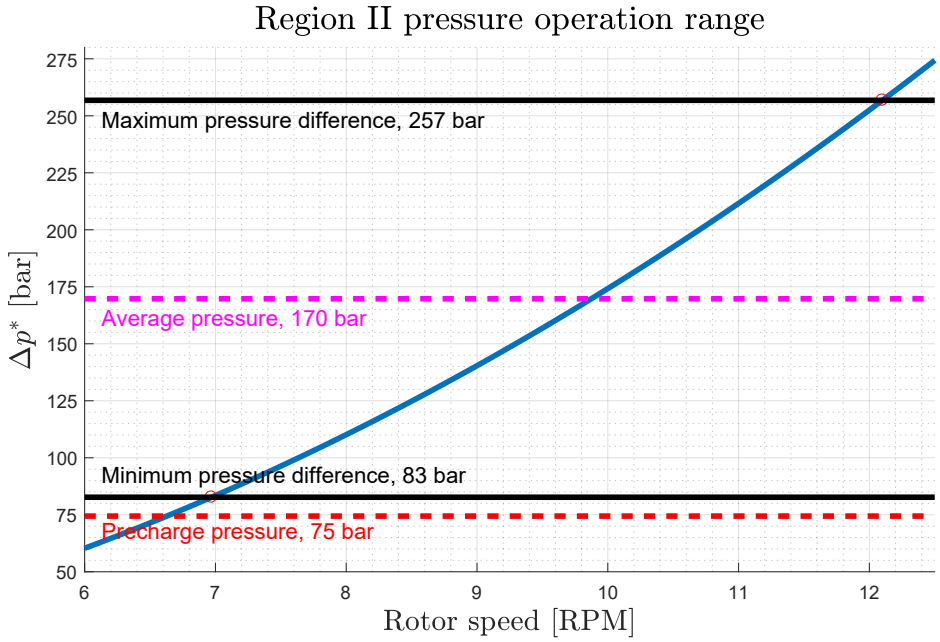

Figure 5.2: Pressure operation range in region II.

Figure 5.1 indicated that the precharge pressure should be chosen as close to the minimum manifold pressure to obtain the largest fluid volume changes with increasing pressure. Utilising this knowledge with Equation (5.16) the precharge pressure is chosen to $p_{pr} = 75$ bar, as shown in Equation (5.18).

$$p_{pr} = p_{H,min} \cdot 0.9 = 75 \; bar. \tag{5.18}$$

The chosen precharge pressure is indicated in Figure 5.2 by the red dotted line.

As indicated in Figure 5.1 the entire accumulator volume V_{acc} will not be utilised in the expected pressure range, hence in the following section the choice of the accumulator volume V_{acc} is investigated.

Accumulator Volume

The accumulator volume is to be chosen in this section. It is investigated how much of the accumulator fluid volume that can be utilised under different manifold pressure conditions within region II.

Figure 5.3 is used to show the normalised fluid volume on the vertical axis depending on the normalised precharge pressure ratios $\frac{p_H}{p_{pr}}$ on the horizontal axis.

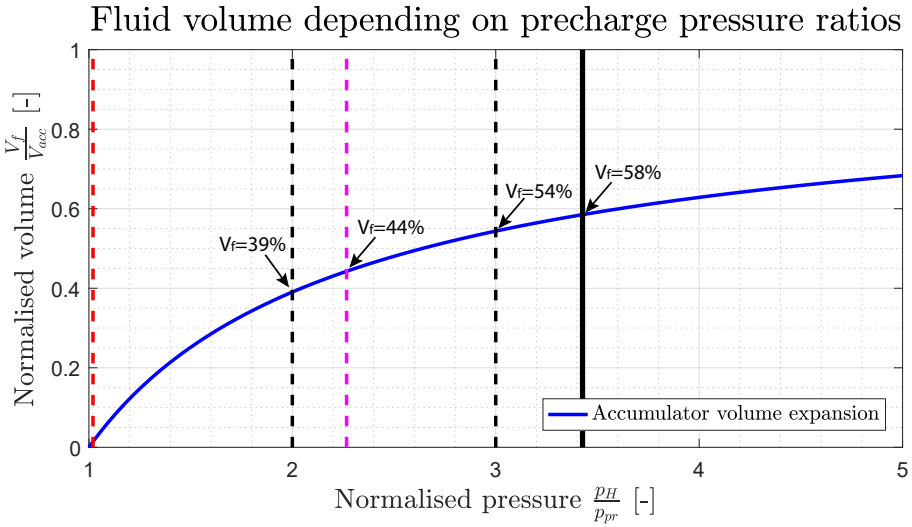

Figure 5.3: Normalised accumulator fluid volume as function of normalised accumulator precharge pressure ratios. The average pressure ratio in the HPM is indicated with the magenta dotted line. The maximum pressure ratio in the HPM manifold during region II is indicated with the solid bold back line.

From Figure 5.3 it is seen that the largest utilisation of the accumulator capacity is occurring when the manifold pressure p_H is between $p_H = p_{pr}$ and $p_H = 2 \cdot p_{pr}$ and it is seen that 39 % of the accumulator volume is utilised at this condition. At $p_H = 3 \cdot p_{pr}$ it is seen that 54 % of the accumulator volume is utilised. At average HPM pressure 44 % of the accumulator volume is utilised and at maximum pressure during region II 58 % of the accumulator volume is utilised.

In order to determine the accumulator volume V_{acc}, it is chosen to investigate the influence of V_{acc} in the frequency domain. This is done to obtain a reasonable trade-off between fast response time and damping of the pressure ripples.

In order to investigate the influence of V_{acc}, the continuity equation from Equation (3.33) is considered and rewritten in Equation (5.19) for convenience.

$$\dot{p_H} = \frac{1}{\frac{V_H}{\beta_{ef}} + \frac{1}{\kappa}\frac{V_g}{p_H}} (\underbrace{Q_P - Q_M}_{\sum Q} - k_{leak}\Delta p) \tag{5.19}$$

The aim is to establish a transfer function $\frac{\Delta p}{\sum Q}$, therefore Equation (5.19) is transferred to the frequency domain as seen in Equation (5.20), where $\sum Q$ is the flow ripple and Δp is the manifold pressure, which should be damped by the accumulator. Utilising the

condition $\Delta\dot{p} = \dot{p}_H$ Equation (5.20) can be established.

$$\frac{\Delta p}{\sum Q} = K\frac{1}{\tau s + 1} \tag{5.20}$$

However, since the pressure dynamics in Equation (5.19) is nonlinear, a linear representation of the HPM is needed and is found in Appendix D and repeated here for convenience in Equation (5.21) and (5.22).

$$K = \frac{1}{k_{leak}} \qquad \tau = \frac{1}{k_{leak}K_{\Delta P}} \qquad K_{\Delta P} = \frac{1}{\frac{V_H}{\beta_{ef}} + \frac{1}{\kappa}\frac{V_g}{p_{H0}}} \tag{5.21}$$

$$V_H = V_{pipe} + V_{acc} - V_g \qquad V_g = V_{acc}\left(\frac{p_{pr}}{p_{H0}}\right)^{\frac{1}{\kappa}} \tag{5.22}$$

The frequency response has the effect of a first order filter and is shown in the bode diagram in Figure 5.4 for different accumulator volumes, where $V_{acc} = 0$ L is considered as an upper limit i.e. the minimal damping that can achieved in the system.

The frequency response is evaluated at the average pressure in region II and, therefore, the linearisation point for this evaluation is chosen to $p_{H,0} = 180$ bar, where Figure 5.2 shows the average pressure during region II marked with the magenta dotted line.

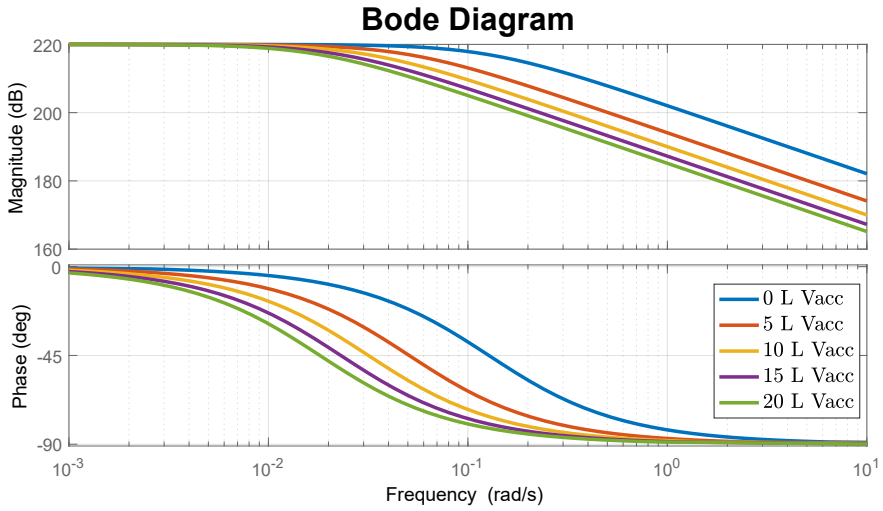

Figure 5.4: Frequency response for HPM without and with accumulator.

It is seen from Figure 5.4 that choosing an accumulator size of 10 L will introduce a significant amount of damping, where the cut-off frequency is seen to be significantly influenced by adding an accumulator to the HPM. However, increasing V_{acc} above 10 L will not contribute significantly. Hence an additional increase in accumulator volume above 10 L will not contribute with an equal amount of increased damping in the system.

Therefore, V_{acc} is chosen to 10 L as a trade-off between accumulator size, damping and response time of the system during region II operation.

In conclusion, the utilised parameters of the HPM with accumulator are summarised in Table 5.2.

Parameter	Symbol	Value	Unit
Pipe volume in the HPM	V_{pipe}	126.8	L
Accumulator volume	V_{acc}	10	L
Accumulator precharge pressure	p_{pr}	75	bar

Table 5.2: Utilised parameters of the HPM with accumulator.

5.3 PMSG Dimensioning

It has been challenging to find data for a 5 MW PMSG with a rated speed of 1500 RPM and a rated frequency of 50Hz. However, data for a 5 MW PMSG is available where the main parameters are found in Table 5.3 [Mazaheri, 2012].

Denotation	Parameter	Value	Unit
P_{nom}	Rated Output Power	5	MW
$\omega_{g,nom}$	Rated Speed	750	RPM
$f_{g,nom}$	Rated Frequency	50	Hz
$u_{g,nom}$	Rated Voltage	4800	V
R_s	Stator phase Resistance	0.0375	Ω
L_s	Stator Phase Inductance	15.37	mH
u_{ind}	Fundamental Induced RMS Line Voltage	5032	V
λ_{mpm}	Flux Linkage Established by Magnets	13.078	Vs
N_{pp}	Number of Pole Pairs	4	-
η_g	Rated Efficiency	98.6	%

Table 5.3: Main data for the PMSG found in [Mazaheri, 2012].

The text marked with red indicates the parameters which are not identical for the rated conditions of the DFPT, if a rated frequency of 50 Hz is desired. The following section will focus on calculations of the maximum phase current which is used to calculate the limits in the model.

Current Calculation

Firstly, the coherence between the fundamental induced RMS line voltage and the maximum flux linkage established by the permanent magnets. The u_{ind} should be converted to phase voltage by dividing with $\sqrt{3}$ and from RMS to peak by multiplying by $\sqrt{2}$. The calculation is given by Equation (5.23).

$$\lambda_{mpm} = \frac{\frac{u_{ind}}{\sqrt{3}} \cdot \sqrt{2}}{2\pi \frac{\omega_{g,nom}}{60s} N_{pp}} = 13.078 Vs \tag{5.23}$$

As seen the value is identical to the one in Table 5.3. The phase current is calculated. To do so the rated torque delivered by a single phase is calculated by Equation (5.24).

$$T_g = \frac{P_{nom}}{3 \cdot \frac{\omega_{g,nom}}{60} \cdot 2\pi} = 21221 Nm \tag{5.24}$$

Hence the torque produced by a single phase is equal to 21221Nm. Utilising Equation 5.24 $I_{ph,RMS}$ can be found by isolating i_q in Equation (3.51) as seen in Equation (5.25).

$$i_q = \frac{2}{3}\frac{1}{\lambda_{mpm}} T_g = 1080A \tag{5.25}$$

Since the rated speed of the PMSG does not match the rated speed of the DFPT, it is decided to establish a possible speed range of the DFPT.

5.3.1 Operation Area of the DFPT

Since the generator shaft are directly coupled to the motor shaft the limitations of the DFPT is investigated. It is decided to investigate the possible displacement reference α_M of the motor for several steady state shaft speeds combinations of the pump and motor. By doing this, it gives an indication of what speed range the motor shaft is allowed to operate within when coupled to the generator.

The steady state analysis is conducted by setting the flow condition Q_P=Q_M such that the output flow of the DFPT is matched with the available input flow. Utilising the given flow condition, the possible displacement references are calculated by Equation (5.26).

$$\alpha_M = \frac{\overline{V}_P \omega_r \alpha_P}{\overline{V}_M \omega_M} \qquad \omega_r = \begin{cases} \frac{\lambda^* v_{mean}}{r_r} & if \quad \omega_r < \omega_{r,nom} \\ \omega_{r,nom} & if \quad \omega_r \geq \omega_{r,nom} \end{cases} \tag{5.26}$$

Where ω_r is found for several mean wind speeds v_{mean} within region II through the following relation $\omega_r = \frac{\lambda^* v_{mean}}{r_r}$, with λ^* being the optimal tip-speed ratio.

The possible displacement references α_M is illustrated in a contour plot in Figure 5.5 where the two vertical constraints indicate region II and the third constraint indicate $\alpha_{M,max}$ which is the maximum possible value.

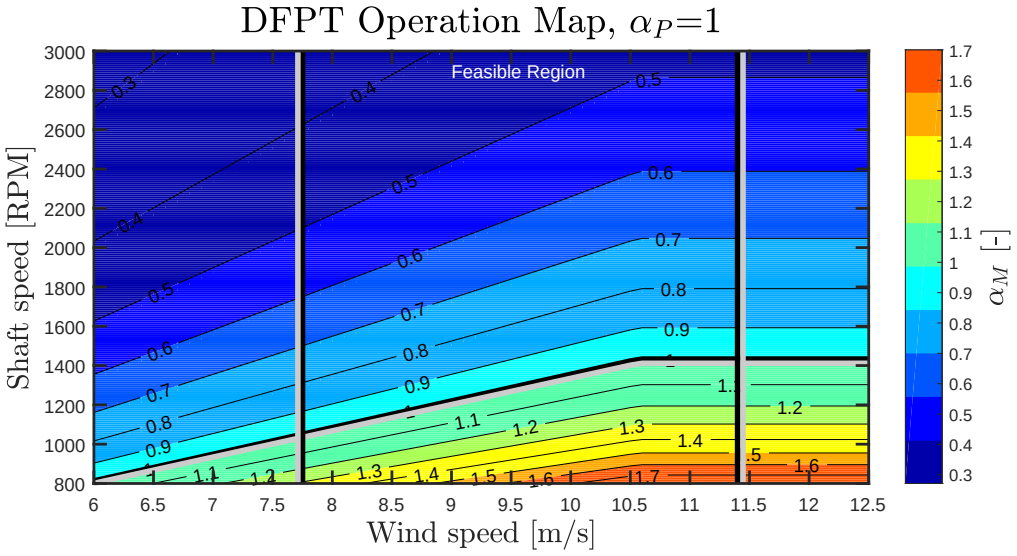

Figure 5.5: Possible speed range of the DFPT at steady state operations.

The figure indicates that a speed below 1000 RPM is not reasonable in region II. The

upper limit of the motor speed set by the DFPT is unbounded, however the displacement reference α_M is desired to operate near maximum displacement of 100 %. Furthermore, considering the rated conditions at a wind speed of 11.4 m/s, the DD motor should operate at 1500 RPM.

5.3.2 Redesign of PMSG Parameters

Since the DFPT are not able to run at 750 RPM without the pressure increases, the number of pole pairs is reduced in order to obtain a larger rated speed. Table 5.4 lists the rated speed for a different number of pole pairs if a rated frequency at 50 Hz is desired.

Number of Pole pairs (N_{pp})	Rated Speed [RPM]
1	3000
2	1500
3	1000
4	750

Table 5.4: Number of pole pairs and the related rated speed at a rated frequency of 50 Hz.

With the operation range established in Section 5.3.1, it is chosen to reduce the number of pole pairs by two giving a rated speed 1500 RPM as given in Table 5.4.
By reducing the number of poles the size of the PMSG is changed, hence the different electrical parameters may have changed too. This is considered as a major task if the parameters should be adjusted in order to match the reduced number of poles. Therefore, it is considered as negligible changes, which not would affect the conclusion in any significant manner.
The parameters which have been subjected to changes are summarised in Table 5.5.

Parameter	Value	Unit
$\omega_{g,nom}$	1500	RPM
N_{pp}	2	-

Table 5.5: Changed parameters for PMSG.

With the changed parameter for the PMSG it is still considered valid to utilise the model, since it is considered difficult to find better data for other 5MW PMSGs.

5.4 Grid Dimensioning

The model of the grid covers the connection from the wind turbine and to the point of connection just before the transformer. The voltage at POC is therefore determined by the requirements of the transformer. The transformer is however not in scope of this project the connection voltage is chosen to be 6.6kV line-to-line RMS voltage as this is the connection voltage closest to the voltage level of the PMSG.

Only two extra parameters must be decided in this section, the resistance and the inductance of the grid.
The inductance of the the grid can be set equal to the leakage inductance of the transformer. The leakage inductance of the transformer can in general be set to 6% of L_b, where L_b is the base inductance which can be found utilising Equation (5.27) [Lorenzen and Nielsen, 2015].

$$L_b = \frac{Z_b}{\omega_b} \qquad \omega_b = 2\pi f_{line} \tag{5.27}$$

Where the subscript b denotes base values. Z_b is impedance of the grid and f_{line} is the frequency of the grid.
The base impedance can be found utilising Equation (5.28).

$$Z_b = \frac{u_b^2}{S_b} \tag{5.28}$$

Where base voltage is set equal to the line to line RMS voltage of the grid and S_b is the base apparent power which is set equal to the one for the generator at full load, hence equal to $6.2MVA$.

$$L_t = 6\% \cdot L_b = 1.3\,mH \tag{5.29}$$

The resistance however is more difficult to find. In this project the resistance is chosen to be 0.5Ω. This value is chosen with help from Associate Professor Tamas Kerekes.
Thus the parameters used to model the grid have been found and listed in Table

Parameter	Symbol	Value	Unit
Electrical grid resistance	R_t	0.5	Ω
Electrical grid inductance	L_t	1.3	mH
Line to line RMS grid voltage	$U_{g,ll}$	6.6	kV

Table 5.6: Parameters used to model the electrical grid.

5.5 Back-to-Back Converter

This section will explain how the capacitance of the DC-link capacitor is chosen for this purpose Equation (5.30) is utilised [Asimmoaei et al., 2006].

$$C_{dc} = \frac{\left(\frac{1}{2}\sqrt{2}I\right) \cdot \frac{T_{sw}}{2}}{4\Delta u_{max}} \tag{5.30}$$

As seen in Equation (5.30) the DC-link capacitance C_{dc} depends on the DC-link current I, the switching period T_{sw} and the maximum allowed voltage ripple Δu_{max}. The different parameters used is seen in Table 5.7.
Firstly the DC-link voltage is determined using a general expression for the dc-bus voltage as seen in Equation (5.31) [Asimmoaei et al., 2006].

$$U_{dc} = k_1 \cdot u_{a,pk} = 10.778kV \qquad u_{a,pk} = \frac{u_{ga,ll}\sqrt{2}}{\sqrt{3}} \tag{5.31}$$

Where k_1 is a safety margin which must be greater than two. $u_{a,pk}$ is the line to neutral peak voltage, in this case it is the grid voltage, since this is the highest voltage in the

Parameter	Symbol	Value	Unit
Grid voltage (RMS)	$u_{g,ll}$	6.6	kV
Voltage ripple	Δu_{max}	$1\% \cdot U_{dc}$	V
Fundamental frequency	f_0	50	$[Hz]$
Switching frequency	f_{sw}	$100 \cdot f_0 = 5$	kHz
Power average of capacitor	P_{dc}	5	MW

Table 5.7: Parameters used for designing the DC-link.

system.
With the voltage across the DC-link determined, the current across the DC-link can be found by considering the power at rated condition as given by Equation (5.32) [Gohil et al., 2014].

$$I = \frac{P_{dc}}{U_{dc}} = 464\,A \tag{5.32}$$

With the values defined these can be substituted into Equation (5.30) hence the capacitance of the DC-link is:

$$C_{dc} = 76.8\mu F$$

5.6 Soft Parameters

Since the project is theoretical the parameters found through this chapter are not based on any physical system. Therefore, some of the parameters are considered soft parameters, i.e. parameters which are considered reasonable to change. To give the reader a overview of the most important soft parameters are stated in Table 5.8 and discussed in this section.

Parameter	Description
V_0	Cylinder chamber dead volume
V_{pipe}	High pressure manifold volume
V_{acc}	Accumulator volume
P_{pr}	Precharge pressure for the accumulator
t_s	Switching time for the valves
B_v	Viscus friction coefficient for the shafts
η	Efficiencies
J_g	Inertia of the generator

Table 5.8: Some of the parameters which are considered as soft parameters.

Dead volume of the cylinder chamber: V_0 is considered as a soft parameter, since the dead volume depends on the cylinder type and in this project no specific cylinder is chosen. For this study V_0 is set equal to the chamber volume, which is rough assumption, however, is chosen due large flow passages that generally are experienced in DD machines [Roemer, 2014, p. 43]. By adjusting V_0 the damping will be influenced.

Volume of the high pressure manifold: V_{pipe} is a soft parameter, since the value is a initial guess based on rough estimates from images of the MHI SeaAngel prototype seen in Supplement B.

The accumulator volume: V_{acc} is found by considering the damping in the system. Therefore, V_{acc} is considered as a soft parameter, because if further damping of the pressure pulsation is desired an increase of the accumulator volume should be made and vice versa.

Acummulator precharge pressure: P_{pr} is based on the lowest pressure obtained in region II as $P_{pr} = p_{h,min} \cdot 0.9$. Therefore, it is considered as a soft parameter.

Valve switching time: t_s is a soft parameter. It is chosen to be 1 ms in order to be able to compare with other studies. However, as mentioned earlier a slower valve will effect the efficiency of the system but not the actual control performance as long as the closing angle is changed in order to match a slower valve. Furthermore, it is to the authors best knowledge not possible to buy commercial valves with closing and opening times of 1 ms.

Viscous coefficient for the shaft: The viscous damping coefficient for the motor shaft are based on rough estimates of overall efficiency and could have been included in the efficiency. However, these values are needed for controller design.

The efficiency coefficients in the system: In general the hydro mechanical efficiency coefficients are estimates. The hydraulic efficiencies are used in order to take the missing friction in the cylinders into account.
The electrical efficiency of the inverter is considered to be 100%. This is justified since that a power evaluation is not in scope of the project.

Generator inertia: J_g is found from the data sheet of the generator. However since the number of poles have been reduced the size and weight of the generator is minimised. Therefore, J_g is considered a semi soft parameter.

5.7 Summary

Through this section the hydraulic components used have been dimensioned in order to fit the 5MW NREL reference wind turbine. In the electrical subsystem the generator has been dimensioned to fit the operation range of the DFPT. The electrical grid have been designed to fit a 6.6kV transformer and the back-to-back converter has been dimensioned in order to fit the generator parameters and the grid parameters.
With the dimensions of the system defined, the system can be linearised with the purpose of linear control design.

CHAPTER 6

Discrete Linear Representation

Chapter Contents

This chapter consists of two parts. The first part considers the hydraulic system and the second part considers the elements of the electrical systems which must be linearised.
From Chapter 4 it was stated that the discrete nature of the DFPT and due to the full stroke control strategy it implies for discrete control of the DFPT. It is desired to design a discrete linear deterministic optimal controller for the DFPT, hence a discrete linear time invariant (DLTI) approximation model of the DFPT must be derived. Firstly, the delta sigma modulator, which is used to determine the binary activation sequence for the cylinders, is presented and then linearised. Secondly, the DLTI approximation model is derived by considering a DLTI approximation model of the DD motor, manifold and simplified rotor dynamics. In the end of the first part the above mentioned models are put on a state space form to ease the design of the deterministic optimal controller.
It is desired to control the DC-link voltage, hence the non-linear governing equations of the DC-link are linearised which results in a transfer function which can be used to design the controller in Chapter 7.

6.1 Delta Sigma Modulator

As mentioned in Chapter 4 the nature of the DD machines apply for discrete control, hence a proper control structure must be developed. To do so a DSM is utilised. The DSM is able to transform a continuous displacement reference to a binary activation sequence used to determine whether a cylinder should be active in the case of a binary input of 1. Or whether it should be inactive in the case of input of 0. Either there will be full displacement or no displacement from a particular cylinder and therefore a displacement error will be present. Utilising a first order DSM the average of the output is approximately equal to the input over time, due to the discrete integrator. This is an advantage when utilising the DSM.

The block diagram of the DSM is seen in Figure 6.1 [Reiss, 2008, p. 53].

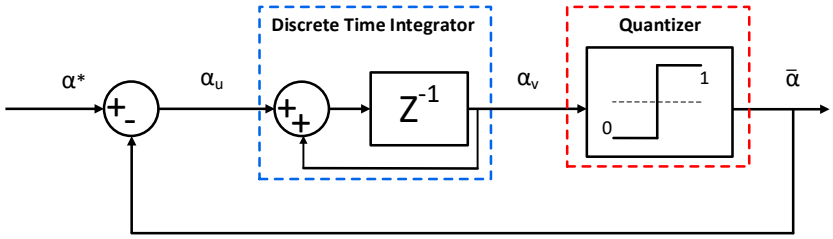

Figure 6.1: First order DSM block diagram.

This block diagram contains a discrete time integrator and a quantizer. The discrete time integrator sums up the displacement error by computing the sum of the previous input to the discrete time integrator with the previous output of the discrete time integrator. The displacement error is thereby compensated in the future sampling instances. The quantizer transforms a continuous signal to a discrete signal. The continuous output signal from the discrete time integrator will always be either 0 or 1 decided at a threshold value at 1/2. An output of the quantizer of 0 corresponds to an idle stroke and 1 corresponds to a pump/motor stroke.

The governing equations for the DSM will be derived using the block diagram in Figure 6.1 from left to right. The displacement error α_u is given by Equation (6.1).

$$\alpha_u(k) = \alpha^*(k) - \overline{\alpha}(k) \tag{6.1}$$

Where k denotes the sampling number in the following equations. α^* is the displacement reference and $\overline{\alpha}$ is the displacement output for a particular cylinder.

The output of the discrete time integrator α_v is given in Equation (6.2).

$$\alpha_v(k) = \alpha_u(k-1) + \alpha_v(k-1) \tag{6.2}$$

The output of the quantizer is given in Equation (6.3).

$$\overline{\alpha}(k) = \begin{cases} 1 & for \quad \alpha_v \geq \frac{1}{2} \\ 0 & for \quad \alpha_v < \frac{1}{2} \end{cases} \tag{6.3}$$

Figure 6.2 shows simulation results of the DSM with a displacement reference of $\alpha^* = 0.6$ to give the reader an understanding of the working principle of the DSM. The simulation time is chosen to be 0.04 s, which is equivalent to the time for one DD motor rotation, when the motor has an angular velocity of 1500 RPM.

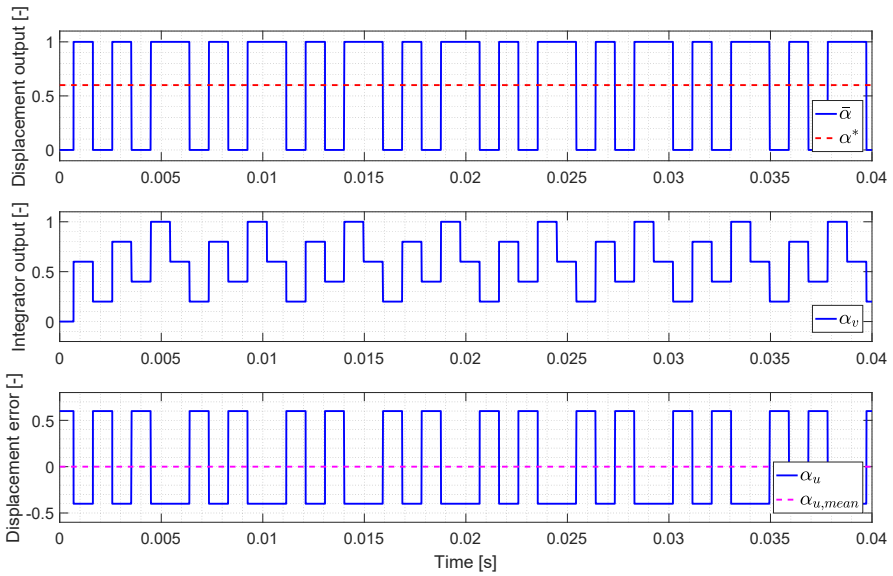

Figure 6.2: Simulation of DSM sequence with input of $\alpha^* = 0.6$.

In Figure 6.2 the dashed red line in the top plot is the input α^* to the DSM. The DSM output $\overline{\alpha}$ approximates this input during a DD motor rotation of 0.04 s, which can be seen by the activation of 25 out of 42 cylinders, $^{25}/_{42} = 0.5952$, which is approximately equal to the input of the DSM. In the middle plot the integrator output α_v is shown, which is seen to memorise the displacement error. In the bottom plot the displacement error α_u is shown. The purple dashed line is the mean displacement error during a DD motor rotation, which is seen to be approximately zero.

6.1.1 Linear Delta Sigma Modulator

The DSM in Figure 6.1 is highly non-linear due to the quantizer, however the quantizer can be considered as an additive zero mean white noise input n as shown in Figure 6.3 [Reiss, 2008, p. 53].

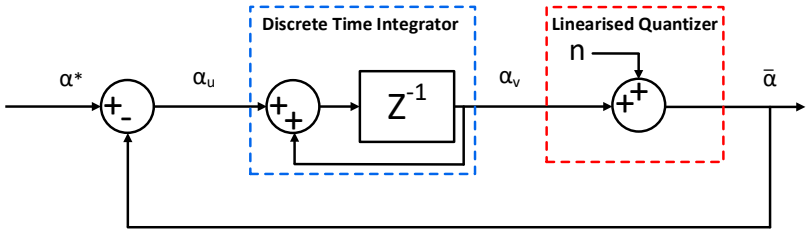

Figure 6.3: Linear representation of the DSM.

From Figure 6.3 the discrete representation of the discrete transfer function is established in Equation 6.4. The noise is considered as zero mean white noise with a value of ± 0.5.

$$\overline{\alpha}(k) = \alpha^*(k-1) + n(k) - n(k-1) \tag{6.4}$$

From Equation (6.4) it can be seen that the output of the LDSM consists of a single sampled delayed input signal and a discrete differentiated noise term representing the quantization error. With the intention to utilise a deterministic optimal controller, the noise term can be neglected and the output of the LDSM is equal to the input with a single sample delay given in Equation (6.5).

$$\overline{\alpha}(k) = \alpha^*(k-1) \tag{6.5}$$

6.2 Discrete Linear Motor Flow Approximation

In this section the DD motor flow will be discretised and a linear relationship between the flow intake of a motor chamber and the displacement reference will be established using a convolution sum model. This discretisation method is used under the assumption that the chamber volume expansion is equal to the chamber flow as shown in Equation (6.6), hence the pressure gradient $\Delta\dot{p}$ is neglected. This assumption is considered sufficient if the change in the pressure gradient $\Delta\dot{p}$ is small, which is considered satisfied except at valve opening or closing.

$$Q_H = \frac{V_c(\theta)}{\beta_{ef}}\dot{\Delta}_p + \dot{V}_c \qquad \dot{V}_c \approx 0 \tag{6.6}$$

The motor chamber flow can be approximated as the difference between two volume samples as shown in Equation (6.7).

$$Q_H[k] \approx \frac{V_c(\theta[k+1]) - V_c(\theta[k])}{T_s} = \frac{V_c(\pi)}{T_s}\Delta\overline{V}_c[k] \tag{6.7}$$

$\Delta\overline{V}_c[k]$ is the normalised displacement fraction to sample k. ${}^{V_c(\pi)}/_{T_s}$ is the maximum flow fraction possible during a sample k. However as seen the maximal flow fraction depends on the sampling time which was presented in Chapter 4, but for convenience is rewritten in Equation (6.8).

$$T_s = \frac{2\pi}{\omega_M N_c} \tag{6.8}$$

As seen the sampling time depends on the DD motor angular velocity ω_M which is variable. Thus the sampling time T_s is variable. Rewriting the flow equation presented in Equation (6.7) using the definition of the sampling time from Equation (6.8) the expression for the DD motor flow is given by Equation (6.9).

$$Q_H[k] \approx \underbrace{\frac{V_c(\pi)\cdot N_c}{2\cdot\pi}}_{k_q}\cdot\Delta\overline{V}_c[k]\cdot\omega_M[k] \tag{6.9}$$

k_q is the maximum displacement fraction possible during a sample k. Hence the normalised displacement fraction $\Delta\overline{V}_c$ is the only unknown. Figure 6.4 is the base of the derivation of the discrete motor mode which is used to find $\Delta\overline{V}_c$.

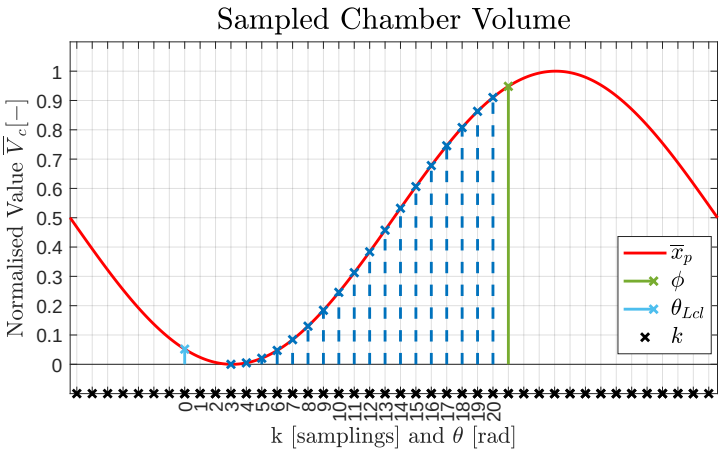

Figure 6.4: Illustration used as base for the discrete approximation model of the motor chamber flow.

From Figure 6.4 the closing angle of LPV is seen at sample $k = 0$, hence the decision to whether the chamber should be in motoring or idling mode is made at this instant. Ideally the motoring stroke should last for a half period from $\theta_e = 0$ to $\theta_e = \pi$, hence with 42 cylinders in the motor the motoring stroke should last for 21 samples.

Since the LPV is passively opened at $\theta_e = \pi$, and due to valve dynamics, a delay of three samples is introduced. ϕ is the closing angle of the discrete flow model and is found by a trial and error process to obtain the best possible cohesion between the discrete and non-linear flow. ϕ is found to be $\theta_{Hcl} + 5.5°$.

The displacement fraction can be calculated utilising Equation (6.10) [Pedersen, 2016*b*].

$$\Delta\bar{V}_c[k] = \begin{cases} 0 & \theta_e[k], \theta_e[k+1] \notin [0; \phi] \\ \bar{V}_c(\theta_e[k+1]) - \bar{V}_c(\theta_e[k]) & \theta_e[k], \theta_e[k+1] \in [0; \phi] \\ \bar{V}_c(\theta_e[k+1]) - \bar{V}_c(0) & \theta_e[k] < 0 < \theta_e[k+1] \\ \bar{V}_c(\phi) - \bar{V}_c(\theta_e[k]) & \theta_e[k] < \phi < \theta_e[k+1] \end{cases} \tag{6.10}$$

Utilising the displacement fractions from Equation (6.10), in the convolutions sum model given by Equation (6.11), the discrete flow Q_H can be found.

$$\alpha_M[k] = \sum_{m=0}^{k} \Delta\overline{V}_c[k-m]\,\overline{\alpha}_M[m] \qquad Q_H[k] = k_q \alpha_M[k]\,\omega_M \tag{6.11}$$

Where α_M is the displacement reference and $\overline{\alpha}$ is the impulse input. The impulse response of the convolution sum model described in Equation (6.11) results in the output flow for a single chamber.
Since the DD motor chamber flow in Equation (6.11) depends on two states $\alpha_M[k]$ and $\omega_M[k]$ the motor flow is non-linear. Therefore it is linearised utilising Taylor series approximation as given by Equation (6.12).

$$\begin{aligned} \delta Q_H &= \left.\frac{\partial Q_H}{\partial \alpha_M}\right|_0 \delta(\alpha_M) + \left.\frac{\partial Q_H}{\partial \omega_M}\right|_0 \delta\omega_M \\ \delta Q_H &= k_q \cdot \left[\omega_{M,0} \cdot \delta(\alpha_M) + \cancelto{\mathbf{0}}{\alpha_M \cdot \delta\omega_M}\right] \end{aligned} \tag{6.12}$$

where 0 indicates the linearisation point. The $\alpha_M \cdot \delta\omega_M$ part of Equation (6.12) is the assumed angular velocity variations occurring for the DD motor during operation. This is considered as a disturbance and is neglected from the linearised expression. This assumption is considered valid since the speed of the motor is externally controlled in a proper manner. Choosing the linearisation parameter for the angular motor velocity $\omega_{M,0}$ as the rated angular velocity of 1500 RPM, the DD motor chamber flow can be approximated as given in Equation (6.13) where the δ has been omitted for simplicity.

$$Q_H[k] \approx k_q \cdot \omega_{M,0} \cdot \alpha_M[k] \tag{6.13}$$

To verify the use of the presented DLTI approximation model of the motor flow, it is compared to the flow from the non-linear model in the following section.

6.2.1 Discrete Motor Model Verification

In Figure 6.5 the impulse response of the DLTI approximation model is compared to a single cylinder flow from the non-linear model.

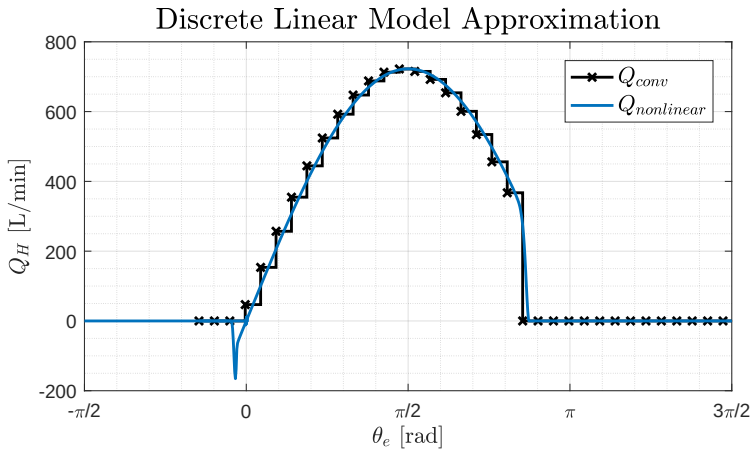

Figure 6.5: Verification of the discrete motor model, where the discrete model are compared to the non-linear flow.

From Figure 6.5 good coherence is seen between the two models. The discrete linear chamber flow model Q_{conv} is seen to follow the output flow from the non-linear model in a reasonable manner. The largest difference between the models is at just before $\theta_e = 0$ where the backflow occurs, due to the pressure difference between p_c and p_H, at passive HPV opening. Furthermore it is seen that the discrete linear model loses some accuracy in the end of the stroke where the pressure gradient is large due to the closing of the HPV. The deviation seen between sample 2 and 3 could be compensated by subtracting an additional flow at $k = 2$. However, as the backflow is pressure dependent, it complicates the DLTI approximation. Therefore the DLTI flow is considered sufficiently to be applicable for control design.

6.3 Manifold and Rotor Dynamics

The purpose of this section is to linearise the manifold and rotor dynamics. As the manifold dynamics is described by the continuity equation, this equation is first linearised and afterwards the rotor dynamics. Both the linearised manifold and rotor dynamics are transformed into the position domain from the time domain by a method called Event-driven Control, to allow for classical discrete control theory.

6.3.1 Manifold

The equivalent continuity equation presented in Equation (3.33) is non-linear due to the variable HPM pressure p_H, which affects the oil bulk modulus and the volumes V_H and V_g as clarified in Equation (6.14) where the combined non-linear term is denoted $K_{\Delta p}$.

$$\dot{p}_H = \underbrace{\frac{1}{\frac{V_H(p_H)}{\beta_{ef}(p_H)} + \frac{1}{\kappa}\frac{V_g(p_H)}{p_H}}}_{K_{\Delta p}} \Big(Q_P - Q_M - k_l \underbrace{(p_H - p_L)}_{\Delta p} \Big) \tag{6.14}$$

It may be difficult to say how the non-linear term $K_{\Delta p}$ evolves as the pressure increases. Therefore, $K_{\Delta p}$ is plotted as a function of the pressure in Figure 6.6.

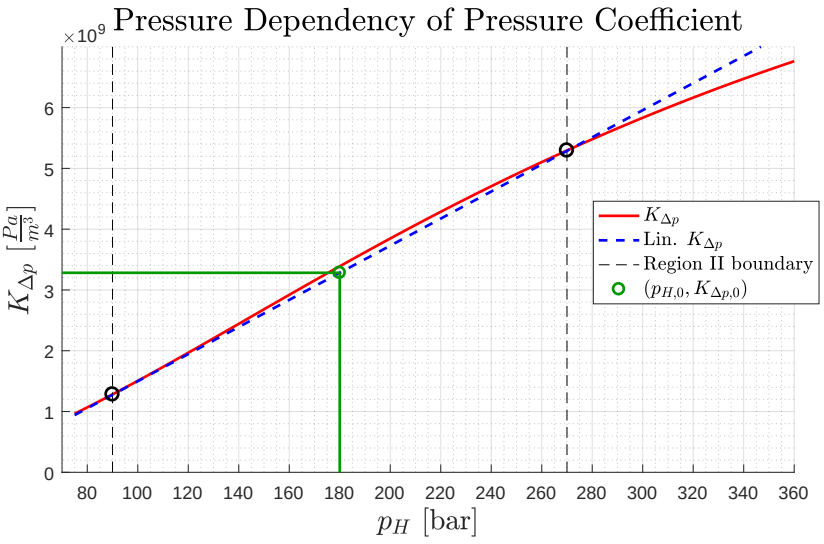

Figure 6.6: Equation (6.14) plotted together with the linear approximation.

As seen in Figure 6.6, indicated by the red line, $K_{\Delta p}$ is almost linear until the pressure exceeds 300 bar. Therefore, it is decided to approximate $K_{\Delta p}$ by a linear coefficient indicated by the blue dashed line to ease the linearisation. The linear approximation of $K_{\Delta p}$ is given by Equation (6.15).

$$K_{\Delta p} \approx \frac{K_{\Delta p,max} - K_{\Delta p,min}}{p_{H,max} - p_{H,min}} \tag{6.15}$$

Where the maximum and minimum values utilised to find the linear approximation of $K_{\Delta p}$ is indicated by the black circles in Figure 6.6.

As seen in Figure 6.6 the difference between the linear approximation of $K_{\Delta p}$ and the non-linear $K_{\Delta p}$ is small, hence it is considered as a representative linear approximation of the non-linear $K_{\Delta p,max}$ The green line in Figure 6.6 indicates the linearisation point of the pressure p_H, which is chosen to be in the middle of the pressure range. The linearised HPM dynamics can then be represented as in Equation (6.16).

$$\delta\Delta\dot{p} = K_{\Delta p,0}\left(\delta Q_P - \delta Q_M - k_{leak}\delta\Delta p\right) \tag{6.16}$$

The rotor dynamics presented in Equation (4.9) is already linear when the rotor torque is linearised at $\omega_{r,0}$, hence no linearisation of the equation is needed.

The equations presented throughout this section are in the time domain. However, since speed of the motor is varying, the sample T_s time is variable hence asynchronous in time. Classical discrete control theory is thus not applicable and Equation (6.16) needs to be transformed into a synchronous angle domain.

To allow for classical discrete control theory a method called Event-driven control is applied, which transforms the asynchronous time-dependent equations into the synchronous position domain. The event-driven control method is described in Section 6.3.2.

6.3.2 Event-driven Control

The transformation into position domain is achieved by considering the motor angle as the independent variable such that the sample time only is available at discrete motor angles which are defined as state-events. The transformation can be described by Equation (6.17) where $t(\theta)$ denotes the time, where the motor shaft angle equals θ [Heemels et al., 1998, p. 14].

$$\frac{d\,\theta(t)}{d\,t} = \omega_M \quad \Rightarrow \quad \frac{d\,t(\theta)}{d\,\theta} = \frac{1}{\omega_M(\theta)} \tag{6.17}$$

Equation (6.17) is valid if $\omega_M \neq 0$ and the motor speed direction does not change which is justified for the operation of the DPFT for the 5 MW wind turbine considered in this study.

The rotor and pressure dynamics are transformed into the position domain by applying Equation (6.17) to Equation (4.9) and (6.16) and are given in Equation (6.18). The linear δ-operator is omitted for simplicity.

$$\begin{aligned}
\frac{d\,\omega_r(\theta)}{d\,\theta} &= \frac{1}{J_r\,\omega_M(\theta)}\Big(\tau_r(\theta) - B_v\,\omega_r(\theta) - \frac{\overline{V}_P}{\eta_P}\Delta p(\theta)\Big) \\
\frac{d\,\Delta p(\theta)}{d\,\theta} &= \frac{K_{\Delta p}}{\omega_M(\theta)}\Big(Q_P(\theta) - Q_M(\theta) - k_l\,\Delta p(\theta)\Big)
\end{aligned} \tag{6.18}$$

Equation (6.18) is non-linear due to the variable motor shaft speed and needs to be linearised in order to use classical linear control techniques for the design of the controller.

The linearisation is achieved utilising a small signal model around a steady state operation point $\omega_{M,0}$ which is 1500 RPM since it is the desired motor shaft speed at all times where the deviations from this point is denoted with δ. The linearised rotor and pressure dynamics are given in Equation (6.19) where the angular dependency has been omitted

for simplicity [Heemels et al., 1998, p. 16].

$$\begin{aligned} \frac{d\,\delta\omega_r}{d\,\theta} &= \frac{1}{J_r\,\omega_{M,0}}\left(\delta\tau_r - B_v\,\delta\omega_r - \frac{\overline{V}_P}{\eta_P}\delta\Delta p\right) \\ \frac{d\,\delta\Delta p}{d\,\theta} &= \frac{K_{\Delta p}}{\omega_{M,0}}\Big(\delta Q_P - \delta Q_M - k_l\,\delta\Delta p\Big) \end{aligned} \tag{6.19}$$

The linear models for the DSM, the motor flow and the system dynamics will be set on state space form in the following section to ease the deterministic optimal control design presented in Chapter 7.

6.4 Discrete Linear State Space Representation

The linearised system equations, presented in Section 6.1 to 6.3, are set on state space form with the aim to utilise a model based state feedback controller.

The discrete state space representation of the system will be established utilising Figure 6.7.

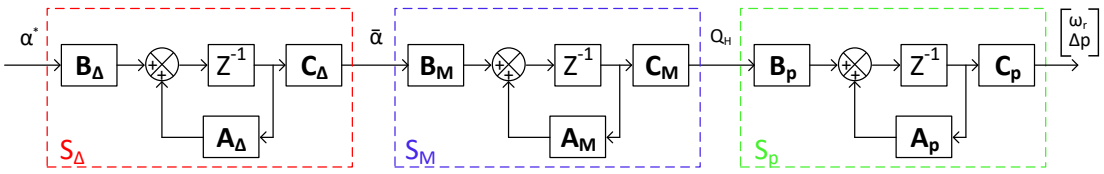

Figure 6.7: Illustration used to establish the combined discrete system state space model.

From Figure 6.7 it can be seen how the different SS models interacts with each other. As seen the output from S_Δ is the input to the SS model of the DD motor S_M and the flow output from S_M is the input for the SS model of the HPM and simplified rotor dynamics.

6.4.1 Delta Sigma Modulator

In Section 6.1.1 it was shown that the LDSM could be represented as a single unit delay if the quantizer is considered as noise and neglected. The state space representation of the LDSM can be setup as shown in Equation (6.20).

$$\begin{aligned} x_\Delta(k+1) &= \underbrace{[0]}_{A_\Delta} x_\Delta(k) + \underbrace{[1]}_{B_\Delta} u(k) \\ y(k) &= \underbrace{[1]}_{C_\Delta} x_\Delta(k) \end{aligned} \tag{6.20}$$

6.4.2 Motor Flow

The state space model of the motor flow is given in Equation (6.21). The input to the motor flow state space model is the output of the delta sigma modulator. The states $\mathbf{x_M}$ are the 20 previous delta sigma modulator outputs.

$$\begin{aligned}
\underbrace{\begin{bmatrix} \overline{\alpha}_M(k) \\ \overline{\alpha}_M(k-1) \\ \overline{\alpha}_M(k-2) \\ \vdots \\ \overline{\alpha}_M(k-p+1) \end{bmatrix}}_{\mathbf{x_M}(k+1)} &= \underbrace{\begin{bmatrix} 0 & 0 & \cdots & 0 & 0 \\ 1 & 0 & \cdots & 0 & 0 \\ 0 & 1 & \cdots & 0 & 0 \\ \vdots & \vdots & \ddots & \vdots & \vdots \\ 0 & 0 & \cdots & 1 & 0 \end{bmatrix}}_{\mathbf{A_M}} \underbrace{\begin{bmatrix} \overline{\alpha}_M(k-1) \\ \overline{\alpha}_M(k-2) \\ \overline{\alpha}_M(k-3) \\ \vdots \\ \overline{\alpha}_M(k-p) \end{bmatrix}}_{\mathbf{x_M}(k)} + \underbrace{\begin{bmatrix} 1 \\ 0 \\ 0 \\ \vdots \\ 0 \end{bmatrix}}_{\mathbf{B_M}} \overline{\alpha}_M[k] \\
\mathbf{y_M}(k) &= \underbrace{k_q\,\omega_{M,0}\begin{bmatrix} \Delta\overline{V}_c[1] & \Delta\overline{V}_c[2] & \Delta\overline{V}_c[3] & \cdots & \Delta\overline{V}_c[p] \end{bmatrix}}_{\mathbf{C_M}} x_M(k) \\
&\quad + \underbrace{k_q\,\omega_{M,0}\begin{bmatrix} \Delta\overline{V}_c[0] \end{bmatrix}}_{D_M} \overline{\alpha}_M(k)
\end{aligned} \tag{6.21}$$

Where $p = 20$ is the last sample in the motoring stroke.

6.4.3 Manifold and Rotor Dynamics

The continuous model of the manifold dynamics in Equation (6.19) can be represented in a state space model given by Equation (6.22), where the rotor torque is considered as external disturbance and is omitted in the control design. Furthermore, the small signal term δ is omitted for simplicity.

$$\begin{aligned}
\underbrace{\begin{bmatrix} \frac{\mathrm{d}\,\omega_r}{\mathrm{d}\,\theta_s} \\ \frac{\mathrm{d}\,\Delta p}{\mathrm{d}\,\theta_s} \end{bmatrix}}_{\dot{\mathbf{x}}} &= \underbrace{\begin{bmatrix} -\frac{B_v}{J_r\omega_0} & -\frac{\overline{V}_P}{\eta_P J_r \omega_0} \\ \frac{\beta\overline{V}_P}{V_H\omega_0} & \frac{-\beta\,k_l}{V_H\omega_0} \end{bmatrix}}_{\mathbf{A}} \underbrace{\begin{bmatrix} \omega_r \\ \Delta p \end{bmatrix}}_{\mathbf{x}} + \underbrace{\begin{bmatrix} 0 \\ -\frac{\beta}{V_H\omega_0} \end{bmatrix}}_{\mathbf{B}} \underbrace{Q_M}_{u} + \underbrace{\begin{bmatrix} \frac{1}{J_r\omega_0} \\ 0 \end{bmatrix}}_{\mathbf{E}} \cancel{\tau_r}^{\,0} \\
\mathbf{y} &= \underbrace{\begin{bmatrix} 1 & 0 \\ 0 & 1 \end{bmatrix}}_{\mathbf{C}} \mathbf{x}
\end{aligned} \tag{6.22}$$

Equation (6.22) is normalised to $-1 \leq \overline{\omega}_r \leq 1$ and $-1 \leq \Delta\overline{p} \leq 1$ to avoid numerical problems in the control design process. The normalisation is achieved utilising a similarity transformation in Equation (6.23) where $\mathbf{P}$=diag$\{[\omega_{r,max} \quad \Delta p_{max}]\}$ [Phillips and Parr, 2011, p. 98-99].

$$\mathbf{A_v} = \mathbf{P}^{-1}\mathbf{A}\mathbf{P} \qquad \mathbf{B_v} = \mathbf{P}^{-1}\mathbf{B} \qquad \mathbf{C_v} = \mathbf{C} \tag{6.23}$$

The transformed states become $\overline{\omega}_r$ and $\overline{\Delta}p$ thus still applicable for feedback control.

The normalised plant in Equation (6.23) is discretised in the position domain by θ_s assuming a zero order hold to the continuous plant such that the input Q_M is constant between two sampling instants $k\theta_s \leq \theta \leq (k+1)\theta_s$. The discretisation is achieved utilising Equation (6.24) [Ogata, 1995, p. 314-315].

$$\mathbf{A_p} = e^{\mathbf{A_v}\theta_s} \qquad \mathbf{B_p} = \mathbf{A_v}^{-1}\left(e^{\mathbf{A_v}\theta_s} - \mathbf{I}\right)\mathbf{B_v} \qquad \mathbf{C_p} = \mathbf{C_v} \tag{6.24}$$

6.4.4 Combined System

From Figure 6.7 Equation (6.25) can be established by combining the state space models of the DSM, the motor flow and the dynamics of the rotor and pressure in the system.

$$\begin{aligned}\underbrace{\begin{bmatrix}\mathbf{x_p}(k+1)\\ \mathbf{x_M}(k+1)\\ x_\Delta(k+1)\end{bmatrix}}_{\mathbf{x_c}(k+1)} &= \underbrace{\begin{bmatrix}\mathbf{A_p} & \mathbf{B_p}\,\mathbf{C_M} & \mathbf{0}\\ \mathbf{0} & \mathbf{A_M} & \mathbf{B_M}\,\mathbf{C_\Delta}\\ \mathbf{0} & \mathbf{0} & A_\Delta\end{bmatrix}}_{\mathbf{A_c}} \underbrace{\begin{bmatrix}\mathbf{x_p}(k)\\ \mathbf{x_M}(k)\\ x_\Delta(k)\end{bmatrix}}_{\mathbf{x_c}(k)} + \underbrace{\begin{bmatrix}\mathbf{0}\\ \mathbf{0}\\ B_\Delta\end{bmatrix}}_{\mathbf{B_c}} \alpha^*(k)\\ \mathbf{y}(k) &= \underbrace{\begin{bmatrix}\mathbf{C_p} & \mathbf{0} & 0\end{bmatrix}}_{\mathbf{C_c}} \mathbf{x_c}(k)\end{aligned} \tag{6.25}$$

This combined state space model will be used in the design of a deterministic optimal controller. The control design is conducted in Chapter 7.

6.5 Linearisation of DC-link

This section is based on [Teodorescu et al., 2011, sec. 9.3.2] if nothing else is stated.
As stated in Chapter 4 the objective of the controller is to control the DC voltage through the i_d current. The control structure contains a cascade loop, where the inner loop is the current controller and the outer loop is the DC-link controller. Therefore, the two loops may be considered decoupled if the DC-link controller is designed to be at least a decade slower than the current controller. Hence the control problem can be considered linearised.
However this assumptions is not valid during start ups and under unbalanced conditions which leads to second harmonics oscillations in the DC-link voltage. Under these conditions the inner and outer loop cannot be considered decoupled, thus the control problem is no longer linear. Through this section the DC-link dynamics will be analysed by considering a small signal linearisation of the instantaneous input-output power balance presented in Section 3.4.2. For convenience the instantaneous input-output power balance is stated in Equation (6.26)

$$\frac{3}{2}\left\{u_{gd}i_d + u_{gq}i_q\right\} = u_{dc}C\frac{d\,u_{dc}}{dt} + u_{dc}i_0 \tag{6.26}$$

The result of the small signal linearisation of Equation 6.26 is given by Equation (6.27).

$$\begin{aligned}&\frac{3}{2}\left\{\left(U_{gd}+\hat{u}_{gd}\right)\left(I_d+\hat{i}_d\right)+\left(U_{gq}+\hat{u}_{gq}\right)\left(I_q+\hat{i}_q\right)\right\}\\ &=\left(U_{dc}+\hat{u}_{dc}\right)C\frac{d\left(U_{dc}+\hat{u}_{dc}\right)}{dt}+\left(U_{dc}+\hat{u}_{dc}\right)\left(I_0+\hat{i}_0\right)\end{aligned} \tag{6.27}$$

Where " ˆ " denotes the perturbations.
As mentioned earlier it is desired to control the voltage of the DC-link with the d component of the grid current. To do so an equation which the transfer function $\hat{u}_{dc}/\hat{i}_d$ can be derived from must be found. Therefore the other perturbations are set equal to zero, hence Equation (6.28) is obtained.

$$\frac{3}{2}\left\{U_{gd}I_d + U_{gd}\hat{i}_d + U_{gq}I_q\right\} = U_{dc}C\frac{d\,\hat{u}_{dc}}{dt} + \hat{u}_{dc}I_0 + U_{dc}I_0 \tag{6.28}$$

Equation (6.28) can be divided up in constants and perturbations as seen in Equation (6.29) and (6.30) respectively.

$$\frac{3}{2}\left\{U_{gd}I_d + U_{gq}I_q\right\} = U_{dc}I_0 \tag{6.29}$$

$$\frac{3}{2}\left\{U_{gd}\hat{i}_d\right\} = U_{dc}C\frac{d\,\hat{u}_{dc}}{dt} + \hat{u}_{dc}I_0 \tag{6.30}$$

By assuming the steady state equivalent resistance is equal to $R_0 = {}^{V_{dc}}/_{I_0}$ and $U_{dc} \simeq \sqrt{3}u_{dg}$. It should be noted that the DC voltage cannot be lower than this value in order to allow for current control, if the DC-link is greater than this value the losses in the IGBT's increases. The transfer function is derived and is given by Equation (6.31).

$$\frac{\hat{u}_{dc}}{\hat{i}_{dc}} = \frac{\sqrt{3}}{2}\frac{R_0}{1 + R_0Cs} \tag{6.31}$$

6.6 Summary

Through this section the linear models of the system equations for the delta sigma modulator, the motor flow and the manifold and rotor dynamics have been established. These linearised equations have been set on state space form with the purpose to design a model based state feedback controller for the hydraulic DFPT. Also for the electrical system, the DC-link dynamics have been linearised for the purpose of being able to design a linear controller for controlling the d component of the grid current. The controller design is conducted in the following chapter.

CHAPTER 7

Controller Design

Chapter Contents

The objective with this chapter is to describe the utilised control strategy for the hydraulic and electrical subsystems. A stability analysis is conducted to evaluate the stability and performance of the controller for the DFPT. For the electrical subsystem Field Oriented Control (FOC) is utilised to control the speed for the generator and Voltage Oriented Control (VOC) is utilised to control the grid side of the back-to-back converter.

System and Control Overview

Through this chapter the three controllers are presented. The controllers are related to the three major subsystems in the system, the DFPT model, the PMSG model and the grid model respectively. This section will seek to give the reader an overview of how the three systems and controllers are connected. Furthermore, it should give the reader an understanding of which of the parameters are controlled. A block diagram of the three systems and controllers is illustrated in Figure 7.1.

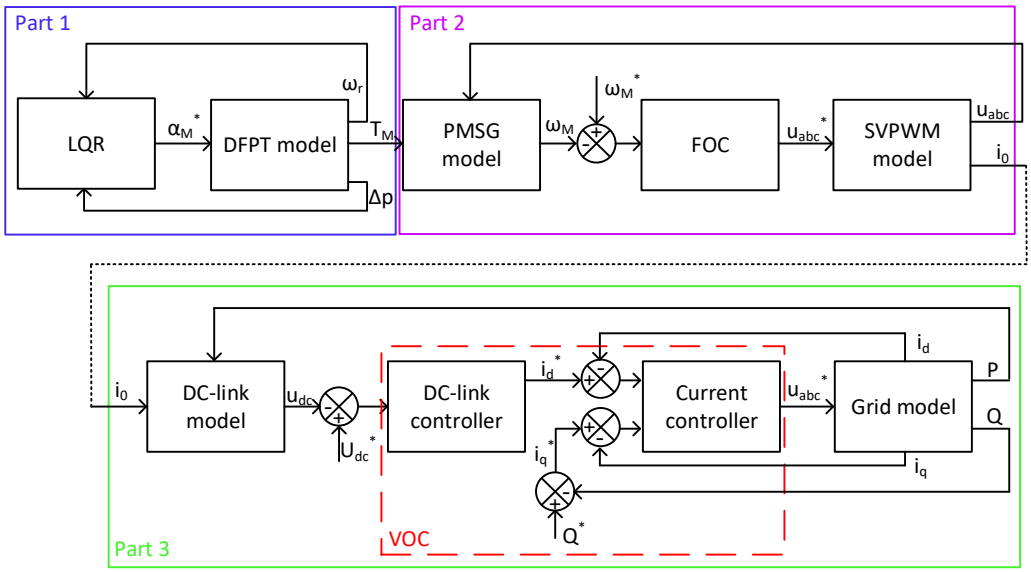

Figure 7.1: Block diagram of the control structures for the different systems.

As seen in Figure 7.1 the block diagram is divided up into three parts. These are briefly described below.

- Part 1: The controller utilised to control the DFPT in part 1 is a Linear Quadratic Regulator (LQR) controller with integral action. The objective for the controller is to follow the pressure reference which results in an optimal TSR. The reference pressure is calculated inside the controller utilising measurements of ω_r and Δp. The output of the DFPT hence the connection to part two is the motor torque T_M created by the DD motor which is the load torque for the generator.
- Part 2: To control the PMSG a Field Oriented Controller (FOC) is utilised. The objective for the field oriented controller is to maintain a constant generator velocity. To do so the current on the q-axis is controlled, since it is directly related to the torque of the generator. The output from the FOC is voltage references used for duty cycle generation in the SVPWM. The connection between the generator side of the inverter and the grid side of the inverter is the current i_0, which relates to the power delivered by the generator.
- Part 3: The controller utilised for the grid side control is a voltage oriented controller (VOC). The objective for the voltage oriented controller is to maintain a constant DC-link voltage i.e. inject the same amount of power to the grid as power delivered by the generator in the form of the current i_0. Furthermore, the VOC controls the reactive power Q i.e. the power factor.

Throughout the rest of this chapter the three controllers are investigated in detail and a more detailed block diagram of each controller is displayed.

7.1 Hydraulic Subsystem

In the following, the control design for the hydraulic subsystem will be described. In Section 6.4 the combined DLTI model of the DFPT was constructed and contains 23 states. Due to the number of states it is chosen to utilise a LQR controller instead of classic pole placement techniques e.g. Ackermann. The objective for the closed loop controller is to obtain an optimal TSR by tracking the pressure reference Δp^* by changing the actual pressure difference Δp, as seen in the control structure illustrated in Figure 7.2, which is similar to the control structure presented in Section 4.2.3.

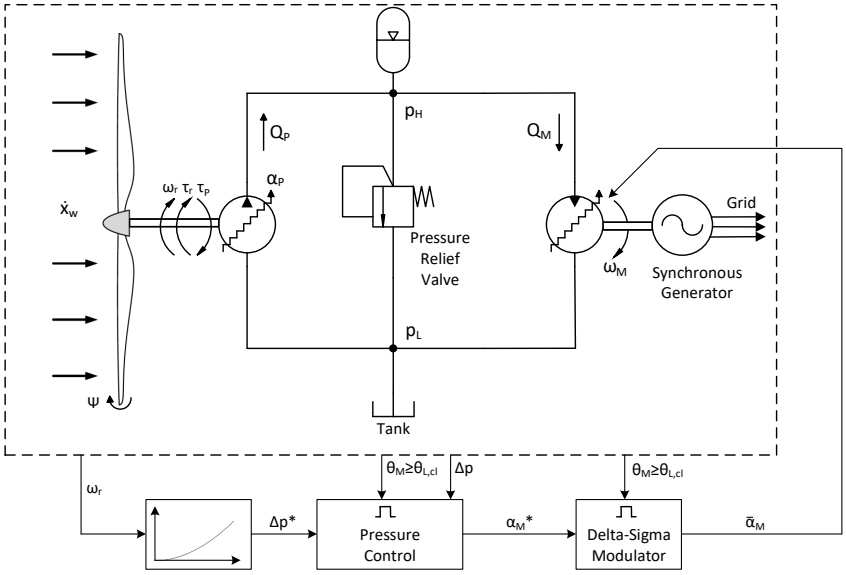

Figure 7.2: Proposed control structure for the DFPT.

To allow for pole placement using LQR, the system has to be controllable. To see if the system is controllable, there should exist an input sequence u(0), u(1),..., u(N) that will drive any initial system state x(0) to any final state x(N) [Phillips and Parr, 2011, p. 656-657]. In order for the system to be controllable the controllability matrix must have full rank, where full rank equals the number of states, hence $N = 23$.

The system matrix $\mathbf{A_c}$ and the input matrix $\mathbf{B_c}$ from the combined discrete state space model in Equation (6.25) is inserted in Equation (7.1) and the controllability is tested.

$$rank\left(\left[\mathbf{B_c}\ \mathbf{A_c}\mathbf{B_c}\ \cdots\ \mathbf{A_c}^{N-1}\mathbf{B_c}\right]\right) = 23 \tag{7.1}$$

From Equation (7.1) it is found that the system is controllable and full state feedback can be utilised for control design.

In order to compensate for model simplifications, disturbances and be able to obtain good pressure tracking, an integral state is added to the system, which is carried out in the following section.

7.1.1 Integral Action

As described in Chapter 4 the control objective is to maintain an optimal tip speed ratio. To be able to track the pressure, the $K_2\omega^2$ control law presented in Equation (4.9) is linearised in a small signal model around a steady state rotor speed $\omega_{r,0}$. The linearised $K_2\omega^2$ control law is given by Equation (7.2), where the linear $\delta-$operator is omitted for simplicity.

$$\Delta p^* = \left(\left. \frac{d\,T_r^*}{d\,\omega_r} \right|_{\omega_{r,0}} - B_v \right) \frac{\eta_P}{\overline{V}_P}\,\omega_r = \underbrace{(2K_2\omega_{r,0} - B_v)\,\frac{\eta_P}{\overline{V}_P}\,\frac{\omega_{r,max}}{\Delta p_{max}}}_{K_{2,0}}\,\overline{\omega}_r \tag{7.2}$$

Where the integral state has been normalised as $\omega_r{=}\omega_{r,max}\,\overline{\omega}_r$ and $\Delta p{=}\Delta p_{max}\,\Delta\overline{p}$ since the HPM plant is normalised in Equation (6.24). Furthermore, $\omega_{r,0}$ is found through the steady wind condition v_{mean} and optimal TSR as $\omega_{r,0} = {}^{\lambda^*\,v_{mean}}/_{R_r}$. The linearisation parameter is chosen to be 8 m/s since it is approximately in the middle of region II illustrated in Figure 4.1.

The integral state x_{int} is based on the error dynamic of the pressure given by Equation (7.3), which is approximated by utilising Forward Euler Method for numerical integration between two sampling instants [Phillips and Parr, 2011, p. 497].

$$\frac{d\,x_{int}(t)}{d\,t} = \Delta p^* - \Delta p \approx \frac{x_{int}(k+1) - x_{int}(k)}{T_s} \tag{7.3}$$

However, as the motor speed is varying, the sampling time T_s is asynchronous in time. Therefore, the error dynamics stated in Equation (7.3) must be transformed into the synchronous position domain, similar to that in Section 6.3.2.

The error dynamics can then be given as in Equation (7.4).

$$\frac{d\,x_{int}(\theta)}{d\,\theta} = \frac{1}{\omega_M(\theta)}\,(\Delta p^* - \Delta p) \tag{7.4}$$

Equation (7.4) becomes non-linear due to the varying motor speed, hence it is linearised in the same way as Equation (6.19). The error dynamics can then be represented in the position domain in Equation (7.5), where it is approximated utilising the Forward Euler Method for numerical integration between two sampling instants in the position domain.

$$\frac{d\,x_{int}(\theta)}{d\,\theta} = \frac{1}{\omega_{M,0}}\,(\Delta p^* - \Delta p) \approx \frac{x_{int}(k+1) - x_{int}(k)}{\theta_s} \tag{7.5}$$

The Forward Euler Method for numerical integration is considered to be sufficiently accurate due the relative large amount of cylinders in the DD motor, hence the sampling angle becomes adequately small.

Inserting the pressure from Equation (7.2) and solving for the integral state at the next sampling instant, Equation (7.6) is established.

$$x_{int}(k+1) = \frac{\theta_s}{\omega_{M,0}}\left(K_{2,0}\overline{\omega}_r(k) - \Delta\overline{p}(k) \right) + x_{int}(k) \tag{7.6}$$

Since the aim is to include the integrator state to the combined system, Equation (7.6) is set on state space form, given by Equation (7.7).

$$x_{int}(k+1) = \underbrace{\begin{bmatrix} K_{2,0}\frac{\theta_s}{\omega_{M,0}} & -\frac{\theta_s}{\omega_{M,0}} \end{bmatrix}}_{\mathbf{K_y}} \underbrace{\begin{bmatrix} \overline{\omega}_r(k) \\ \Delta\overline{p}(k) \end{bmatrix}}_{\mathbf{y}(k)} + x_{int}(k) \tag{7.7}$$

Combining Equation (7.7) with the existing state space representation of the system in Equation (6.25), the augmented state vector $\mathbf{x_a}$, consisting of 24 states, is constructed and is given in Equation (7.8).

$$\begin{aligned} \underbrace{\begin{bmatrix} \mathbf{x_c}(k+1) \\ x_{int}(k+1) \end{bmatrix}}_{\mathbf{x_a}(k+1)} &= \underbrace{\begin{bmatrix} \mathbf{A_c} & \mathbf{0} \\ \mathbf{K_y}\,\mathbf{C_c} & 1 \end{bmatrix}}_{\mathbf{A_a}} \underbrace{\begin{bmatrix} \mathbf{x_c}(k) \\ x_{int}(k) \end{bmatrix}}_{\mathbf{x_a}(k)} + \underbrace{\begin{bmatrix} \mathbf{B_c} \\ 0 \end{bmatrix}}_{\mathbf{B_a}} u_\Delta(k) \\ \mathbf{y_a}(k) &= \underbrace{[\mathbf{C_p} \quad \mathbf{0} \quad 0]}_{\mathbf{C_a}} \mathbf{x_a}(k) \end{aligned} \tag{7.8}$$

Since the integrator is represented in the combined state space model, it is now possible to proceed with the design of the controller.

7.1.2 LQR-Optimal Control

The Linear Quadratic Regulator is a pole placement method that places the poles in an optimal manner in order to minimise the cost function J given by Equation (7.9).

$$J = \sum_{k-1}^{\infty} \left(\mathbf{x_a}(k)^T \mathbf{Q} \mathbf{x_a}(k) + u_\Delta(k)^T R u_\Delta(k) \right) \tag{7.9}$$

The LQR is based on the principle of minimising the cost function J. The matrix $\mathbf{Q}$ is the weighting of the importance to drive the states $\mathbf{x_a}$ to zero and the scalar R is the weighting of the control input. The weightings of $\mathbf{Q}$ and R are relative to each other and must both be at least positive semi-definite.

Increasing $\mathbf{Q}$ relative to R will increase the importance to drive the states to zero relative to the control effort. The optimal control law is given by Equation (7.10).

$$u_\Delta = -\mathbf{K_a}\,\mathbf{x_a}(k) \tag{7.10}$$

Where the state gain matrix $\mathbf{K_a}$ is found utilising Equation (7.11).

$$\mathbf{K_a} = \left(\mathbf{B_a}^T \mathbf{P} \mathbf{B_a} + R \right)^{-1} \left(\mathbf{B_a}^T \mathbf{P} \mathbf{A_a} \right) \tag{7.11}$$

where $\mathbf{P}^T = \mathbf{P} \geq 0$ and is the unique solution to the algebraic Ricatti equation seen in Equation (7.12) [Ogata, 1995, p.589].

$$\mathbf{0} = \mathbf{Q} + \mathbf{A a}^T \mathbf{P A_a} - \mathbf{P} - \mathbf{A_a}^T \mathbf{P B_a} \left(\mathbf{R} + \mathbf{B_a}^T \mathbf{P B_a} \right)^{-1} \mathbf{B_a}^T \mathbf{P A_a} \tag{7.12}$$

The gains of the full state feedback matrix $\mathbf{K_a}$ is found utilising MATLAB.

The controller implementation of the DLTI model with full state feedback LQR controller and integral action are as seen in Figure 7.3, which is similar to the implementation of the controller in a MATLAB/Simulink environment.

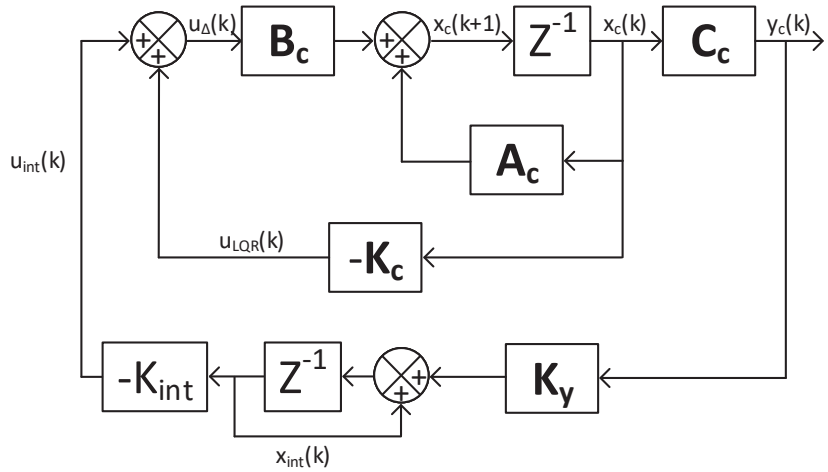

Figure 7.3: Block diagram of the full state feedback controller implementation in the DLTI model.

The gains $\mathbf{K_c}$ and K_{int} are found from $\mathbf{K_a}$ as seen in Equation (7.13).

$$\mathbf{K_a} = \begin{bmatrix} \mathbf{K_c} & K_{int} \end{bmatrix} \tag{7.13}$$

The objective for the controller is to track the optimal TSR, hence it is desired to weight the integral state high in order to drive the tracking error of the pressure towards zero. Therefore, it is desired to sweep for different values for $\mathbf{Q}$ relative to R=1.

Weighting Sweep

To investigate the influence of the weighting of the integral state in $\mathbf{Q}$ matrix, the value of $\mathbf{Q}$ is swept and R is kept constant as seen in Equation (7.14) where x indicates the parameter which has been swept for.

$$Q = \text{diag}\begin{bmatrix} 0 & 0 & 0 & \cdots & x \end{bmatrix} \qquad R = 1 \tag{7.14}$$

x is swept for the following values

$$x = \begin{bmatrix} 0.1 & 5 & 10 & 500 & 1000 \end{bmatrix} \tag{7.15}$$

The influence of the different weightings is evaluated by mapping the poles of the system in the discrete z-domain. A higher weighting of $\mathbf{Q}$, relative to R, will results in a more aggressive controller. Since the z-plane is related to the continuous s-plane through $z = e^{s\theta_s}$, it is expected that a higher weighted Q would drag the dominant pole towards origo, hence z $\rightarrow$ 0. The closed loop poles are found by considering the characteristic equation of the closed loop system $\mathbf{A_{cl}} = \mathbf{A_a} - \mathbf{B_a}\mathbf{K_a}$. Solving for the roots ϵ in the characteristic equation of the system $|\epsilon I - \mathbf{A_a} + \mathbf{B_a}\mathbf{K_a}| = 0$, the 24 poles (for each

weighting of **Q**) are given in Figure 7.4, where a zoom plot of the dominant poles are illustrated in Figure 7.5 and 7.6.

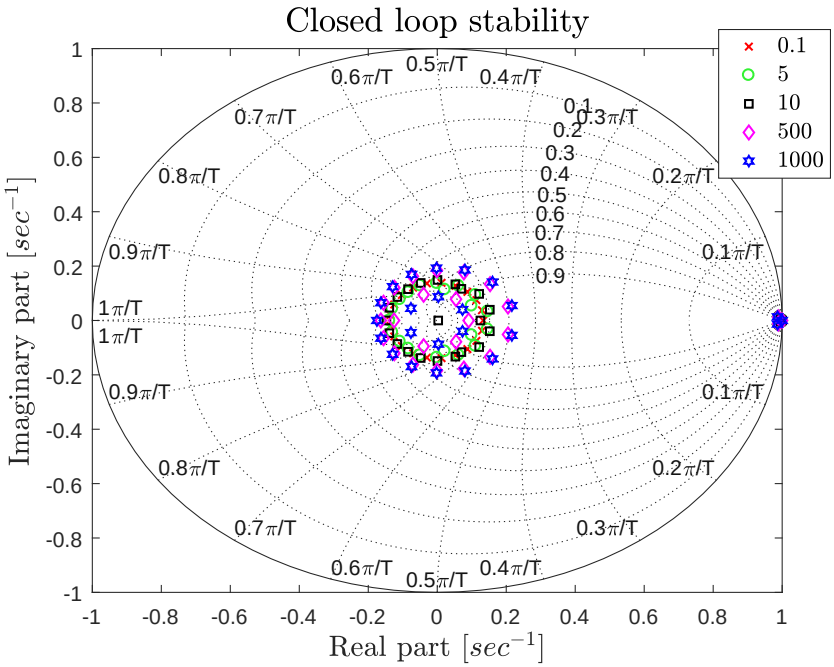

Figure 7.4: Pole map used to determine the weightings for **Q**.

As seen in Figure 7.4 the location of the poles near origo does not change in any significant manner. Furthermore, these are not the dominant poles of the system, hence the influence of the poles is not significant. However, it is not possible to conclude how the poles near [1,0] travels, hence a zoom plot of the poles are created which is displayed in Figure 7.5 and 7.6.

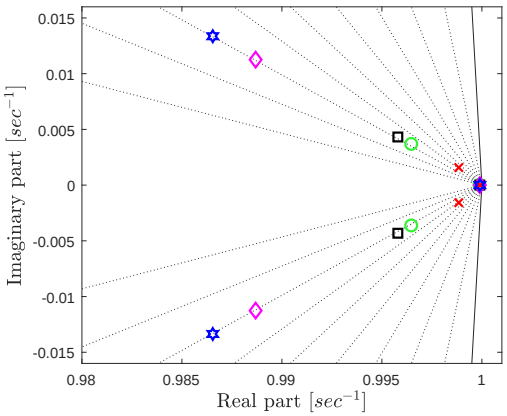

Figure 7.5: Zoom plot of dominating poles near [1,0].

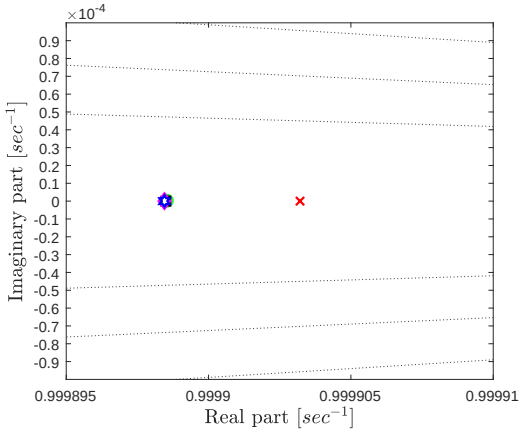

Figure 7.6: Zoom plot of dominating poles at [1,0].

From Figure 7.5 it can be seen that the higher weighting of **Q** relative to R, the poles travels towards origo, hereby obtaining a faster response of the system with the same

damping. However, the slowest and dominating pole of the system is shown in Figure 7.6, where the increase of the relative weighting > 1 is seen to be insignificant. Hence it can be concluded that the weighting does not influence the dominant pole location in any significant manner. Therefore, the weighting is chosen as seen in Equation (7.16).

$$\mathbf{Q} = \begin{bmatrix} 0 & 0 & 0 & \cdots & 0 \\ 0 & 0 & 0 & \cdots & 0 \\ 0 & 0 & 0 & \cdots & 0 \\ \vdots & \vdots & \vdots & \ddots & \vdots \\ 0 & 0 & 0 & \cdots & 10 \end{bmatrix} \qquad R = 1 \tag{7.16}$$

The weighting has been chosen this way since it was seen a higher value did not contribute to faster response. Taking the controller saturation into consideration, this weighting has been chosen.

With the weightings of the $\mathbf{Q}$ and R found, it is desired to test the stability of the controller in operations points different from the one the controller is designed for. Hence the following section will test the closed loop stability of the DFPT with controller.

7.1.3 Stability Analysis

The LQR controller is designed in a specific operation point. However, the wind turbine operates at different conditions most of the time, hence it is desired to test the controller under different operation conditions in order to investigate the stability of the system. The parameters to be tested for are the HPM pressure p_H, the motor speed ω_M and the rotor speed ω_r. The three parameters lead to 3^3 combinations, which complicates the analysis of the different conditions. Based on experience from Hauge et al. [2016] where the operation point of the rotor speed was found to be of negligible influence, it is only chosen to evaluate for p_H and ω_M. Hence the number of combinations are reduced to 2^3 where it is chosen to test in the worst case conditions. The operation range and linearisation point is defined as in Equation (7.17).

$$\begin{aligned} p_H &\in \{90, ..., 270\}\text{bar}, & p_{H,0} &= 180\text{bar} \\ \omega_M &\in \{1000, ..., 2000\}\text{RPM}, & \omega_{M,0} &= 1500\text{RPM} \end{aligned} \tag{7.17}$$

Where the pressure range is based on the expected operation in region II and the speed range is based on Figure 5.5.

To evaluate the stability of the system, the poles of the system have been mapped in a pole map for different operation, evaluated at worst case conditions, which is the lower and upper limits given in Equation (7.17).

The different combinations for the parameters p_H and ω_M are given by Table 7.1.

The closed loop poles are evaluated with the controller gain found in the linearisation point, where the closed loop representation is given by Equation (7.18). i, j denotes the operation point of the pressure and motor speed respectively.

$$\mathbf{A_{a,cl}}|_{p_i,\omega_{M,j}} = \left[\mathbf{A_a}|_{p_i,\omega_{M,j}} - \mathbf{B_a}\,\mathbf{K_a}|_{p_0,\omega_{M,0}}\right] \tag{7.18}$$

p_H	ω_M	Pole symbol
$p_{H,0}$	$\omega_{M,0}$	×
$p_{H,min}$	$\omega_{M,min}$	○
$p_{H,min}$	$\omega_{M,max}$	□
$p_{H,max}$	$\omega_{M,min}$	◇
$p_{H,max}$	$\omega_{M,max}$	★

Table 7.1: Worst case operation conditions used in the pole map with the respective pole symbol.

The pole map containing the poles for the system under the conditions defined in Table 7.1 is seen in Figure 7.7, where corresponding zoom plots of the dominating poles are displayed in Figure 7.8 and 7.9.

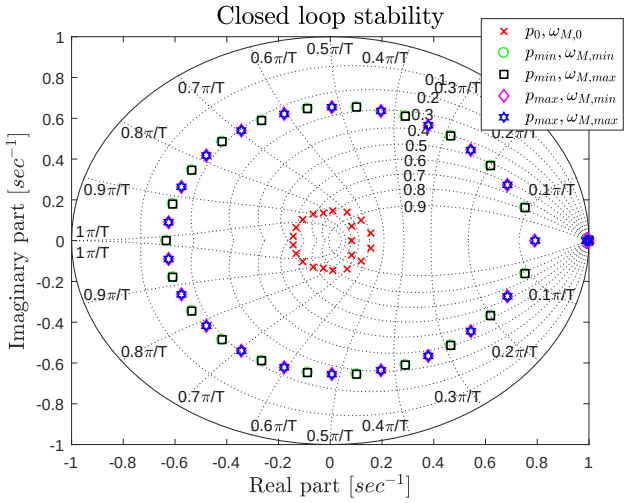

Figure 7.7: Pole map for worst case operation points.

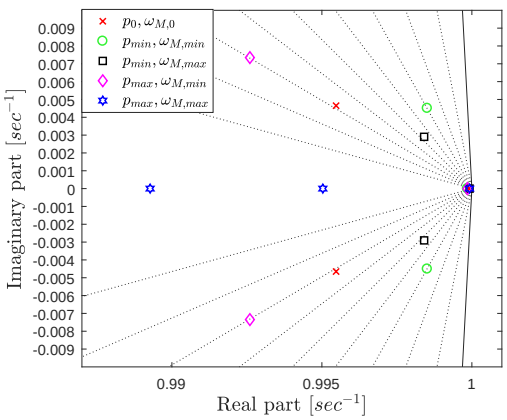

Figure 7.8: Zoom plot of dominating poles near [1,0].

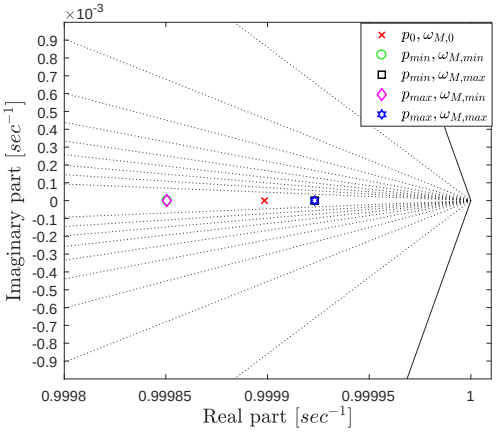

Figure 7.9: Zoom plot of dominating poles at [1,0].

From Figure 7.7 it can be seen that it is the pressure in the system, which is the dominating parameter when considering the pole locations. Taking a closer look on the dominating pole in Figure 7.8 and 7.9 the same tendency can be observed, where the pressure is the dominating parameter. However, considering the two cases with $p = p_{max}$, it can be seen that the system tends to get over damped as the speed of the DD motor increases. Hence it may be concluded that operating under the specified conditions, which causes the system to be over damped, should be avoided in order to maintain a fast response. However, it can be concluded that the system is stable under the tested conditions.

In order to test the closed loop control performance in the linear case, it is investigated whether the LQR controller with integral state is able to drive the Δp state to zero, when giving an initial condition $\neq 0$. The other states are set to zero. The test of the initial condition has been done, since the pressure reference is an integrated part of the control structure (recall Figure 7.3). The response of the closed loop controller is seen in Figure 7.10.

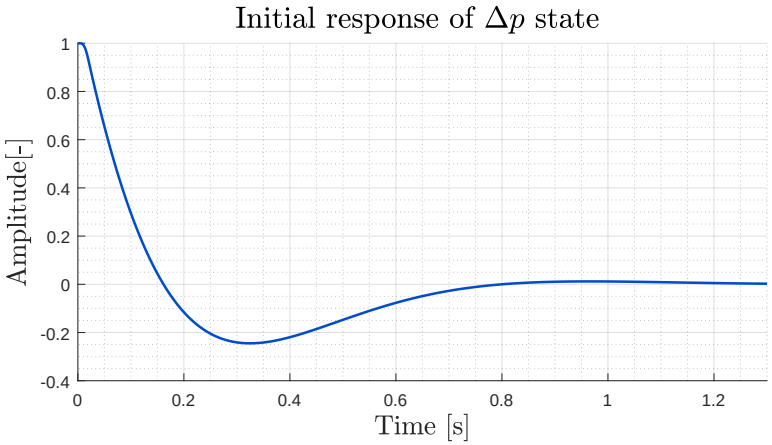

Figure 7.10: LQR controller with integral state response, when giving an initial condition of the state Δp.

The controller is able to drive the state to zero within reasonable time, which can be estimated based on the dominant poles locations from Figure 7.8 and 7.9.

7.2 Electrical Subsystem

This section will present the controllers used to control the generator and the grid side. Firstly, the Field Oriented Controller (FOC) utilised to control the angular velocity of the generator will be presented. For grid side control a Voltage Oriented Controller (VOC) is chosen to control the power factor and frequency for the voltage and current delivered to the grid. This will be explained in the end of this section.

7.2.1 Field Oriented Control

In Chapter 4 it was stated that the generator should control the velocity of the DD motor in order to obtain a constant velocity. To do so, Field Oriented Control has been chosen as controller. To explain the working and design principle of field oriented control the controller is divided up into four steps which also is illustrated in Figure 7.11 as dashed coloured boxes.

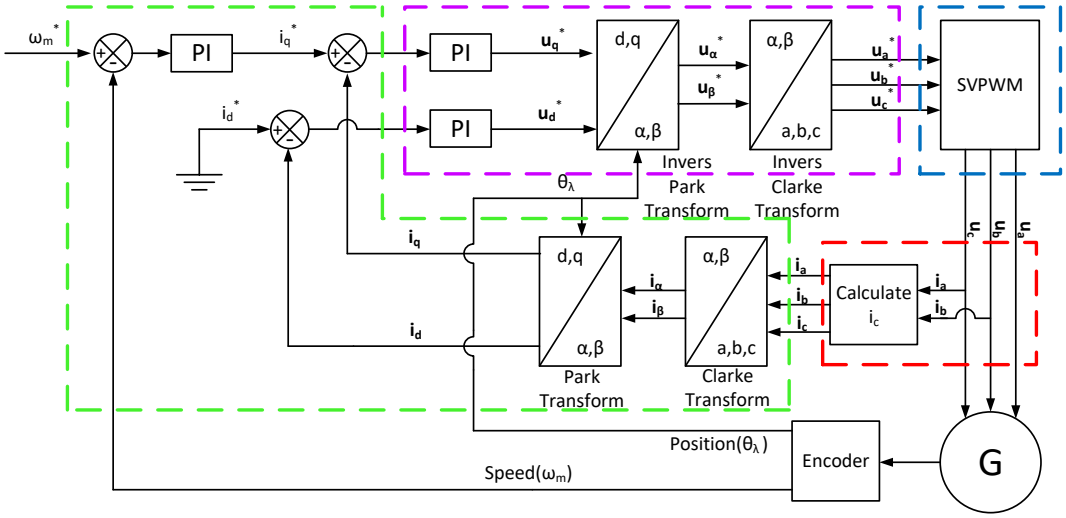

Figure 7.11: Block diagram of the Field Oriented Control utilised to control the speed of the generator.

The four steps are briefly stated below where the text is coloured to match the respective steps in Figure 7.11.

Step 1: Measure the currents.
Step 2: Generate error signals.
Step 3: Amplify the error signals.
Step 4: Modulate the correction voltages.

These steps are explained in detail throughout the rest of this section and in the end of this section the procedure of finding the control gains are explained.

Step 1

The first step is to measure the currents. It is only necessary to measure two of the three currents, since the generator can be considered as a large current node, hence Kirchhoffs first law, which state that the sum of currents into a node must be equal to the sum of currents leaving the node as given by Equation (7.19).

$$-1 \cdot (i_a + i_b) = i_c \tag{7.19}$$

Hence the last current can be calculated as in Equation (7.19). However, it should be noted that the industry often uses three currents sensors, to detect any faults in the

generator.
Adding the three current vectors together gives the stator current vector $\mathbf{i_s}$ (also called the net current vector) as seen in Figure 7.12. $\mathbf{i_s}$ is given by Equation (7.20).

$$\mathbf{i_a} + \mathbf{i_b} + \mathbf{i_c} = \mathbf{i_s} \tag{7.20}$$

The net current is the one which has to be regulated in order to control the speed of the generator.
With the net current vector $\mathbf{i_s}$ defined it is possible to go to step two.

Step 2

The net current vector must be controlled in order to control the speed. To do so the net current vector should be orthogonal to the rotor flux axis in order to produce a maximum of torque.
Step two will therefore go through the generation of the error signals, by comparing the net current vector with the desired current vector. The desired current vector is orthogonal to the stator flux axis, hence in order to know if the net current vector is at the right angle, the rotor flux angle(θ_λ) must be known. θ_λ is defined as the angle between the magnetic axis of phase A and the direct axis (d-axis) which is aligned with the north pole. If the angle is different from 90° an error signal can be generated as seen Figure 7.12.

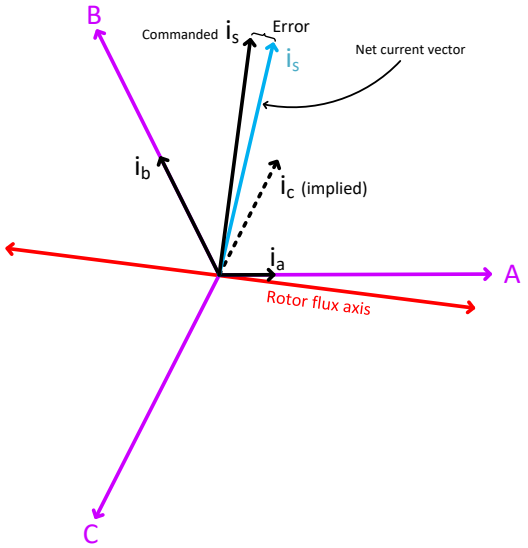

Figure 7.12: Illustration of the comparison of the net current vector and the commanded/desired current vector.

A controller must be designed in order to drive this error signal to zero. The desired

phase currents can be calculated using Equation (7.21).

$$\begin{aligned} i_a^* &= I_m sin\left(\theta_\lambda\right) \\ i_b^* &= I_m sin\left(\theta_\lambda - \frac{2\pi}{3}\right) \\ i_c^* &= I_m sin\left(\theta_\lambda + \frac{2\pi}{3}\right) \end{aligned} \tag{7.21}$$

Where I_m is the amplitude of the desired/commanded signal. Since the angle θ_λ is known, the commanded currents for the three phase currents is known. Thus a controller must drive the currents to the values of the currents found in Equation (7.21). To do so each current could be measured and compared to the commanded currents in Equation (7.21). A PI controller is then utilised to generate appropriate correction voltages in order to drive the error to zero. This type of FOC would require three PI controllers to control the currents.
However, the measured $\mathbf{i_s}$ is a 2-D vector and in order to create 2-D vector only two axes are required. This is illustrated in Figure 7.13 where the Clarke transformation has converted the three phase currents into two currents in an arbitrary stationary reference frame called $\alpha\beta$ utilising Equation (7.22).

$$\begin{bmatrix} i_\alpha \\ i_\beta \end{bmatrix} = \frac{2}{3} \cdot \begin{bmatrix} 1 & -\frac{1}{2} & -\frac{1}{2} \\ 0 & \frac{\sqrt{3}}{2} & -\frac{\sqrt{3}}{2} \end{bmatrix} \begin{bmatrix} i_a \\ i_b \\ i_c \end{bmatrix} \tag{7.22}$$

The general Clarke transformation is explained in Appendix F.

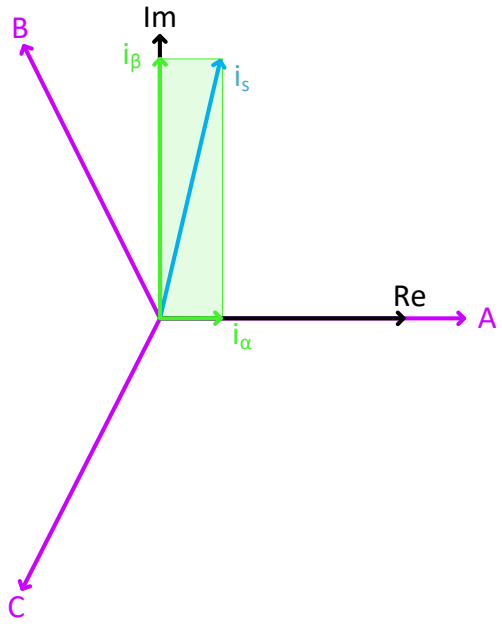

Figure 7.13: An illustration of the $\alpha\beta$ reference frame and the abc reference frame.

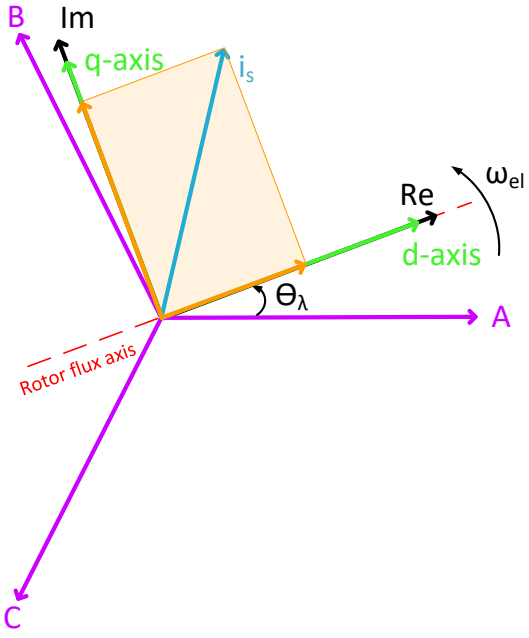

Figure 7.14: Illustration of the dq reference frame where the d axis is aligned with the rotor flux axis.

However, since it is a stationary reference frame, the tracking is difficult. The faster the generator rotates, a higher frequency of the current sine waves is obtained for the α and β reference components. Instead, a synchronous rotating reference frame, called dq, is utilised as seen in Figure 7.14 where d is the direct axis which is always aligned with the north pole, thus also aligned with the rotor flux. Utilising a synchronous reference frame makes the dq reference components to DC values instead of sine waves.
From Figure 7.14 it is clear to see that there are current components of $\mathbf{i_s}$ on the *d-axis* an *q-axis*, however, in order to produce torque the current must be orthogonal to the rotor flux axis i.e. the *d-axis*, hence the current on the *d-axis* does not produce any torque. In order to produce the maximum amount of torque $\mathbf{i_s}$ must be aligned with the *q-axis* which is perpendicular to the *d-axis* i.e. the rotor flux axis.
In order to go from the $\alpha\beta$ reference frame to the dq reference frame a method called Park transformation is utilised as in Equation (7.23). The general Park transformation is found in Appendix F.

$$\begin{aligned} i_d &= i_\alpha cos\left(\theta_\lambda\right) + i_\beta sin\left(\theta_\lambda\right) \\ i_q &= -i_\alpha sin\left(\theta_\lambda\right) + i_\beta cos\left(\theta_\lambda\right) \end{aligned} \tag{7.23}$$

Where the i_d and i_q are the d and q current component of the measured current $\mathbf{i_s}$.

The current on the *d-axis* does not produce torque as mentioned but only flux and under normal conditions the permanent magnets produces all the flux needed. Hence the reference for $i_d = 0$. The current reference to i_q is directly related to the torque.

Step 3 and 4

Step number three is to generate the correction voltages which must be applied. However, from the reference current i_d and i_q it is only possible to generate two voltage correction signals and there must be one for each motor winding, thus the process must be reversed. Therefore, the inverse Park transform is applied to go from dq reference frame to the $\alpha\beta$ and the inverse Clarke transformation is utilised to go from $\alpha\beta$ to the *abc* reference frame, hence three voltages are found and can be the input to the SVPWM algorithm which is step 4. Hereby, the four steps that define the FOC and illustrated in Figure 7.11, have been presented. With the control it is possible to find the controller gains which is carried out in the following.

Controller Gains

From Figure 7.11 the inner current loops and the outer speed loop are seen. The objective for this section is to calculate the controller gains for the two current controllers and the speed loop controller. Since the control structure is a cascade loop, the design will start with the inner current loops for the d- and q-axis. The bandwidth of the inner loop is required to be 10 times faster than the outer loop in order to design the inner and outer loop controllers separately. When the gain of the current controllers are found, the speed controller is designed.

Since the d-axis and q-axis are equal, the controller gains will be equal and found utilising the same method, which is why only the i_q is considered. The plant of the q-axis from Equation (3.50), when considering the speed of the motor as disturbance, is a first order system. The block diagram of the plant with a PI controller is illustrated in Figure 7.15.

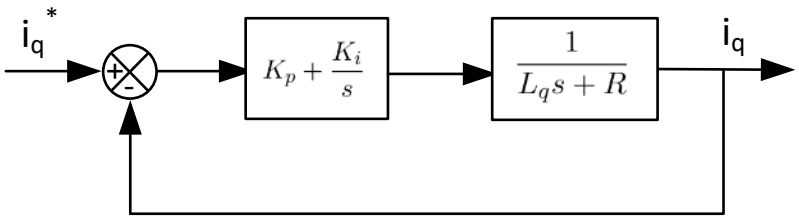

Figure 7.15: Block diagram of inner current loop for the i_q-current.

The open loop transfer function is found in Equation (7.24).

$$\begin{aligned} G_{ol} &= K_p \left(\frac{s + z_0}{s} \right) \frac{1}{s + {}^{R}/_{L_q}} \\ &= K_p \frac{s + z_0}{s(s + {}^{R}/_{L_q})} \end{aligned} \tag{7.24}$$

Where the PI controller adds a zero $z_0 = \frac{K_i}{K_p}$ and a pole at the origin.

It is decided to utilise root locus analysis to determine the open loop gain, i.e. the proportional gain K_p. Since the two open loop poles of Equation (7.24) is on the real axis, the zero can be placed such that zero-pole cancellation can be achieved. Placing the zero between $s = 0$ and $s = -\frac{R}{L_q}$=2.4 rad/s, the pole at origin will terminate at the zero of the open loop G_{ol} [Phillips and Parr, 2011, 252]. Assuming ideal PMSG parameters, such that any inaccuracies in the machine components is insignificant, the zero-pole cancellation method is considered valid.

The controller gains should be found, such that a maximum overshoot in the i_q-current of 2 % is obtained. However, utilising the zero-pole cancellation, the system has the response of a first order system, hence avoiding any overshoot.

The root locus is illustrated in Figure 7.16 showing the open loop poles and the placed zero.

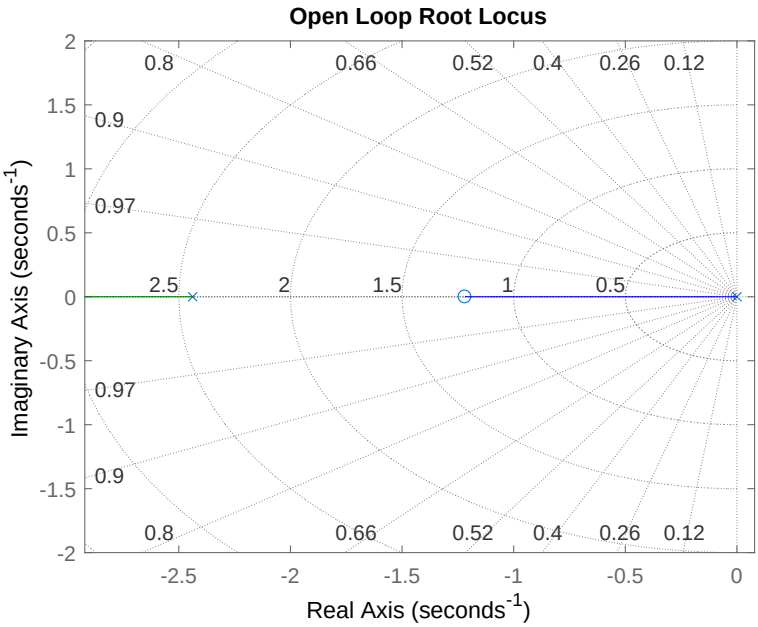

Figure 7.16: Root locus of the open loop current.

Placing the zero at $s = \frac{R}{L_q}/2 = 1.2$ rad/s, which is in the middle between the two poles, the proportional gain K_p is varied until the desired response is obtained. The current controller is designed to obtain a settling time of 1.5 ms. Due to the the first order system, the damping will be $\zeta = 1$ and the frequency of the closed loop pole ω_n can be estimated by Equation (7.25).

$$t_s = \frac{4}{\zeta \omega_n} \quad \Rightarrow \quad \omega_n = \frac{4}{1.5ms} = 2660\, ^{rad}/_{s} \tag{7.25}$$

Increasing the gain K_p, the second pole, which originates at $s = 2.4$ rad/s, moves towards the zero at negative infinity. When the frequency of the pole reaches 2660 $^{rad}/_{s}$, the gain K_p is obtained.

K_p is found to be 55, where the integral gain K_i then is determined as $K_i{=}z_0\, K_p{=}67$. The closed loop response of the current is tested with a step input given in Figure 7.17, where the settling time is seen to be 1.3 ms.

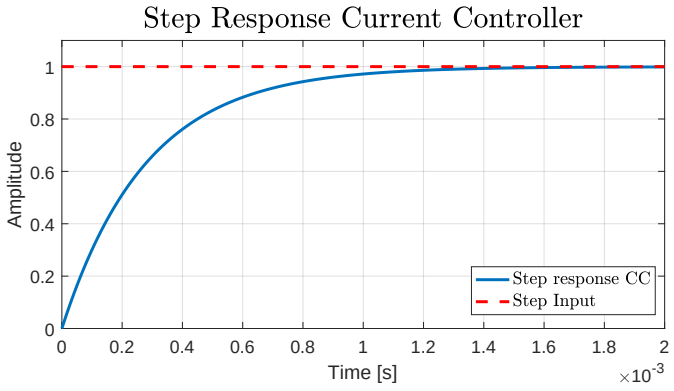

Figure 7.17: Step response of the i_q-current controller.

The controller gains for the q-axis and d-axis have been found. To be able to comply with the frequency relations between the inner and outer loop, the bandwidth of the current controller is investigated.

The bandwidth of the current controller are calculated where the gain of the closed loop system equals -3dB and is given as 3568 rad/s. The speed loop must be designed to be approximately 10 times slower than this in order to be able to neglect the dynamics of the inner loop. However, the bandwidth of the current loop is relatively high compared to the speed loop, hence no complication between the two loops is considered.

The design of the speed loop is based on the block diagram given in Figure 7.18.

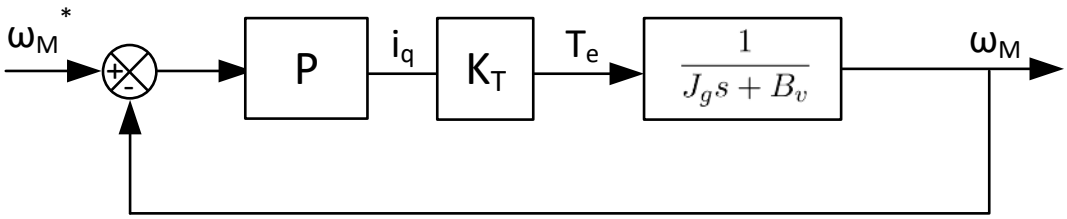

Figure 7.18: Block diagram of the outer speed loop, where the current loop is neglected due to the cascade loop.

Where K_T is based on Equation (3.51) and states the relation between the i_q current and the T_e and is given in Equation (7.26).

$$K_T = \frac{T_e}{i_q} = \frac{3}{2} N_{pp} \lambda_{mpm} \tag{7.26}$$

The plant is found by considering the shaft dynamics, where the motor torque is regarded as disturbance and is omitted in the control design. The plant is given by Equation (7.27).

$$\begin{aligned} \dot{\omega}_M &= \frac{1}{J_g} \left(T_e - B_v \omega_M \right) \\ G_p &= \frac{\omega_M}{T_e} = \frac{1}{J_g s + B_v} \end{aligned} \tag{7.27}$$

It is chosen to utilise a proportional controller to investigate whether this results in acceptable performance of the shaft speed. Hereby the open loop transfer function contains one pole at $s = -\frac{B_v}{J_g}$. Plotting the root locus, the pole will move towards the zero at negative infinity, hence the proportional can be infinitely gained, if not considering controller saturation. The time constant of the plant is found to be $\tau = {}^{J_g}/_{B_v} \approx$70 rad/s, hence a settling time of 0.6 s is considered reasonable. Correspondingly this gives a desired pole frequency of 6.7 rad/s, hence the gain K_p is found to be 40.

In Figure 7.19 a step response of the closed loop system is illustrated.

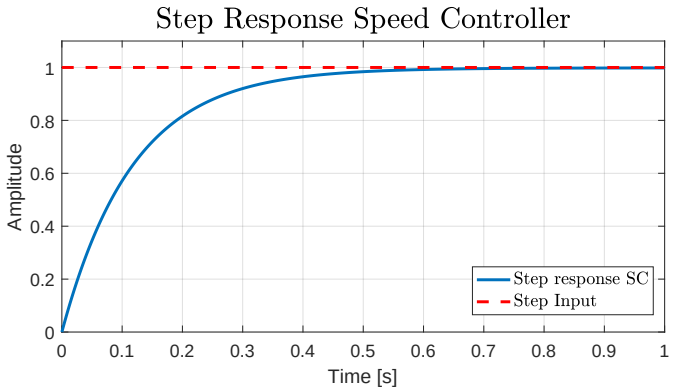

Figure 7.19: Step response for speed controller.

7.2.2 Voltage Oriented Control

To meet the requirement specification of the grid side it is chosen to control the grid side of the back-to-back converter utilising Voltage Oriented Control (VOC) as proposed in Teodorescu et al. [2011]. VOC often utilise the dq reference frame where the d current component controls the active power P and the q component is related to the reactive power Q. The block diagram for the VOC is illustrated in Figure 7.20.

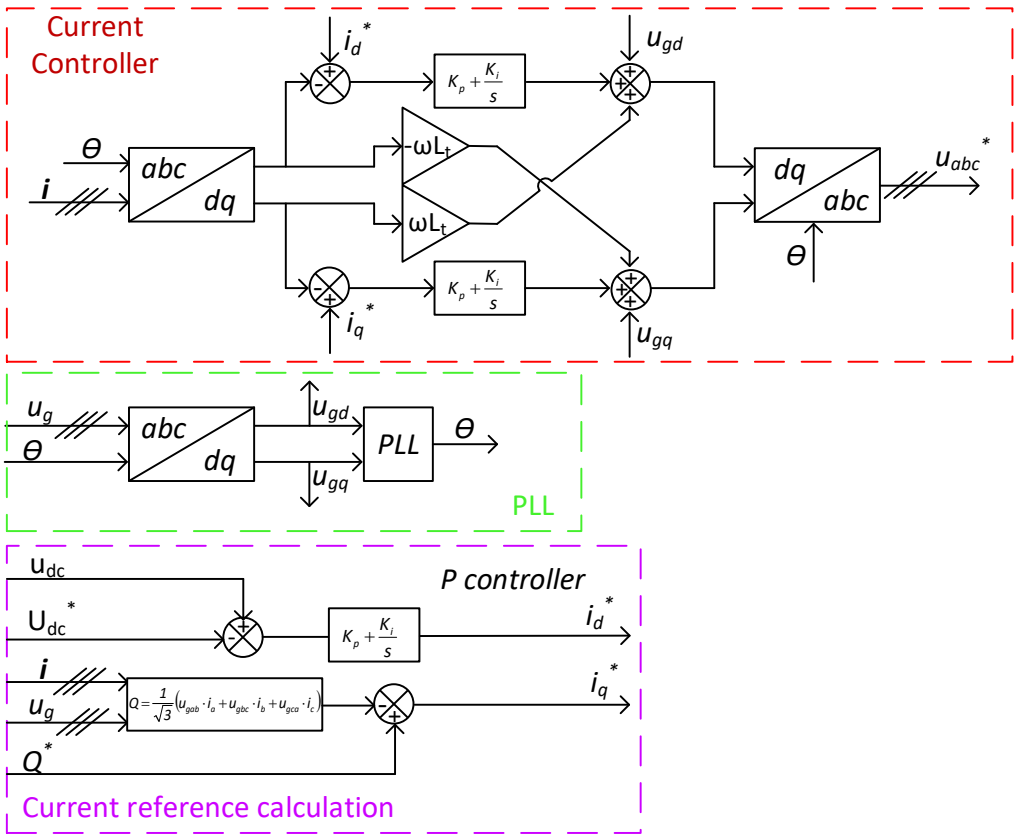

Figure 7.20: Control scheme for Voltage Oriented Control utilised to control the active and reactive power for the grid side of the power converter.

The closed loop VOC is split up into three parts, a Phase Locked Loop (PLL) used for grid synchronisation framed by the green dashed box, a outer loop utilised to calculate the current references framed by the purple dashed box and an inner loop with the current controller which is framed by a red dashed box. These three parts will be further discussed and analysed in the following section.

Phase Locked Loop

This section is based on Teodorescu et al. [2011, sec. 4.2.2] unless otherwise is stated.
The PLL is utilised to obtain the synchronisation of the grid in order to calculate the angle used to calculate the *dq* components. The PLL structure utilised in the VOC is illustrated in Figure 7.21.

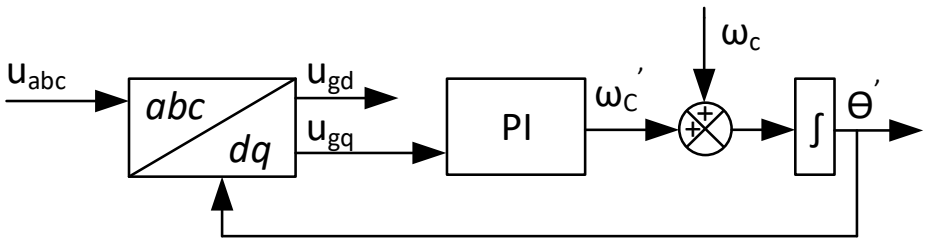

Figure 7.21: Block diagram of the PLL utilised in this project.

Where $\mathbf{u_{abc}}$ is the voltage measured from the grid, ω_c' is the error which should be driven to zero, ω_c is the frequency of the grid, hence in Denmark 50Hz. θ' is the angle calculated by the PLL.
The design of the PLL is based on the transfer function of the PLL which is given by Equation (7.28).

$$H_\theta(s) = \frac{\theta'(s)}{\theta(s)} = \frac{K_p s + \frac{K_p}{T_i}}{s^2 + K_p s + \frac{K_p}{T_i}} \tag{7.28}$$

The transfer function for the PLL can be generelised as in Equation (7.29).

$$H_\theta(s) = \frac{2\zeta\omega_n s + \omega_n^2}{s^2 + 2\zeta\omega_n s + \omega_n^2} \tag{7.29}$$

From Equation (7.29) the expression for the natural frequency ω_n and the damping ζ as in Equation (7.30).

$$\omega_n = \sqrt{\frac{K_p}{T_i}} \qquad \zeta = \frac{\sqrt{K_p T_i}}{2} \tag{7.30}$$

In order to obtain the desired performance i.e. the desired natural frequency and damping, the values of K_p and T_i must be found. To do so an expression for the settling time t_s stated in Equation (7.31).

$$t_s = 4.6 \cdot \tau \qquad \tau = \frac{1}{\zeta\omega_n} \tag{7.31}$$

It should be noted that the above expression for the settling time is for a standard generalised under damped second order transfer function [Phillips and Parr, 2011].
K_p and T_i is isolated, thus an expression for K_p and T_i is obtained in Equation (7.32).

$$\begin{aligned} K_p &= 2\zeta\omega_n = \frac{9.2}{t_s} \\ T_i &= \frac{2\zeta}{\omega_n} = \frac{t_s\zeta^2}{2.3} \end{aligned} \tag{7.32}$$

ζ is determined to be $\frac{1}{\sqrt{2}}$ which is a good compromise between the rise time and settling time, hence the overshoot in a step response is limited to 4.3% [Phillips and Parr, 2011, p.138]. The settling time t_s is chosen to be $10ms$ which is half of the grid fundamental period at 50Hz.
Utilising these values the PLL step response is tested in MATLAB. The result is displayed in Figure 7.22.

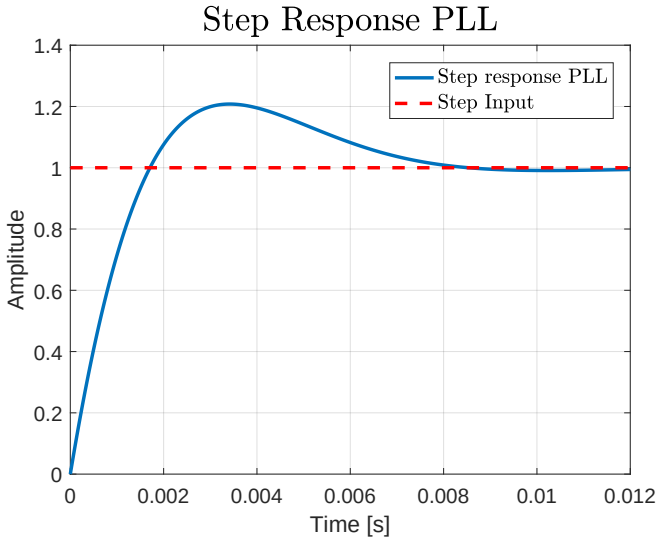

Figure 7.22: Step response of the PLL.

As seen in Figure 7.22 the settling time is approximately $10ms$. However it is seen that the overshoot is approximately 20% instead to the desired 5%. This is caused by the zero in the transfer function, which was neglected in the design procedure where it was assumed that the system was a standard second order system. Depicted the higher overshoot the PLL designed is considered acceptable, since the frequency of the grid is constant, thus the overshoot is only seen during start up. The zero could be removed by adding a lead term to the PI controller. By designing the lead term in a proper manner a zero pole cancellation can be obtained. However, this would require the parameters and model to be precise. A zero pole cancellation is not considered in this project since the grid is assumed ideal, thus the frequency is constant during the whole simulation.
A simulation of the PLL is illustrated in Figure 7.23

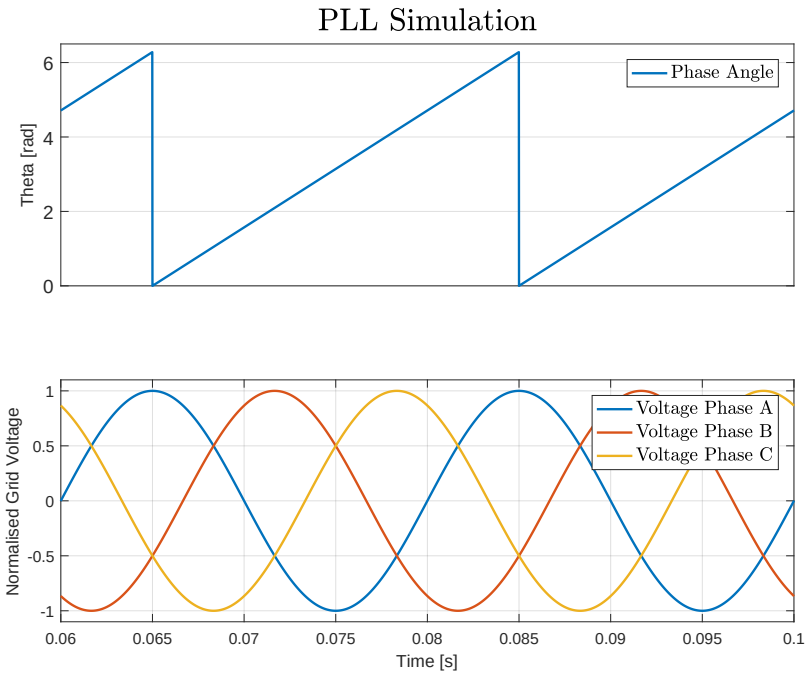

Figure 7.23: Simulation of the PLL.

From Figure 7.23 it is clear to see that the phase angle output of the PLL is in phase with the phase angle of phase A.

Current Reference

This section will describe how the current reference is calculated in order to control the active and reactive power. Firstly the active power controller is described followed by the reactive power controller.

DC-link Control Objective

The active power is controlled by the DC-link controller. There are two ways to control the active power, first by controlling the DC voltage across the DC-link or by controlling the AC components across the DC-link. In this project it is chosen to control the DC voltage across the DC-link. Hence the objective for the DC-link controller is to maintain a constant DC-link voltage equal to the one found in Section 5.5. Therefore, this value is the reference for the DC-link controller denoted as U_{dc}^{*} as seen in Figure 7.24.

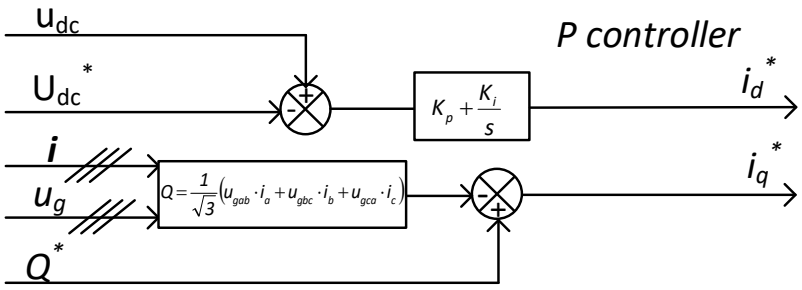

Figure 7.24: Illustration of the current reference generation.

As seen the reference is the one which is subtracted form the measured DC-link voltage where it is normally the other way around. This is because the DC-link voltage changes due to the power input from the generator. Therefore, if the DC-link voltage u_{dc} increases, it is due to an extra power produced by the generator, hence extra power must be injected to the grid by increasing i_d^*. If the power production decreases the DC-link voltage decreases, hence i_d^* must be decreased in order to inject less active power to the grid. I.e. the voltage variation must be compensated by an increased or decreased power injection to the grid.

DC-link Controller Design

As stated the purpose with the DC-link voltage is to control the DC-link voltage u_{dc} regulating i_d. The transfer function for $\hat{v}_{dc}/\hat{i}_{dc}$ was found in Section 6.5. The transfer function is stated for convenience in Equation (7.33).

$$\frac{\hat{u}_{dc}}{\hat{i}_{dc}} = \frac{\sqrt{3}}{2}\frac{R_0}{1+R_0Cs} \tag{7.33}$$

Assuming $R_D \gg 3\ T_s$, where R_D is the damping resistance in the capacitor, the pole becomes insignificant and is thus neglected. Hence the DC-voltage loop can thus be seen as an integrator, given by the block diagram illustrated in Figure 7.25.

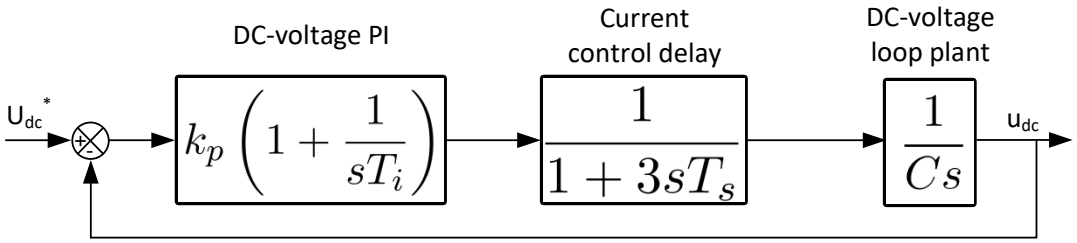

Figure 7.25: Block diagram of the DC-link control.

In Figure 7.25 the block diagram of the small signal model of the DC-voltage control loop is seen. Where T_s is the sampling period, T_i is the time constant of the PI controller.

The PI controller should be designed to a decade slower than the inner loop in order to have the two systems decoupled. The block diagram of the system including PI controller and the current loop delay is seen in Figure 7.25. The open loop system transfer function can be derived from the block diagram and the result is obtained in Equation (7.34).

$$H_{ov}(s) = \frac{\sqrt{3}k_p\left(1+T_i s\right)}{2T_i s\left(1+3T_s s\right)\left(Cs\right)} \tag{7.34}$$

As seen the k_p and T_i is included in the transfer function. The main idea is to select k_p and T_i in a such manner that a the crossover frequency (ω_c) at the geometric mean of the phase plot is obtained. This would ensure a maximum phase margin (ϕ), which leads to the optimal damping of the DC voltage loop. The phase margin and crossover frequency is related as seen in Equation (7.35).

$$\begin{aligned} a &= \frac{1+cos\left(\phi\right)}{sin\left(\phi\right)} \\ \omega_c &= \frac{1}{3aT_s} \\ T_i &= a^2 3T_s \end{aligned} \tag{7.35}$$

At the crossover frequency ω_c is given by Equation (7.36)

$$k_p = \frac{C}{2\sqrt{3}aT_s} \tag{7.36}$$

By determine the phase margin or a the controller gains for the PI controller can be found. The phase margin is chosen to be 45°, hence a is equal to 2.4 which results in the following gains.

$$\begin{aligned} k_p &= 0.12 \cdot \frac{C}{T_s} = 0.045 \\ T_i &= 17 \cdot T_s = 0.0035 \end{aligned}$$

Hence the gains of PI controller used to control the DC-link voltage have been found.

The open loop bode plot is given in Figure 7.26, where the gain margin is seen to be 41 ° at the cross-over frequency, which is considered as a sufficiently close to the desired phase margin. The step response is shown in Figure 7.27

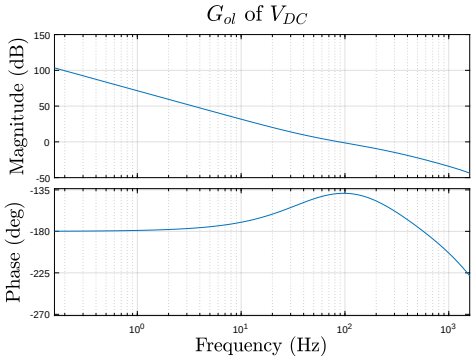

Figure 7.26: Bode plot of open loop transfer function for V_{dc}.

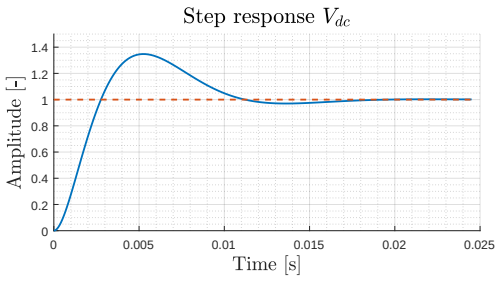

Figure 7.27: Step response of the closed loop transfer function for V_{dc}.

The following will explain how the reactive power Q is controlled.

Reactive Power Control

The i_q current component controls the reactive power. Normally the reactive power references is given by the transmission system operator (TSO), hence is normally not determined by the converter operator. Sometimes reactive power must be injected to the grid and sometimes some reactive power must be drawn from the grid, this depends on how stable the grid are. In this project a unity power factor is desired.
The reactive power depends on the power factor, hence if the power factor is equal to 1 the reactive power is zero. The active and reactive power in the system can be calculated as in Equation (7.37).

$$\begin{aligned} P &= \frac{3}{2} \cdot u_{dg} \cdot i_{dg} \\ Q &= -\frac{3}{2} \cdot u_{dg} \cdot i_{qg} \end{aligned} \tag{7.37}$$

The reference for the reactive power is calculated as in equation.

$$Q^* = S \cdot (1 - PF) \tag{7.38}$$

Where PF is the power factor and S is the apparent power. With a unity power factor the apparent power is equal to the active power.

Current Control

With the reference currents found and with the phase angle and the dq components from the voltage found using the PLL it is possible to generate the voltage reference signals. In this model the inverter model has been neglected, hence the reference is directly fed into the system. This is done due to instability when third harmonics was injected in the voltage input. This will not affect the result in any significant manner. The block diagram for the controller is illustrated in Figure 7.28.

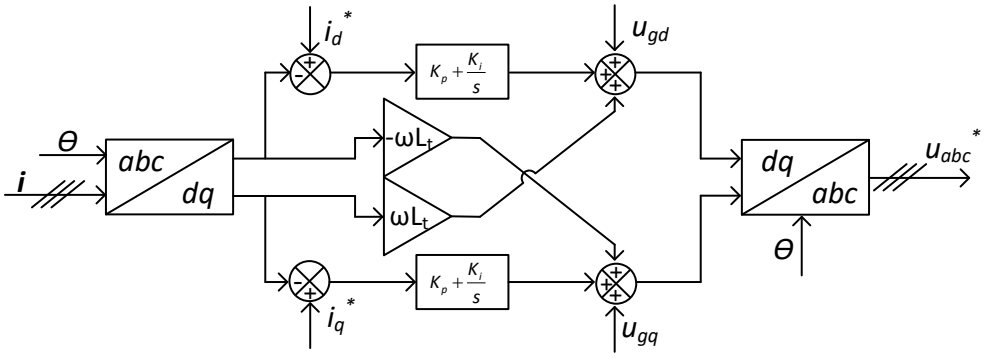

Figure 7.28: Block diagram illustration of the current controller.

As seen the current in the system is measured and the park transformation is utilised to convert the three phase current signal into dq components. The measured current is compared to the current references. This error is fed into the PI controllers, the output

of the PI controller is added together with a decoupling term and the dq components of the grid voltage which results in the desired voltage references u_d^* and u_q^*, which is transformed frame the dq rotating reference frame into the standard abc reference frame. The PI controllers are similar to each other and designed based on the transfer function of the L filter designed in Chapter 5. The transfer function for the filter is given by Equation (7.39).

$$G_{Lt} = \frac{R_t}{L_t s + R_t} \Rightarrow \frac{1}{\frac{L_t}{R_t} s + 1} \tag{7.39}$$

Where R_t is the total resistance in the windings and L_t is the total inductance in the filter.
With the transfer function for the filter defined in Equation (7.39), it is possible determine the different gains for the PI controller. The transfer function for the PI controller is given by Equation (7.40)

$$G_{PI} = \frac{K_p s + K_i}{s} = K_p \frac{T_i s + 1}{T_i s} \tag{7.40}$$

Utilising the transfer function to the right in Equation (7.39), it is possible to utilised the method, described in Blaabjerg et al. [2002], to determine K_p and T_i.
The PI time constant T_i should be chosen to be equal to the time constant of the system, G_{Lt} as in Equation (7.41), in order to achieve an overshoot of 5%.

$$T_i = \frac{L_t}{R_t} \tag{7.41}$$

The constant K_p should found utilising Equation (7.42).

$$K_p = \frac{L_t}{3T_s} \tag{7.42}$$

where T_s is the sampling time.

7.2.3 Tuning of Controller Gains

The controllers have been implemented in their respective model in a MATLAB/Simulink environment and tested. During the test some of the controllers have been further tuned. The controllers which have been tuned are stated below and corrected gains are stated in Table 7.2.

PLL

It was found that the PLL tends to be unstable at high voltage levels. Thus the gains of the PI controller was decreased as in proposed in Lorenzen and Nielsen [2015]. The PLL control gains used in the final model are given in Table 7.2 dentoed with *"PLL."*.

DC-link Controller

The DC-link voltage controller was found to be unstable, which is due to a small value of k_p. The small k_p can be explained by a small DC-link capacitance, which directly affects

the controller gain. By increasing k_p with 0.05 the system was stable and able to track the reference. The newly found k_p would correspond to a DC-link capacitor of $0.159\,mF$ compared to the one found in Chapter 5 which was $0.761\,\mu F$. It is chosen to utilise the capacitance found in Chapter 5. The controller gains for the DC-link voltage controller is found in Table 7.2 denoted *"DC."*.

Current Controller

Some small corrections were made on the gains for this controller. These are denoted *"cc."* in Table 7.2.

Parameter	Original	Correction	Final Value
$PLL.k_p$	920	-500	420
$PLL.k_i$	$4.232 \cdot 10^5$	-1000	$4.222 \cdot 10^5$
$DC.k_p$	0.0455	0.05	0.0955
$DC.k_i$	13	-	13
$cc.k_p$	2.24	2	4.24
$cc.k_i$	833.3	-	833.3

Table 7.2: The tuned gains for the VOC used to control the grid side inverter.

7.3 Summary

Through this section the different controllers utilised in this project have been presented, the controllers have been tested in a MATLAB/Simulink environment and were fine tuned when needed. With the tuned controller gains in place it is possible to test the system performance. Hence the following chapter will described the evaluation procedure used to evaluate the system and in the end the results of the performance evaluation are presented.

CHAPTER 8

Performance Evaluation

Chapter Contents

This chapter is divided up into five different parts. First the comprehensive simulation time is considered. Due to simulation time the systems will be divided up into two systems, the advantages and disadvantages of dividing the model into two models will de discussed. This is followed by part two to part five which briefly explains the conditions for the simulation followed by an evaluation of the DFPT and an mechanical evaluation. In the end the electrical subsystem simulation condition and evaluation of the performance commenced. However, to give a more detailed overview of the chapter the following section will describe the different parts.

Chapter Overview

This chapter is divided into five main parts. These five parts are illustrated in Figure 8.1 where each part is indicated by a colour.

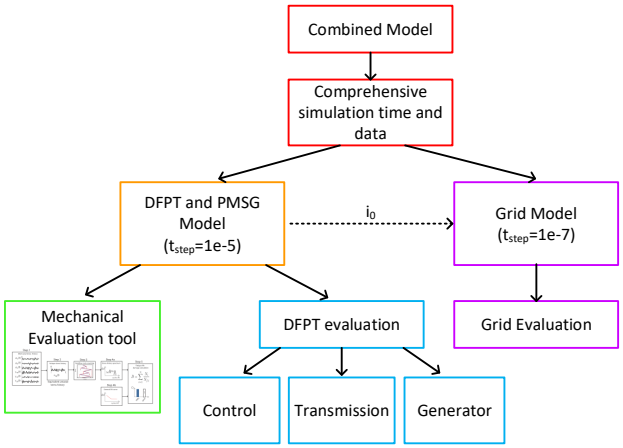

Figure 8.1: Flow diagram used to create an overview of the chapter.

The order of this chapter section and the purpose of each section is briefly described below.

- **The first part** will describe why the model is divided into a grid model and a DFPT-PMSG model as seen Figure 8.1 instead of one combined model and simulation.
- **The second part** describes the simulation conditions used to simulate the DFPT-PMSG model, which is the base for the mechanical, DFPT and PMSG evaluation as illustrated in Figure 8.1. From Figure 8.1 it can be seen that the connection between the models is the i_0 current.
- **The third part** will evaluate the performance of the DFPT. The performance evaluation is categorised into three evaluations. The first evaluation will consider the control performance, followed by an evaluation of the data from the hydraulic transmission. Lastly an evaluation of the PMSG performance is considered. Throughout the second part the performance of the DFPT will be compared with the NREL wind turbine.
- **The fourth part** of this chapter will commence the evaluation of the influence of the DFPT on the mechanical loading of the wind turbine. To be able to concluded how the DFPT influence the mechanical structure it is benchmarked with the NREL wind turbine.
- **The fifth part** briefly describes the simulation condition before commencing the evaluation of the grid control performance. To evaluate the grid side controller, the power injected to the grid, the ability to maintain the constant DC-link voltage and how well the current controller tracks its reference are examined. Lastly the power factor will be considered.

8.1 Evaluation Methods

This section seeks to present the models used to evaluate the performance of the system. The evaluation takes basis in a 700 seconds wind profile with a mean wind speed of $8^m/_s$. A 700 seconds simulation time is a common simulation time for wind turbines and is the simulation time used by Fatigue, Aerodynamic, Structure, and Turbulence (FAST) [Jonkman et al., 2009]. The system evaluation is divided into two evaluations, since the electrical grid requires a time step of $t_{step} = 1 \cdot 10^{-7}$ s and the DFPT only requires a time step of $t_{step} = 1 \cdot 10^{-5}$ s which would result in a comprehensive computational time. The system will be divided up into two simulations as in Figure 8.2 in order to deal with the comprehensive computational time.
As seen in Figure 8.2 the blue dashed box indicates the components which will be included in the DFPT evaluation and mechanical evaluation. The red dashed box includes the different components which are included in the electrical evaluation. The link between the two simulation is the current i_0 using Equation (3.60), to be able to simulate the system framed by the blue box, the DC-link is assumed constant. By assuming the DC-link voltage constant, the FOC has ideal conditions for speed control, however it is considered reasonable, since the DC-link voltage is controlled. By dividing the system up into two simulations it is possible to simulate the system, however due to the long simulation time and small time step, a computer with 256GB RAM was utilised in order to be able to store the amount of data. The simulation of the DFPT and PMSG model took 1.5 days, where the electrical grid took 13 hours. The main difference in

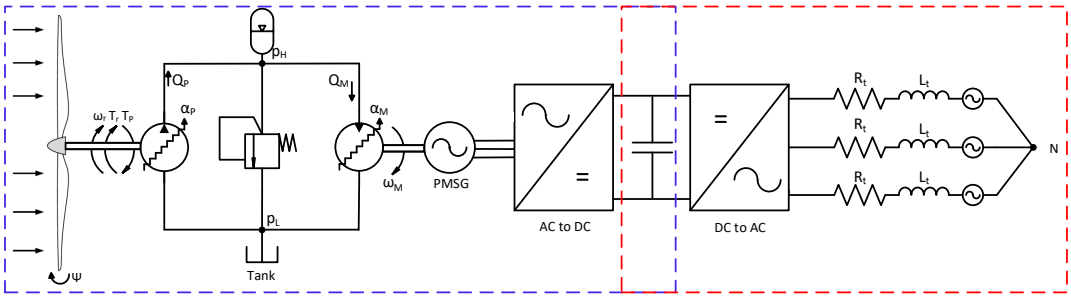

Figure 8.2: The combined system considered in this project. The blue dashed box indicates the components which is considered during the mechanical evaluation and DFPT control. The red dashed box frames the components used during the grid side evaluation and control evaluation.

computational time is due restrictions in the solver configurations. The following section will explain the procedure used for the DFPT-PMSG simulation.

8.2 DFPT-PMSG Simulation

The system used in the simulation is illustrated in Figure 8.3 where the DC-link voltage is assumed constant.

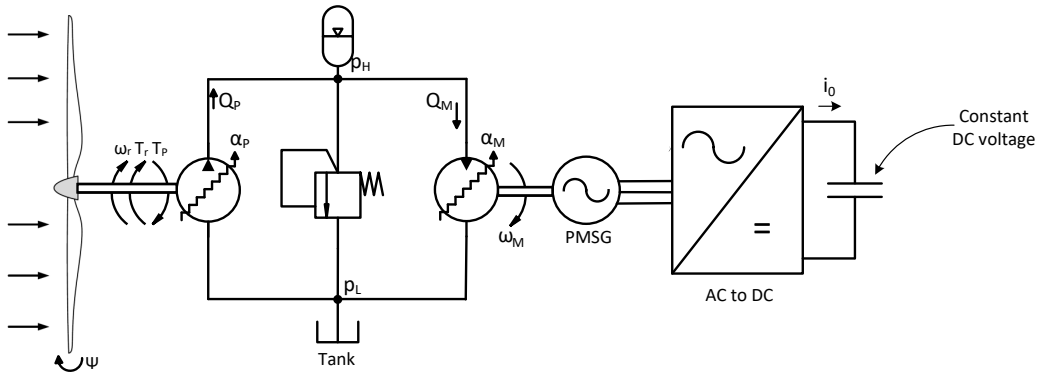

Figure 8.3: The system used during the simulation of the DFPT-PMSG evaluation.

The simulation is carried out utilising the common simulation and evaluation tool FAST, which is based on the NREL 5 MW reference offshore wind turbine, developed by Jonkman et al. [2009]. It is an advanced model which included 24 degrees of freedom for the tower, blades and drive train.

The input file to the FAST model is the wind profile. The wind profile is generated as Normal Turbulence Model with turbulence intensity equal to 12 % which is a reasonable offshore representation [Jonkman et al., 2009]. The wind profile is generated with a mean speed of 8 m/s, which also was the linearisation point of the DFPT controller.

The model is simulated over a 700 second period in order to obtain a representative

simulation, meaning that the simulation results can be seen as an average production and thus can be scaled to represent general power production.

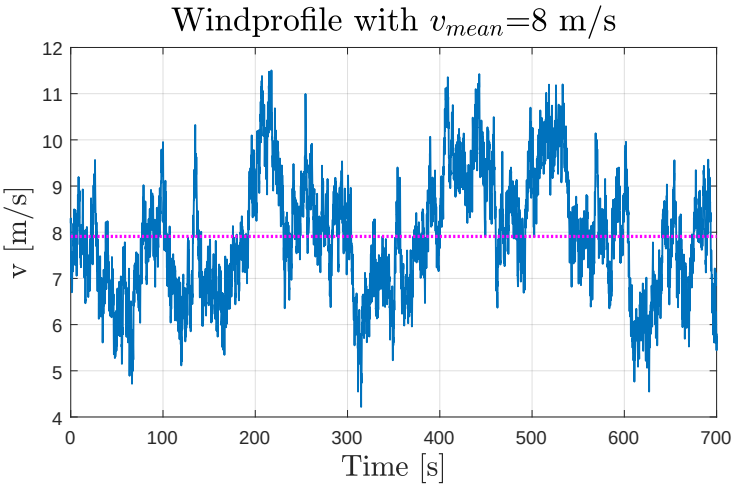

Figure 8.4: Input wind profile used for simulation with mean wind speed of 8 m/s.

In order to evaluate the control performance of the DFPT it is chosen to compare with simulation results from the NREL 5 MW reference model. The same control properties exist for both systems, where the transmission systems are controlled to maintain an optimal TSR of 7.55. Both systems utilise the $K_2\omega^2$ control law used, where the NREL model feedback the high-speed generator, whereas the DFPT feedback the low-speed rotor speed. Since it is the control performance, which is in scope of this project and not the actual power production, the focus for comparison will be the control of the TSR. Therefore, the efficiencies of the drive trains have been set to 100 % in the FAST code.

8.3 DFPT Controller Evaluation

This section is divided into three subsection, a controller evaluation, a transmission evaluation and a generator performance evaluation.

To give the reader an overview of the large amount of data the results from the full 700 second simulation is presented briefly in Figure 8.5 through 8.7. Hereafter, different segments of the simulation are chosen and detailed explained and discussed in order to ease the analysis of the results. The three segments investigated briefly explained below:

- **Control performance related data**, such as control of the pressure Δp to maintain optimal TSR. The DFPT will be compared to the NREL in this section.
- **Transmission related data**, such as the transmission flows and control signal α_M^* to the DD motor.
- **Generator related data**, such as speed control of the DD motor using the generator side inverter.

First, the simulation results for the entire simulation period of 700 seconds is presented. Then, a more detailed discussion of the results are given by fractions of the full period, where the results will be given in zoom plots. The fractions are marked by the orange

dashed boxes in the figures. The three segments have different time constants, where the first **Control performance related data** are the slowest and **Generator related data** are fastest, which explains the different size of the orange dashed boxes.

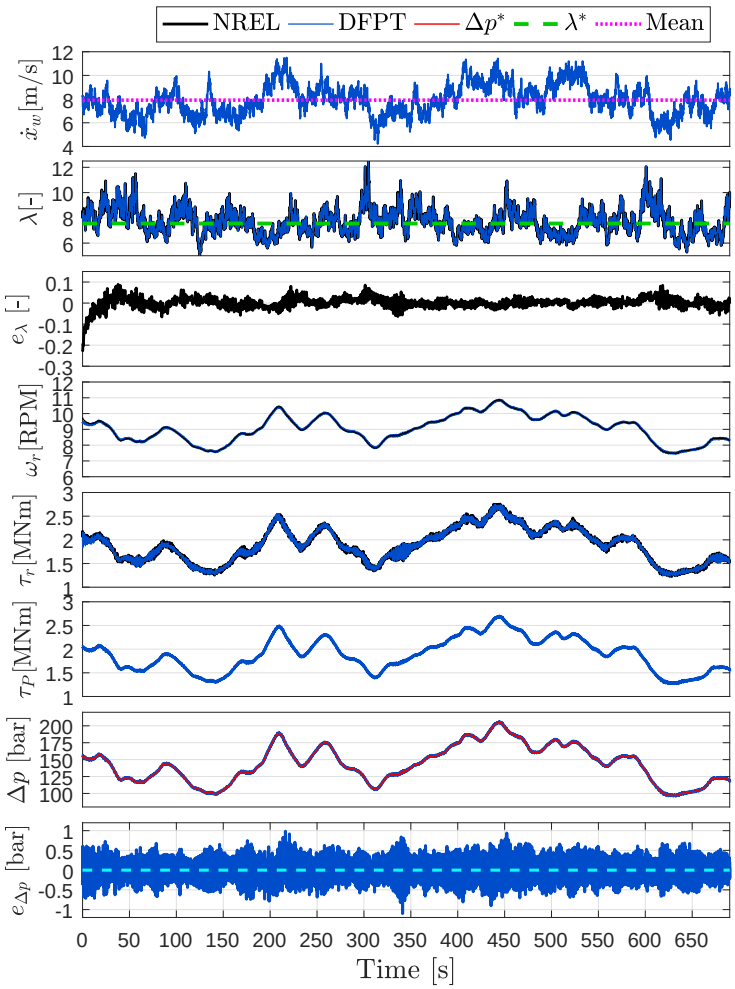

Figure 8.5: Control performance data over 700 seconds.

Figure 8.5

Focusing on the TSR (λ), it is seen that the DFPT performs similar to the NREL, where the Root Mean Square (RMS) error is found to be 0.06. The reason for the deviation may partly be explained by the difference in the K_2 constant in the $K_2\omega^2$ control law.

Focusing on the DFPT, the control of the tip speed ratio is achieved by controlling the HPM pressure Δp to follow the reference Δp^*, where a RMS error of 0.2 bar is found. This is, however, not seen to affect the control of the TSR and thus the control objective is considered satisfactory.

The pressure directly affects the reactive pump torque T_P on the rotor shaft, which is why an analysis of the mechanical loading on the rotor shaft is conducted. This is done is Section 8.4.2. The analysis is carried out to investigate the discrete effects that occur from the DD pump and DD motor. Therefore, the flows in the DFPT is investigated, which leads to Figure 8.6.

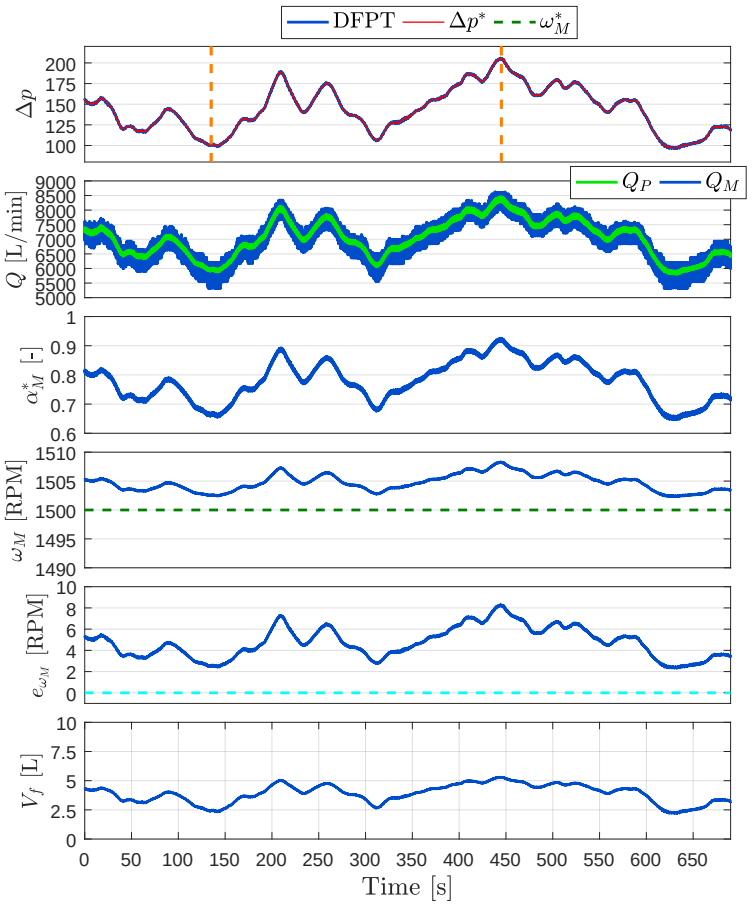

Figure 8.6: Control performance data over 700 seconds.

Figure 8.6

In this figure, the flows in the transmission are investigated. The pump flow Q_P is only depending on the rotor speed due to the fixed displacement. Whereas the motor flow Q_M depends on both the displacement reference (α_M^*) and the speed of the motor shaft (ω_M). The larger oscillatory behaviour in the DD motor is partly due to the displacement rate of the cylinder and partly due to the back flow at valve opening.

The displacement reference is the control signal and is seen to vary in the interval [70-90] %, thus activating roughly three out of every four cylinders in the DD motor, hence no saturation occurs.

The accumulator fluid volume (V_f) is seen to increase when the pump flow increases relatively to the motor flow. Furthermore, it can be observed that the maximum fluid volume is $\approx$ 5 L, which also was expected due to the analysis in Section 5.2.

The motor shaft speed is desired to operate at 1500 RPM, which is controlled by the generator side inverter. The motor is seen to operate at super-synchronous speed with a RMS error of 4.97 RPM. This error is due to the fluctuating motor torque due to the pressure pulsations. This error could have been reduced if an integral term had been designed for the speed controller. However, the control is considered to be acceptable since the speed is close to the operation point of 1500 RPM, at which the DFPT pressure controller was linearised. It could be interesting to redesign

the speed controller to investigate whether this would enhanced the tracking of the tip-speed-ratio.

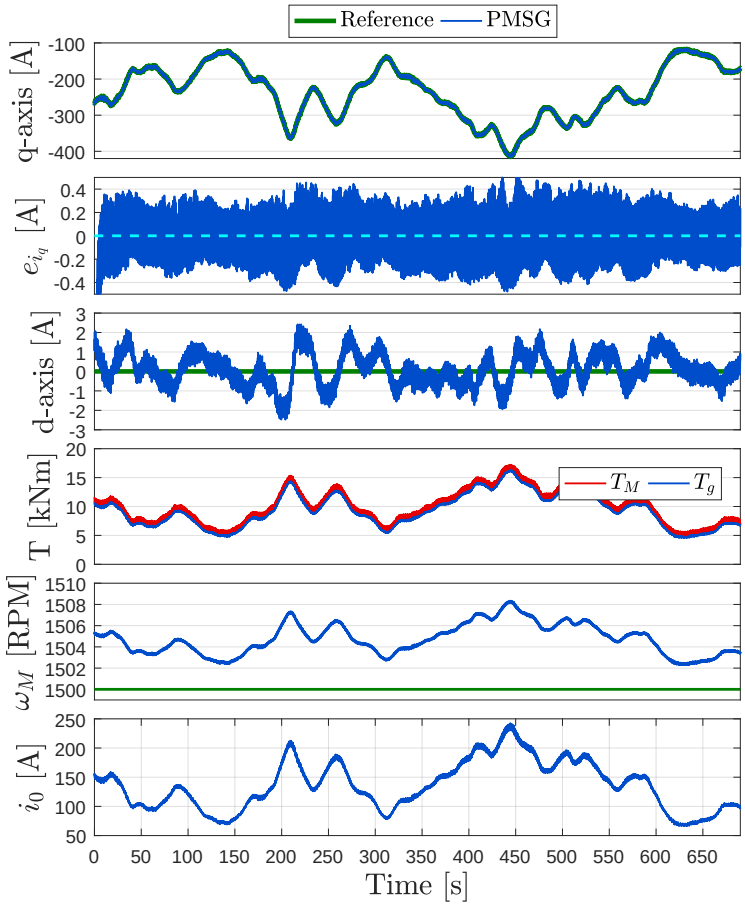

Figure 8.7: Generator data over 700 seconds.

Figure 8.7

This part focuses on the control of the motor shaft speed, hereby presenting the stator currents in the dq- reference frame, where the control of the i_q current is directly related to the torque of the generator T_g. It is seen that the control of the q-axis current, shows good tracking response, where the current is tracked throughout the entire simulation period. Lastly, the input current to the DC-link i_0, which is the coupling between the hydraulic DFPT and the electrical simulation.

In the following, the results will be discussed in details, starting with the turbine related data. The discussion of the results will be based on the boundaries of the pressure range, hence Δp_{min}=100 bar and Δp_{max}=210 bar.

Control Performance Data

In this section the two segments indicated by the orange dashed boxes in Figure 8.5 will be shown in zoom plots. It is investigated, how the pressure operation area affects the control performance of the TSR. The control of the TSR with DFPT will be compared

to the conventional NREL wind turbine. Figure 8.8 and 8.9 shows the control results when operating at the minimal pressure and at the maximum pressure respectively.

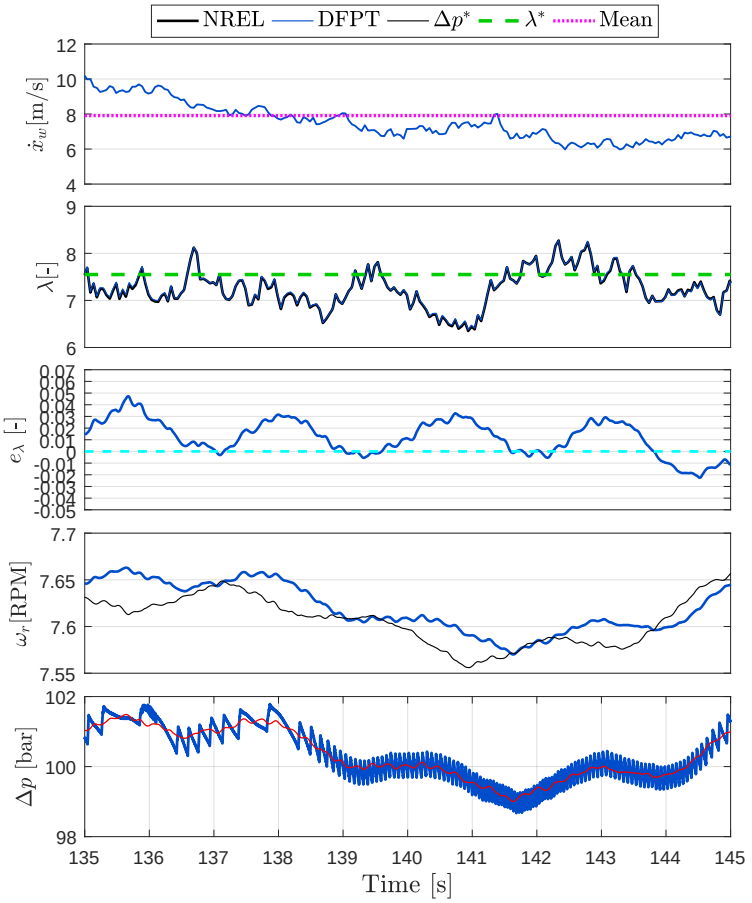

Figure 8.8: Zoom plot of Figure 8.5, focusing on the minimum operation pressure of Δp_{min}=100 bar.

Referring to Figure 8.8, it is seen that the TSR is controlled equally to the NREL. As seen the ω_r of the DFPT lags the ω_r of the NREL. This may be due to the fact, that it is the DD motor, which indirectly controls the torque of the DD pump through the pressure in HPM. The HPM acts like a filter due to the oil stiffness, which may explain the lagging ω_r for the DFPT. However, this does not affect the control of the TSR in any significant manner. Focusing on the pressure Δp, it is seen that the reference pressure is tracked, however, an oscillatory behaviour is observed due to the discrete effects from the DD machines. The high frequency oscillations does not affect the control of the TSR, however, the pressure directly affects the reactive pump torque, which affects the mechanical structure of the wind turbine. This will be investigated in Section 8.4.2.

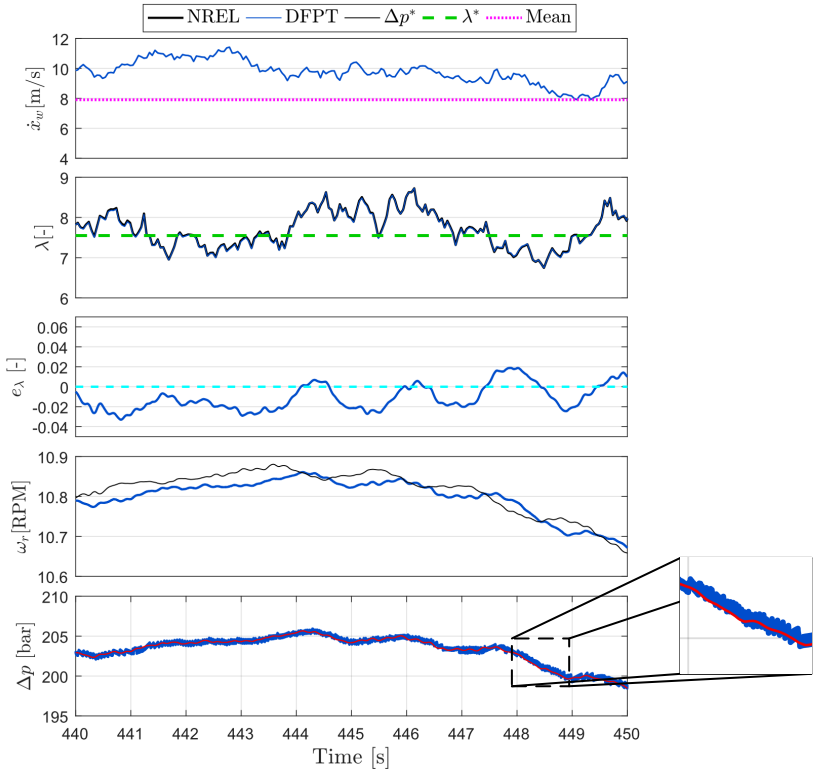

Figure 8.9: Zoom plot of Figure 8.5, focusing on the maximum operation pressure of Δp_{max}=210 bar.

Moving on to Figure 8.9, where operating in the maximum pressure area, the pressure tracking is seen to loose some accuracy around 448 seconds. This may be explained by the fact that the speed controller looses accuracy as the pressure increases, thus increasing DD motor torque i.e. increases the load torque seen by the generator. The load torque is considered as disturbance on the generator and is directly related to the steady state error in the motor speed. Since the DFPT is linearised at 1500 RPM and the actual speed is 1508 RPM, the largest error in the pressure tracking is obtained. However, it does not affect the tracking of the TSR which is the objective of the DFPT controller. Hence the TSR is being controlled satisfactorily at the boundaries of the operation region.

It can be concluded, that TSR tracking is possible, with satisfactory response when comparing with the NREL control. However, the high frequency oscillations of the pressure needs further investigation, which is why the transmission flows are presented in the following subsection.

Transmission Data

Due to the lower time constant of the hydraulic system compared to the time constant of the turbine, the zoom plots of this section will be based on periods of 100 ms. It will be investigated, how the transmission flows affects the pressure tracking. Figure 8.10 shows the system operating at minimum pressure, where Figure 8.11 is based on the maximum system pressure.

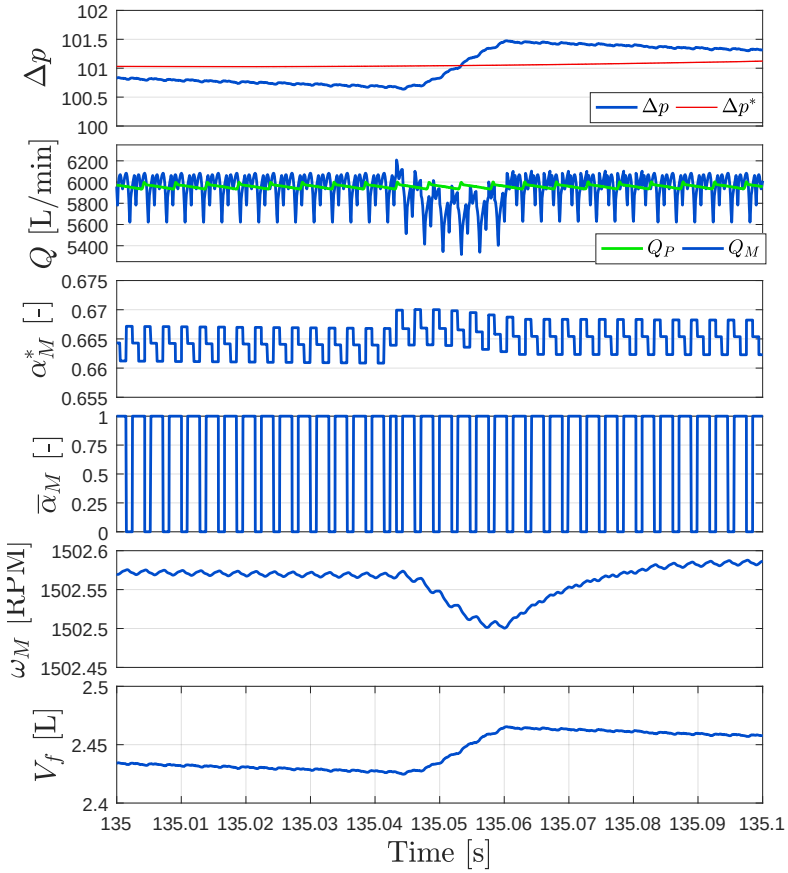

Figure 8.10: Zoom plot of Figure 8.6, where system pressure is Δp_{min}=100 bar.

In Figure 8.10 the motor flow Q_M is seen to have larger amplitude of the pulsations compared to the flow of the fixed displacement pump flow Q_P, this can be explained by the larger displacement rate of the cylinder chamber in the DD motor compared to the DD pump . At t=135.04 s the motor flow Q_M is seen to decrease. This can be explained by the number of active cylinders. Through the most of the period 2/3 of the cylinders are activated as seen in the plot of $\overline{\alpha}_M$ which corresponds to α_M^* approximately. However, at 135.04 s this number is reduced to 1/3 due to the decreasing pressure. As seen it takes a half rotation before the Q_M is back at a flow level corresponding to flow of 2/3 of the cylinders, due to the fact that the flow from one cylinder affects the total motor flow approximately a half rotation. This corresponds with the flow model in Chapter 3.

Considering the pressure tracking, the pressure is seen to vary about the reference with some small deviation which is due to the discrete nature of the system.

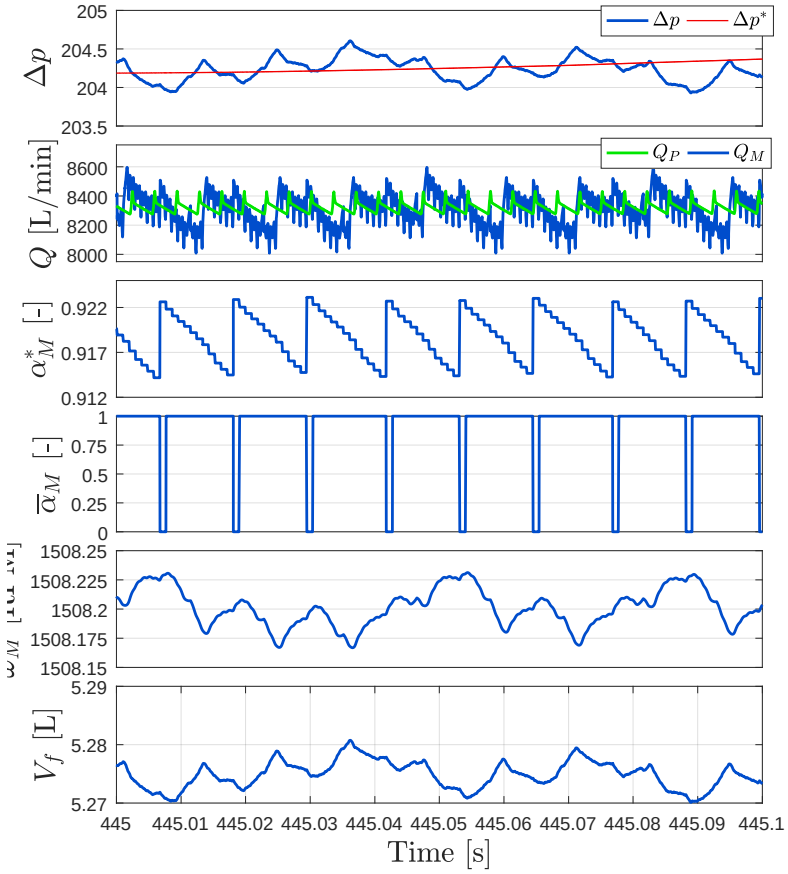

Figure 8.11: Zoom plot of Figure 8.6, where system pressure is Δp_{max}=210 bar.

Focusing in the maximum operation pressure in Figure 8.11 the pressure oscillations are seen to be of larger amplitude. This follows from larger oscillations in the motor flow, where the lower peaks are due to the back flows into the HPM. However, the pressure tracking is still seen to be around the reference. Approximately 9/10 cylinders are activated which corresponds to the input reference α_M^*.

It can be concluded that pressure tracking is possible, with small oscillations around the pressure reference. Due to the highly fluctuating power in the wind, the power transfer through the fluid will obtain similar characteristics, however, the oil acts as a low pass filter, thus filtering out the high frequently oscillations. Still, the pressure never settles exactly at the reference, however, recall that the control of the TSR showed satisfactory response, thus fulfilling the control objective of the DFPT.

Before investigating whether the loading of the DFPT is problematic, the externally controlled motor speed is investigated in the following section.

Generator Data

This section aims to discuss the Field Oriented Control (FOC) performance, where the speed control and current control of the PMSG stator currents are investigated. Since the time constant of the electrical system is lower than the mechanical and hydraulic, the time segments used in this section will be 10 ms.

Figure 8.12 shows the stator currents in the dq-reference frame, the acting of the torque on the motor shaft, where T_v is the viscous damping of the shaft and lastly, the motor shaft speed.

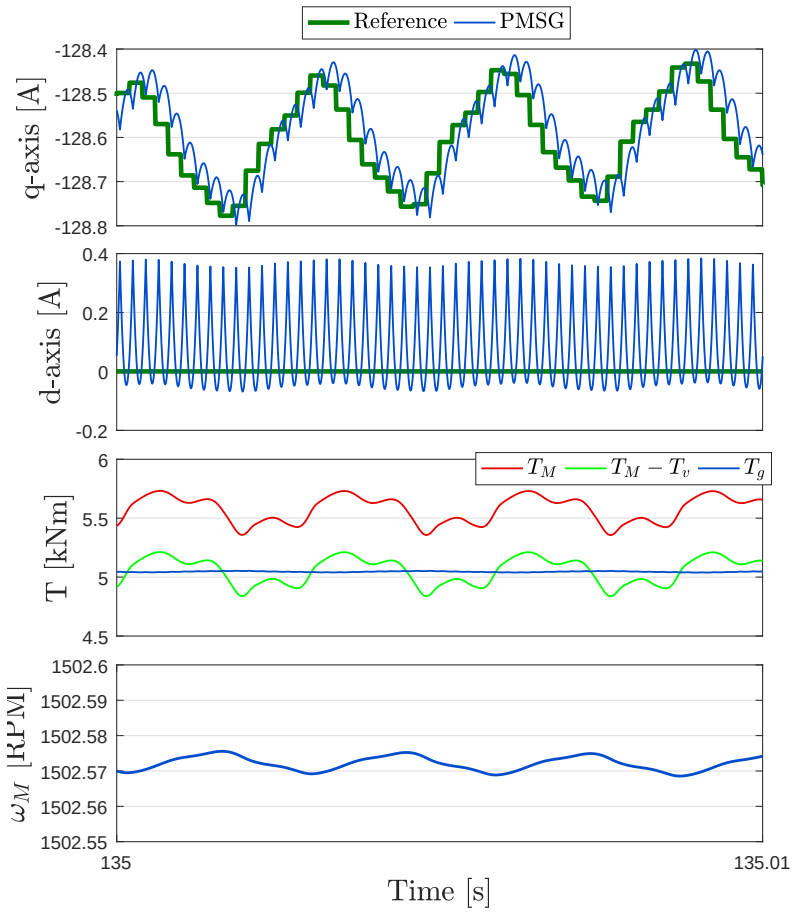

Figure 8.12: Zoom plot of Figure 8.7, where system pressure is Δp_{min}=100 bar.

The i_q-current is seen to follow the reference with oscillatory behaviour one sampling instance slower than the reference. Recall that the sampling frequency is 5 kHz, thus the influence on the generator torque T_g is negligible, as observed in the figure. It is seen that the i_d current is controlled to obtain a value of approximately zero as desired. The deviation will result in a increased loss however this is considered minimal. oscillatory behaviour hence maximising the torque per ampere, since all current is flowing through the q-current component.

The torque output from the motor T_M is seen to have much larger oscillations due to the

pressure pulsations in the DFPT. The same oscillatory behaviour is thus seen in the motor shaft speed ω_M, however, damped through the inertia of the generator. Since the speed controller was designed based on a no load condition, this error is expected. This could have been compensated by an integral term in the PI-controller utilised for the speed controller, however, the speed response is close to the reference and is thus considered to be acceptable. However, it could be interesting to re-tune the controller in order to investigate, whether a better speed control would result in better pressure response and consequently, a better power tracking of the TSR. This is, however, considered for future work, partly due the heavy computational time of the full 700 seconds.

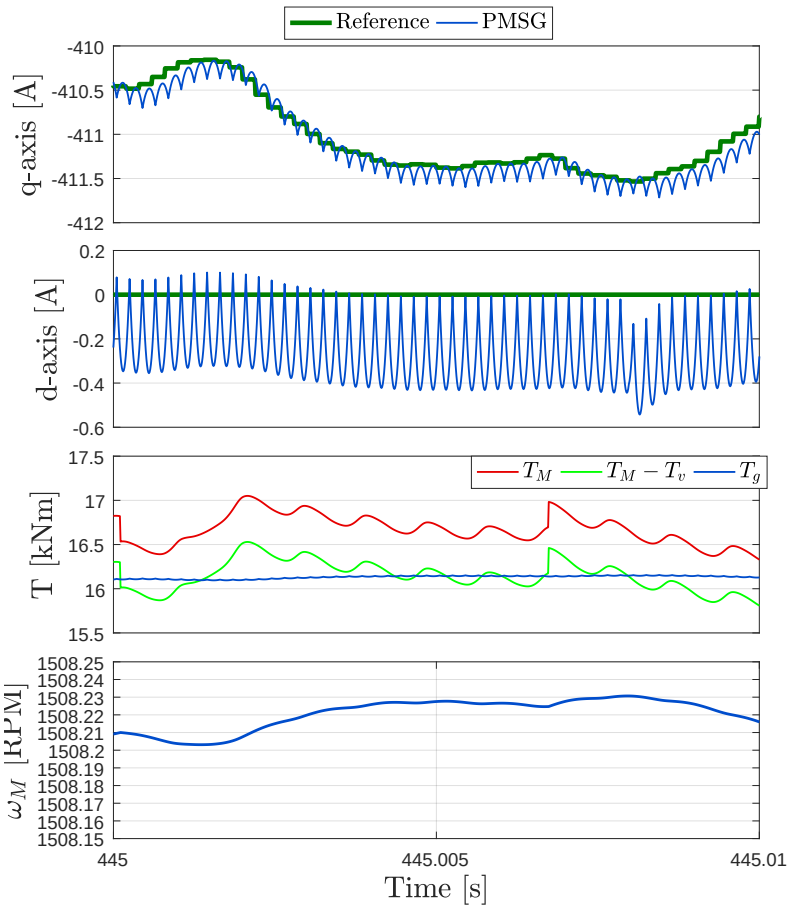

Figure 8.13: Zoom plot of Figure 8.7, where system pressure is Δp_{max}=210 bar.

Moving on to Figure 8.13, where the DFPT operates at maximum pressure of Δp_{max} = 220 bar, it is observed that current range, and hence torque range, is increased by approximately three times. Focusing on the i_q-current it is seen that it lags the reference by one sampling instance, thus similar conclusion can be drawn as in the case of minimum pressure operation and the pressure range does not affect the speed control significantly, since the speed varies with $\approx$ 6 RPM from minimum to maximum pressure.

With satisfactory control of the pressure in the DFPT to obtain maximum power point tracking and speed control of the motor shaft speed, it is now investigated whether the large amount of pressure ripples observed in the simulations leads to an undesired loading

effect on the rotor and motor shaft. This is conducted in the following section.

8.4 Mechanical Evaluation

This section aims to investigate the mechanical loading achieved from loading history for the 700 second simulation presented in section 8.2. The result of the loading analysis will give an indication of, whether the use of a DPFT for the 5 MW wind turbine, is problematic, when considering the load cycles on the mechanical structure.

The section is divided into two parts. First, the evaluation method is presented, where the comparison criteria for the mechanical loading is outlined. After that, the simulation results regarding the loading are presented, ending with a fatigue strength which can be applied for an estimation of the fatigue life assuming repeatable load cycles experienced at the 700 second simulation.

8.4.1 Evaluation Method

To ease the presentation of the results, the evaluation method is only briefly described. The evaluation method is described in detail in Appendix B.
In Niesłony [2009] a method for determination of fatigue life damage in the case of multiaxial loading is presented. A similar method is presented in Melters [2017], which in addition has developed an open-source software tool named *FATLAB*, which incorporates the use Finite Element Model (FEM) to determination of fatigue damage estimation. However, such a detailed model requires a Computer Aided Drawing (CAD) model of the shafts, which are not available in this project and is considered out of scope of this project.

With inspiration from Niesłony [2009] and Melters [2017], the fatigue life estimation at the rotor shaft considered for this project is carried out in five steps, which is illustrated in Figure 8.14.

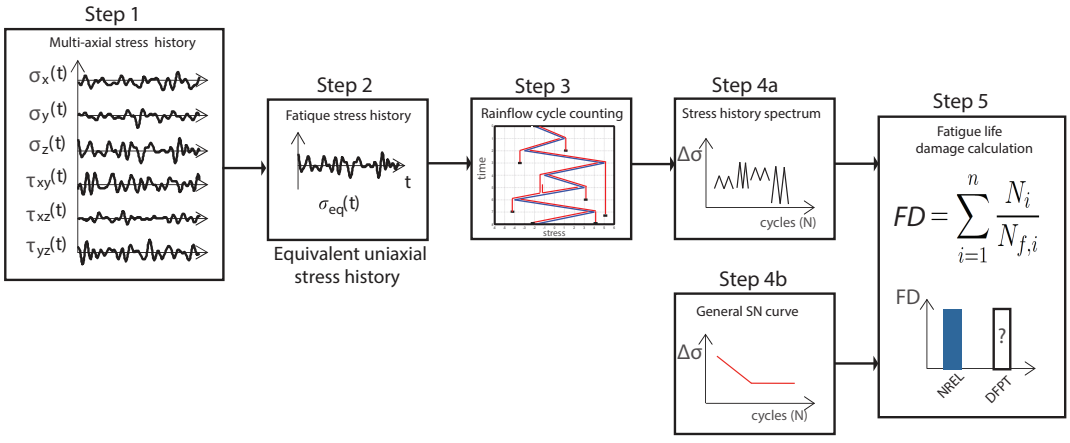

Figure 8.14: Procedure for fatigue damage calculation. Inspired by Niesłony [2009] and [Melters, 2017].

In step 1 the multi-axial stress tensor components are found from simulation data from

the FAST tool. Since fatigue life calculation under multi-axial stress states requires reduction to uniaxial stress state, a proper failure criterion is chosen in order to proceed to step 2. For this study the failure criterion is defined as the plastic region of the material used for the shaft of high strength steel (ASTM-A242). Having obtained the uniaxial stress equivalent history, it allows for stress cycle counting which is achieved in step 3. The cycle counting counts the number of cycles at specific stress levels, thus being able to achieve the stress spectrum in step 4a. The stress spectrum results is denoted as N_i in step 5, where i denotes the associated stress level. In step 4b the general material properties for the chosen material is utilised to determine the number of cycles to failure ($N_{f,i}$ in step 5) under simple tension experimental measurements for the specified material. In step 5 the total fatigue damage, FD, is found as a result of particular damage contributions from the $i\text{-}th$ stress level.

8.4.2 Results

The results from the 700 seconds simulation are presented in Figure 8.4.2, where the five step procedure has been applied. For better display, step number four has been left out. The results is based on the rotor shaft. The results in the figure are discussed below the figure.

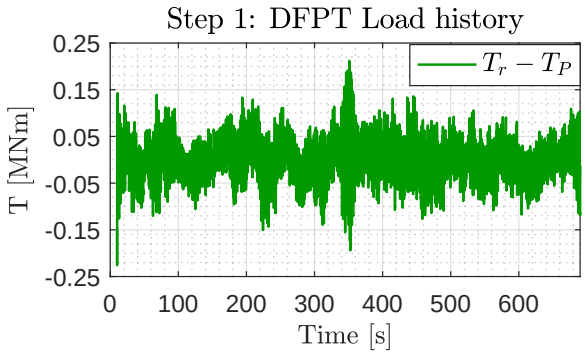
Step 1: DFPT Load history
$T_r - T_P$
T [MNm]
Time [s]

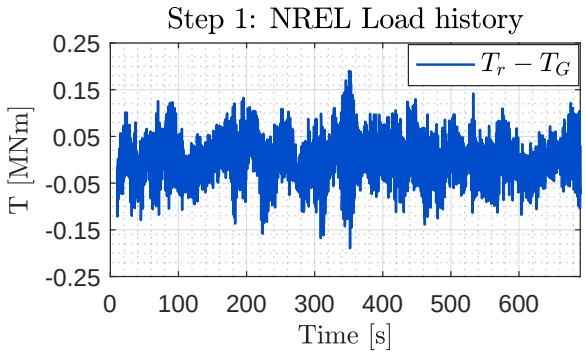
Step 1: NREL Load history
$T_r - T_G$
T [MNm]
Time [s]

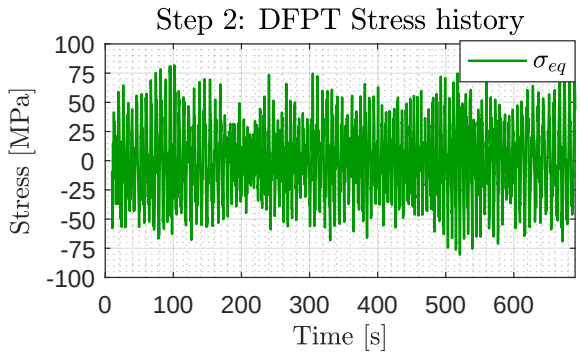
Step 2: DFPT Stress history
σ_{eq}
Stress [MPa]
Time [s]

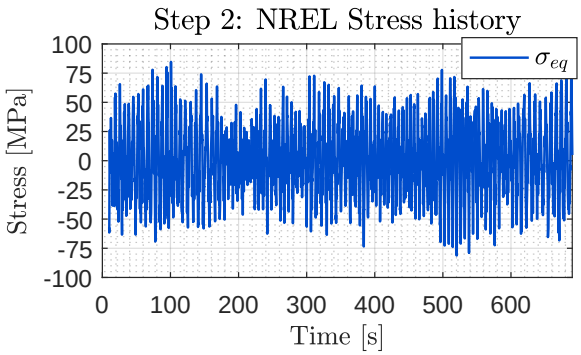
Step 2: NREL Stress history
σ_{eq}
Stress [MPa]
Time [s]

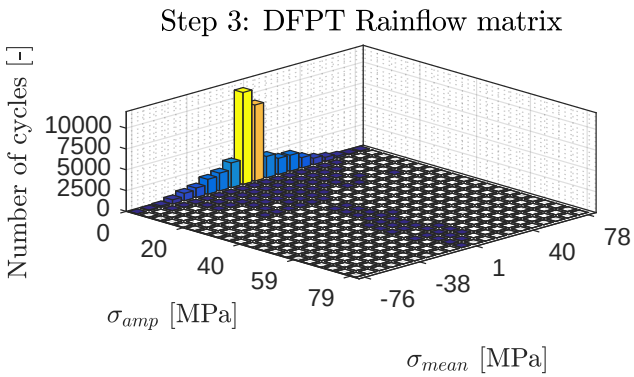
Step 3: DFPT Rainflow matrix
Number of cycles [-]
σ_{amp} [MPa]
σ_{mean} [MPa]

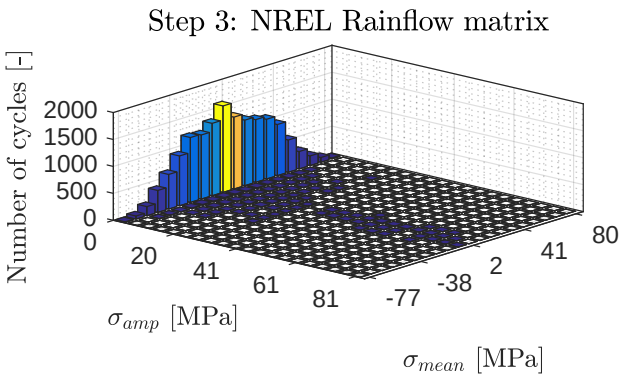
Step 3: NREL Rainflow matrix
Number of cycles [-]
σ_{amp} [MPa]
σ_{mean} [MPa]

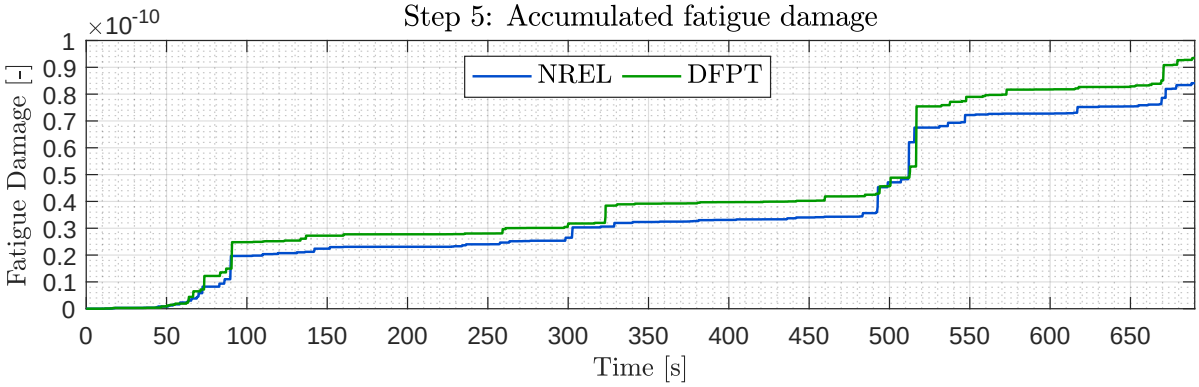
Step 5: Accumulated fatigue damage
NREL
DFPT
Fatigue Damage [-]
Time [s]

Step 1: Load History

In the simulation the load history is logged where the available data from FAST allows for calculation of the multi-axial stress on the rotor shaft. In the DFPT the resulting torques ($T_r - T_P$) acting on the rotor shaft are shown, which contributes to shear stress at the surface of the rotor shaft. Recall the pressure pulsations from Figure 8.8 that directly affects the reactive pump torque T_P. To investigate how the ripples influences the mechanical rotor shaft, the resulting torques from NREL are shown. The resulting torques are calculated as ($T_r - 97\,T_G$) where the gearing ratio of the NREL mechanical gearbox transform the generator torque to the rotor side. This is done by assuming ideal gears, which not has been taking into account since the NREL turbine is not in focus in this project. The NREL torques are seen to have similar amplitude of the load history. In order to determine how these load histories affect the fatigue life of the rotor shaft, the multi-axial stress states are transformed into an equivalent uni-axial stress state, known as the Von-Mises stress. This is shown in step 2.

Step 2: Stress History

The equivalent stress for both the DFPT and NREL is seen to be similar in amplitude, hence nothing yet can be concluded on the fatigue damage. Therefore, the stress cycles must be distinguished, where the common rain flow counting method is utilised.

Step 3: Load Cycle Counting

The distinguishing of the load cycles are performed utilising the widely and common rain flow counting method, which allows for determination of the different load cycles with mean value σ_{mean} and corresponding amplitude σ_{amp}. Then, every load cycle counted that have same mean and amplitude level adds up given the total number of cycles, presented on z-axis in the figure.

It is observed that the stress cycles with low amplitude and low mean value are seen to be dominant, where it is most significant for the DFPT. This is due to the large amount of pressure ripples observed from Figure 8.8 and 8.9. Most of the stress cycles are located around zero mean, which is where the minimum damage effect occur. In the cycle counting method this is counted as a minimal fatigue damage contribution, where the gradient of the stress cycle is not taking into account and instead is counted as a large amount of low amplitude contributions. Consequently, an investigation of the stress cycle gradients would be an interesting future work. However, in Niesłony [2009] a proposed method of utilising an intensity factor, which takes the gradient of the fatigue damage into account. For this study, however, this is not considered and the fatigue damage contribution calculated in the next step is hence calculated where each of the stress cycles contributes to fatigue damage. This is justified by the same method is utilised for both the DFPT and NREL and thus the relative influence can be investigated.

Step 5: Fatigue Damage

The accumulated fatigue damage level of both the DFPT and NREL are shown in the figure. It can be seen that the loading caused by the use of DFPT is slightly larger than that observed in the NREL. Both load histories lead to larger steps in the fatigue damage accumulation at approximately same time instants, which can be identified in the stress histories to occur the maximum stress levels. At the end of the 700 second simulation it was seen that 24.000 extra low amplitude stress cycles were added to the system by the DFPT. Hence the accumulated fatigue

damage was relatively larger compared to the NREL, which is equal to 7.6 % more damage relative to the NREL damage.
This may lead to the conclusion, that the use of DFPT in a 5 MW wind turbine might become problematic. This is based on the larger relative fatigue damage using the DFPT compared to the NREL. It should, however, be noted that a more advanced study on the mechanical loading is needed, where the use of Finite Element Models (FEM) and ideally experimental measurements are needed to give a better indication on the influence on the life time of the rotor shaft. This have however not have been available to the authors. Another possibility could be to redesign the system e.g. the accumulator. This have however not done before hand in of the report partly due to long simulation times and is considered as future work.

Due to large difference in axis scales of the rain flow matrices, it is chosen to display zoom plot results of the stress cycles counting. These zoom plots are shown in Figure 8.15 and 8.16.

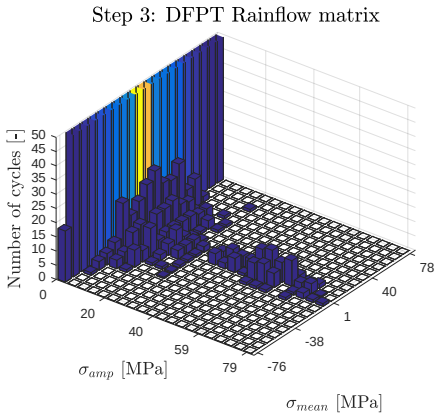

Figure 8.15: Zoom plot of rain flow matrix for DFPT.

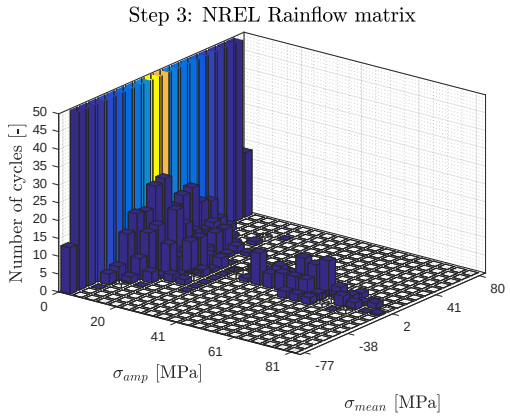

Figure 8.16: Zoom plot of rain flow matrix for NREL.

It can be observed that similar number of cycles occur for both stress histories, where the amplitude and mean stress ranges are approximately equal. Hereby, it is concluded that the fatigue damage accumulation is mainly influenced by the low amplitude cycles in the range 0-5 MPa, which is a result of the discrete nature of the DD machines, hereby indicating that further study can be done regarding damping of the pressure pulsations in the system.

8.5 Electrical Grid Evaluation

The electrical system used during the performance evaluation of the system is seen in Figure 8.17.
As illustrated in Figure 8.17 the system consist of the DC-link, grid side inverter and the grid model. As mentioned the rest of the model, i.e. generator and DFPT have been left out in order to be able to simulate the model within reasonable time and due to the comprehensive amount of data. To simulate the electrical system a time step of

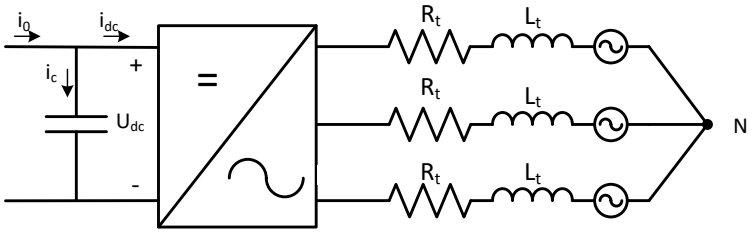

Figure 8.17: The model used for the electrical performance evaluation.

$t_{step} = 10^{-7}$ has to be utilised in order to be able to obtain a stable system. However, it was found that the data could be sampled with a sample rate of $t_{sample} = 10^{-5}$ without any loss of information. Furthermore, some assumptions had to be made in order to be able to simulate the system. The inverter model, which consist of SVPWM calculations had to be leaved out, since the model of the inverter made the system unstable, which have been caused by the third harmonics in the voltage signal. Therefore, the voltage references are transformed from *dq* to *abc* reference frame and fed directly into the system. This assumptions is considered reasonable, since the difference between SVPWM and a simple sine reference for the inverter is small. To ease the data presentation, the data presentation is presented and analysed in different sections where each section will consider a main subject of the system. The main subjects considered are listed below.

- Active and reactive power
- DC-link voltage tracking
- Current reference tracking
- Power factor

As seen the voltage reference tracking are not considered, since the inverter has been left out and the reference is used as input to the model as mentioned earlier.

8.5.1 Active and Reactive Power

The active and reactive power depends on the *dq* current components respectively. The first objective is to have a unity power factor, hence Q should be zero. The second objective is that the power produced by the generator P_g should be injected to the grid in order to maintain a somewhat constant DC-link voltage. The active and reactive power are displayed in Figure 8.18 and 8.19 respectively.

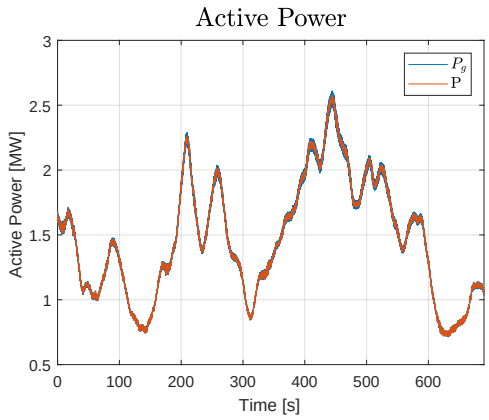

Figure 8.18: Power produced by the generator and the power injected to the grid during the simulation.

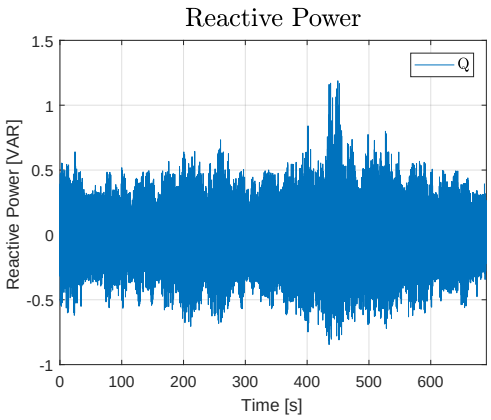

Figure 8.19: The reactive power during 700 seconds.

From the Figure 8.18 the power produced from generator P_g and the power injected to the grid P can be seen. As seen the power P follows P_g in a satisfying manner. As expected P_g tends to oscillate more compared to P, due to the discrete nature of the DFPT. Hence the following section will evaluate the DC-link voltage in order to see if the DC-link is somewhat constant.

8.5.2 DC-link Voltage Tracking

The reader should recall that during the design of the DC-link in Chapter 5 the maximum allowed voltage ripple was chosen to be 1% of the DC-link voltage, hence the maximum allowed voltage ripple is approximately 108V. The DC-link voltage during the 700s simulations is plotted together with DC-link voltage reference in Figure 8.20 and the error of the DC-link voltage tracking is plotted in Figure 8.21.

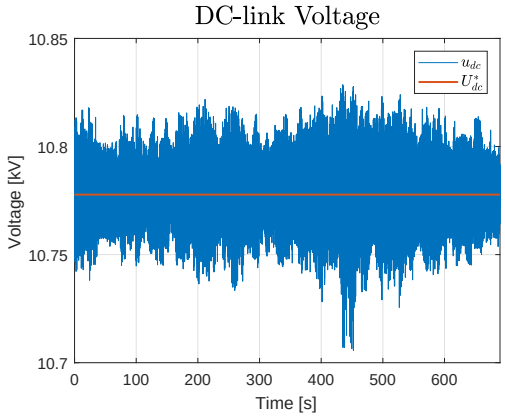

Figure 8.20: DC-link voltage tracking plotted together with the reference.

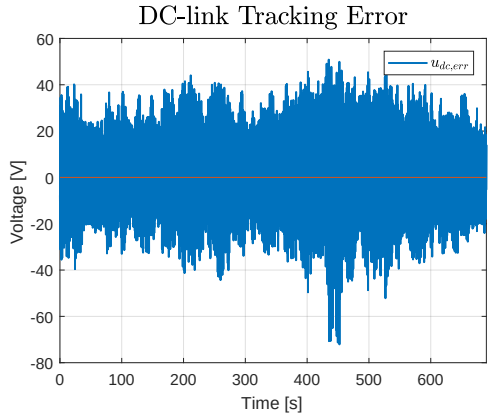

Figure 8.21: DC-link voltage tracking error.

As seen in Figure 8.20 the DC-link voltage oscillates around the reference as expected.

Taking a closer look on the amplitude of the ripples compared to the reference in Figure 8.21 it can be seen that the maximum error is around -70V, hence it is below the maximum allowable DC-voltage ripple. Calculating the RMS error gives an error of approximately 11.1V. As seen around 450 seconds two large undershoots in the voltage are obtained indicating that the injected power to the grid is larger than the amount of produced power delivered by the generator. Hence the power balance of the DC-link is calculated as $P_{diff} = P_g - P$ and plotted in Figure 8.22.

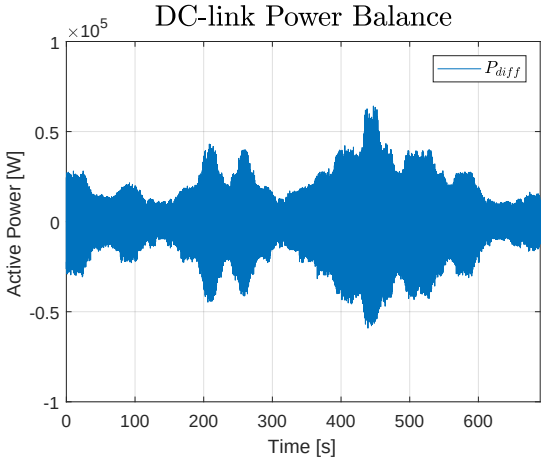

Figure 8.22: Zoom plot of the DC-link voltage.

To see how the dynamics of the DC-link voltage behaves two zoom plots of Figure 8.20 have been made and displayed in Figure 8.23.

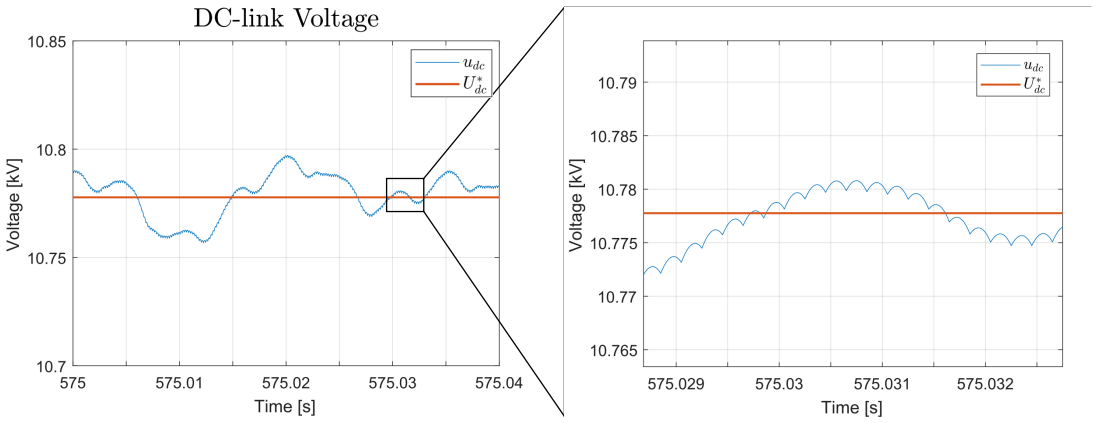

Figure 8.23: Zoom plot of the DC-link voltage.

As seen from Figure 8.23 the DC-link voltage is a continuous signal which oscillates around the reference. By zooming further in on the DC-link voltage in can be seen how small voltage ripples are obtained. These ripples have approximately the same frequency as the current ripples in i_0, hence these small ripples were expected. As it is the current i_d which control is related to the injected power it is the current reference tracking which is to be scrutinised. Hence it can be concluded that it is possible to control the DC voltage with good accuracy when utilising the DFPT as drive unit for the PMSG. However, it must be considered future work to simulate the FOC simulation with the varying DC-link voltage to see how accurate the speed control of the PMSG would be at

these voltage ripple levels.

8.5.3 Current Reference Tracking

As mentioned it is the current which is directly related to the amount of power injected to the grid, hence it is desired to see how the current controller perform during the simulation. The i_d current is seen in Figure 8.24 together with i_d^* and a zoom plot of the two signals is made in Figure 8.25.

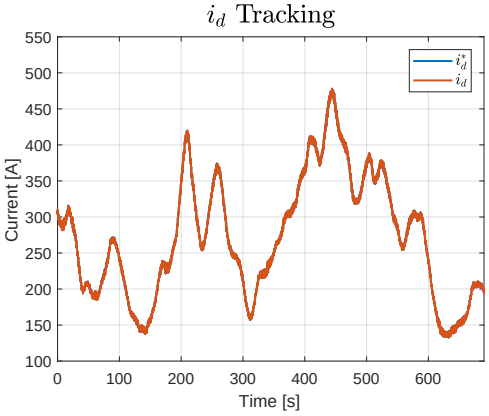

Figure 8.24: The d current component during the 700s simulation plotted together with the reference.

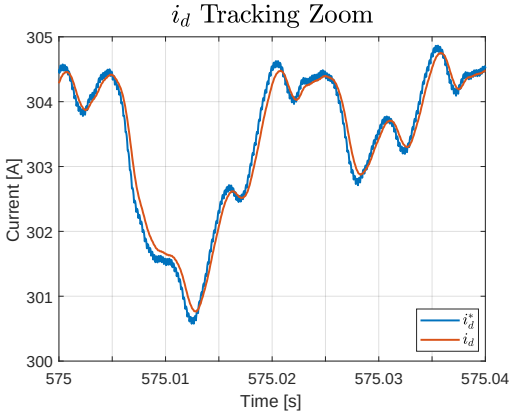

Figure 8.25: Zoom plot of the d current component during the 700s simulation plotted together with the reference.

As seen in Figure 8.24 and 8.25 the current controller tracks the reference i_d^* satisfactory. Calculating the RMS error for the i_d it is found to be $11.6 \cdot 10^{-2}$ which is considered good.
The i_q is directly related to the reactive power. During this simulation a power factor of one has been desired, hence the active power should be equal to the apparent power meaning that the reactive power should be zero during the simulation, hence the current should ideally be zero. The current i_q is plotted together with the reference in Figure 8.26.

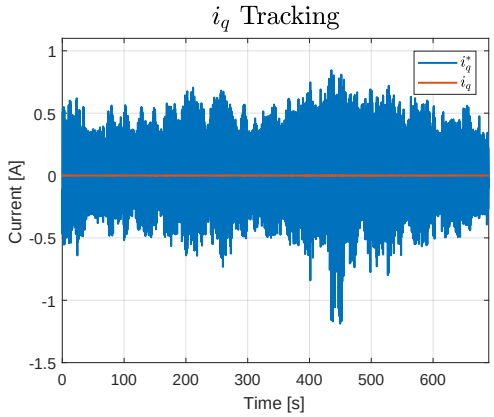

Figure 8.26: i_d^* and i_q* plotted for 700s.

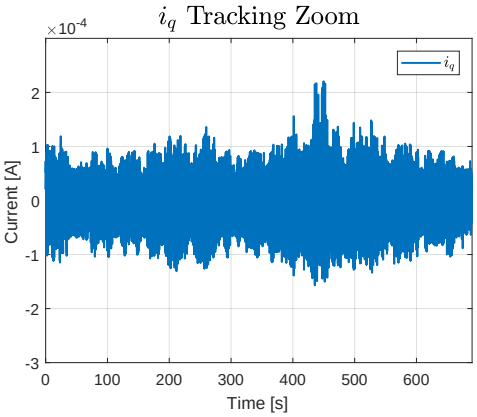

Figure 8.27: i_d^* plotted for 700s.

From Figure 8.26 it can be seen that the i_q^* is equal to $-Q$ when comparing with Q displayed in Figure 8.19. However, it seems like the i_q is zero during the whole simulation. Therefore, the plot of i_q current is seen in Figure 8.27. Calculating the the RMS error of the i_q tracking an error of $10.7 \cdot 10^{-2}$ which is considered acceptable and in the same region as for the other controller.

8.5.4 Power Factor

This sections sees to evaluate the power factor performance through the simulation. As mentioned in Chapter 4 it is normally the TSO which specifies the power factor which the system must operate under. In this project however, there is no TSO, hence it is desired to obtain unity power factor. At unity power factor the grid current and grid voltage must be in phase. In figure 8.28 the grid current and grid voltage is plotted for a small period of the 700s simulation.

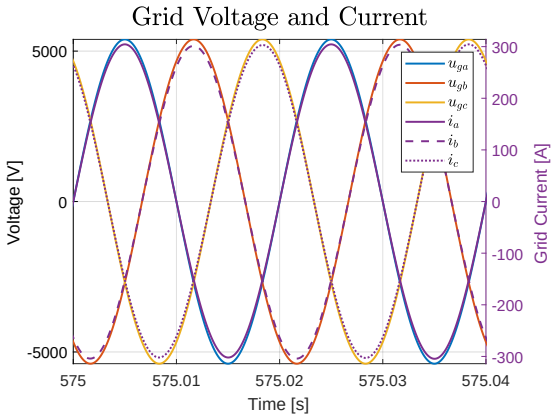

Figure 8.28: i_d^* and i_q* plotted for 700s.

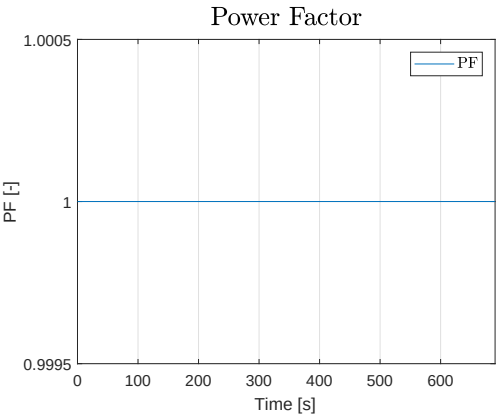

Figure 8.29: i_d^* plotted for 700s.

From Figure 8.28 it is clearly seen that the current and voltage are in phase. Calculating

the power factor through the whole simulations confirms that the power factor is one during the whole simulations. The power factor is plotted in Figure 8.29. and as seen the power factor is clearly within the bounds specified in Section 1.5 as it is equal to one during the whole simulation.

8.6 Summary

Through this chapter the evaluation results from the DFPT evaluation, mechanical evaluation and electrical evaluation have been presented. The model was divided up into two models and simulation in order to deal with the comprehensive simulation time and data. Hence a model of the DFPT-PMSG and the model of the grid was simulated separately where the inpuit to the grid model was the current i_0 found in the other simulation.
The DFPT evaluation was divided into three evaluation categories, control performance, turbine and PMSG which were benchmarked to the NREL wind turbine. It was found that the it was possible to control the TSR with an RMS error of 0.06 compared to the NREL. The deviation may be caused by two different K_2 constant in the control law, hence it was considered that it was possible to control the TSR as good as the conventional TSR. The maximum error obtained in the speed of the DD motor was 8RPM at high pressure as expected.
Furthermore, it was found that the pressure oscillation in the DFPT added an extra 24.000 load cycles to the mechanical structure, hence the accumulated damage for the DFPT was relatively higher compared to the accumulated damage of the NREL.
The above mentioned results was simulated under the assumption that the DC-link voltage was constant, hence the speed control of the generator had somewhat ideal conditions. It was desired to investigate how a more fluctuating motor torque would influence the DC-link voltage, in order to validate the assumption of a constant DC-link. It was found that the RMS error was 11.1V hence a small error below the maximum voltage ripple of 108V i.e. 0.1% of the DC-link voltage reference. Thus it is considered a valid assumption since the DFPT does influence the DC-link voltage in any significant manner.

CHAPTER 9

Discussion

This chapter seeks to discuss the simulation and evaluation methods utilised throughout this project.

9.1 Simulation Method

Due to different time constants of the DFPT system and the electrical power converter/grid, it was considered impossible to simulate the two systems in a combined model within reasonable time for the 700 seconds simulation, since the simulation of the DFPT with a time step of 10^{-5} s took 1.5 days and the combined model would require a time step of 10^{-7} s. It was chosen to use the DC-link input current as the coupling between the generator and grid. By assuming constant DC-voltage the FOC had ideal conditions for optimal control of the angular velocity of the PMSG and motor. This choice is justified by it was proven that the angular velocity did not affect the location of the poles of the DFPT with controller in any significant manner. However, the influence from a more inaccurate/pulsating speed control on the pressure pulsation is not considered which is one of the downsides by dividing the simulation into two.

An alternative method for evaluation could be to log the torques acting on the motor/generator shaft and then simulating the generator model with the back-to-back converter and grid. However, again, this becomes an approximate evaluation since the DC-link dynamics influences the control of the generator.

9.2 Mechanical Evaluation

The loading on the mechanical structure has been limited to an analysis on the low speed rotor shaft. It could be interesting to evaluate the loading on the generator shaft, to investigate the potential use of hydraulic transmission in a wind turbine, since the generator shaft and rotor shaft are mechanically decoupled, which could improve the reliability.

Several assumptions has been applied and discussed in Appendix B in order to develop the analysis tool for fatigue damage calculation, where the analysis was delimited to focus on the operational loads of the wind turbine, i.e. how the transmission loads acts.

This project has not been able to estimate the expected lifetime for the wind turbine utilising the DFPT, hence not been able to investigate the full potential of the DFPT in a large scale wind turbine. In order to be able clarify the full potential of the DFPT, an estimated lifetime must be calculated. However, this requires more advanced methods utilising finite element methods.

9.2.1 Power factor Evaluation

As mentioned in the report it is normally the TSO which specifies the power factor during operation. Large wind turbines are considered as power plants, hence they must be able to support the grid if voltage dips occur or the grid frequency increases or decreases. Therefore, the wind turbine must be able to inject or take reactive power to/from the grid. During the evaluation the desired power factor was equal to one through the whole simulation which was successfully obtained. However, the Q controller was not tested for varying power factors. Therefore, further simulations with realistic power factor references from the TSO must be conducted, but this is considered as future work.

CHAPTER 10

Conclusion

The main objective for the Master's Thesis has been to design a controller for a DFPT used in a 5 MW offshore wind turbine in order to maximise the energy production below rated wind speed, i.e. track the optimal Tip-Speed-Ratio λ^* without violating the mechanical and electrical requirements. To be able to evaluate the tracking of the optimal Tip-Speed-Ratio, the results have been compared with the National Renewable Energy Laboratory (NREL) reference wind turbine.

In order to do so, a non-linear model have been developed of a Digital Fluid Power Transmission (DFPT) containing the Digital Displacement® (DD) machines, high pressure manifold with accumulator, and non-linear model of the electrical system including Permanent Magnet Synchronous Generator (PMSG), back-to-back converter and a model of the transmission grid from the wind turbine to the point of connection just before the transformer.

The different components in the non-linear model have been dimensioned in order to be able to fit the 5 MW NREL reference wind turbine. Due to the discrete nature of the DD machines the accumulator volume have been dimensioned by considering the damping and utilisation during the simulation.

To control the λ^* the popular $K_2\omega^2$ control law was modified to give a pressure reference Δp^* in order to allow λ^* to be controlled by the DD motor since the utilised DD pump was a fixed displacement pump. However, as the DD motor control Δp^* it cannot control the speed, thus a Field Oriented Controller (FOC) controller was utilised to control the speed of the PMSG and DD motor. Voltage Oriented Control (VOC) was applied on the grid side of the back-to-back converter in order to control the DC-link voltage, power factor and frequency of the injected current.

To allow for discrete linear deterministic optimal control of the DFPT, a Discrete Linear Time Invariant (DLTI) approximation model of the DFPT has been made and put on a state space model to ease the control design. It was chosen to use a Linear Quadratic Regulator (LQR) due to the relative large number of system states. Furthermore, an integral state was included to account for model simplification and disturbances in the model. The stability of the closed loop system was tested under extreme working conditions and it was found that the system was stable under these conditions.

Due to comprehensive computational time, a large amount of data and the different time constants of the models it was considered impossible to simulate the combined system. Hence the system was divided into two simulation models, a model of the DFPT-PMSG and a model of the grid respectively. To be able to do so, the DC-link voltage was assumed constant during the simulation of the DFPT-PMSG model. The input current i_0 to the power converter from the PMSG was logged and used as input to the simulation model of the grid. The model of the DFPT-PMSG was simulated over 700 s with the tool Fatigue, Aerodynamic, Structure and Turbulence (FAST).

From the simulation results it can be concluded that it is possible to control λ^* similar to the NREL with only a RMS error of 0.06. This RMS error might be explained by the different values of the constant K_2 in the control law. Considering the electrical system it was found that it was possible to control the velocity of the DD motor with

a RMS error of 4.98 RPM. Furthermore, it can be concluded that the VOC controlled the power factor in a satisfying way and DC-link voltage within the specified allowable ripples. However, it cannot be concluded how the ripples affects the speed control of the FOC due to the fact that the two models were simulated separately.

As expected the pressure pulsation occurred due to the discrete nature of the DD machines which directly affects the torque of the DD pump, hence the overall structure of the wind turbine. This was also observed mechanical evaluation where it was seen that the DFPT added approximately 24.000 extra low amplitude stress cycles to the system compared to the NREL. Therefore, it was found that the accumulated fatigue damage of the rotor shaft was relative higher using the DFPT compared to the NREL, however, a more detailed structural analysis must be made in order to get an estimate of the lifetime.

Lastly, it can be concluded that it was possible to control λ^* below rated wind speed in a satisfying way. However, it was not possible to damp the pressure pulsation in such a way that the accumulated fatigue damage was equal to or below the accumulated fatigue damage of the NREL. Changing the parameters of the accumulator or the number of accumulators may reduce the mechanical loading, however this have not been done before project hand in, thus it is considered for future work.

Bibliography

Andersen, T. O. [2003], 'Fluid Power Systems'.

Andersen, T. O. [2007], 'Fluid Power Curcuits'.

Ansel, C. U. and Saul, K. F. [2003], *Advanced Strength and Applid Elasticity.*

Artemis [2016], 'MHI Hydraulic Driven 7MW Offshore Wind Turbine - Online Video at Artemis Intelligent Power Official Youtube Channel'.
URL: *https://www.youtube.com/watch?v=ydupJZm_NzU*

Artemis [2017], 'Artemis Wind Power'.
URL: *http://www.artemisip.com/applications/renewable-energy/wind-power/*

Asimmoaei, L., Aeloiza, E., Kim, J. H., Enjeti, P., Blaabjerg, F., Moran, L. T., Sul, S. K. and Asiminoaei, L. [2006], 'An Interleaved Active Power Filter with Reduced Size of Passive Components', *Twenty-First Annual IEEE Applied Power Electronics Conference and Exposition, 2006. APEC '06.* pp. 969–976.
URL: *http://ieeexplore.ieee.org/lpdocs/epic03/wrapper.htm?arnumber=1620656*

Bathias, C. and Pineau, A. [2009], *Fatigue of Materials and Structures.*

Blaabjerg, F., Liserre, M. and Dell'Aquila, A. [2002], 'Design and control of a three-phase active rectifier under non-ideal operating conditions', *Conference Record of the 2002 IEEE Industry Applications Conference. 37th IAS Annual Meeting (Cat. No.02CH37344)* **2**(Cluster 13), 1181–1188.

Bueno Gayo, J. [2011], 'RELIAWIND Project final report. Report prepared for: European Commission', (212966), 1–62.

Energinet.dk [2016], 'Technical regulation 3.2.5 for wind power plants above 11 kW', pp. 1–108.

Fried, L. [2017], Global Wind Statitis 2016, Technical report, Global Wind Energy Council.
URL: *http://www.gwec.net/wp-content/uploads/vip/GWEC_PRstats2016_EN_WEB.pdf*

Gohil, G., Bede, L., Teodorescu, R., Kerekes, T. and Blaabjerg, F. [2014], 'Analytical Method to Calculate the DC Link Current Stress in Voltage Source Converters'.
URL: *http://ieeexplore.ieee.org/document/7041953/*

GS-Hydro [2017], 'Hydraulic piping standard handbook'.
URL: *http://www.gshydro.com/sites/default/files/attachments/Global/Publications/gs-hydro_hydraulic_piping_standard_handbook_revision_1.pdf*

Hauge, H., Kinch, R. and Daugbjerg, N. [2016], 'Control of Digital Displacement Wind Turbine Transmission'.

Heemels, W., Gorter, R., van Zijl, A., van den Bosch, P., Weiland, S. and Vonder, M. [1998], 'Asynchronous measurement and control: a case study on motor synchronisation', (June).

Irwin, J. [2011], *Basic Engineering Circuit Analysis*, Vol. 53, 10 edn.

Johansen, P. [2014], *Aalborg Universitet Tribodynamic Modeling of Digital Fluid Power Motors Johansen, Per.*

Jonkman, J., Butterfield, S., Musial, W. and Scott, G. [2009], 'Definition of a 5-MW reference wind turbine for offshore system development', *Contract* (February), 1–75.

Kameda, T., Uchida, M., Uehara, O., Dodson, H., Robertson, A. and Rampen, W. [2014], 'Hydraulic Pump, Method for Maintaining Same, and Wind Power Generation Device', **1**(19), 1–40.

Kazuhisa, Tsutsumi; Atsushi, Maekawa; Masayuki, Shimizu; Stephen, Salter; Uwe, Stein; William, Rampen; Robert, Fox; Hauke, K. [2010], 'Wind turbine generator and tidal current generator with a hydraulic transmission'.

Krause, P., Wasynczuk, O., Sudhoff, S. and Pekarek, S. [2013], *Analysis of Electrical Machinery and Drive Systems*, third edit edn.

Lorenzen, S. L. and Nielsen, A. B. [2015], Control of a Gid Connected Converter Duringer Weak Grid Conditions, Technical report, Aalborg University.

Mazaheri, A. [2012], A 5 MW Wind Turbine Generator System for a DC Grid Application, Master of sience, Chalmers University of Technology.

Melters, M. [2017], 'fatiguetoolbox'.
URL: *http://fatiguetoolbox.org/*

MHI Vestas Offshore Wind [2014], 'V164-8.0 MW® breaks world record for wind energy production'.
URL: *http://www.mhivestasoffshore.com/wp-content/uploads/2015/03/21-10-2014-Press-release.pdf*

Niesłony, A. [2009], 'Determination of fragments of multiaxial service loading strongly influencing the fatigue of machine components', *Mechanical Systems and Signal Processing* **23**(8), 2712–2721.

Norton, R. L. [2004], *Design of machinery.*

Ogata, K. [1995], *Discrete-Time Control Systems*, second edi edn.

Park, R. H. [1929], 'Two Reaction Theory of Synchronous Machines Generalized Method of Analysis-Part I', *Winter Convention of A.I.E.E.* pp. 716–727.

Pedersen, N. H. [2016*a*], 'Control of Digital Displacement Wind Turbine Transmission', pp. 1–3.

Pedersen, N. H. [2016*b*], 'LQR Feedback Control Development For Wind Turbines Featuring A Digital Fluid Power Transmission System'.

Phillips, C. L. and Parr, J. M. [2011], *Feedback Control Systems*, 5. edn.

Rabi, M. G. E.-D. M. [2009], *Fluid Power Engineering*, McGraw-Hill.

Reiss, J. [2008], 'Understanding Sigma-Delta Modulation: The Solved and Unsolved Issues', (January 2008).

Roemer, D. B. [2014], *Design and Optimization of Fast Switching Valves for Large Scale Digital Hydraulic Motors.*

Sasaki, M., Yuge, A., Hayashi, T., Nishino, H. and Uchida, M. [2014], 'Large Capacity Hydrostatic Transmission with Variable Displacement', *The 9th International Fluid Power Conference* .

Siemens [2014], 'What is the real cost of offshore wind?'.
URL: *www.energy.siemens.com/br/pool/hq/power-generation/renewables/wind-power/SCOE/Infoblatt-what-is-the-real-cost-of-offshore.pdf*

Singh, M., Muljadi, E., Jonkman, J. and Gevorgian, V. [2014], 'Simulation for Wind Turbine Generators — With FAST and MATLAB-Simulink Modules Simulation for Wind Turbine Generators — With FAST and MATLAB-Simulink Modules', (April).

Sniegucki, M., Gottfried, M. and Klingauf, U. [2013], *Optimal control of digital hydraulic drives using mixed-integer quadratic programming*, Vol. 9, IFAC.
URL: *http://dx.doi.org/10.3182/20130904-3-FR-2041.00013*

Taylor, J., Rampen, W., Robertson, A. and Caldwell, N. [2011], 'Digital Displacement ® Hydraulic Hybrids Parallel Hubrid Drives for Commercial Vehicles', *JSAE Annual Congress* (1).

Teodorescu, R., Liserre, M. and Rodriguez, P. [2011], *Grid Converters for Photovoltaic and Wind Power Systems*, 1. edn, John Wiley & Sons, Ltd.

APPENDIX A

Lookup Table Validation

In this appendix the validation of the lookup tables for both the DD pump and DD motor are described. First, the worst case gradients of the input signals to the lookup tables are defined. Then, the lookup tables are validated by comparing lookup simulation results to the dynamic single chamber simulations. Lastly, since the aim is to overcome the problem of comprehensive computational time, the accuracy of the lookup tables is tested for different time steps.

A.1 Maximum Signal Gradients

Since the lookup tables are constructed of breakpoints, the accuracy are tested when interpolating between the breakpoints. Therefore, the aim of this section is to find the maximum gradients of the inputs (breakpoints) of the lookup tables, which can be expected during operation. The gradients to be found are listed as:

- $\dot{\omega}_{r,max}$
- $\dot{p}_{H,max}$ (common for pump and motor)
- $\dot{\omega}_{M,max}$

First, the maximum rotor acceleration is found. The maximum gradient is found by considering a no load condition given by Equation (A.1), where the viscous damping is neglected.

$$\begin{aligned} \dot{\omega}_{r,max} &= \frac{1}{J_r}\left(T_{r,max} - T_P\right) \\ &= \frac{1}{3.87 \cdot 10^7}\left(4.36 \cdot 10^6 - \cancelto{0}{T_P}\right) \approx 1.08^{RPM}/_{s} \end{aligned} \tag{A.1}$$

The maximum pressure gradient is based on a case, where no accumulator is present, hereby obtaining larger gradients to test the lookup tables. The flow will be accumulated for a short time period due to the different speed of the pump and motor. Hence the maximum accumulated flow will be the flow from one motor cylinder ($\Delta Q_{M,max}$), which equals 722 $^{L}/_{min}$, thus given Equation (A.2).

$$\begin{aligned} \dot{p}_{H,max} &= \frac{\beta}{V_{pipe}}\Big(Q_P - (Q_P - \Delta Q_{M,max})\Big) \\ &= \frac{16000\,bar}{125\,L}\Big(\frac{722}{60000}\Big) \approx 1500 \cdot {}^{bar}/_{s} \end{aligned} \tag{A.2}$$

Where it has been assumed, that no leakage between the two manifolds exist. The leakage would add additional damping, however, due to the use of digital on/off seat valves, it is considered to be negligible.

The motor shaft acceleration is, similar to the rotor, found by considering a no load condition. Neglecting the viscous damping in the motor shaft, the maximum gradient is

given by Equation (A.3).

$$\begin{aligned}\dot{\omega}_{M,max} &= \frac{1}{J_g}\left(T_{M,max} - T_G - B_v\omega_M\right) \\ &= \frac{1}{231.3}\left(\overline{V}_M\,\Delta p\,\underbrace{\alpha_M}_{=1}\,\eta_M\right) = 1407.6^{RPM/s}\end{aligned} \tag{A.3}$$

Where η_M is the hydro-mechanical efficiency of 0.95.

A.2 DD pump

This section covers the validation of the lookup table for the DD pump, where the lookup table is compared to the dynamical model at the same time step of 0.1 μs. The lookup table is tested for one full pumping stroke, where the most dynamics is expected, hence the idling stroke is not considered. Given the gradients determined in the previous section, the corresponding results are presented in Figure A.1 and A.2, where the Root Mean Square (RMS) error is calculated for each gradient.

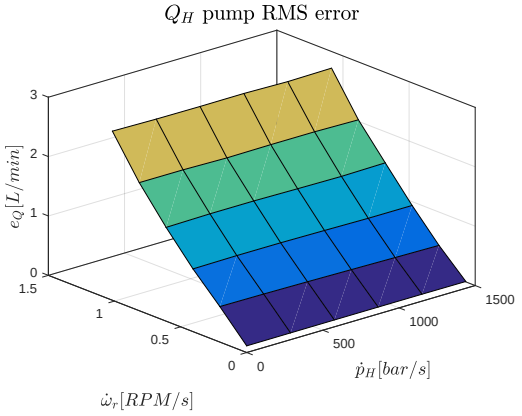

Figure A.1: Error plot of the pump flow for one chamber.

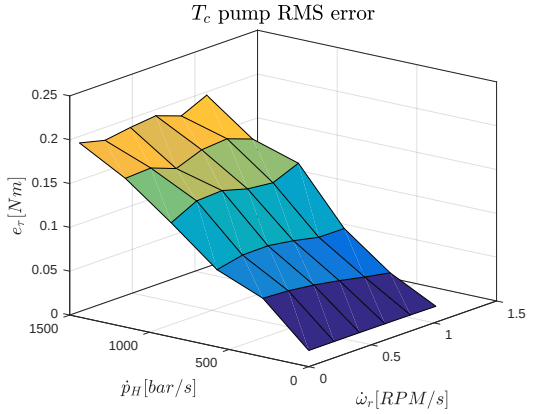

Figure A.2: Error plot of the pump torque for one chamber.

In Figure A.1 it is seen that the RMS error is increasing for an increasing acceleration, which also is expected since ω_r determines the compression rate of the chamber volume. A small RMS error at zero gradient is observed, which is due to a small flow spike for a very short time period in the lookup table flow, in the end of the pump flow, hence $Q_H \approx 0$. This error is, however, not considered to be significant due to the relatively low value. Any change in the pressure gradient does not affect the error of the lookup table significantly. This is due to the high resolution of the pressure breakpoint, a step of 2 bar is chosen. This is chosen since the initial step of 10 bar showed poor accuracy. Considering the maximum possible RMS error, it is seen to be 3 $^{L}/_{min}$ which at gives a maximum relative error of 1 %.

Considering the torque in Figure A.2 the RMS error is seen to increase with increasing pressure gradient, which also is expected. Since Deviations in the error dependent on the

pressure gradient are observed however the maximum RMS error is 0.2 Nm corresponding to a maximum RMS error of 0.005 %

Based on these results the lookup table model is considered sufficient for describing the original response of the pump flow and pump torque.

A.3 DD motor

This section covers the validation of the lookup table for the DD motor and is tested for one motoring stroke. The corresponding results are presented in Figure A.3 and A.4, where the Root Mean Square (RMS) error is calculated for each gradient.

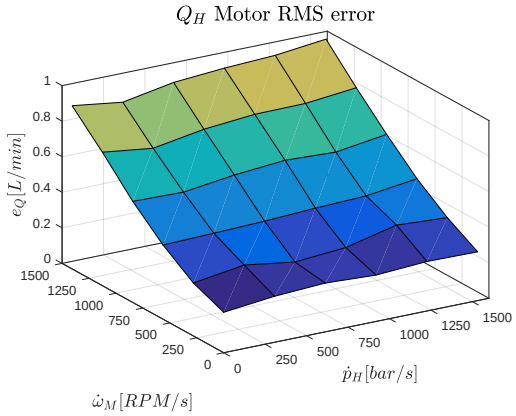

Figure A.3: RMS Error plot of the motor flow for one chamber.

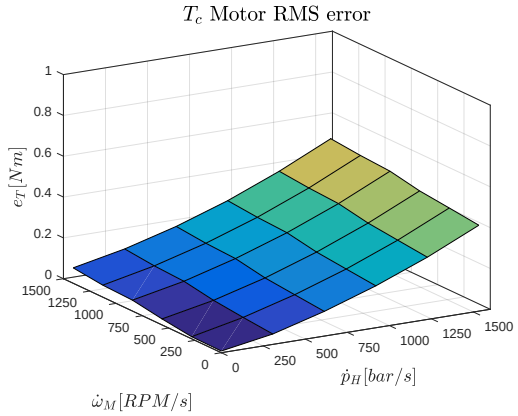

Figure A.4: RMS Error plot of the motor torque for one chamber.

In Figure A.3 it is seen that the error is increasing for increasing rotor acceleration, which also is expected since ω_M determines the compression rate of the chamber volume. A zero deviation at zero gradient could have been expected, however, this is due some inaccuracy around zero flow at the end of the motor cycle at, which is considered to be insignificant. The deviation can be reduced by increasing the number of motor speed breakpoints of the lookup table, however, a breakpoint step of 5 RPM is considered adequately. Any change in the pressure gradient does not affect the error of the lookup table significantly. Considering the maximum possible RMS error it is seen to be 1 $^{L}/_{min}$ which is found to give a maximum relative error of 0.25 %.

Considering the torque in Figure A.4 the RMS error is seen to increase with increasing pressure gradient, which also is expected. However, the maximum error is seen to be 0.55 Nm corresponding to a relative error of 0.05 % and is thus considered to be insignificant.

Based on these results the lookup table model is considered sufficient for describing the original response of the motor flow and motor torque.

A.4 Lookup Table Simulation Time Step

In this section the accuracy of the lookup table is investigated based on the time step of the simulation. The aim is to overcome the problem of comprehensive computational time hence the largest time step possible is desirable. A time step equal to $10^{-7}s$ was in the previous section found to be sufficiently accurate and thus becomes the reference when evaluating the precision.

In Figure A.5 a zoom plot of the lookup flows Q_H for both the DD pump and DD motor are shown. The zoom plots are based on time periods, where the largest gradients occur. The largest gradient for the pump flow is when the HPV is passively opened and for the motor at the backflow when the HPV is opened.

The flows are simulated for time steps in the span $[10^{-7}, ..., 10^{-4}]s$ with the same input signal sequence given for the previous sections.

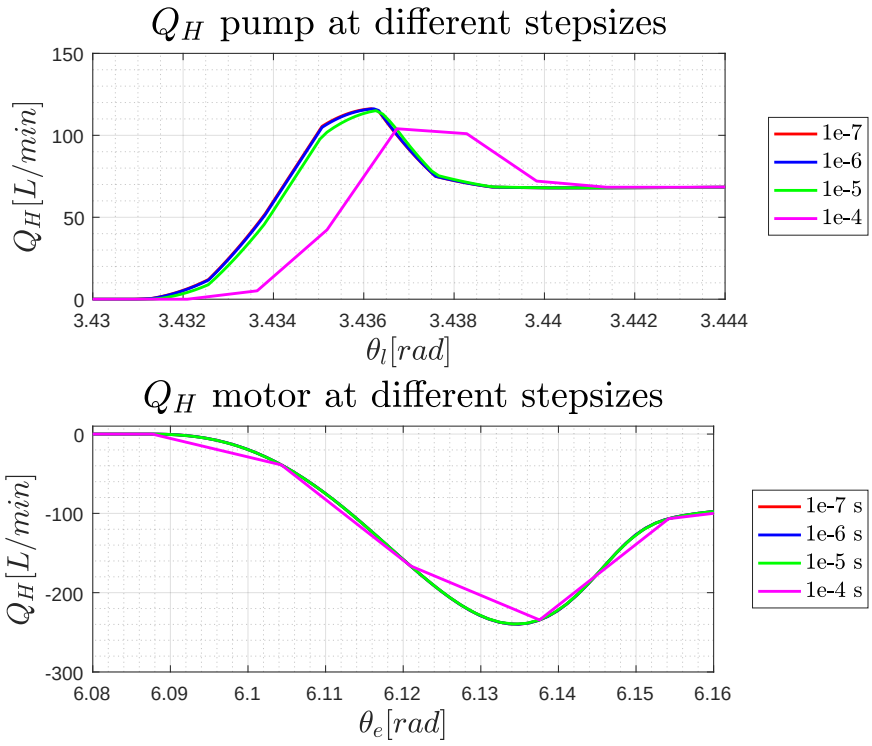

Figure A.5: Lookup table flow Q_H for both DD pump and DD motor at different time steps.

The precision of the simulation is seen to be insufficient for time step equal to $10^{-4}s$, thus a simulation of at least $10^{-5}s$ must be used in order to achieve acceptable simulation precision.

Hence the computational time of a single chamber simulation for the pump can be reduced from 30 seconds to 5 seconds. This can be even further reduced, when considering the combined model of 100 cylinders in the pump and 42 cyinders in the motor. If a dynamic model of each cylinder should be included, the computational time would be heavy which both requires heave hardware and long simulation times.

APPENDIX B

Mechanical Stress Evaluation

This chapter aims to describe the evaluation tool used for calculation of the parameters used as mechanical requirement.

The approach for the development of this evaluation tool needs three areas to be considered and is divided into three sections:

- Analysis simplifications and assumptions
- Introduction to fatigue damage and mechanical stress
- Fatigue damage calculation utilising a 5 step procedure

First, the choice of analysis method is discussed and the applied simplifications and assumptions are presented. Then, general fatigue damage of materials is described, where general background theory for mechanical stress briefly is presented. Lastly, the approach for calculating the fatigue damage, used as evaluation tool for the mechanical loading on the wind turbine structure, is presented in a five step procedure.

B.1 Analysis Simplifications and Assumptions

Several theories for mechanical stress calculations exist, which is why an appropriate analysis method must be chosen. Two different approaches exist which is the simple *Mechanics of materials* and more mathematically comprehensive *Theory of elasticity*. It is decided to utilise *Mechanics of materials* approach due to its simplicity which focuses on approximate solutions to practical problems [Ansel and Saul, 2003, p. 1]. This is considered sufficient for the analysis in this project, since the aim is to develop a tool for comparison of two systems and not used for structural design of the mechanical components. Thus, the main literature used throughout this chapter is [Ansel and Saul, 2003].

Since the approach for evaluating the loading on the shafts may become a tedious process, it is chosen to simplify the analysis. The assumptions and simplification used for this fatigue damage evaluation is listed in the following.

- In order reduce the number of influences on the mechanical loading and thus focus on the impact on the discrete effects that occur from the DD machines, it is only chosen to investigate the operational loadings, which are associated with the loading caused by the random nature of wind profile and the effects from the transmission components. Thereby, the gravitational loads are not considered.
- The shafts is assumed to be prismatic, meaning that the cross section of the shafts are constant along the shaft. This means that engineering stress (rather than the more advanced true stress) analysis is utilised, such that changes of the cross sectional area of the shafts are neglected.
- The shafts are homogeneous such that the matter of the material is uniformly distributed over its volume thereby the material has the same elastic properties at any point in the material [Ansel and Saul, 2003, p. 1+146]
- Material is isotropic meaning it has the same properties in all directions.
- The material of the shafts are chosen to be high-strength steel (ASTM-A242) since

data sheet values is available [Ansel and Saul, 2003, p. 524].
- Thermal effects e.g. the temperature of the body are neglected.
- The environmental effects such as air humidity and corrosion is not considered.
- Superposition of the different loads are utilised, such that Equation (B.3) can be utilised as only one load are producing the stresses [Ansel and Saul, 2003, p. 12].
- blades and hub to be a rigid body, thus the interaction from the blades and hub does not alter the analysis at the rotor and generator shaft.
- Fatigue damage contributions is assumed to be independent of where it occurs in the loading history, which is assumed in the widely used Palmgren-Miner's theory.

With the chosen analysis method and applied simplifications, the uncertainties and inadequacies must be accounted for if the structural design were to be considered. Hereby safety factors should be included. Since the aim is to derive an evaluation tool for comparing two systems, the applied simplifications and chosen analysis method is considered adequately for the purpose of this study.

B.2 Introduction to Fatigue Damage and Mechanical Stress

The fatigue life of a given material is defined as the number of repetitive stress cycles before it fails. The fatigue life are generally found from experimental measurements, where the number of cycles, N, required to break the material at fluctuating stress levels, S, are measured. This relation can be established in a SN-curve (also known as a Wöhler curve) for steel illustrated in Figure B.1 [Ansel and Saul, 2003, p. 150]. The point (N_f,σ_f) indicates the point where the steel fails. The point (N_{en},σ_{en}) is the

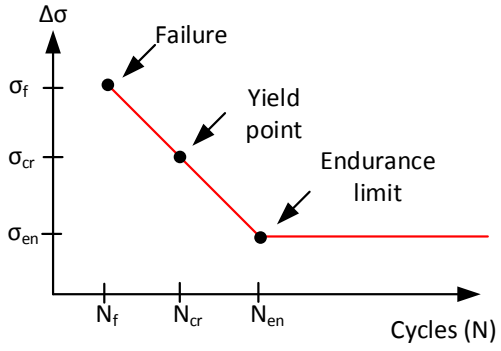

Figure B.1: Typical SN-curve for steel.

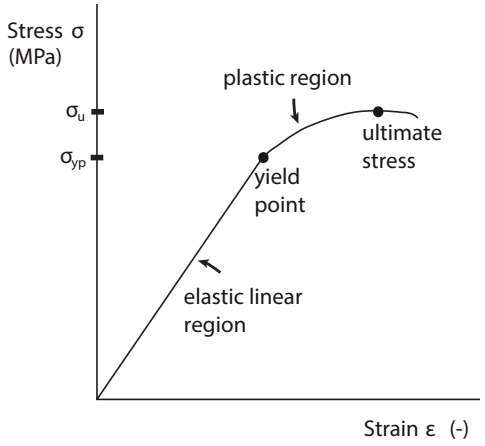

Figure B.2: General stress-strain relation of the material.

endurance limit, where no failure will occur. The stress level σ_{cr} is the fatigue strength and denotes the complete stress reversal, which is equal to the yield point in Figure B.2. This point indicates, whether a material will stay deformed after the stress loading has been removed [Ansel and Saul, 2003, p. 63]. If the material is able to stay in its original structural formation it is in the linear elastic region as indicated in Figure B.2. If it is not, it is in the plastic region, where the material is permanently deformed. With the approach of *Mechanics of materials*, the strain ϵ, which concerns the deflection of

the material, is not considered and thus only the stress is investigated. Lastly, when referring to Figure B.2, σ_u is the ultimate tensile strength which indicates a decreased load carrying capability.

As indicated from Figure B.1 and Figure B.2 the stress level is used as a measure to determine the fatigue life of a material. Hence the definition of stress is needed, which is carried out in the following.

Introduction to Stress

This subsection will briefly describe the theory for mechanical stress following the approach of *Mechanics of materials*.

The analysis of the fatigue damage on the mechanical structure is concerned with the internal forces working on the material. The internal forces are related to the atomic level and are the forces that hold together the particles, which are the structure of the material [Ansel and Saul, 2003, p. 1]. Thus in this section, a general description of the internal forces will be investigated when external forces are applied to the structural member to give the reader a briefly understanding of mechanical stress.

In order to investigate the internal forces, a general description is considered, where a structural member in equilibrium is illustrated in Figure B.3. The figure shows a body under the action of external forces $\vec{F}_{ext}$, which results in a reaction of internal forces, $\vec{F}_{in}$, indicated at the random plane cut between the two parts.

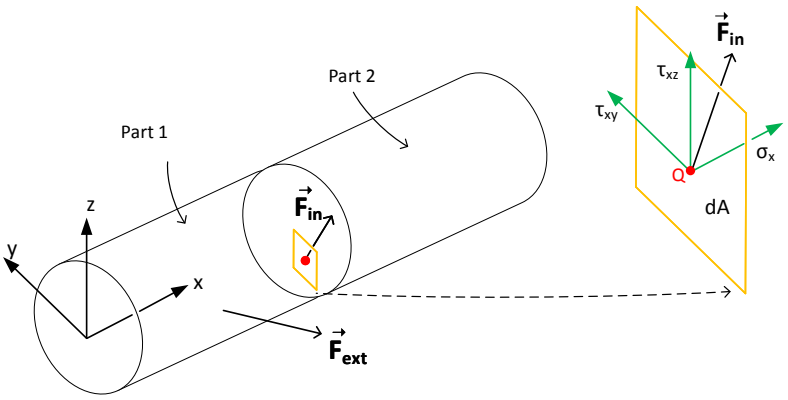

Figure B.3: General drawing a cylindrical shaft which could represent the rotor and generator shaft.

Since the forces acting on the entire structural member (both parts) are in equilibrium, the forces acting on part one must be in equilibrium as well. This requires a reaction of internal forces, which are represented as the internal force $\vec{F}_{in}$ in Figure B.3.

To the right in Figure B.3 a zoom plot of an element area dA located at point Q of the cut plane is illustrated. Decomposing $\vec{F}_{in}$ into components, the normal stress σ and shear stress τ are defined and are the intensity of the internal forces, i.e. how the forces are distributed throughout the material. The normal stress is perpendicular to the cut plane surface and the shear stress is parallel to to the cut plane surface.

The components of $\vec{F}_{in}$ are given in Equation (B.1).

$$\sigma_x = \frac{d\,F_{in,x}}{d\,A}, \qquad \tau_{xy} = \tau_{yx} = \frac{d\,F_{in,y}}{d\,A}, \qquad \tau_{xz} = \tau_{zx} = \frac{d\,F_{in,z}}{d\,A}, \tag{B.1}$$

Equation (B.1) is based on assuming, that the area dA is large compared to the inter-atomic distance in the body, but small compared to the area of the investigated body. This assumption leads to an average stress on the area dA, which is considered adequately for engineering purposes [Ansel and Saul, 2003, p. 5].

The equality of shear stresses in Equation (B.1) is found by considering the rotational equilibrium of the three dimensional infinitesimal cube in Figure B.2. Since the matter of the material is fixed, the infinitesimal cube will be in rotational equilibrium, hence the shearing stresses on mutually perpendicular planes will be equal, e.g. τ_{zx}=τ_{xz}. Utilising this conditions, the three dimensional stress tensor can be established as in Figure B.5.

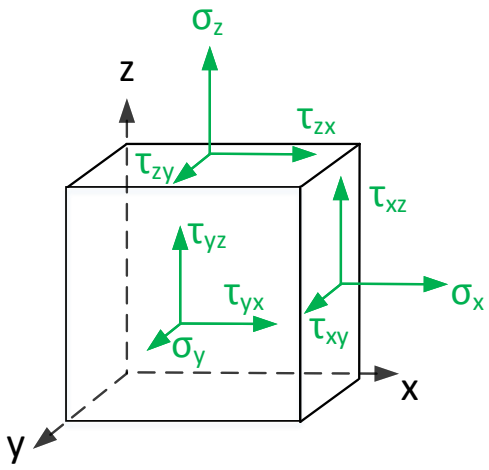

Figure B.4: Infinitesimal cube representing the matter of the investigated material. It shows the three dimensional stresses.

$$\sigma = \begin{bmatrix} \sigma_x & \tau_{xy} & \tau_{xz} \\ \tau_{xy} & \sigma_y & \tau_{yz} \\ \tau_{xz} & \tau_{yz} & \sigma_z \end{bmatrix} \tag{B.2}$$

Figure B.5: Three dimensional stress tensor.

Lastly, the sign convention of the stresses is that when the normal stress points outward on the cut plane, both the normal and shear stress acts in a positive direction with respect to the coordinate system. Thus, the stresses illustrated in Figure B.4 are all positive.

B.3 Fatigue Damage Calculation Utilising a 5 Step Procedure

In Niesłony [2009] a method for determination of fatigue life damage in the case of multi-axial loading is presented. A similar method is presented in Melters [2017], which in addition has developed an open-source software tool named *FATLAB* which incorporates the use Finite Element Model (FEM) to determination of fatigue damage estimation. However, such a detailed model requires a Computer Aided Drawing (CAD) model of

the shafts, which are not available to the authors and is considered out of scope of this project.

With inspiration from Niesłony [2009] and Melters [2017], the fatigue life estimation at the shafts considered for this project is carried out in five steps, which is illustrated in B.6. In step 1 the multi-axial stress tensor components are found from simulation

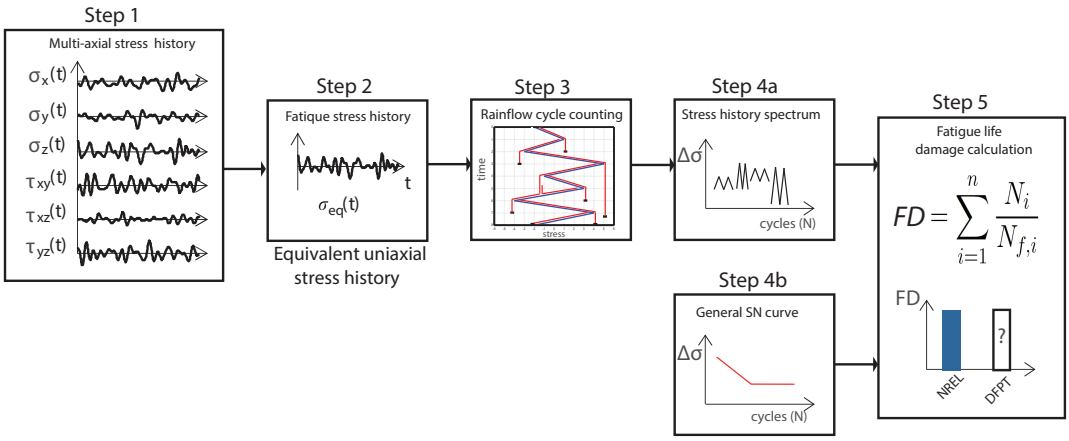

Figure B.6: Procedure for fatigue damage calculation. Inspired by Niesłony [2009] and [Melters, 2017].

data from the FAST tool. Since fatigue life calculation under multi-axial stress states requires reduction to uniaxial stress state, a proper failure criterion is chosen in order to proceed to step 2. Having obtained the uniaxial stress equivalent history, it allows for stress cycle counting which is achieved in step 3. The cycle counting counts the number of cycles at specific stress levels, thus enabling for achieve the stress spectrum in step 4a. The stress spectrum thus results in the symbol N_i in step 5, where i denotes the associated stress level. In step 4b the general material properties for the chosen material is utilised to determine the number of cycles to failure ($N_{f,i}$ in step 5) under simple tension experimental measurements for the specified material. In step 5 the total fatigue damage, D, is found as a result of particular damage contributions from the i-th stress level.

In the following the five steps will be presented and elaborated.

B.3.1 Step 1: Obtain Stress Resultants

The multiaxial stress components are calculated with the basis in the available simulation data from FAST. The data is available at the main bearing, where the main bearing is illustrated in a 2-D conceptual drawing in Figure B.8. The available data from FAST is illustrated in Figure B.7.
A definition of the available data is given as:

- F_x: Axial loading, which is the thrust on the shaft and tends to compress (shorten) or stretch(lengthen) the shaft in the longitudinal direction.
- T_r: Torque, applied at the shaft and sets the shaft in rotational motion.
- M_y: Bending moment about the y-axis, which causes the shaft to bend in the z-axis direction.

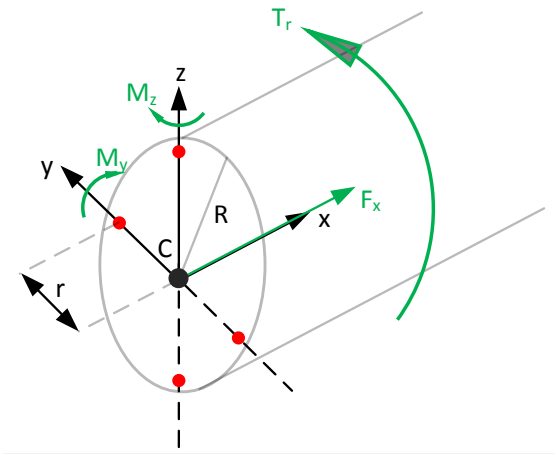

Figure B.7: Shows a cylindrical shaft with coordinate system and the available data measurements from FAST. The four red dots are the points chosen for the stress analysis, which are needed later in the analysis.

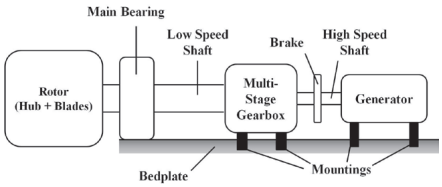

Figure B.8: Sketch of the different components related to stress analysis [Singh et al., 2014, p.64].

- M_z: Bending moment about the z-axis, which causes the shaft to bend in the y-axis direction.

Utilising the method of *Mechanics of materials* the elementary formulas for finding the relation between the internal-force resultants and the stresses are given as in Equation (B.3) [Ansel and Saul, 2003, p. 11].

$$\underbrace{\text{Axial: } \sigma = \frac{F}{A} \qquad \text{Bending: } \sigma = \frac{Mr}{J}}_{\text{Normal stress}} \qquad \underbrace{\text{Torsion: } \tau = \frac{Tr}{J_p}}_{\text{Shear stress}} \tag{B.3}$$

Where F is the applied load force, A is the cross sectional area of the shaft, r is the radius from origo to the investigated point, J is the moment of inertia about the neutral axis, i.e. a relative measure of how the area is distributed about the neutral axis. J_p is the polar moment of inertia of the cross sectional area A with respect to an axis through the origo C. The calculation of the inertias are given in Equation (B.4) through (B.6).

$$J_y = \int_A r_z^2 dA = \frac{\pi}{4} r_z^4 \tag{B.4}$$

$$J_z = \int_A r_y^2 dA = \frac{\pi}{4} r_y^4 \tag{B.5}$$

$$J_p = J_y + J_z = \frac{\pi}{2} r^4 \tag{B.6}$$

Where r_y=r_z=r since the four points are placed with equally distance from the origo C.

Elaborating on the formulas in Equation (B.3), it is seen the maximum stress contribution will occur at the surface of the shaft since r $\approx$ R, which is why the stress analysis will be based at the surface of the shaft as indicated by the four red dots in Figure B.7.

The following description is based on point (0,y,0) in Figure B.7, since the same method applies for all four points, however with different signs of the stresses. In the comparison, the point (0,y,0) will thus be in focus. Since it is assumed that the matter is uniformly distributed within the material, the stress analysis can be simplified to consider only one point in which three perpendicular planes goes through [Ansel and Saul, 2003, p. 5].

The plane perpendicular to the x-axis is denoted as face x and is illustrated in Figure B.9, showing the stress acting on face x and similar definition exist for face y and face z. The three perpendicular planes, all passing through the point (Q), are illustrated in Figure B.9, which is the basis for the derivation of the stress resultants.

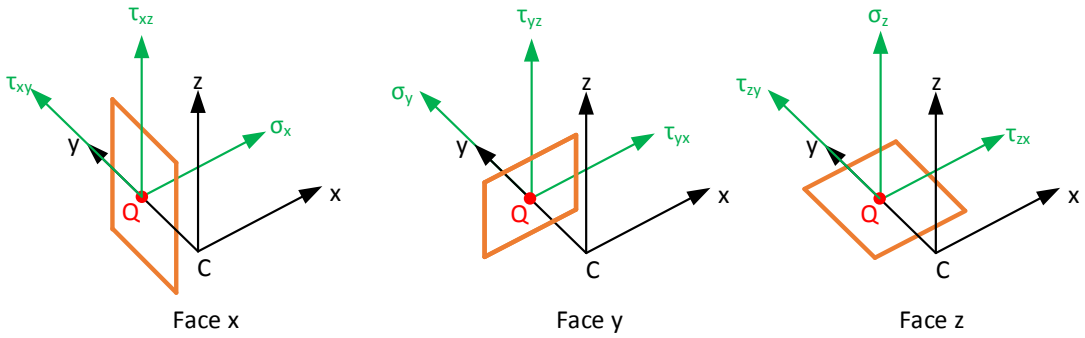

Figure B.9: Three perpendicular planes through one of four investigated points.

Following the theory of *Mechanics of materials* and since the shaft are subjected to axial load in the x-direction, the normal and shear stresses experienced at face x are numerically much larger than the stresses in the y-and z direction. As a consequence of this, the 3-D stress tensor at the point (Q) can be written as in Equation (B.7).

$$\sigma = \begin{bmatrix} \sigma_x & \tau_{xy} & \tau_{xz} \\ \tau_{xy} & 0 & 0 \\ \tau_{xz} & 0 & 0 \end{bmatrix} \tag{B.7}$$

Hence, the derivation of the stress resultants will be conducted only in on face x, which is carried out in the following.

The stresses acting on face x are calculated with the use of the formulas in Equation (B.3) and are given in Equation (B.8).

$$\begin{aligned} \sigma_x &= \frac{F_x}{A} + \frac{M_z r_y}{J_z} \\ \tau_{xy} &= \frac{T_r r_y}{J_p} = \tau_{yx} \\ \tau_{xz} &= \frac{T_r r_z}{J_p} = \tau_{zx} \end{aligned} \tag{B.8}$$

In Equation B.8 the principle of superposition is utilised, since both axial loading and bending moments contributes to the normal stress. The principle of superposition allows for calculation of simultaneous loadings and then combining the individual contributions, which is valid when the material is linear elastic, which is true as long as the material not has failed.

The obtained three independent stress components follows from multi-axial stress. However, to predict the fatigue damage and fatigue life it is chosen to utilise cycle counting method, which is why the multi-axial loading must be corrected to an equivalent stress loading [Bathias and Pineau, 2009, p. 37].

B.3.2 Step 2: Calculate Equivalent Stress

In order to calculate the fatigue stress an equivalent/effective stress is used. To be able to obtain that, a definition of the material failure is needed. For this study, it chosen to use the *failure by yielding* definition, i.e. the material is said to have failed when the stress level exceeds the yielding point.

A widely accepted theory for predicting the inelastic behaviour of the material utilised in this analysis exist, which is Von-Mises theory, also known as the maximum distortion energy theory [Ansel and Saul, 2003, p. 154]. The Von-Mises theory states, that failure occur when the distortion energy per unit volume (at any point in the material) becomes equal to that observed in a simple tension test.

The Von-Mises equivalent stress is found by Equation (B.9).

$$\sigma_{vm} = \sqrt{\frac{1}{2}\left((\sigma_x - \sigma_y)^2 + (\sigma_y - \sigma_z)^2 + (\sigma_z - \sigma_x)^2 + 6(\tau_{xy}^2 + \tau_{xz}^2 + \tau_{yz}^2)\right)} \tag{B.9}$$

It is seen that it is the differences between the normal stresses that defines the equivalent stress, thus increasing each stress with an equal amount does not affect whether the material will obtain failure by yielding or not.

It follows from Equation (B.9) that only equivalent tensile stresses are obtained due to the positive sign. To correct for this, and hereby being able to obtain compressive stresses, a sign function is utilised which is given in Equation (B.10) Melters [2017].

$$\sigma_{eq} = \sigma_{vm} sign \underbrace{(\sigma_x + \sigma_y + \sigma_z)}_{I_1} \tag{B.10}$$

Where I_1 is an invariant coefficient of the 3-D stress tensor, which is independent of the coordinate system x,y,z, hence the sign is determined from the actual multi-axial normal stresses. The derivation of this is a comprehensive process and it is therefore referred to the literature [Ansel and Saul, 2003, p. 29-32].

The equivalent time history is illustrated in Figure B.10. As seen in the figure, the equivalent stress is of compressional nature, which would have been of tensional stresses without the sign function.

In order to calculate the fatigue damage from the equivalent stress history, the load cycles of σ_{eq} must be distinguished. The load stress cycles are found using a cycle counting method, where it is chosen to utilise a common method named rain flow counting.

B.3.3 Step 3: Rainflow Cycle Couting

A common cycle counting method is the rainflow counting, which identifies the mean stress value and amplitude of each load cycle, hereby obtaining distinguished load cycles.

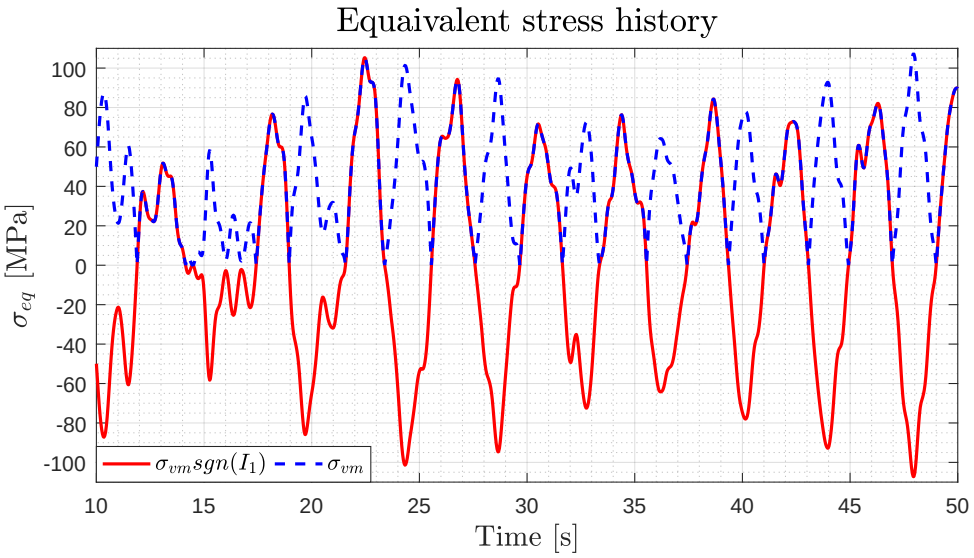

Figure B.10: Equivalent stress with and without sign function.

The identification of the load cycles is illustrated in Figure B.11, where a random sequence of the equivalent stress history is shown. The stress time history is rotated 90° clockwise such that the figure can be read from top-to-bottom, just like following rain flowing downwards, as indicated by the blue lines. In the following, a reader's guide is presented to be able to describe the rain flow counting method. The rain flow counting method is described by starting with Figure B.11, where the results are listed in Table B.1. Lastly, the table data can graphically presented in Figure B.12.

Figure B.11

First, the turning points (red circles) of the stress history is located and denoted with letters. Then, the turning points are combined (black dotted lines) which leads to different stress cycle paths, e.g. point B-E. Starting from point B, the "water" flow downwards to point C, then falls down onto path D-E, which ends the rain flow cycle. Since $\sigma_B \neq \sigma_E$, i.e. the end stress value is different from the initial stress value, the cycle is denoted as a half cycle. Thus, path B-E is a defined load cycle with mean value $\sigma_m = \frac{\sigma_B + \sigma_E}{2}$ and amplitude $\sigma_a = \frac{\sigma_B - \sigma_E}{2}$. These values can then be listed in Table B.1.

A full cycle is identified in G-H and J-K. The path of J-K itself is a half cycle, however, the path of K-L is overlapped from path I-L. The K-L contribution, which is indicated by magenta in the figure, adds a half cycle equal to J-K, hereby obtaining a full cycle. Similar case is encountered for the path G-H, where the H-I contribution results in the full cycle.

The path of C-D is a special case since it obtains the D-E contribution and thus counts as a half cycle. Lastly, it should be noted that the cycle counts of A-B and G-H does not affect the path C-F and I-L respectively.

Table B.1 and **Figure B.12**

Identifying all the load cycles from Figure B.11, the results are shown in Table B.1 where the path and type of cycle are listed along with the corresponding mean stress value and amplitude. All these load cycles can be represented as number of cycles at a specific mean stress level and amplitude in a 3-D bar plot shown in Figure B.12. Full cycles count as 1 and is illustrated as yellow bars in Figure B.12,

where the half cycles are illustrated by blue bars. It should be noted, that the rain flow counting algorithm adds the two half cycles CD and DE since these are approximately equal in mean value and amplitude.

Path	Cycle	Mean	Amp.
A-B	1/2	58.4	3.2
B-E	1/2	-19.8	81.5
C-D	1/2	-79.3	12.3
C-F	1/2	8.1	99.6
D-E	1/2	-84.2	17.1
E-F	Adds 1/2 cycle to D-E		
F-I	1/2	10.2	97.5
G-H	1	16.0	2.6
H-I	Adds 1/2 cycle to G-H		
I-L	1/2	-24.9	62.3
J-K	1	-40.1	19.7
K-L	Adds 1/2 cycle to J-K		
L-M	1/2	29.8	7.7

Table B.1: Rainflow stress cycles. Units in MPa.

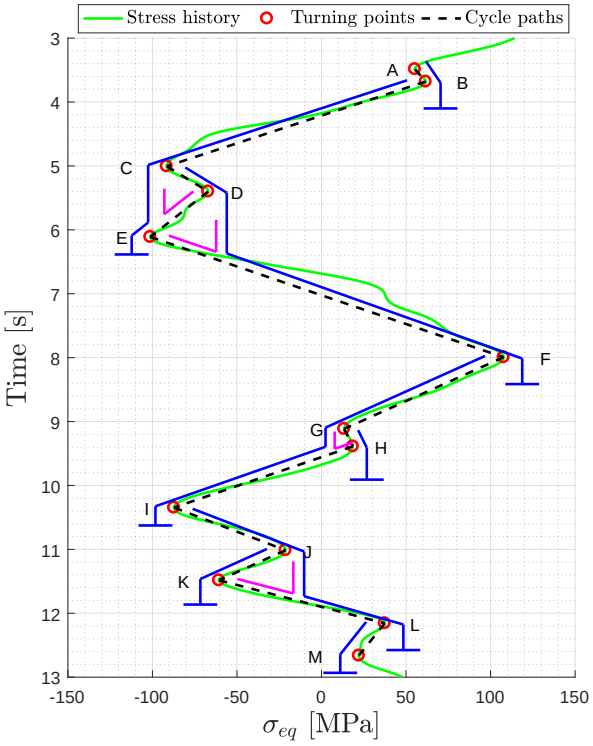

Figure B.11: Rain flow counting of time stress history.

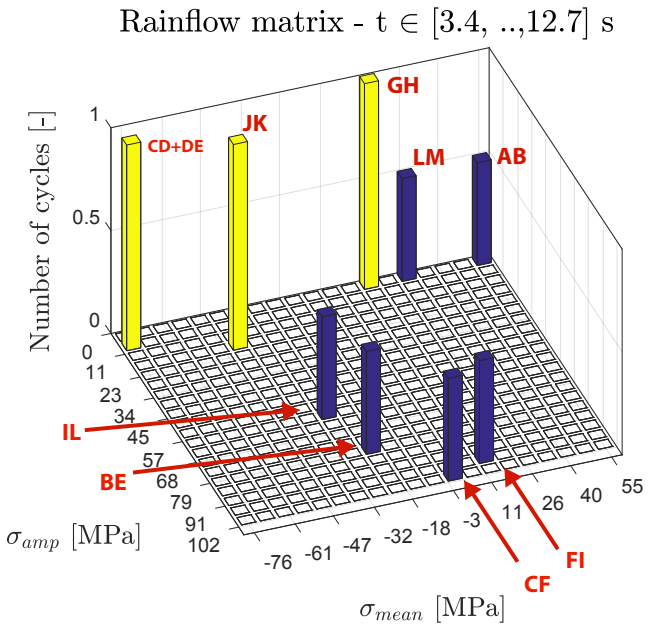

Figure B.12: Rain flow counting matrix showing the number of cycles at different mean and amplitude stress levels.

Having obtained the number of cycles at different mean and amplitude levels, it is possible to proceed to the next step, where the stress levels are grouped hereby obtaining the stress spectrum of the loading history.

B.3.4 Step 4: Stress Spectrum

In this step the loading data are rearranged in a 2-D plot, where the mean and amplitude levels are grouped with the corresponding number of cycles. The stress spectrum of the loading data will consist of two parts. The first part (Step 4a) is based on the simulated time stress history found through step 1-3. The second part (Step 4b) is obtained based on general material properties in order to obtain the strength of the material.

Step 4a: Simulated Load History

The data presented in the rain flow matrix is rearranged into a 2-D plot where the x-axis is the number of cycles N_i at a specific mean level and amplitude indicated by $\Delta\sigma$ in Figure B.13 .

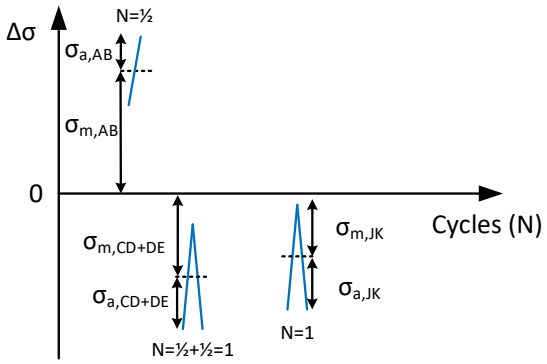

Figure B.13: Stress spectrum of load history, where n is the number distinguished stress levels.

As indicated in Figure B.13 the load cycles have been distinguished, thus the stress history is known and can then be compared to general material properties under the same load cycles at simple experimental tension test. This is obtained in the following step.

Step 4b: General Material Properties

Having obtained the time loading history, it is needed to know the strength of the material, which is generally obtained based on experimental fatigue tests [Ansel and Saul, 2003, p. 150]. The testing is conducted in simple tension test, where the material is subjected to fluctuating loadings at different mean stress levels and amplitudes.

Several approaches exist for interpreting fatigue data, where the relation of mean stress-alternating stress relations with respect to fatigue life of a material established. For this study the modified Goodman relation is chosen, since it has experimental support and is shown to give a precise prediction of fatigue failure [Ansel and Saul, 2003, p. 167].

The modified Goodman fatigue criterion is given in Equation (B.11).

$$\frac{\sigma_{ea}}{\sigma_{cr}} + \frac{|\sigma_{em}|}{\sigma_u} = 1 \tag{B.11}$$

$$\sigma_{ea} = \sigma_{cr}\left(1 - \frac{|\sigma_{em}|}{\sigma_u}\right) \tag{B.12}$$

Where $|\sigma_{em}|$ is the mean stress effect and given in absolute value since both tension and compression stress are considered, σ_{ea} is the alternating stress level, σ_{cr} is the complete reversal stress which identifies the stress level at which the material becomes in-elastic. Consequently, σ_{cr} is equal the yield point stress σ_{yp} (recall Figure B.2). σ_u is the ultimate tensile strength.

Equation (B.11) indicates the allowable level of the mean stress and amplitude before the material fails. This may be graphically explained by isolating for σ_{ea}, thus establishing the upper limit between the allowable mean stress and amplitude before the material fails, which is illustrated by the red line in Figure B.14. It is chosen to utilise the mean

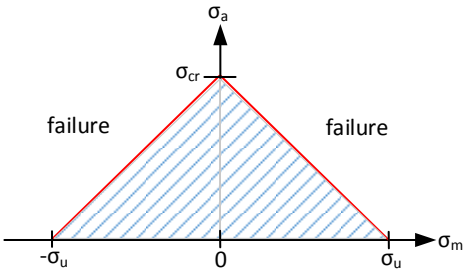

Figure B.14: Modified Goodman relation. The hatched area indicates that the material is safe.

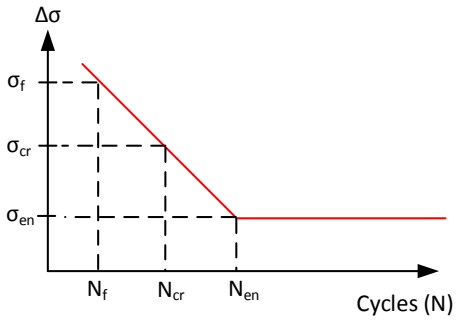

Figure B.15: General SN-curve for steel, which is needed for calculation of the fatigue life of the material.

and amplitude levels of the stress found in step 3, such that the general loading case is tested with the same stress levels. By doing this, the complete reversal stress σ_{cr} is the only unknown in Equation (B.11) since σ_u is known from data sheets. σ_{cr} is needed in order to estimate the fatigue life.

The fatigue life N_{cr} is indicated in the SN-curve in Figure B.15 and can be described by Equation (B.13) [Ansel and Saul, 2003, p. 170].

$$N_{cr} = N_f\left(\frac{\sigma_{cr}}{\sigma_f}\right)^{\frac{1}{b}}, \quad b = \frac{ln(\sigma_f/\sigma_{en})}{ln(N_f/N_{en})} \tag{B.13}$$

Where N_f is the number of cycles to failure at a corresponding failure stress level σ_f and b is the slope of the SN-curve, which is found from data sheet values for the high

σ_u	σ_f	N_f	σ_{en}	N_{en}
400	$0.9\sigma_u$	10^3	$0.5K\sigma_u$	10^6

Table B.2: Data sheet values for high strength steel utilised in this analysis [Ansel and Saul, 2003, p. 170,524]. Stress units in MPa.

strength steel [Ansel and Saul, 2003, p. 524]. The end points of the SN-curve (σ_f,N_f) and (σ_{en},N_{en}) is provided in Table B.2.

Where K is a fatigue-strength reduction factor typically found from experiments or finite-element analysis, where K should be chosen to K $>$ 0.3. For this study, it is chosen to use K=1, since neither of aforementioned methods are available to the authors, and is considered sufficient to give an indication of the fatigue life. Due to the definition of failure criterion in step 2, the number of cycles N_{cr} of complete reversible stress becomes the threshold at which the load history from step 4a is compared to. This is discussed in the following and final step, where the fatigue damage calculation is conducted.

B.3.5 Step 5: Damage Calculation and Fatigue Life

In order to calculate the fatigue damage contribution from each stress cycle, the assumption of linear damage accumulation is used. Hereby the widely used Palmgren-Miner linear damage hypothesis can be utilised and is given in Equation B.14.

$$FD = \sum_{i=1}^{n} \frac{N_i}{N_{cr,i}}, \qquad 0 \leq FD \leq FD_{crit} \tag{B.14}$$

Where D_{crit} is the critical damage, which defines failure of the material of macroscopic crack initiation. A critical damage of 1 the failure limit [Bathias and Pineau, 2009, p. 37+50].

Utilising Palmgren-Miner's rule, it is assumed that the total damage D of the loaded component can be found as a sum of each group stress N_i contribution at the $i-$th stress level found in step 4a and the corresponding fatigue life $N_{cr,i}$ found in step 4b.

Although the Palmgren-Miner hypothesis is commonly used by engineers, it has some limitations. The cycles lead to the same damage contribution regardless of time in the loading sequence. Fatigue crack propagations may be influenced by the time loading history, thus this effect it is not encountered in this method. However, for this study a failure-by-yielding criterion is chosen which is not considered to affect the choice of this method.

B.3.6 Verification of Method

Since no experimental test setup is available, the utilisation of the five step fatigue damage algorithm is verified by comparison of two loading histories. In the first loading history the NREL model is simulated with the FAST tool over 700 s. The second load history is found by low pass filtering the loading signals such as the torques, bendings moments and rotor thrust.

The resulting equivalent stress history is presented in Figure B.16 showing a 20 second period and in Figure B.17 a zoom plot is shown. It can be seen that the ripples and thus

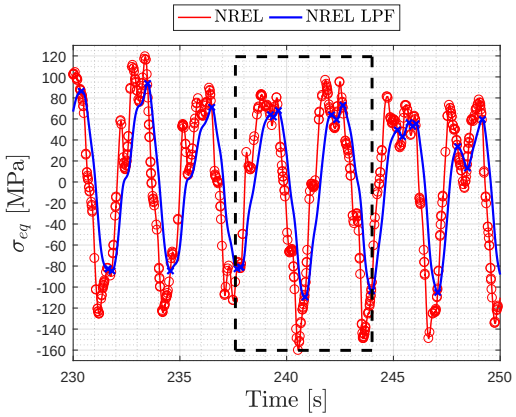

Figure B.16: Comparison of two Von-Mises equivalent stress time histories.

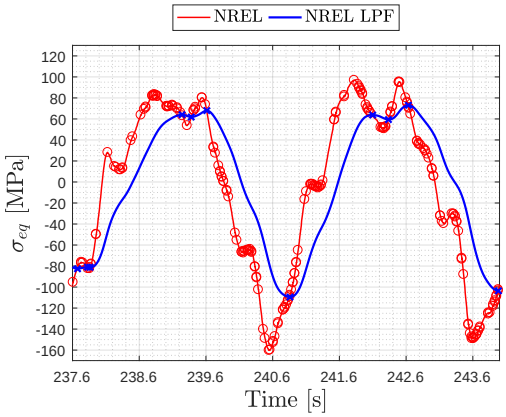

Figure B.17: Zoom plot of two Von-Mises equivalent stress time histories.

stress cycles are significantly reduced. Therefore the low pass filtered loading history.

Performing the cycle counting method presented in Step 3, the rain flow matrix for both time loading histories is presented in Figure B.18 and B.19. Conducting step 4 in order

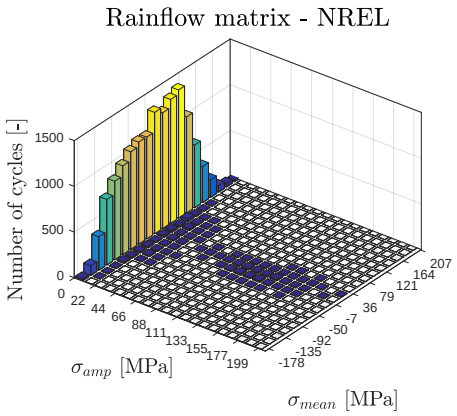

Figure B.18: Rain flow matrix over 700 seconds for NREL simulation data.

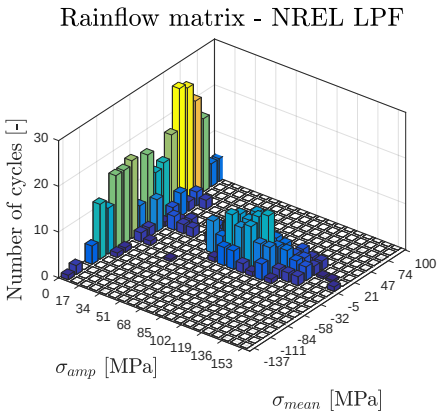

Figure B.19: Rain flow matrix over 700 seconds for low pass filtered NREL simulation data.

to find the stress spectrum of the loading histories based on the results from the rain flow counting and utilising Palmgren-Miner linear damage hypothesis, the total fatigue damage for both loading histories are obtained and presented in Table B.3. As seen the fatigue damage is lower for the low pass filtered loading history which also was expected based on the rain flow matrices in Figure B.18 and B.19. In the original loading history a large amounts of low amplitude cycle are seen in the order of 1000 cycles, whereas the low pass filtered loading history is in the order of 10 cycles and the amplitude range is reduced. However, a larger number of cycles at the amplitude range [70,..,140] MPa are

Load history	Damage [-]
NREL	$8.2 \cdot 10^{-10}$
NREL LPF	$6.2 \cdot 10^{-11}$

Table B.3: Total fatigue damage over a 700 second simulation.

experienced in the low pass filtered data (not seen in Figure B.18 due to the large axis scale), which also is observed from Figure B.17. Compared to the low amplitude cycles of the NREL data, this would result in an increase in fatigue damage contribution.

APPENDIX C

Accumulator Derivations

C.1 Derivative of Gas Chamber Volume

The derivative of the gas chamber volume will be obtained in this appendix.

The polytropic relation for the accumulator gas chamber is given by Equation (C.1).

$$p_g(t)V_g^{\kappa}(t) = p_{pr}V_{acc}^{\kappa} = \text{const.} \tag{C.1}$$

Setting the left side of Equation (C.1) equal to z in Equation (C.2) and differentiating with the chain rule given by Equation (C.3)

$$z = p_g(t)V_g^{\kappa}(t) \tag{C.2}$$

$$\frac{\mathrm{d}z}{\mathrm{d}t} = \frac{\partial z}{\partial p_g}\frac{\mathrm{d}p_g}{\mathrm{d}t} + \frac{\partial z}{\partial V_g}\frac{\mathrm{d}V_g}{\mathrm{d}t} \tag{C.3}$$

the following Equation (C.4) is obtained for the differentiated polytropic relation

$$\frac{\mathrm{d}z}{\mathrm{d}t} = V_g^{\kappa}\frac{\mathrm{d}p_g}{\mathrm{d}t} + \frac{\kappa p_g V_g^{\kappa}}{V_g}\frac{\mathrm{d}V_g}{\mathrm{d}t} \tag{C.4}$$

which can be stated as Equation (C.6) utilising the relation in Equation (C.5)

$$V_g^{\kappa-1} = \frac{V_g^{\kappa}}{V_g} \tag{C.5}$$

$$V_g^{\kappa}\dot{p}_g + \kappa p_g V_g^{\kappa-1}\dot{V}_g = 0 \tag{C.6}$$

Solving (C.6) for $\dot{V}_g$ the derivative of the gas volume is found as given by Equation (C.7).

$$\dot{V}_g = \frac{-1}{\kappa}\frac{V_g}{p_g}\dot{p}_g \tag{C.7}$$

C.2 Equivalent Continuity Equation

The full derivation of the equivalent continuity equation of the high pressure manifold with accumulator will be obtained in this appendix.

Having the negative change of the gas volume equivalent to the flow into the accumulator given by Equation (C.8).

$$\dot{V}_f = -\dot{V}_g \qquad\qquad \dot{V}_g = \frac{-1}{\kappa}\frac{V_g}{p_g}\dot{p}_g \tag{C.8}$$

Inserting (C.8) into the continuity equation below describing the high pressure manifold with accumulator the equivalent continuity equation can be formulated given by Equation (D.1).

The condition $p_g = p_H$ applies because the mass and friction of the piston in the accumulator is neglected.

$$
\begin{aligned}
&\dot{p_H} = \frac{\beta_e}{V_H}(Q_P - Q_M - \dot{V}_f - k_l \Delta p) \\
&\Downarrow \\
&\dot{p_H} = \frac{\beta_e}{V_H}(Q_P - Q_M + \dot{V}_g - k_l \Delta p) \\
&\Downarrow \\
&\dot{p_H} = \frac{\beta_e}{V_H}\left(Q_P - Q_M + \frac{-1}{\kappa}\frac{V_g}{p_H}\dot{p_H} - k_l \Delta p\right) \\
&\Updownarrow \\
&\left(1 + \frac{1}{\kappa}\frac{V_g}{p_H}\frac{\beta_e}{V_H}\right)\dot{p_H} = \frac{\beta_e}{V_H}(Q_P - Q_M - k_l \Delta p) \\
&\Updownarrow \\
&\dot{p_H} = \frac{\frac{\beta_e}{V_H}}{1 + \frac{1}{\kappa}\frac{V_g}{p_H}\frac{\beta_e}{V_H}}(Q_P - Q_M - k_l \Delta p) \\
&\Updownarrow \\
&\dot{p_H} = \frac{1}{\frac{V_H}{\beta_e} + \frac{1}{\kappa}\frac{V_g}{p_H}}(Q_P - Q_M - k_l \Delta p)
\end{aligned}
\tag{C.9}
$$

APPENDIX D

HPM Linearisation

The purpose with this appendix is to linearise the HPM manifold with the focus on the accumulator parameters. In Section 6.3.1 the linearisation of the HP manifold was evaluated for the pressure p_H, which affects the oil bulk modulus and the volumes V_H and V_g, by combining the non-linear terms in a term denoted $K_{\Delta p}$. In this linearisation the focus is to establish a expression where the influence from the accumulator precharge pressure p_{pr} and accumulator volume V_{acc} can be investigated.

The expression for the combined HPM with accumulator and the volumes V_H and V_g are shown in Equation (D.1), (D.2) and (D.3).

$$\dot{p_H} = \frac{1}{\frac{V_H}{\beta_e} + \frac{1}{\kappa}\frac{V_g}{p_H}}(Q_P - Q_M - k_{leak}\Delta p) \tag{D.1}$$

$$V_H = V_{pipe} + V_{acc} - V_g \tag{D.2}$$

$$V_g = V_{acc}\left(\frac{p_{pr}}{p_H}\right)^{\frac{1}{\kappa}} \tag{D.3}$$

It is assumed that the operation pressure of the HPM is p_H>p_{pr}>30 bar. Thus, the gradient of the effective oil bulk modulus is $\dot{\beta}_{ef} \approx 0$ and is therefore considered constant.

Inserting the expressions for the volumes, from Equation (D.2) and (D.3), in Equation (D.1), Equation (D.4) is established.

$$\dot{p}_H = \frac{1}{\frac{V_{pipe}+V_{acc}}{\beta_{ef}} - \frac{V_{acc}{p_{pr}}^{\frac{1}{\kappa}}{p_H}^{-\frac{1}{\kappa}}}{\beta_{ef}} + \frac{V_{acc}{p_{pr}}^{\frac{1}{\kappa}}}{\kappa}\frac{{p_H}^{-\frac{1}{\kappa}}}{p_H}}\Big(Q_P - Q_M - k_l\Delta p\Big) \tag{D.4}$$

From Equation (D.4) the constants K_H and K_g are found and defined in Equation (D.5) to simplify Equation (D.4).

$$K_H = \frac{V_{pipe} + V_{acc}}{\beta_{ef}} \qquad K_g = \frac{V_{acc} \cdot {p_{pr}}^{\frac{1}{\kappa}}}{\beta_{ef} \cdot \kappa} \tag{D.5}$$

Utilising the defined constants in Equation (D.5), substituting $p_H = \Delta p$+p_L and using the condition $\dot{p}_H$=$\Delta\dot{p}$, Equation (D.4) may be reduced to Equation (D.6)

$$\Delta\dot{p} = \frac{1}{\underbrace{K_H - \kappa K_g(\Delta p + p_L)^{-\frac{1}{\kappa}} + \beta_{ef}K_g(\Delta p + p_L)^{-\frac{\kappa+1}{\kappa}}}_{g_{\Delta p}}}\Big(Q_P - Q_M - k_l\Delta p\Big) \tag{D.6}$$

Where the auxiliary function $g_{\Delta p}$ is the denominator and is used to simplify the linearisation.

The linearisation of Equation (D.9) is done utilising first order Taylor approximation, neglecting higher order terms. For convenience, the first order derivative of Equation (D.9) may be described by the general expression given in Equation (D.7), which applied

to Equation (D.9), yields Equation (D.8).

$$\left[\frac{f()}{g()}h()\right]' = \frac{f()'g() - f()g()'}{g()^2}h()\bigg|_0 + \frac{f()}{g()}\bigg|_0 h()' \tag{D.7}$$

$$\delta\Delta\dot{p} = \frac{-1g'_{\Delta p}}{g^2_{\Delta p}}\Big(Q_P - Q_M - k_l\Delta p\Big)\bigg|_0 + \frac{1}{g_{\Delta p}}\bigg|_0 \Big(\delta Q_P - \delta Q_M - k_l\delta\Delta p\Big) \tag{D.8}$$

The linearisation point of the sum of flows is chosen under steady state operation such that $(Q_P - Q_M - k_l\Delta p)\big|_0 = 0$. Thus, the final linearised HPM pressure dynamics becomes that in Equation (D.9).

$$\delta\Delta\dot{p} = \underbrace{\frac{1}{g_{\Delta p}}\bigg|_0}_{K_{\Delta p}} \Big(\delta Q_P - \delta Q_M - k_l\delta\Delta p\Big) \tag{D.9}$$

APPENDIX E

Requirements

This section will describe some basic properties of AC power. The section is based on [Irwin, 2011, p. 557] .

The relationship between the apparent power, active power and reactive power is illustrated in the Power Triangle in Figure E.1. The relation is given in Equation (E.1).

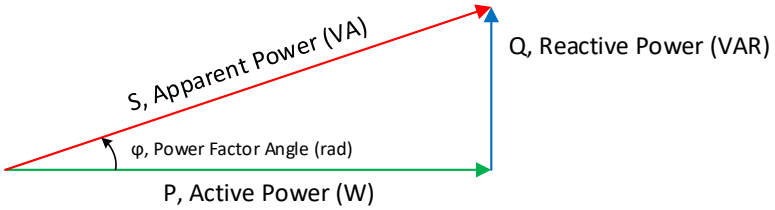

Figure E.1: Illustration of the relationship between apparent power, active power and reactive power indicated by the Power Triangle.

$$S = Pcos(\varphi) + Qsin(\varphi) \tag{E.1}$$

Where S is the apparent power, P is the active power and Q is the reactive power. φ is the power factor angle.

Active power P is given by Equation

$$P = UIcos(\varphi) \tag{E.2}$$

Reactive power Q is given by Equation

$$Q = UIsin(\varphi) \tag{E.3}$$

Where U and I are RMS phase voltage and RMS phase current, respectively.

The power factor can be calculated by Equation E.4.

$$PF = cos(\varphi) \tag{E.4}$$

APPENDIX F

Arbitrary Reference Frames

Reference frames are used to simplify the respective differential equation used to model an electrical machine and removing all position dependent variable. Furthermore, the arbitary reference frame is used to present the a given vector e.g. current or voltage utilising only two variables compared to three variables if utilising the standard *abc* reference frame seen in Figure F.1 [Krause et al., 2013].

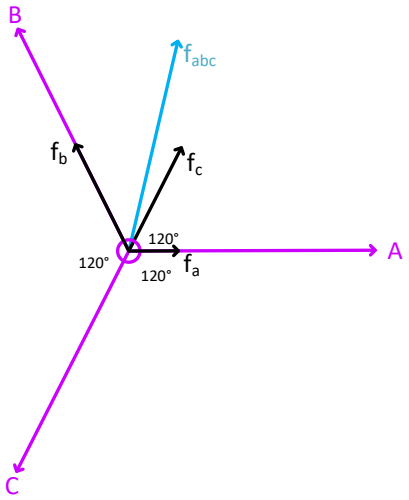

Figure F.1: The standard abc reference frame with the axis displaced a 120° apart.

As ít can be seen the axis are displaced 120° apart. This appendix will present the theory behind the utilised arbitrary reference frames in this project i.e. the Clark and Park Transformations.

F.1 Clarke Transformation

The Clarke transformation is a so called stationary $\alpha\beta$ reference frame with α axis aligned with the a axis of the *abc* reference frame and the real axis in a complex coordinate system. The β axis is always displaced 90° from the α axis i.e. the β axis is aligned with the imaginary axis of the as illustrated in Figure F.2. To go from the *abc* reference frame the the $\alpha\beta$ the Clarke Transformation is utilised which is defined by Equation (F.1).

$$\begin{bmatrix} \mathbf{f_\alpha} \\ \mathbf{f_\beta} \\ \mathbf{f_0} \end{bmatrix} = \frac{2}{3} \cdot \begin{bmatrix} 1 & -\frac{1}{2} & -\frac{1}{2} \\ 0 & \frac{\sqrt{3}}{2} & -\frac{\sqrt{3}}{2} \\ \frac{1}{2} & \frac{1}{2} & \frac{1}{2} \end{bmatrix} \begin{bmatrix} \mathbf{f_a} \\ \mathbf{f_b} \\ \mathbf{f_c} \end{bmatrix} \tag{F.1}$$

When assuming a balanced symmetrical system the zero component f_0 is equal to zero.

$$\mathbf{f} = \mathbf{f}_\alpha + j\mathbf{f}_\beta \tag{F.2}$$

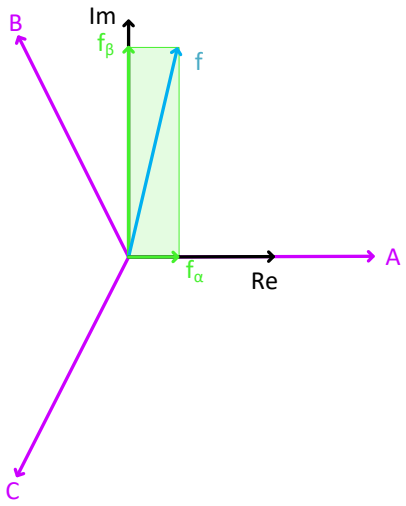

Figure F.2: The $\alpha\beta$ stationary reference frame obtained utilising the Clarke Transformation.

F.2 Park Transformation

The Park transformation is utilised to obtain a rotating reference frame compared to the Clarke transformation which only provides a stationary reference frame. Similar to the Clark transformation reduce the number of vectors from the three vectors, used in the abc to two components called $d-q$ components, hence the Park transformation is also known as the dq transformation. The d-axis is aligned with the real axis and the q axis is aligned with the imaginary axis. This frame is ratating with the synchonous speed of the electrical components in the system. By obtaining a synchronous speed the d-q components will obtain DC-values i.e. constant values which simplifies control of e.g. generators since DC references for the d-q components can be given. The Park Transformation is illustrated in Figure F.3.

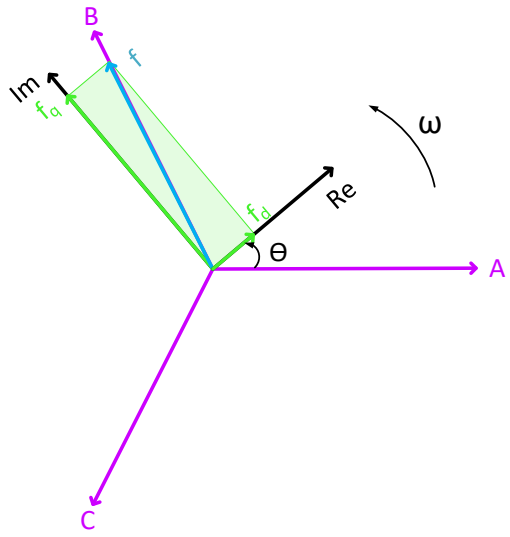

Figure F.3: Illustration of the *dq* rotating reference frame obtain utilisng the Park transformation.

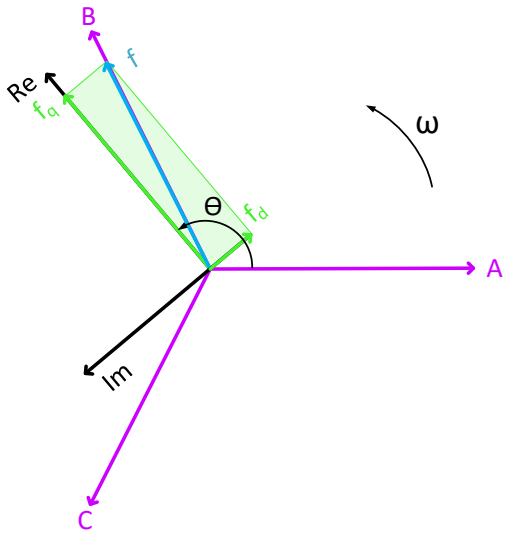

Figure F.4: Illustration of the *qd* rotating reference frame obtain utilisng the Park transformation.

The transformation matrix used to go from the abc reference frame to the dq reference frame is denoted $\mathbf{K_s}$ and given in Equation (F.3) [Park, 1929].

$$\begin{bmatrix} \mathbf{f_d} \\ \mathbf{f_q} \\ \mathbf{f_0} \end{bmatrix} = \frac{2}{3} \underbrace{\begin{bmatrix} cos\left(\theta\right) & cos\left(\theta - \frac{2\pi}{3}\right) & cos\left(\theta + \frac{2\pi}{3}\right) \\ sin\left(\theta\right) & sin\left(\theta - \frac{2\pi}{3}\right) & sin\left(\theta + \frac{2\pi}{3}\right) \\ \frac{1}{2} & \frac{1}{2} & \frac{1}{2} \end{bmatrix}}_{\mathbf{K_s}} \begin{bmatrix} \mathbf{f_a} \\ \mathbf{f_b} \\ \mathbf{f_c} \end{bmatrix} \tag{F.3}$$

Similar to the Clarke transformation, the zero component $\mathbf{f_0}$ is equal to zero in a balanced system. The vector f in Figure F.3 can be found utilising Equation (F.4) where the a axis is the reference

$$\mathbf{f} = \left(\mathbf{f_d} + j\mathbf{f_q}\right) e^{j\theta} \tag{F.4}$$

Another version of the park transformation is also utilised in this project. This version is called *qd* transformation and is illustrated in Figure F.4. The difference from the traditional *dq* reference frame is that it is the *q* axis which is aligned with the real axis and the *d* axis is aligned with the negative imaginary axis hence the following relation can be made:

$$\theta_{qd} = \theta_{dq} + \frac{\pi}{2}$$

And the vector $\mathbf{f}$ can be found utilising Equation (F.5).

$$\mathbf{f} = \left(\mathbf{f_q} - j\mathbf{f_d}\right) e^{j\theta} \tag{F.5}$$

APPENDIX G

SVPWM Sectors

This appendix contains the matrices used to define the duty cycle for each of the six sector in a three phase two level inverter.
For ease the process for the reader the space vector modulation diagram is displayed in Figure G.1.

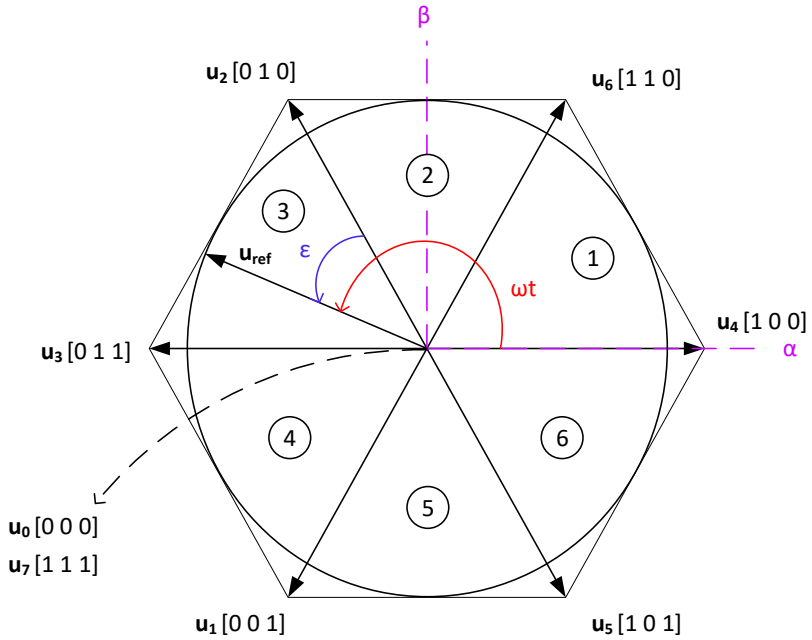

Figure G.1: A SVPWM diagram illustrting the 6 different sectors and the related voltage vectors and null vectors.

Sector 1

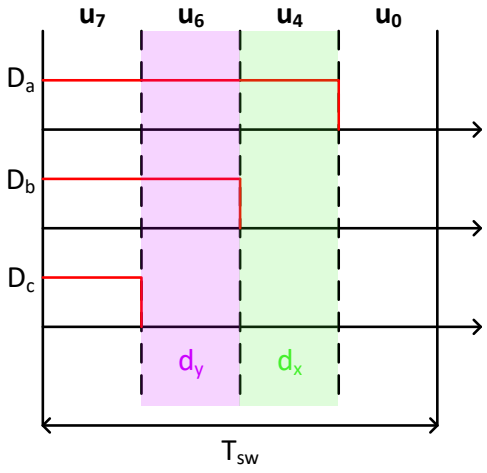

$$\begin{bmatrix} 1 \\ d_x \\ d_y \end{bmatrix} = \begin{bmatrix} 1 & 0 & 1 \\ 1 & -1 & 0 \\ 0 & 1 & -1 \end{bmatrix} \begin{bmatrix} D_a \\ D_b \\ D_c \end{bmatrix}$$
$$\begin{bmatrix} D_a \\ D_b \\ D_c \end{bmatrix} = \frac{1}{2} \cdot \begin{bmatrix} 1 & 1 & 1 \\ 1 & -1 & 1 \\ 1 & -1 & -1 \end{bmatrix} \begin{bmatrix} 1 \\ d_x \\ d_y \end{bmatrix} \tag{G.1}$$

Sector 2

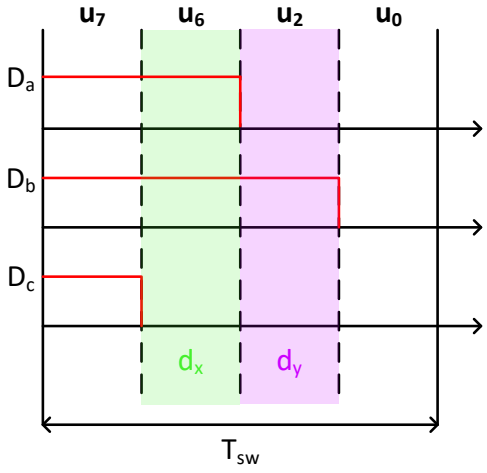

$$\begin{bmatrix} 1 \\ d_x \\ d_y \end{bmatrix} = \begin{bmatrix} 0 & 1 & 1 \\ 1 & 0 & -1 \\ -1 & 1 & 0 \end{bmatrix} \begin{bmatrix} D_a \\ D_b \\ D_c \end{bmatrix}$$
$$\begin{bmatrix} D_a \\ D_b \\ D_c \end{bmatrix} = \frac{1}{2} \cdot \begin{bmatrix} 1 & 1 & -1 \\ 1 & 1 & 1 \\ 1 & -1 & -1 \end{bmatrix} \begin{bmatrix} 1 \\ d_x \\ d_y \end{bmatrix} \tag{G.2}$$

Sector 3

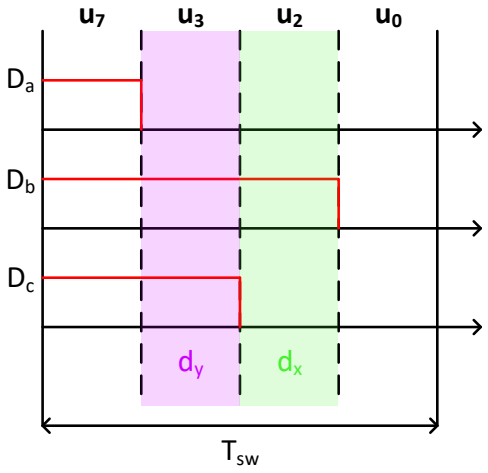

$$\begin{bmatrix} 1 \\ d_x \\ d_y \end{bmatrix} = \begin{bmatrix} 1 & 1 & 0 \\ 0 & 1 & -1 \\ -1 & 0 & 1 \end{bmatrix} \begin{bmatrix} D_a \\ D_b \\ D_c \end{bmatrix}$$
$$\begin{bmatrix} D_a \\ D_b \\ D_c \end{bmatrix} = \frac{1}{2} \cdot \begin{bmatrix} 1 & -1 & -1 \\ 1 & 1 & 1 \\ 1 & -1 & 1 \end{bmatrix} \begin{bmatrix} 1 \\ d_x \\ d_y \end{bmatrix} \tag{G.3}$$

Sector 4

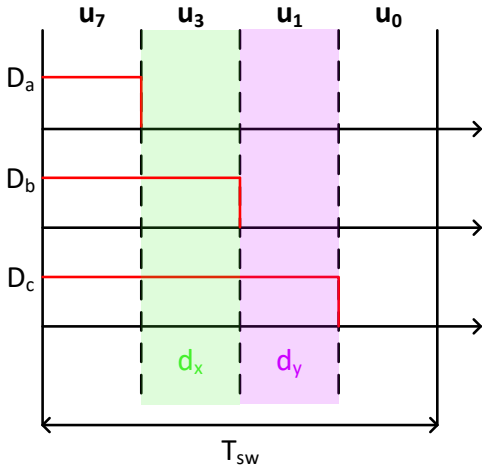

$$\begin{bmatrix} 1 \\ d_x \\ d_y \end{bmatrix} = \begin{bmatrix} 1 & 0 & 1 \\ -1 & 1 & 0 \\ 0 & -1 & 1 \end{bmatrix} \begin{bmatrix} D_a \\ D_b \\ D_c \end{bmatrix}$$
$$\begin{bmatrix} D_a \\ D_b \\ D_c \end{bmatrix} = \frac{1}{2} \cdot \begin{bmatrix} 1 & -1 & -1 \\ 1 & 1 & -1 \\ 1 & 1 & 1 \end{bmatrix} \begin{bmatrix} 1 \\ d_x \\ d_y \end{bmatrix} \tag{G.4}$$

Sector 5

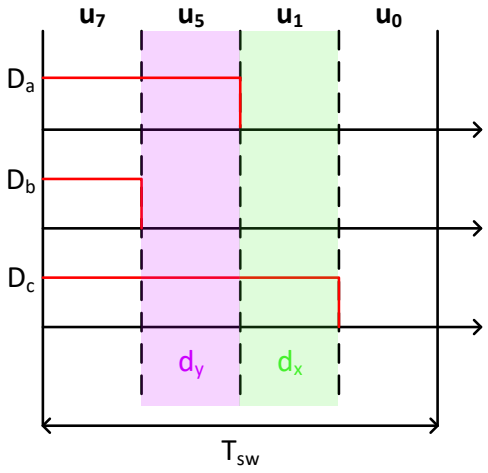

$$\begin{bmatrix} 1 \\ d_x \\ d_y \end{bmatrix} = \begin{bmatrix} 0 & 1 & 1 \\ -1 & 0 & 1 \\ 1 & -1 & 0 \end{bmatrix} \begin{bmatrix} D_a \\ D_b \\ D_c \end{bmatrix}$$
$$\begin{bmatrix} D_a \\ D_b \\ D_c \end{bmatrix} = \frac{1}{2} \cdot \begin{bmatrix} 1 & -1 & 1 \\ 1 & -1 & -1 \\ 1 & 1 & 1 \end{bmatrix} \begin{bmatrix} 1 \\ d_x \\ d_y \end{bmatrix} \tag{G.5}$$

Sector 6

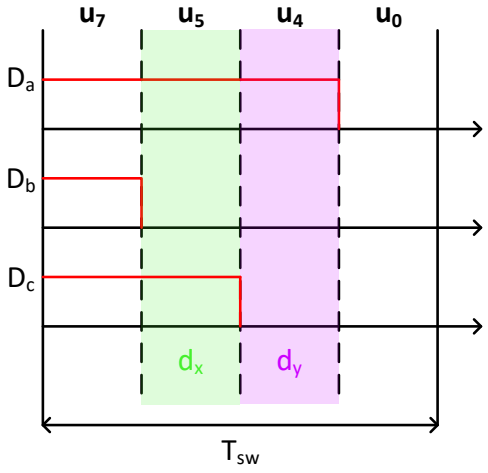

$$\begin{bmatrix} 1 \\ d_x \\ d_y \end{bmatrix} = \begin{bmatrix} 1 & 1 & 0 \\ 0 & -1 & 1 \\ 1 & 0 & -1 \end{bmatrix} \begin{bmatrix} D_a \\ D_b \\ D_c \end{bmatrix}$$
$$\begin{bmatrix} D_a \\ D_b \\ D_c \end{bmatrix} = \frac{1}{2} \cdot \begin{bmatrix} 1 & 1 & 1 \\ 1 & -1 & -1 \\ 1 & 1 & -1 \end{bmatrix} \begin{bmatrix} 1 \\ d_x \\ d_y \end{bmatrix} \tag{G.6}$$

Supplements

SUPPLEMENT A

Simulink Constants

In this supplement the MATLAB constants, used to simulate the model, are presented. The constants are divided up into hydraulic constant and electrical constants.

A.1 Hydraulic Constants

Wind Turbine

Parameter	Symbol	Value	Unit	Source
Rotor Radius	r_r	63	m	[1]
Rotor swept area	A_r	$1.247 \cdot 10^4$	m^2	[1]
Tower Hight	H_t	90	m	[1]
Optimal TSR	λ^*	7.55	$-$	[1]
Rotor inertia	J_r	$3.87 \cdot 10^7$	$kg \cdot m^2$	[1]
Rated Rotor Speed	$\omega_{r,nom}$	12.1	RPM	[1]
Initial rotor speed	$\omega_{r,ini}$	11.1	RPM	[1]
Max power coefficient	C_p	0.485	$-$	[1]
Density of air	ρ_{air}	1.225	$\frac{kg}{m^3}$	[1]
Viscous damping coefficient	B_v	$50 \cdot 10^3$	$\frac{N \cdot m \cdots}{rad}$	[1]
Initial rotor speed	$\omega_{r,ini}$	11.1	RPM	[1]
Cut in wind speed	v_{in}	4	$\frac{m}{s}$	[1]
rated wind speed	v_{nom}	11.4	$\frac{m}{s}$	[1]
Cut out wind speed	v_{out}	25	$\frac{m}{s}$	[1]

Table A.1: [1][Pedersen, 2016*b*].

DD Pump

Parameter	Symbol	Value	Unit	Source
Piston stroke length	$L_{P,cyl}$	$5.4 \cdot 10^{-2}$	m	[1]
Piston diameter	D_p	$10.8 \cdot 10^{-2}$	m	[1]
Piston area	$A_{P,p}$	$9.2 \cdot 10^{-3}$	m^2	[1]
Lobe radius	r_c	$2.7 \cdot 10^{-2}$	m	[1]
Cylinder displacement volume	V_p	$4.9469 \cdot 10^{-4}$	m^3	[1]
Cylinder dead volume	V_0	$4.9469 \cdot 10^{-4}$	m^3	[1]
Number of cylinders in a module	N_{cyl}	25	-	[1]
Number of lobes in a module	N_{lobe}	16	-	[1]
Number of modules	N_m	4	-	[1]
Total displacement volume	V_P	0.126	m^3	[1]
Hydro mechanical efficiency	η_P	0.95	-	[1]
Valve actuation time	t_S	$1 \cdot 10^{-3}$	s	[1]
Chamber flow coefficient	k_f	$0.5 \cdot 10^5$	$\frac{\sqrt{Pa}s}{m^3}$	[1]
Maximum speed	$\omega_{r,max}$	12.1	RPM	[1]
LPV closing angle	θ_{Lcl}	3.1208	rad	[1]
HPV closing angle	θ_{Hcl}	6.2624	rad	[1]

Table A.2: [1][Pedersen, 2016*b*].

DD Motor

Parameter	Symbol	Value	Unit	Source
Piston stroke length	$L_{M,cyl}$	$5 \cdot 10^{-2}$	m	[1]
Piston diameter	D_p	$6.25 \cdot 10^{-2}$	m	[1]
Piston area	$A_{M,p}$	$3.1 \cdot 10^{-3}$	m^2	[1]
Eccentric radius	r_c	$2.5 \cdot 10^{-2}$	m	[1]
Cylinder displacement volume	V_m	$1.534 \cdot 10^{-4}$	m^3	[1]
Cylinder dead volume	V_0	$1.534 \cdot 10^{-4}$	m^3	[1]
Number of cylinders in a module	N_{cyl}	7	-	[1]
Number of modules	N_m	6	-	[1]
Total displacement volume	V_M	$1 \cdot 10^{-3}$	m^3	[1]
Hydro mechanical efficiency	η_P	0.95	-	[1]
Rated speed	$\omega_{M,nom}$	1500	RPM	
Initial motor speed	$\omega_{M,ini}$	1500	RPM	
Viscous damping coefficient	B_v	3.3	$\frac{N \cdot m \cdot s}{rad}$	
Valve actuation time	t_S	$1 \cdot 10^{-3}$	s	[1]
Chamber flow coefficient	k_f	$0.5 \cdot 10^5$	$\frac{\sqrt{Pa}s}{m^3}$	[1]
Maximum speed	$\omega_{r,max}$	12.1	RPM	[1]
LPV closing angle	θ_{Lcl}	5.8102	rad	[1]
HPV closing angle	θ_{Hcl}	2.5569	rad	[1]

Table A.3: [1][Pedersen, 2016*b*] [2] Roemer [2014].

Pipeline

Parameter	Symbol	Value	Unit	Source
Pipe diameter	D_p	0.2	m	[1]
Pipe length	L_p	4	m	[1]
Pipe volume	V_{pipe}	126.8	L	[1]

Table A.4: [1] Chapter 5.

Oil properties

Parameter	Symbol	Value	Unit	Source
Bulk Modulus	β_{ef}	16000	bar	-
Percent air in oil at atmospheric pressure	$V_{\%-air}$	1	%	-
Transmission leakage coefficient	k_{leak}	$0.1 \cdot 10^{-10}$	$\frac{m^3}{Pa}$	-
High Pressure Level	$p_{H,max}$	360	bar	-
Low Pressure Level	$p_{L,max}$	10	bar	-
Atmospheric Pressure	p_{atm}	1	bar	-

Table A.5

Accumulator

Parameter	Symbol	Value	Unit	Source
Accumulator total volume	V_{acc}	10	L	[2]
Precharge precharge	p_{pr}	75	bar	[2]
Polytropic constant	κ	1.4	-	[1]

Table A.6: [1][Rabi, 2009], [2] Chapter 5.

A.2 Electrical Constants

PMSG

Parameter	Symbol	Value	Unit	Source
Maximum Flux Linkage	λ_{mpm}	13.08	Wb	[1]
Number of pole pairs	N_{pp}	2	-	[2]
Inertia	J_g	231.3	$Kg \cdot m^2$	[1]
Rated velocity	ω_{rat}	1500	RPM	[2]
Switching Frequency	f_s	10^3	Hz	[2]
Inverter Frequency	f_{spwm}	$5 \cdot 10^3$	Hz	[2]
Stator Inductance	L_d	15.4	mH	[1]
Stator Phase Resistance	R_s	37.5	$m\Omega$	[1]
Rated Current	I_{rat}	1080	A	[1]
Maximum current in phase	$i_{ph,max}$	$I_{rat}\sqrt{2}3$	A	[2]
Maximum RMS phase voltage	U_s	4800	V	[1]
Maximum phase voltage	$u_{ph,max}$	$u_s \cdot \sqrt{2}$	V	[2]

Table A.7: [1][Mazaheri, 2012], [2] Chapter 5.

Grid and DC-link

Parameter	Symbol	Value	Unit	Source
Grid inductance	L_t	1.3	mH	[1]
Grid Resistance	R_t	0.5	Ω	[1]
Line to line RMS grid voltage	$u_{g,ll}$	6.6	kV	[1]
Voltage ripple	Δu_{max}	$1\% \cdot u_{dc}$	V	[1]
Fundamental frequency	f_0	50	$[Hz]$	[1]
Switching frequency	f_{sw}	$100 \cdot f_0 = 5$	kHz	[1]
Power average of capacitor	P_{dc}	5	MW	[1]
DC-link capacitor	C_{dc}	1.5218	μF	[1]

Table A.8: [1] Chapter 5

SUPPLEMENT B

Hydrostatic Transmission Images

To give a sense of scale of the hydrostatic transmission, some images of the Artemis DFPT are shown in Figure B.1 and B.2. The Artemis DFPT is utilised in the 7 MW wind turbine prototype called SeaAngle from MHI.

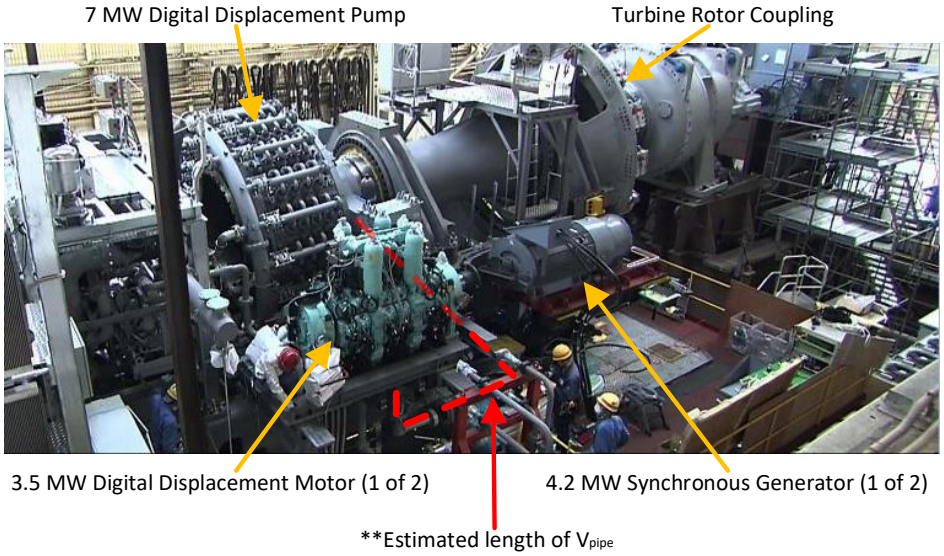

Figure B.1: Image of Artemis hydrostatic transmission utilised in the prototype 7 MW wind turbine SeaAngel [Artemis, 2016]. The ** indicate that the pipe connection is a rough estimate.

In Figure B.1 the Artemis DFPT is seen to consist of a 7 MW DD Pump mounted directly on the rotor shaft. On each side of the DD Pump two 3.5 MW DD Motors are placed. A 4.2 MW Synchronous generator is connected directly to each of the DD Motors.

In Roemer [2014, p. 10] the dimensions of the DD pump and DD motor in the Artemis DFPT have been investigated from the images of the Artemis DFPT and from patent descriptions. This data are repeated in Table B.1 with the purpose to have a basis for the dimensioning estimates in this project based on this data.

Dimensions	**DD Pump**	**DD Motor**
Size**	ø4.5 m x 1.5 m	ø0.8 m x 2 m

Table B.1: Size dimensions of the DD pump and DD motor from [Roemer, 2014, p. 10]. The ** indicate that the values are rough estimates.

B.0.1 HPM length estimation

To dimensioning the length of V_{pipe} in the HPM connecting the DD pump and DD motor is this project, the images of the Artemis DFPT have been investigated to give a qualified guess on the manifold pipe length. This connection is shown in Figure B.1 with

the dotted red line as it is seen from Figure B.2 that the HP and LP connection pipes is connected from below the DD motor.

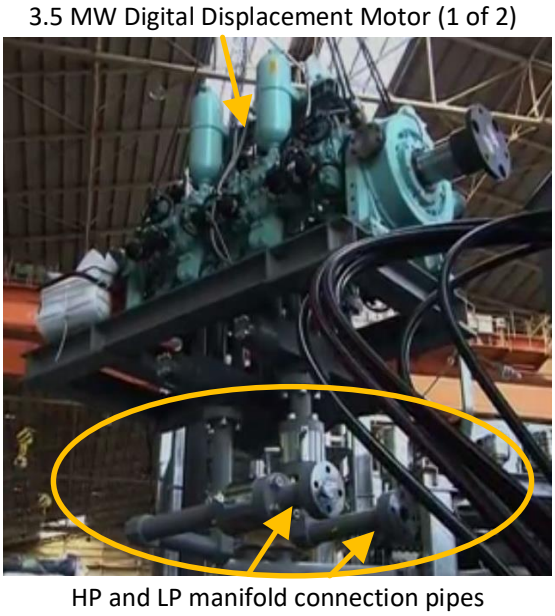

Figure B.2: Image of Artemis 3.5 MW DD motor utilised in the prototype 7 MW wind turbine SeaAngel [Artemis, 2016].

Taking a rough estimate by investigating the images in Figure B.1 and B.2 and taking the sizes of the components from Table B.1 into consideration, the length of V_{pipe} is estimated to be 4 metres from DD pump to each DD motor.